PHOTOELECTROCHEMICAL CHARACTERIZATION OF DYE SOLAR CELLS BASED ON NANOSTRUCTURED ZINC OXIDE SUBSTRATES

Elena Guillén Rodríguez

Department of Physical, Chemical and Natural Systems

University Pablo de Olavide

Sevilla, May 2011

PHOTOELECTROCHEMICAL CHARACTERIZATION OF DYE SOLAR CELLS BASED ON NANOSTRUCTURED ZINC OXIDE SUBSTRATES

DIRECTOR

JUAN ANTONIO ANTA MONTALVO

Profesor Titular del Departamento de Sistemas Físicos, Químicos y Naturales de la Universidad Pablo de Olavide

Trabajo presentado para la obtención del título de Doctora con Mención Europea

Elena Guillén Rodríguez

Licenciada en Ciencias Ambientales

Department of Physical,
Chemical and Natural Systems
University Pablo de Olavide

Juan Antonio Anta Montalvo, profesor titular del Departamento de Sistemas Físicos, Químicos y Naturales de la Universidad Pablo de Olavide

CERTIFICA:

Que la presente memoria titulada "Photoelectrochemical characterization of dye solar cells based on nanostructured zinc oxide substrates" presentada por Elena Guillén Rodríguez para la obtención del título de Doctora, ha sido realizada bajo mi dirección en este departamento, dentro del programa de Ciencia y Tecnología de Coloides e Interfases y cumple los requisitos para poder optar a la Mención Europea.

Sevilla, Mayo de 2011

Juan Antonio Anta Montalvo

Abstract

This thesis is focused on the study of dye-sensitized solar cells (DSCs) based on the semiconductor zinc oxide (ZnO) as electron conductor.

The work presented in this thesis is divided in four main topics: (1) the search for an appropriate sensitizer for ZnO, (2) the suitability of ionic-liquid-based electrolytes for the development of ZnO solar cells with high long-term stability, (3) the influence of the semiconductor morphology on the performance of ZnO-based solar cells and (4) the study of the electronic properties of this semiconductor in DSCs.

Finding an appropriate dye is a key issue for DSCs based on ZnO. In this work, several sensitizers have been tested, including xanthene derivatives, ruthenium-complex dyes and an indoline derivative. The study points out the poor properties of ruthenium-complex dyes as sensitizers for ZnO and the great potential of organic dyes. It is found that the sensitization process is less critical in the case of organic dyes than in the case of ruthenium-complex dyes. Good absorbing properties together with an efficient sensitization process lead to a better performance of the indoline dye D149 with respect to other dyes tested, including ruthenium derivatives. However, a recurrent topic along this thesis has been the dye-oxide interaction in ZnO DSCs. This interaction is proved to be weak and dye desorption in the presence of ionic-liquid-based electrolytes and additives usually employed in DSCs have been observed for both, ruthenium and organic dyes, although this effect is more critical for organic sensitizers.

One of the cell components limiting the long-term stability of DSCs is the organic solvent electrolyte. The replacement of organic solvents by room temperature ionic liquids (RTIL) is very promising due to their negligible vapour pressure, which avoids evaporation problems. The use of this type of electrolyte in ZnO cells had not been explored before and an important part of this thesis has been devoted to the study of ZnO solar cells based on RTIL-based electrolytes. Several ionic-liquid-based systems have been tested and the suitability of this kind of electrolyte for ZnO solar cells as well as the main limitations have been identified and described. It is found that the cell performance is not only determined by the viscosity of the electrolyte, but also by the nature of the anion of the ionic liquid. By mixing RTILs with different viscosity and containing different anions, the performance of the cells can be optimized.

Higher recombination with respect to organic-solvent-based electrolytes has turned out to be the main limitation of ZnO solar cells based on RTIL electrolytes. Nevertheless, remarkable efficiencies have been obtained for ZnO solar cells with fully organic dyes and ionic-liquid-based electrolytes. However, dye desorption has been observed at prolonged illumination limiting cell stability.

One of the most interesting properties of ZnO is the possibility of fabricating a wide range of different nanostructures. Specifically, the use of one-dimensional ZnO nanostructures as electrodes is a hot topic in DSC research. However, despite the efforts devoted to the development of ordered nanostructures, their efficiencies lie well below the ones obtained with mesoporous nanoparticle electrodes. This fact is usually attributed to low light harvesting properties due to the lower surface area of one-dimensional nanostructures. In this thesis, a comparative study of ZnO solar cells sensitized with the highly absorbing dye D149 and based on ordered nanowire array electrodes, on the one hand, and a randomly oriented nanoparticle electrode, on the other hand, is presented. The study points out that recombination rather than low surface area is the main limitation of these one-dimensional nanowires. In addition, a significant blocking of the recombination in nanowire solar cells is achieved by the deposition of nanoparticles onto the nanowires, improving significantly the efficiency of the cells.

The last part of the work has been devoted to a comprehensive study of the electronic behaviour of dye-sensitized solar cells based on ZnO. The same theories as used for TiO_2 can be applied to describe the transport and recombination behaviour of ZnO solar cells, yielding, however, different characteristic parameters. The results highlight very good electronic properties of ZnO solar cells, with diffusion lengths several orders of magnitude larger than the film thickness. A poor injection from the dye to the semiconductor is proposed as the main limitation of the ZnO solar cells studied here.

Contributing work and publications

The original work presented in this thesis is mostly included in the following publications:

"Photovoltaic performance of nanostructured zinc oxide sensitised with xanthene dyes", E. Guillén, F. Casanueva, J. A. Anta, A. Vega-Poot, G. Oskam, R. Alcántara, C. Fernández-Lorenzo, J. Martín-Calleja. *Journal of Photochemistry and Photobiology A: Chemistry*, 364-370 (2008)

"Solvent-free ZnO dye-sensitised solar cells", E. Guillén , C. Fernández-Lorenzo, R. Alcántara, J. Martín-Calleja, J. A. Anta. *Solar Energy Materials and Solar Cells*, 93, 1846-1852 (2009)

"Numerical Simulation of the current-voltage curve in dye-sensitised solar cells" J. Villanueva, J. A. Anta, E. Guillén, G. Oskam. *Journal of Physical Chemistry C*, **113**, 19722–19731 (2009)

"ZnO-based dye solar cell with solvent-free electrolyte and organic sensitizer", E. Guillén, J. Idígoras, T. Berger, J. A. Anta, C. Fernández-Lorenzo, R. Alcántara, J. Martín-Calleja, *Physical Chemistry Chemical Physics.* **13**, 207-213 (2011)

"ZnO solar cells with an indoline sensitizer: a comparison between nanoparticulate films and electrodeposited nanowire arrays", E. Guillén, E. Azaceta, L. M. Peter , A. Zukal , R. Tena-Zaera , J. A. Anta. *Energy & Environmental Science*, DOI:10.1039/C0EE00500B, (2011)

"Transport and recombination in ZnO-based dye sensitized solar cells", E. Guillén, L. M. Peter, J. A. Anta. Manuscript in preparation, (2011）

Table of Contents

Chapter 1

Introduction

1.1. Introduction to solar energy and solar cells

The growing worldwide energy demand and the environmental impact of the extensive exploitation of fossil fuels during the last decades have motivated the search for alternative sources of energy. Special attention is paid nowadays to the development of new technologies allowing for the utilization of so-called renewable energy sources. Renewable energy is derived from natural processes that are replenished constantly. Tapping into these energy sources is desirable both from an ecological and an economic point of view. Nowadays, renewable energy is the fastest-growing source of electricity generation with main contributions from hydroelectric and wind power. Furthermore, solar power generation has experienced accelerated growth during the last decade. The renewable share of worldwide electricity generation is expected to grow from 18 percent in 2007 to 23 percent in 2035[1]. The optimization of the existing processes for power generation and the development of new technologies are, therefore, a matter of scientific, technological, economic and public concern.

Mankind has exploited solar power since ancient times, but it was not until the 19th century that a first approach to a photovoltaic use of solar energy was made. Since that time, the idea of using the clean and abundant energy of the Sun and converting it into electricity has been a recurring topic in the scientific community and in society in general. However, it was not until the beginning of the 21st century that grid connected photovoltaic systems started to make a real contribution to electrical power generation. The photovoltaic industry has boomed over the past decade. Apart from the increasing public awareness that the Earth´s oil reserves will run out in a not so distant future, the development of photovoltaic technology is also promoted by an environmental concern among the society. In this respect, solar power generation comprises a promising electric power generation technology due to relatively low life cycle emissions of global warming gases.

Concerned about climate change and energy dependence, governments introduced incentives to promote the adoption of solar energy and to shift consumption away from fossil fuels to a more secure supply. As a consequence of these incentives the photovoltaic industry grew in the last decade at a rate exceeding 30% per year (**Figure 1.1**). An example of the booming of the photovoltaic market can be found in Spain. The energy system in Spain depends strongly on importations with about 80% of the energy

consumption deriving from imported sources[2]. At the same time, Spain possesses the most important solar resources in Europe (1200-1800 kWh m^{-2} $year^{-1}$ [3]). In 2005, the Spanish government approved the Renewable Energy Plan 2005–2010[4]. Its overall aim was to meet the target of supplying 12% of Spain's primary energy needs and 30% of its demand for electricity from renewable sources by 2010. A great boost was given to the photovoltaic (PV) sector with very attractive tariffs, and in 2008 Spain became the PV market leader with 2.6 GW of new grid-connected installations (**Figure 1.1**).

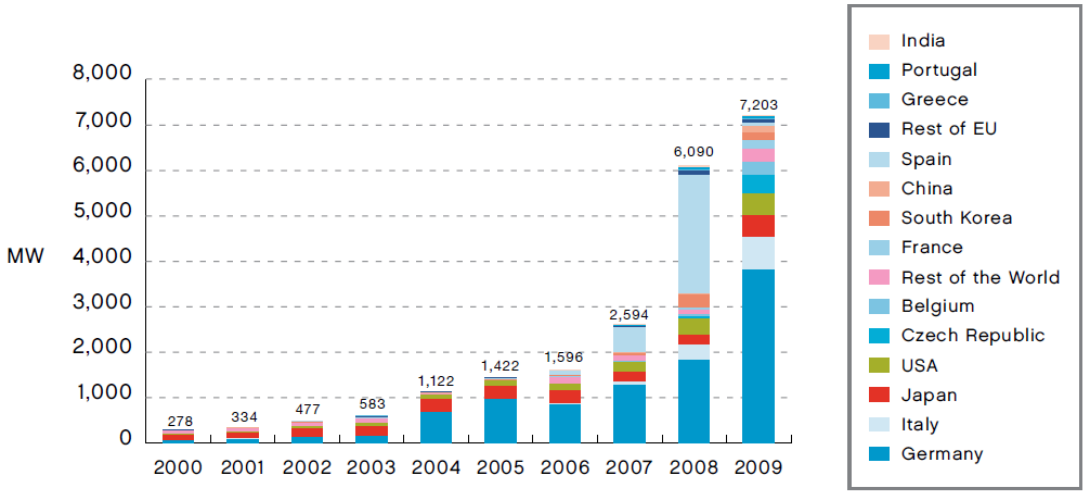

Figure 1.1 Evolution of the World annual PV market (2000-2009). Source [5].

Although remarkable, this explosive growth was only possible thanks to the heavily subsidized program implemented by the government. After this record-breaking year in 2008, the Spanish government placed a cap limiting the number of new PV installations, because it was not possible to economically support the incentive program. As a consequence of this fact, together with the financial crisis, the number of new photovoltaic installations plumed dramatically to only 69 MW in 2009[5] (**Figure1.1**).

What happened in Spain is not a representative case and what is needed for continuous market development is not a high feed-in tariff, but a stable and long-term policy and program. However, the example of Spain shows a characteristic that shares currently the global PV market: the strong dependence on government support programs and incentives. The main problem in this context is the currently too high $/Wp cost of energy generated by PV modules. There is still a long way to go in order to make the cost of photovoltaic energy generation comparable to that of electricity generated by power plants based on fossil fuels.

Current production of PV modules is dominated by crystalline silicon modules based on bulk wafers (including both large-grain polycrystalline and single-crystalline Si)[6]. These devices are the main exponents of a group named as the first generation of photovoltaic cells and they comprised about 85% of the market in 2009[7].

The p-n junction is the classical model of a conventional solar cell[8]. This junction is created by doping different regions of the same semiconductor with different impurities. In this way, an interface between p-type and n-type materials is obtained, which creates a built-in electric field as a consequence of the different chemical potentials that electrons and holes have across the interface. This intrinsic electric field favours charge-separation when a photon of energy larger than the band-gap creates an electron-hole pair near the interface.

There have been several theoretical calculations on the maximum power conversion obtainable for solar radiation using a single-junction (p-n) solar cell. The theoretical considerations of Shockley and Queisser establish an upper limit of the efficiency of 31% for a semiconductor with a band gap energy (E_g) of 1.3 eV under AM 1.5 illumination[9]. There are two main reasons for such a low maximum efficiency. On the one hand, photons with an energy $E < E_g$ are not absorbed by the solar cell. On the other hand, even electrons excited by photons with an energy $E > E_g$ can only deliver the band gap energy (E_g) to the electric circuit, whereas the rest (E-E_g) is lost by thermal dissipation[10]. Based on this theoretical maximum conversion efficiency and on the nature of materials, photovoltaic cells can be grouped in three major categories or generations. The first group includes cells that use materials of high purity and containing low concentrations of structural defects. These are the most efficient cells up to date. To this group belong, as already mentioned, crystalline silicon solar cells with a confirmed record efficiency of 25% by the time of writing[11(i)]. Although it has been the material most frequently employed and studied, silicon is not an ideal semiconductor for photovoltaic conversion. Its optical absorption coefficient is low due to the fact that it is an indirect semiconductor. Therefore, Si wafers with a thickness of more than hundred microns are needed to efficiently absorb most of the incident light. This, together with costly purification and crystallisation processes of silicon, make the production of silicon cells very expensive. Binary II-IV and II-V semiconductors such as GaAs,

[i] Cell area: 4 cm^2.

GaAlAs, GaInAsP, InAs, InSb and InP also fall into this group. They are interesting solar cell materials because they have near-optimal band gaps[8]. However, these materials are extremely expensive. They have been used mainly in space solar cells, where performance is more important than costs. Also they can find a place in concentrating systems where the active surface area of the cells can be reduced significantly and, therefore, expensive materials can be used. Si-based first-generation photovoltaics is a robust and proven PV technology, but its cost reduction potential seems to be limited. In addition, although there is still room for improvement, efficiencies of silicon solar cells are yet close to the theoretical Shockley-Queisser limit for a single junction cell[6].

Two different approaches have been made to face the problems associated with first generation photovoltaics: (a) to work on reducing the costs and (b) to increase the energy conversion efficiency beyond the Shockley–Queisser limit. The major thrust along the first approach is in developing thin film solar cells. These devices are usually referred to as second generation photovoltaics. On the other hand, approaches focused on devices, which could theoretically overcome the Shockley-Queisser limit, form the basis of third-generation PV technologies.

The second generation of solar cells is based on thin film technology. These cells are based on a single junction and, therefore, share with first generation photovoltaics the theoretical efficiency limit. Thin film devices comprise a smaller but rapidly growing segment of the PV activity. In the year 2009, the market share of thin film solar cells reached 15%[6]. The driving force for the development of thin film solar cells has been their potential for the reduction of manufacturing costs. The most efficient examples are solar cells made up of cadmium telluride (CdTe) and copper indium gallium diselenide (CIGS). These materials are direct semiconductors, thus, only a thin film (of about 10 μm thickness) is required for complete light absorption[12]. CdTe, for example, has a direct optical band gap of 1.5 eV that lies near the optimum band gap according to Shockley and Queisser[6]. In addition thin film semiconductor materials can be deposited onto large surfaces, which is beneficial for volume production. PV modules based on crystalline silicon, in contrast, have to be assembled from individual cells. The efficiencies of second generation devices, however, are typically lower than efficiencies of first generation cells. In contrast to PV devices based on Si wafers, which are already very close to the theoretical efficiency limit, thin film solar cells are still well below

their potential. Thin film technologies are in the early manufacturing phase, and efficiencies of small-area laboratory devices do not easily translate into efficiencies of large modules. The highest performance obtained among all thin film technologies was for a CIGS cell of 1 cm^2 with 19.4 %[11]. The main issues associated with this kind of technology are the use of toxic materials as, e.g., cadmium and rare elements as telluride and indium. The implementation of a technology marketed as environmentally friendly that uses hazardous metals is quite controversial.

During the past decades several approaches to a third generation of solar cells have been suggested. The term third generation includes various technologies. Generally this term is used to describe systems which do not fall into the first or second generation and/or which try to circumvent the 31% Shockley-Queisser limit[12]. Various approaches to achieve efficiencies above 30% have been explored. Tandems of cells provide the best known example of how such high efficiency might be achieved. In this case, conversion efficiency can be increased by stacking cells of different band gaps thus increasing the spectral sensitivity[13]. In principle, by stacking a large number of suitably tailored and designed cells, efficiencies as high as 67% and 86% for unconcentrated and maximally concentrated solar illumination are theoretically possible[6].

In the 1990s, new concepts of solar cells based on nanostructured and organic materials were conceived as a new approach to low-cost photovoltaics. The most active research fields comprise organic heterojunctions[14], extremely thin absorber (ETA) cells[15-17], hybrid solar cells[18,19] and dye-sensitized solar cells[20]. These new solar cells have a big potential of development since molecular and nanostructural engineering approaches can be exploited for further improvement. In an organic heterojunction the active layer is made up of two materials: a donor (n-type) and an acceptor (p-type). Poly-phenylene vinylene derivatives and poly-alkylthiophenes are common donors; fullerene and its derivatives are common acceptors. The best confirmed photoconversion obtained for this type of devices is 5.15%[11(ii)]. The three-phase ETA cells are completely made up of solid inorganic materials. In these cells, a thin light-absorbing semiconductor is sandwiched between two transparent, highly interpenetrated nanostructured semiconductors which act as electron and hole conductors[16,21,22]. Usually, wide band gap semiconductors as TiO_2 and ZnO are used as electron

[ii] Cell area: 1.021 cm^2

conductors and CuSCN as hole conductor. A wide variety of inorganic absorbers can be employed and the best efficiencies (3.5-4%[15,23]) up to now for completely inorganic ETA cells have been obtained using In_2S_3. In hybrid solar cells, in contrast to the previous two kinds of cells, both organic and inorganic materials are combined. They are usually composed of a conjugated polymer, which absorbs light and transports holes, and an inorganic electron conductor, both assembled together in a heterojunction. Power conversion efficiencies above 5% have been achieved with this type of cells[24].

Finally, dye-sensitized solar cells (DSCs)[20] are based on nanostructured wide band gap semiconductor films photosensitized with a dye. In 1991, M. Grätzel and B. O´Regan reported on a device made of sensitized nanoporous TiO_2 with a conversion efficiency of 7.1%[20]. This discovery opened a new field of scientific research and since then many research groups have worked on the improvement of the efficiency and the stability of this kind of solar cells. This field has experienced a boom in the last decade, with two or three research articles published every day[10]. At the time of writing, the record AM 1.5[iii] efficiency for a DSC stood at 11.1%[25 iv].

It is still not clear, which one of all the technologies described above will determine the future of photovoltaics. Most probably the optimum solution will depend on the respective application and on other factors as, for example, the location. In that case, a major diversification of the photovoltaic market will be the most likely scenario in the near future.

1.2. Dye-sensitized solar cells

As shown in the previous section, the widespread accepted paradigm in traditional solar energy conversion is to use highly pure semiconductor materials (avoiding defects and interfaces) and to rely on a built-in electrical field to assist the separation of photogenerated electron-hole pairs. Besides, a semiconductor band gap close to an optimum for solar energy absorption is desirable. In this regard, dye-sensitized solar cells (DSCs) marked a fundamental innovation as they rely on nanostructured, wide band gap semiconductors. As will be described in this Chapter, DSCs work without the

[iii] Standard spectral illumination used for photovoltaic solar cell testing. More details can be found in **Chapter 4**.

[iv] Cell area: 0.219 cm^2

need for a built-in electrical field, without a strict control of the purity of materials, and besides, the presence of a huge internal interface is crucial for their good functioning. The backbone of a dye-sensitized solar cell is a mesoporous layer of semiconductor oxide nanoparticles, which are sintered together to establish a good electric contact between the particles. The film thickness (*d*) is usually around 10 µm and the nanoparticles are around 25 nm in diameter. This film is deposited on a glass plate covered with a transparent conducting oxide (TCO), which allows light to enter in the cell. Attached to the surface of the oxide there is a monolayer of dye molecules, which are responsible for harvesting the light. The sensitized film is surrounded by an electrolyte solution of high ionic strength, usually composed of an organic solvent containing a redox pair (**Figure 1.2**).

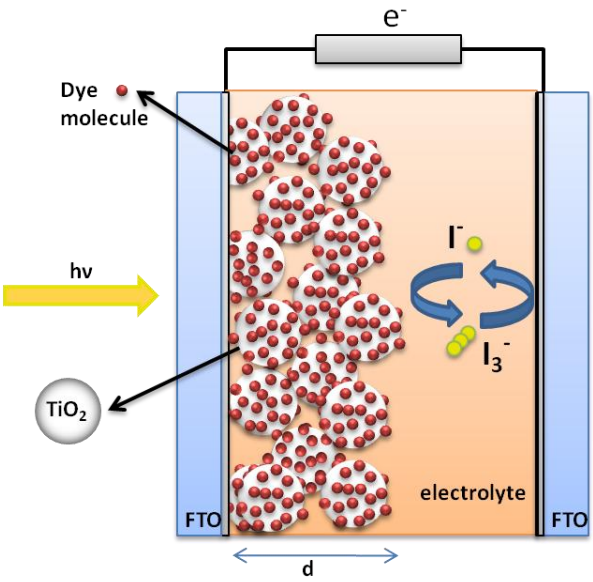

Figure 1.2 Schematic view of a dye-sensitized solar cell device

Nearly all the components of a DSC are tunable. Up to now the most successful combination of materials is still the one reported in the pioneering work by the Grätzel group[20], which opened the research field of dye-sensitized solar cells. In this configuration the main components are a layer of titanium dioxide nanoparticles sensitized by a ruthenium-complex dye with the I^-/I_3^- redox couple in an organic solvent, which acts as the redox mediator. Grätzel and O´Regan found a successful combination of a nanostructured semiconductor electrode with an efficient and stable dye. The key factor of that combination, as Tsubomura et al.[26] already pointed out for ZnO mesoporous electrodes in 1976, was the surface area. In a mesoporous film, the

incoming photons can be captured efficiently although the surface is covered only by a monolayer of dye[27]. The reason is that a mesoporous structure can have a surface area available for dye adsorption more than a thousand times larger than a flat electrode of the same geometric area. The work in this thesis is based on alternative materials to this standard configuration. The characteristic of each standard component as well as the advantages and disadvantages of alternative materials will be described in the following Chapters.

1.2.1. Operational principles of dye-sensitized solar cells

Dye-sensitized solar cells are photoelectrochemical devices where several electron transfer processes run in parallel and in competition. In a DSC optical absorption and charge-generation are separate functions. The role of dye molecules is the same as that of chlorophyll in leaves: they must absorb the incident sunlight and induce an electron transfer reaction. Dye-sensitized solar cells are photoregenerative devices. A scheme of their basic working principles can be found in **Figure 1.3** and **Table 1.1.**

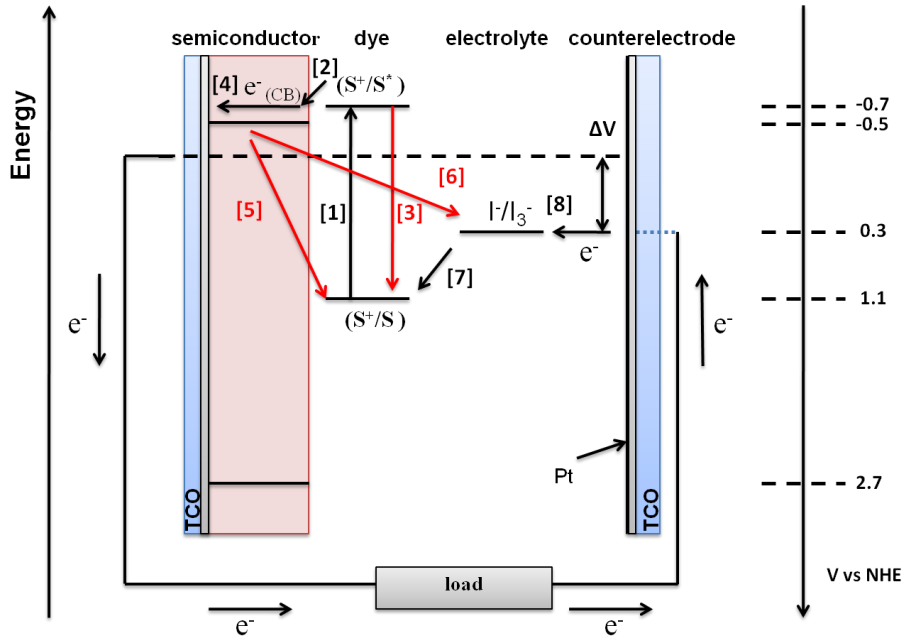

Figure 1.3. Dynamics of different electron transfer processes taking place in the photoconversion by a DSC. An energy diagram of DSCs as the one shown in the figure should not be taken as a real interpretation of the actual energetic situation in a DSC. The indicated values may be taken from measurements of the individual components, excluding effects caused by the interaction among them[10] and potential energy (e.g. conduction band energy) and free energy (redox energy) scales are mixed[28].

Upon illumination, photoexcitation of the dye results in the injection of an electron into the conduction band of the oxide. The oxidized sensitizer thus formed can recombine with the injected electron or it can be regenerated by the electron donor in the electrolyte. Also relaxation of the excited dye before electron injection may occur. The photogenerated electron travels through the mesoporous oxide film by a random walk process[29,30] towards the external contact. The extracted electron can then perform work in an external circuit and return to the counter electrode. The oxidized species in the electrolyte produced upon the dye regeneration step diffuses to the platinum-coated counter electrode, where it is reduced back, closing the regenerative cycle. The major loss channel in the process is the recombination of the injected electrons with the oxidized redox mediator. The timescale of the different processes is the key point for obtaining high energy conversion efficiency of these devices, as will be discussed below.

Table 1.1 Reactions that describe the functioning of a DSC. Symbols: S (fundamental state of the dye), S* (excited state of the dye), S^+ (oxidized state of the dye), SC (semiconductor), CB (conduction band), TCO (transparent conducting oxide).

[1] Photoexcitation	$S + h\nu \rightarrow S^*$
[2] Electron injection	$S^* \rightarrow e^-_{(CB)}\ (SC) + S^+$
[3] Relaxation	$S^* \rightarrow S + h\nu$
[4] Electron transport	$e^-_{(CB)}\ (SC) \rightsquigarrow e^-\ (TCO)$
[5] Recombination with the dye	$S^+ + e^-_{(CB)}\ (SC) \rightarrow S$
[6] Recombination	$2\ e^-_{(CB)}\ (SC) + I_3^- \rightarrow 3I^-$
[7] Dye regeneration	$2S^+ + 3I^- \rightarrow 2S + I_3^-$
[8] Reaction at the counter electrode	$I_3^- + 2e^-\ (Pt) \rightarrow 3I^-$

The maximum theoretical value for the photovoltage at open circuit condition is determined by the potential difference between the conduction band edge of the TiO_2 and the redox potential of the I^-/I_3^- couple in the electrolyte.

Dye-sensitized solar cells are highly complex systems. There are a lot of processes interconnected with each other and the chemical complexity of the device makes it difficult to study separately the single processes affecting the functioning of the cell. In fact, these processes must be studied in complete devices, because their characteristics are affected by the overall functioning.

1.2.2. The dye: light harvesting and charge separation

The semiconductor oxides used in DSCs are wide band gap materials, which do not absorb in the visible. The function of harnessing the solar light is carried out by the sensitizer molecules attached to their surface. The absorption spectrum of the optimum dye for DSCs should cover the whole visible region and even part of the near-infrared (ideally, a threshold of 920 nm should be harvested[31]). In addition, the dye must have suitable anchoring groups, which firmly attach the molecule to the semiconductor oxide.

Upon light absorption, the dye molecule is promoted to its excited state (**Table 1.1** and **Figure 1.3**, reaction [1]). From this excited state, the dye molecule can return to its ground state (reaction [3]) or can inject an electron into the conduction band of the semiconductor (reaction [2]). In order to understand the mechanism of charge separation in DSCs, the time scale of processes [2] and [3] must be compared. The key rate requirement at this step is that injection must be at least 100 times faster than the relaxation of the dye from its excited state[32]. The kinetics depends on several factors, which are principally determined by the kind of dye and the semiconductor. In the case of standard cells with ruthenium-complex dyes, the relaxation of the sensitizer is believed to occur with a rate that is several orders of magnitude slower (~10^{-8} s) than the forward injection (~10^{-13}s)[33]. The presence of a local electrostatic field is not required because the charge separation is achieved thanks to the large kinetic asymmetry between the forward electron transfer and the back relaxation.

In the injection dynamics of DSCs, the energy difference between the conduction band of the semiconductor and the excited state of the sensitizer is a determining factor[34] and for successful sensitization, the dye LUMO level must be higher in energy than the conduction band of the semiconductor[28]. The driving force necessary for a rapid vectorial charge displacement is believed to be small (around 0.1 eV) for ruthenium-complex dyes. Generally, it is accepted that electron injection is very fast and, at least for ruthenium-based dyes and titanium dioxide, injection is not considered

a limiting factor in the DSC performance. However, recently Koops et al.[32] reported a slow injection time in the presence of tert-butylpyridine and Li^+. These are common electrolyte additives that, as will be discussed in following Chapters, are added to the device to improve cell performance. According to these authors, in some cases injection is slow enough for kinetic competition with relaxation of the dye.

Ruthenium-complex dyes are the most used as well as the most successful sensitizers for application in DSCs. These dyes exhibit a strong absorption in the visible and a long-lived excited state (20-60 ns)[10] due to the metal-to-ligand charge transfer (MLCT) character of their light absorption[35]. In a molecule with a MLCT transition the highest occupied molecular orbital HOMO is located near the metal, meanwhile the lowest unoccupied molecular orbital LUMO is located near the molecule ligands. In a ruthenium-complex dye, upon illumination, electrons are promoted from the ruthenium metal center to the carboxylated bipyridil ligands. These carboxylate groups are directly coordinated to the surface titanium ions producing intimate electronic contact between the sensitizer and the semiconductor[33]. Therefore, the ruthenium-complex dye possesses directionality in the excited state and this directionality is one of the reasons for the fast electron transfer process at the ruthenium dye/TiO_2 interface.

Thousands of dyes have been explored in the last two decades and, up to know, the best performing dye-sensitized solar cells have been fabricated with ruthenium-complex dyes. However, although this kind of complexes seem to be appropriate sensitizers for TiO_2, it has been proved that ruthenium dyes are not suitable for ZnO. Looking for a more appropriate dye for this semiconductor has been one of the aims of this thesis.

1.2.3. The electrolyte: regeneration of the dye and hole conduction

The electrolyte is a key component in a dye solar cell, which plays different roles in the functioning of the device. The basic components of a standard electrolyte are a solvent and a redox couple. Besides, some additives are usually present in the electrolyte. These additives, although not essential for the functioning of the cell, have proved to lead to better cell performances, and the effect of some of them in the performance of ZnO solar cells will be analyzed in detail in **Chapter 6**. The most frequently used and at the same time the most successful electrolyte up to now in a DSC is composed of the redox couple I^-/I_3^- in an organic solvent. Some other redox shuttles as for example cobalt-based systems[36], SCN^- / SCN_3^- [37,38] and $SeCN^-/SeCN_3^-$ [37,39] have

also been explored. However iodide-based electrolytes are particularly well suited for DSCs and no other known redox couple works nearly as well[31].

After photoinduced electron injection from the dye into the conduction band of the semiconductor, the dye is in its oxidized state and must be reduced by an electron donor in the electrolyte. The regeneration of the dye to its ground state must be faster than the recombination with conduction band electrons (**Table 1.1**, reaction [5]). The concentration of iodide ions in the DSC is usually very high ($>10^{20}$ cm^{-3} /0.5 M) and the regeneration of the dye by the most common ruthenium-complex sensitizers is a very fast reaction (~10^{-6}-10^{-9} s)[10,40-42]. A rapid regeneration kinetics of the oxidized dye by iodide was also observed in organic sensitizers such as chlorophyll derivates[43] and a porphyrin (ZnTPPC)[44]. Thus, recombination with the dye is usually neglected[45] as a loss mechanism in a dye-sensitized solar cell.

The driving force that makes possible the regeneration of the dye is the difference in the oxidation potential of the dye and the electrolyte (**Figure 1.3**). A driving force ≥ 0.5 V has been measured for ruthenium-complex sensitizers and also for some organic dyes[43,44]. However, recently Wenger et al.[46] demonstrated that a metal-free organic sensitizer with a measured driving force for regeneration of only 0.150 V can operate functionally in dye-sensitized solar cells. This opens the possibility of reducing photovoltage losses due to poor energetic alignment of the components and of using dyes with smaller bad gaps that consequently absorb in the infrared. The detailed mechanism of the dye regeneration reaction has not been fully elucidated and numerous factors appear to influence its rate. Apart from the oxidation potential of the dye, this rate was found to depend strongly on the nature and concentration of the cations present in the electrolyte solution[40]. Pelet et al.[40] found that the nature of the cation of the iodide salt has a significant effect on regeneration: rapid regeneration occurs in the presence of small cations capable of specifically adsorbing onto the TiO_2 surface, such as Li^+ and Mg^{2+}, whereas much slower regeneration was found with TBA^+ ions. This effect was attributed to the resulting higher local iodide concentration near the TiO_2 surface when positive charge is adsorbed.

The photovoltage of the cell depends to a great extent on the redox couple, which sets the electrochemical potential at the counter electrode. The electrolyte also affects the electrochemical potential in the semiconductor oxide, as recombination of electrons

with the oxidized species in the electrolyte is the main loss mechanism in the cell. In fact, the main quality of the iodide/triiodide couple is a much slower kinetics of recombination with electrons in the conduction band as compared to other redox couples.

Transport of the redox mediator between the electrodes is mainly driven by diffusion. Triiodide must migrate from the photoelectrode to the counter electrode, where it is reduced to iodide. Simultaneously, the reduced iodide must diffuse to the vicinity of the oxidized dye molecules within the cell. These processes will depend on mass transport of both species in the electrolyte. In typical electrolytes, sufficient excess of I^- is employed and its concentration is around ten times higher than that of tri-iodide. This higher concentration, in addition to a higher diffusion coefficient of I^- with respect to I_3^-, makes the current limitation mainly due to diffusion of the triiodide ions. Apart from diffusion coefficient and concentration of the species, another key factor in this diffusion process is the distance between the electrodes[47].

Different alternatives to the standard electrolyte described above have been explored as hole conductors for dye-sensitized solar cells. To overcome problems associated to evaporation of the organic solvents, they are often replaced by ionic liquids. Ionic liquids have a much higher viscosity than organic solvents, but they have a negligible vapour pressure. Therefore, they do not present evaporation problems. The use of ionic-liquid-based electrolytes will be explored in detail in **Chapters 6** and **7**. Other alternatives to the standard dye-sensitized solar cell electrolyte are used in solid state devices. In this kind of DSC the liquid electrolyte is replaced by a p-type semiconductor or a p-type organic material. The hole conductor needs an intimate contact with the dye monolayer covering the porous semiconductor to efficiently regenerate the dye. In standard dye-sensitized solar cells this is easily achieved as the liquid electrolyte penetrates completely in the nanostructure. In contrast, inefficient pore filling, together with high recombination rates with conduction band electrons are the main limitations of solid-state devices. Spiro-MeOTAD is the most used p-type material[48,49].

1.2.4. The counter electrode: regeneration of the oxidized species in the electrolyte

After diffusion through the electrolyte, triiodide is reduced to iodide at the counter electrode. The counter electrode in a DSC is usually formed by a thin catalytic layer of platinum onto a conducting glass substrate. An overpotential is needed to drive this reaction at a certain current density. This exchange current density for the redox system should be as high as possible in order to minimize the kinetic overpotential. It has been shown that the overpotential at the counter electrode is small, less than 20 mV[37], as the exchange current density at a platinum-coated electrode is sufficiently high at about 10-100 mA cm^{-2} [33]. This is indicative of the excellent catalytic properties of platinum. The rate of electron transfer from the conduction band of the oxide to the oxidized species in the electrolyte is much slower than from the platinum-coated electrode[45], therefore, voltage losses arise primarily from the effects of diffusion[28].

1.2.5. The mesoporous semiconductor: ZnO as electron conductor in dye-sensitized solar cells

The semiconductor oxide is the physical support of the sensitizer molecules and the electron conductor in a dye-sensitized solar cell. As mentioned before, the mesoporous structure of the films is crucial for a high dye loading in the semiconductor. The wide band gap semiconductor titanium dioxide has been by far the most widely used DSC photoelectrode material. Titanium dioxide is a very versatile, non-toxic, cheap and chemically stable material and its suitability for dye-sensitized solar cells has been extensively proved. Many other wide band gap oxide semiconductors have been also explored as potential electron conductors in DSCs. However, up to now, no other material has reached efficiencies comparable to titanium dioxide. Nevertheless, some semiconductors present special characteristics that make them very attractive candidates as alternatives to titanium dioxide. The conduction band edge of SnO_2, for example, lies around 0.5 V lower than the one of TiO_2. SnO_2 can be used, therefore, in combination with dyes with absorption close to the infrared that are unable to sensitize TiO_2. The band gap and conduction band edge of ZnO are similar to that of anatase TiO_2[50,51]. However, single-crystalline ZnO presents a much higher electron mobility than anatase TiO_2, which should favour electron conduction[50-54].

Zinc oxide is a direct wide band gap semiconductor with a large and diverse application potential. It crystallizes in three polymorphs: wurtzite, zinc blende and rocksalt structure. At ambient conditions, the thermodynamically stable phase is wurtzite, a hexagonal structure where each anion is surrounded by four cations at the corners of a tetrahedron and vice versa. The relatively open structure of zinc oxide allows plenty of sites to accommodate intrinsic defects and extrinsic dopants[55]. ZnO with a wurtzite structure is naturally an n-type semiconductor. It can be intrinsically doped via oxygen vacancies and/or zinc interstitials[56,57]. Extrinsically, ZnO can be doped both, n and p-type[58]. A wide range of properties of this material depend on doping, including a range of conductivity from metallic to insulating, piezoelectricity, room-temperature ferromagnetism and chemical-sensing effects. The point of zero charge (pzc) of ZnO is observed at pH8 - pH9, depending on the preparation method and experimental conditions[56]. ZnO has a relatively poor chemical stability and is easily etched in acids and alkalis. Thanks to this relatively poor chemical stability ZnO has probably the richest variety of nanostructures based on a very wide range of synthesis routes. Their morphologies include highly ordered nanowire arrays, tower-like structures, nanorods, nanobelts, nanosprings, nanocombs and nanorings among others.

ZnO has a very diverse application field. Historically, due to its UV-absorbing characteristic, it has been used as pigment, protective coating on metal surfaces and also in cosmetics as UV protection in sun creams. It has been employed in photodetectors, in particular in visible-blind UV detectors. ZnO nanostructures have been widely used for sensing applications because of their high sensitivity to the chemical environment. Other applications are in light emitting diodes and lasing.

In the last years, a great interest has been paid to this oxide in the field of dye-sensitized solar cells and ZnO is the second most used semiconductor[10]. However, despite many efforts to improve the efficiency of ZnO-based dye-sensitized solar cells, it remains lower than the one of TiO_2-based cells. The best result for a ZnO DSC up to now was achieved by Saito and Fujihara[59], who obtained a 6.58% [v] overall efficiency. This is around the half of the maximum efficiency obtained for TiO_2[25]. Along this thesis, the reasons for this lower performance will be analyzed.

[v] This record efficiency was obtained with open cells and a cell area of 0.25 cm^2

1.2.6. Scale-up and commercialization of dye-sensitized solar cells

DSCs are not only a matter of scientific research. The industry is starting to pay attention to this new technology and more than one hundred industrial laboratories worldwide are working on the development of DSC-based photovoltaic devices[31].

DSC technology possesses some clear advantages with respect to other photovoltaic devices. The first and probably the most attractive for a practical application is its price. The DSC technology shares the cost advantage of all thin film devices with respect to conventional photovoltaic technology. But, in contrast, it uses non-toxic materials and avoids costly production steps (e.g. high vacuum, high temperature, clean-room demands). However, as discussed below, there are still some bottlenecks in potential fabrication costs such as the price of the transparent conducting oxides used as substrate and of the dyes based on precious metals.

Efficiency of the new DSC technology must be above a certain threshold in order to successfully compete with technologies already established. Although record efficiencies above 11% have been reached in the laboratory for small cell areas (typically in the sub-square-centimeter-range), these values reduce to around 8% as a consequence of the scale-up of the area within a working module (25-100 cm^2). In addition, a very controversial topic is the fact that after more than 20 years of research, the record efficiency is not much higher (11%[25]) than the one reported by Grätzel and O´Regan (7%[20]) in the Nature work, which opened the dye-sensitized solar cell research field.

Another key for industrial success is long-term stability. DSC stability is a very controversial topic and it is one of the weak points of this technology. For a 20-year lifetime of a device, its components must withstand several millions of turnovers. In addition, as any photovoltaic device, they have to stand very high temperatures, which can lead to structural transformation of the dye-TiO_2 system. Another crucial factor in the stability is the sealing. DSCs (at least for the standard configurations) are liquid-based devices. The sealing materials must avoid the evaporation of the electrolyte as well as the accumulation of H_2O inside the cell. At the same time the sealing material must be chemically compatible with the solvent and components of the electrolyte. Industrialization of DSCs is in progress to overcome these issues and several successful tests of solar cells under outdoor conditions have been carried out. The stability of

DSCs was tested over 20,000 hours of simulated sunlight at an average light level corresponding to 0.8 sun[vi] [31]. With respect to lifetime, the industrial DSC company Dyesol, reported accelerated aging tests, which indicated a service life of at least 25 years in the climate conditions of southern Europe. As will be described in **Chapter 6,** the substitution of organic solvents by non-volatile solvents is a very promising approach towards reaching such high stability demands. In this thesis special attention has been paid to the stability of DSCs and the use of non-volatile electrolytes such as ionic-liquid-based ones has been analyzed.

Another controversial issue concerning the industrialization of DSC technology is the use of a dye based on a precious metal. Ruthenium is rather rare and the relatively small size of the market leads to highly volatile prices. However, the search for alternative dyes is a very active field and pure organic sensitizers have reached practically the same yield as ruthenium complexes[60]. Nevertheless, the contribution of ruthenium to the total price of the device is less than 0.01€/pWatt[61] given the small amount employed. Nowadays the component of the DSC that contributes most significantly to the final price of this technology is the transparent conducting oxide substrate (TCO). The most frequently used TCOs are fluorine- and indium-doped tin oxides. The price and availability of these TCOs significantly depend on the demand and the availability of Sn. Taking this into account, alternatives to Sn-based TCOs must be considered. DSCs are compatible with various supporting materials as, for example, flexible ones. Apart from obvious advantages of flexible substrates in terms of versatility, they provide a mayor benefit to mass production: in contrast to glass, flexible substrates can be used in continuous roll-to-roll processes, making possible an extensive and low cost production.

At the moment, DSCs cannot compete with other photovoltaic technologies for grid connected solar farm applications. Photovoltaic devices in solar farms are designed to work under an optimal orientation and relatively strong light intensities. These working conditions are more suited for traditional PV. However, silicon panels suffer from significant loss of efficiency when working at low intensity levels or high temperatures[62]. In contrast, DSCs perform particularly well under conditions corresponding to ~ 0.2 to 0.5 sun, and their efficiencies are practically independent of temperature in the range 25-65ºC[61]. Over the same range of temperature the efficiency

[vi] One sun is equivalent to 100 mW cm^{-2} illumination (see **Chapter 4**).

of Si solar cells diminishes approximately by 20%[61]. In addition, the efficiency of standard silicon technologies is much more dependent on the angle of incidence than in DSCs. DSCs perform well under diffuse light illumination or cloudy conditions and show high tolerance to partial shading.

The combination of all the characteristics described above makes the integration of DSCs into building architecture (an area known as *Building Integrated Photovoltaic Applications*, BIPV) one of the most interesting field of application for this new technology. First and second generation solar cells are only useful for roofs due to their high dependence on angle of incidence and direct light illumination. However, DSCs are suitable also for some applications where the angle of incidence is far from optimal, as, for example, on façades[63]. DSCs present also aesthetic advantages such as a wide range of available colors, non-reflectivity and partial optical transparency. The second main application for dye-sensitized solar cells is as alternative to batteries for stand-alone electronic equipment as, for example, mobile-phone chargers or decorative articles. An important property of this kind of products is their relatively short product life (up to five years, approximately). This makes possible a wider range of choice of materials due to the less demanding stability requirements. Flexible DSCs are very suitable for this kind of applications, competing with flexible amorphous silicon. The key qualities of DSCs are the customized colour options, wide variety of shapes, low light performance, excellent performance in diffuse light and a better average performance across the light range. Some of the application areas of DSCs under development and the main companies working on this technology are summarized in **Table 1.2**.

Table 1.2 Some application areas of DSCs under development in various countries. Source [31].

Companies	Type of application
Sharp, Sony, Nanomax, IPP, FIS	Large area solar panels for terrestrial power generation
Dyesol Italian BIPV Company, Color-Sol project of Germany	BIPV
Dyesol	Flexible power plastics
3G Solar of Israel	Power generation for remote area needs
SJC-Shimane Inst. of Industrial Tech.	Street lights and road signs
Sony´s self-powering lamp shades	Consumer household electronics

DSC technology is rapidly evolving toward full commercial viability. However several issues must be overcome before reaching a stage where it is ready to compete with other photovoltaic technologies.

1.3. Scope and structure of the work

The main objective of this study is to identify the advantages and limitations of ZnO as electron conductor in dye-sensitized solar cells. To achieve this general objective, this work has been divided in four main topics: (1) the search for an organic dye sensitizer suitable for ZnO, (2) the substitution of organic solvent electrolytes by ionic liquids to develop ZnO-based DSCs with high stability, (3) the influence of the semiconductor morphology on the performance of ZnO-based DSCs and (4) the study of the transport and recombination properties of this semiconductor in DSCs.

Chapter 2 is devoted to the theoretical description of recombination and electron transport in DSCs, which will set the basis for the subsequent analysis of the experimental results. In **Chapter 3** and **Chapter 4** the methods and procedures employed for the characterization and the fabrication of DSCs are described.

From **Chapter 5** to **Chapter 9** the results of the research carried out along this thesis are detailed. In **Chapter 5**, a comparative study between xanthene derivative dyes and a ruthenium-complex dye is carried out, highlighting the advantages and limitations of the different dyes as sensitizers for ZnO. The following two Chapters are devoted to the study of ZnO dye-sensitized solar cells with ionic-liquid-based electrolytes. Firstly, in **Chapter 6**, several combinations of ionic liquids are tested as electrolytes for ZnO-based cells sensitized with a ruthenium-complex dye. Subsequently, in **Chapter 7**, these electrolytes are employed in ZnO-based cells sensitized with an organic dye. In particular, the importance of the oxide-dye interaction to obtain long-term stable ZnO-based cells sensitized with organic dyes will be pointed out. **Chapter 8** is devoted to the study of the influence of the semiconductor structure on the performance of ZnO dye-sensitized solar cells. Electrodes based on one-dimensional nanowire arrays are compared to nanoparticle-based electrodes, and the differences between them are analyzed. In **Chapter 9**, the electronic and recombination properties of ZnO-based cells are analyzed by means of a wide variety of complementary techniques. The same theories, which are used to describe the behaviour of TiO_2-based cells, are applied to ZnO and the differences and similarities between both oxides are described.

Finally in **Chapter 10**, conclusions are drawn together with an outlook on the future research of ZnO-based solar cells. Complementary information and additional results can be found in the **Appendix**.

1.4. References to Chapter 1

1. International Energy Outlook 2010 http://www.eia.doe.gov/oiaf/ieo/pdf/0484(2010).
2. Dinçer, F. The analysis on photovoltaic electricity generation status, potential and policies of the leading countries in solar energy. *Renewable and Sustainable Energy Reviews* **15**, 713-720 (2011).
3. García Casals, X. Solar absorption cooling in Spain: Perspectives and outcomes from the simulation of recent installations. *Renewable Energy* **31**, 1371-1389 (2006).
4. IDAE, Instituto para la Diversificacion y Ahorro de la Energía http://www.idae.es.
5. Global Market Outlook for Photovoltaics until 2014 http://www.epia.org.
6. Avrutin, V., Izyumskaya, N. & Morkoç, H. Semiconductor solar cells: Recent progress in terrestrial applications. *Superlattices and Microstructures* **49**, 337-364 (2011).
7. Photon International, Issue March 2009.
8. Nelson, J. *The Physics of Solar Cells*. (Imperial College Press: 2003).
9. Shockley, W. & Queisser, H.J. Detailed Balance Limit of Efficiency of p-n Junction Solar Cells. *Journal of Applied Physics* **32**, 510-519 (1961).
10. Hagfeldt, A., Boschloo, G., Sun, L., Kloo, L. & Pettersson, H. Dye-sensitized solar cells. *Chemical Reviews* **110**, 6595-6663 (2010).
11. Green, M.A., Emery, K., Hishikawa, Y. & Warta, W. Solar cell efficiency tables (version 36). *Progress in Photovoltaics: Research and Applications* **18**, 346-352 (2010).
12. Lobato, K. Charge Transport and Recombination in Dye-Sensitized Nanocrystalline Solar Cells. University of Bath. (2007).
13. M.A. Green *Third Generation Photovoltaics - Advanced Solar Energy Conversion*. (Springer: 2006).
14. Travis, L. Organic Solar Cells: An Overview Focusing on Active Layer Morphology. *Photosynthesis Research* **87**, 73-81
15. Belaidi, A., Dittrich, T., Kieven, D., Tornow, J., Schwarzburg, K. & Lux-Steiner, M. Influence of the local absorber layer thickness on the performance of ZnO nanorod solar cells. *physica status solidi. (RRL)* **2**, 172-174 (2008).
16. Itzhaik, Y., Niitsoo, O., Page, M. & Hodes, G. Sb_2S_3-Sensitized Nanoporous TiO_2 Solar Cells. *The Journal of Physical Chemistry C* **113**, 4254-4256 (2009).
17. Ernst, K., Belaidi, A. & Konenkamp, R. Solar cell with extremely thin absorber on highly structured substrate. *Semiconductor Science and Technology* **18**, 475–479 (2003).
18. Greene, L.E., Law, M., Yuhas, B.D. & Yang, P. ZnO−TiO_2 Core−Shell Nanorod/P3HT Solar Cells. *The Journal of Physical Chemistry C* **111**, 18451-18456 (2007).
19. Lira-Cantu, M. & Krebs, F.C. Hybrid solar cells based on MEH-PPV and thin film semiconductor oxides (TiO_2, Nb_2O5, ZnO, CeO_2 and CeO_2-TiO_2): Performance improvement during long-time irradiation. *Solar Energy Materials and Solar Cells* **90**, 2076-2086 (2006).
20. O'Regan, B. & Grätzel, M. A low-cost, high-efficiency solar cell based on dye-

sensitized colloidal TiO_2 films. *Nature* **353**, 737-740 (1991).
21. Lèvy-Clèment, C. Nanostructured ETA-Solar Cells. *Nanostructured Materials for Solar Energy Conversion. Elsevier* 447-484 (2006).
22. Lèvy-Clèment, C., Tena-Zaera, R., Ryan, M.A., Katty, A. & Hodes, G. CdSe-Sensitized p-CuSCN/nanowire n-ZnO heterojunctions. *Advanced Materials* **17**, 1512–1515 (2005).
23. Krunks, M., Kärber, E., Katersi, A., Otto, K., Oka Acik, I., Dedova, Y. & Mere, A. Extremely thin absorber layer solar cells on zinc oxide nanorods by chemical spray. *Solar Energy Materials and Solar Cells* **94**, 1191-1195 (2010).
24. Chandrasekaran, J., Nithyaprakash, D., Ajjan, K.B., Maruthamuthu, S., Manoharan, D. & Kumar, S. Hybrid solar cell based on blending of organic and inorganic materials-An overview. *Renewable and Sustainable Energy Reviews* **15**, 1228-1238 (2011).
25. Chiba, Y., Islam, A., Watanabe, Y., Komiya, R., Koide, N. & Han, L.Y. Dye-sensitized solar cells with conversion efficiency of 11.1%. *Japanese Journal of Applied Physics Part 2-Letters & Express Letters* **45**, L638–L640 (2006).
26. Tsubomura, H., Matsumura, M., Nomunara, Y. & Amamiya, T. Dye sensitised zinc oxide: aqueous electrolyte: platinum photocell. *Nature* **261**, 402-403 (1976).
27. Grätzel, M. Dye-sensitized solar cells. *Journal of Photochemistry and Photobiology C: Photochemistry Reviews* **4**, 145-153 (2003).
28. Peter, L.M. Dye-sensitized nanocrystalline solar cells. *Physical Chemistry Chemical Physics.* **9**, 2630-2642 (2007).
29. Nelson, J. & Chandler, R.E. Random walk models of charge transfer and transport in dye sensitized systems. *Coordination Chemistry Reviews* **248**, 1181-1194 (2004).
30. Anta, J.A. Random walk numerical simulation for solar cell applications. *Energy & Environmental Science* **2**, 387–392 (2009).
31. *Dye-Sensitized Solar Cells*. Edited by K. Kalyanasundaram (EPFL Press: 2010).
32. Koops, S.E., O'Regan, B.C., Barnes, P.R.F. & Durrant, J.R. Parameters Influencing the Efficiency of Electron Injection in Dye-Sensitized Solar Cells. *Journal of the American Chemical Society* **131**, 4808-4818 (2009).
33. Hagfeldt, A. & Grätzel, M. Light-Induced Redox Reactions in Nanocrystalline Systems. *Chemical Reviews* **95**, 49-68 (1995).
34. Gerischer, H. & Willig, F. Reaction of excited dye molecules at electrodes. *Physical and Chemical Applications of Dyestuffs* **61**, 31-84-84 (1976).
35. Oskam, G. Dye-sensitized, nanostructured metal oxide photoelectrodes for solar energy conversion. *Current Topics in Electrochemistry* **10**, 141–162 (2004).
36. Wang, H., Nicholson, P.G., Peter, L., Zakeeruddin, S.M. & Grätzel, M. Transport and Interfacial Transfer of Electrons in Dye-Sensitized Solar Cells Utilizing a $Co(dbbip)_2$ Redox Shuttle. *The Journal of Physical Chemistry C* **114**, 14300-14306 (2010).
37. Oskam, G., Bergeron, B.V., Meyer, G.J. & Searson, P.C. Pseudohalogens for Dye-Sensitized TiO_2 Photoelectrochemical Cells. *The Journal of Physical Chemistry B* **105**, 6867-6873 (2001).
38. Bergeron, B.V., Marton, A., Oskam, G. & Meyer, G.J. Dye-Sensitized SnO_2 Electrodes with Iodide and Pseudohalide Redox Mediators. *The Journal of Physical Chemistry B* **109**, 937-943 (2005).
39. Wang, P., Zakeeruddin, S.M., Moser, J., Humphry-Baker, R. & Grätzel, M. A Solvent-Free, $SeCN^-/(SeCN)_3^-$ Based Ionic Liquid Electrolyte for High-Efficiency Dye-Sensitized Nanocrystalline Solar Cells. *Journal of the American Chemical Society* **126**, 7164-7165 (2004).

40. Pelet, S., Moser, J. & Grätzel, M. Cooperative Effect of Adsorbed Cations and Iodide on the Interception of Back Electron Transfer in the Dye Sensitization of Nanocrystalline TiO_2. *The Journal of Physical Chemistry B* **104**, 1791-1795 (2000).
41. Clifford, J.N., Palomares, E., Nazeeruddin, M.K., Grätzel, M. & Durrant, J.R. Dye Dependent Regeneration Dynamics in Dye Sensitized Nanocrystalline Solar Cells: Evidence for the Formation of a Ruthenium Bipyridyl Cation/Iodide Intermediate. *The Journal of Physical Chemistry C* **111**, 6561-6567 (2007).
42. Mori, S.N., Wataru, K., Taisuke, K., Naruhiko, M. Yuji, W. & Shozo, Y. Investigation of the Effect of Alkyl Chain Length on Charge Transfer at TiO_2/Dye/Electrolyte Interface. *The Journal of Physical Chemistry C* **111**, 3522-3527 (2007).
43. Kay, A., Humphry-Baker, R. & Grätzel, M. Artificial Photosynthesis. 2. Investigations on the Mechanism of Photosensitization of Nanocrystalline TiO_2 Solar Cells by Chlorophyll Derivatives. *The Journal of Physical Chemistry* **98**, 952-959 (1994).
44. Montanari, I., Nelson, J. & Durrant, J.R. Iodide Electron Transfer Kinetics in Dye-Sensitized Nanocrystalline TiO_2 Films. *The Journal of Physical Chemistry B* **106**, 12203-12210 (2002).
45. Peter, L.M. Characterization and Modeling of Dye-Sensitized Solar Cells. *The Journal of Physical Chemistry C* **111**, 6601-6612 (2007).
46. Wenger, S., Bouit, P.A., Chen, Q., Teuscher, J., Censo, D., Humphry-Baker, R., Moser, J.E., Delgado, J.L., Martin, N., Zakeeruddin, S. & Grätzel, M. Efficient Electron Transfer and Sensitizer Regeneration in Stable π-Extended Tetrathiafulvalene-Sensitized Solar Cells. *Journal of the American Chemical Society* **132**, 5164-5169 (2010).
47. Hauch, A. & Georg, A. Diffusion in the electrolyte and charge-transfer reaction at the platinum electrode in dye-sensitized solar cells. *Electrochimica Acta* **46**, 3457-3466 (2001).
48. Howie, W.H., Harris, J.E., Jennings, J.R. & Peter, L.M. Solid-state dye-sensitized solar cells based on spiro-MeOTAD. *Solar Energy Materials and Solar Cells* **91**, 424–426 (2007).
49. Fabregat-Santiago, F., Bisquert, J., Le, C., Peter, C., Wang, M., Zakeeruddin, S. & Grätzel, M. Electron Transport and Recombination in Solid-State Dye Solar Cell with Spiro-OMeTAD as Hole Conductor. *Journal of the American Chemical Society* **131**, 558–562 (2009).
50. Bauer, C., Boschloo, G., Mukhtar, E. & Hagfeldt, A. Electron Injection and Recombination in $Ru(dcbpy)_2(NCS)_2$ Sensitized Nanostructured ZnO. *The Journal of Physical Chemistry B* **105**, 5585-5588 (2001).
51. Katoh, R., Furube, A., Yoshihara, T., Hata, K., Fujihashi, G., Takano, S., Murata, S., Arakawa, H. & Tachiya, M. Efficiencies of Electron Injection from Excited N3 Dye into Nanocrystalline Semiconductor (ZrO_2, TiO_2, ZnO, Nb_2O5, SnO_2, In_2O3) Films. *The Journal of Physical Chemistry B* **108**, 4818-4822 (2004).
52. Look, D.C., Reynolds, D.C., Sizelove, J.R., Jones, R.L., Litton, C.W., Cantwell, G., & Harsch, W.C. Electrical properties of bulk ZnO. *Solid State Communications* **105**, 399-401 (1998).
53. Seager, C.H. & Myers, S.M. Quantitative comparisons of dissolved hydrogen density and the electrical and optical properties of ZnO. *Journal of Applied Physics* **94**, 2888-2894 (2003).
54. Forro, L., Chauvet, O., Emin, D., Zuppiroli, L., Berger, H. & Levy, F. High mobility n-type charge carriers in large single crystals of anatase (TiO_2). *Journal of*

Applied Physic. **75**, 633-635 (1994).
55. Schmidt-Mende, L. & MacManus-Driscoll, J.L. ZnO - nanostructures, defects, and devices. *Materials Today* **10**, 40-48 (2007).
56. Boschloo, G., Edvinsson, T. & Hagfeldt, A. Dye-sensitized nanostructured ZnO electrodes for solar cell applications. *Nanostructured Materials for Solar Energy Conversion* 227-254 (2006).
57. Look, D.C., Farlow, G.C., Pakpoom, R., Sukit, L., Zhang, S.B. & Nordlund, K. Evidence for Native-Defect Donors in n-Type ZnO. *Physical Review Letters* **95**, 225502 (2005).
58. Zhang, S. B., Wei, S-H. & Zunger, A. Intrinsic n-type versus p-type doping asymmetry and the defect physics of ZnO. *Physical Review B* **63**, 075205 (2001).
59. Saito, M. & Fujihara, S. Large photocurrent generation in dye-sensitized ZnO solar cells. *Energy & Environmental Science* **1**, 280-283 (2008).
60. Zhang, G., Bala, H., Cheng, Y., Shi, D., Lv, X., Yu, Q. & Wang, P. High efficiency and stable dye-sensitized solar cells with an organic chromophore featuring a binary π-conjugated spacer. *Chemical Communications.* 2198-2200 (2009).
61. Grätzel, M. Photovoltaic and photoelectrochemical conversion of solar energy. *Philosophical Transactions of the Royal Society A: Mathematical, Physical and Engineering Sciences* **365**, 993 -1005 (2007).
62. Radziemska, E. The effect of temperature on the power drop in crystalline silicon solar cells. *Renewable Energy* **28**, 1-12 (2003).
63. Hinsch, A., Brandt, H., Veurman, W., Hemming, W., Nittel, M., Würfel, U., Putyra, P., Land-Koetz, C., Stabe, M., Beucker, S. & Fichter, K. Dye solar modules for facade applications: Recent results from project ColorSol. *Solar Energy Materials and Solar Cells* **93**, 820-824 (2009).

Chapter 2

Theoretical Description of Dye-Sensitized Solar Cells

2. Theoretical description of dye-sensitized solar cells

2.1. Current-voltage characteristics

A solar cell is a particular case of a diode, an electrical device, which favours current flow in one direction, but not in the opposite. A diode has a certain characteristic relationship between produced current and applied voltage. This relation is known as the current-voltage characteristics or IV curve of the diode, and it is expressed as

$$J = J(V) \tag{2.1}$$

where J is the dc electrical current density running through the device and V is the externally applied bias. The universal shape of an IV curve in a solar cell (**Figure 2.1**) is a consequence of the balance of two opposing mechanisms: (1) light-induced charge separation and subsequent current generation and (2) loss processes (recombination). The application of an external forward bias to the solar cell implies the accumulation of electrons within the anode. This leads to an increase of the dark current that opposes the current generated by the cell. The net current tends to cancel at sufficiently high bias (open circuit conditions). At zero bias the cell produces its maximum current (short circuit conditions). The solar cell generates power when it produces current at non-zero bias (**Figure 2.1**).

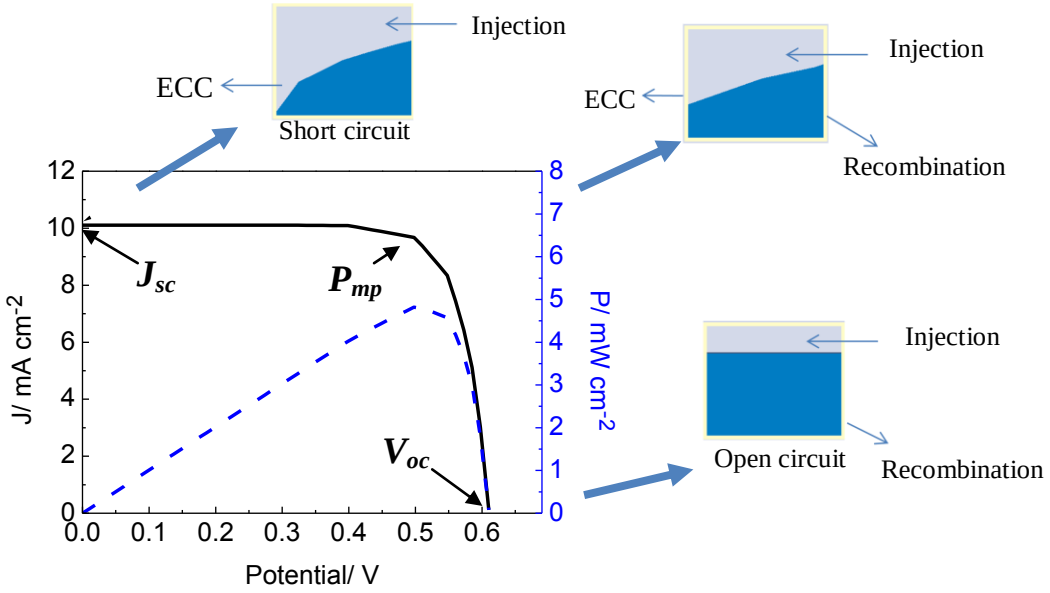

Figure 2.1 An example of an IV curve where the different key parameters are shown: J_{sc} (short circuit current), V_{oc} (open circuit voltage), P_{mp} (maximum power point). ECC stands for external current collection. The output power ($J \cdot V$) is also plotted in the graph (dashed line).

From a practical point of view, the most important piece of information one can obtain from an IV curve is the maximum output power of the device per unit area, P_{mp}. The maximum power point in an IV characterization is defined by the square under the IV curve with the largest area, a point which yields the maximum product of current and voltage (V_{mp}·J_{mp}) (**Figure 2.1**). Other important parameters in every IV curve are the current density at short circuit conditions (short circuit current density, J_{sc}) and the voltage at open circuit conditions (open circuit voltage, V_{oc}).

The behaviour of a solar cell can be described, in its simplest form, by the diode equation. Assuming no series or shunt resistances, this can be written as[1]

$$J = J_{sc} - J_0 \left(exp\left(\frac{qV}{mkT} - 1\right)\right) \tag{2.2}$$

where J_{sc} is the short circuit photocurrent, J_0 is the exchange-current, q the elementary charge, k the Boltzmann constant, T the absolute temperature and m the ideality factor. The shape of an IV curve is described by the fill factor (FF). The fill factor is a phenomenological quantity, with a value between 0 and 1, being close to one in the case of an ideal diode (m = 1) and related to the non ideality factor m. It defines the ratio of the actual maximum power (V_{mp}·J_{mp}) to the maximum power theoretically attainable by the solar cell (J_{sc}·V_{oc}). The overall solar-to-electrical energy conversion efficiency of a solar cell (η) can be expressed as

$$\eta = \frac{J_{sc}V_{oc}}{P_{in}}\, FF \tag{2.3}$$

where P_{in} is the power density (W m^{-2}) of the incident light.

2.2. Electron recombination and the origin of the photovoltage in dye-sensitized solar cells

As already mentioned, the main loss process in a dye-sensitized solar cell is the recombination of injected electrons in the conduction band of the semiconductor with oxidized species in the electrolyte. The majority of theoretical and experimental studies about the recombination kinetics in DSCs are based on the iodide/triiodide redox couple. It is generally accepted that the net recombination reaction between TiO_2 and this redox couple is a two electron reaction[2] given by

$$I_3^- + 2e^- \rightarrow 3I^- \quad (2.4)$$

Two possible intermediate steps are possible for the reaction expressed in **Equation 2.4**, a first elementary step consisting in electron capture by I_3^- to form iodine radical ion I_2^-

$$I_3^- + e^- \rightarrow I_2^- + I^- \quad (2.4.1)$$

followed by two possible second steps involving I_2^-,

$$I_2^- + e^- \rightarrow 2I^- \quad (2.4.2)$$

or

$$2I_2^- \rightarrow I_3^- + I^- \quad (2.4.3)$$

Therefore, it is believed that the reaction is constituted of a multiple-step mechanism, very probably involving the species I_2^- with one of the steps being rate-determining. After more than one decade of research, the exact nature of this electron transfer is not known in detail yet. It is believed to depend on specific factors of the device such as the dye molecule and the electrolyte solvent[3]. In any case the reaction has been shown to be approximately first order with respect to either of these iodide species, I_2^- or I_3^- [4].

According to classical chemical kinetics, the rate of the back reaction (U) (measured in $cm^{-3}\ s^{-1}$) depends on the reactant concentrations and the rate constants for electron transfer

$$U = k_0 n^{\upsilon_n} [I_3^-]^{\upsilon_{I_3^-}} \quad (2.5)$$

where k_0 is the rate constant for the back reaction of electrons, n the electron concentration and the exponents represent the reaction order with respect to electrons and tri-iodide ions, respectively. In order to make progress towards a simple model that describes the recombination process in DSCs several assumptions are made:

- The reaction is first order in both, electron and triiodide concentration
- Electrons can be transferred only from the conduction band (i.e. they are not trapped when recombining)

- Triiodide concentration is many orders of magnitude larger than the electron concentration in the oxide and can be treated as a constant

Assuming these statements, **Equation 2.5** can be formulated as a first order reaction in terms of the free electron concentration:

$$U_n = k_r n_c \tag{2.6}$$

where k_r corresponds to $k_r = k_0[I_3^-]$ and n_c is the free electron concentration (concentration of electrons in the conduction band). This linear recombination term was introduced in the theoretical model proposed by Södergren et al.[5] in an early stage of DSC research. However, it has been found that this model cannot describe DSC characteristics quantitatively[6]. As will be shown several times in this thesis, this simple recombination term implies an ideal behaviour of the solar cell (an ideal diode). However, evidence for non-linearity in the recombination is often found in DSCs, also for the ZnO solar cell studied here. For example, the measurement of the charge transfer resistance or recombination resistance in a DSC is commonly affected by non-ideal features. To get insight into this point it is necessary to start from the definition of the recombination current, j_{rec}

$$j_{rec} = qdU_n \tag{2.7}$$

where q is the elementary charge and d the thickness of the film. From the reciprocal derivative of this recombination current with respect to voltage[7] the recombination or charge transfer resistance (R_{ct}) is obtained

$$R_{ct} = \frac{1}{A}\left(\frac{\partial j_{rec}}{\partial V}\right)^{-1} \tag{2.8}$$

where A is the cell surface area. Substituting **Equation 2.7** in **Equation 2.8,** the recombination resistance can be related to the derivative of the recombination rate

$$R_{ct} = \frac{1}{qdA}\left(\frac{\partial U_n}{\partial V}\right)^{-1} \tag{2.9}$$

Experimentally it is found that the resistance fits to the following empirical equation when measured as a function of applied (forward) bias

$$R_{ct} = R_{ct,0} exp\left(-\beta \frac{qV}{kT}\right) \tag{2.10}$$

where $R_{ct,0}$ is a constant and β the so-called transfer parameter. In a linear (ideal) model β would be equal to one. However, in experimental measurements of the charge transfer resistance for DSCs usually a parameter β <1 is observed. This is interpreted as an indication of nonlinear recombination in DSCs[6]. If we assume a non linear recombination model, **Equation 2.6** can be rewritten as

$$U_n = k_r n_c^{\beta} \tag{2.11}$$

where β, the transfer coefficient, defines the recombination order in the sublinear recombination kinetics. Using **Equations 2.9**, **2.11** and the relation between the free electron concentration and the voltage that will be described below (**Equation 2.18**), the empirical expression of **Equation 2.10** is obtained. Hence, the experimental transfer coefficient is shown to be equivalent, according to this description, to the electron reaction order in **Equation 2.11**.

The origin of non-linearity or non-ideality (we have just shown that both concepts are related, the first being connected to the kinetics of the recombination reactions, the second being an empirical feature) is an open problem. In dye-sensitized solar cells electrons can be transferred from the conduction band (free electrons) or from surface states located in the band gap of the oxide[7,8]. A recombination order lower than one is an empirical way of describing that electron transfer from the TiO_2 layer to I_3^- ions may take place also from those occupied surface energy levels located in the energy gap[9]. However, a recombination through surface states is not the only explanation for sublinear recombination kinetics. A recombination order different to 1 can also arise from movements of the conduction band edge under illumination and kinetic complications due to the fact that reduction of triiodide is a two-electron process.

The most important indirect measurement of the conduction band electron density is the open circuit photovoltage (V_{oc}). The V_{oc} in any solar cell corresponds to the difference in electrochemical potentials (or Fermi energies) of electrons in the contacts on each side[10]. The number of electrons in the conduction band can be derived from the density of states function $N_c(E)$ of electrons in the conduction band and the probability that an electron state is occupied $f(E)$[11]

$$n_c = \int_{-\infty}^{+\infty} N_c(E)\ f(E) dE \tag{2.12}$$

The probability of occupation is given by the Fermi-Dirac distribution function

$$f(E) = \frac{1}{1 + exp\left(\frac{E - E_F}{kT}\right)} \tag{2.13}$$

where E_F is the Fermi level, k the Boltzmann constant and T the absolute temperature. If we assume $E - E_F >> kT$, we can apply the Boltzmann approximation to the Fermi Dirac distribution, which is reduced to[12]

$$f(E) \approx exp\left(-\frac{E - E_F}{kT}\right) \tag{2.14}$$

It is possible then to relate the Fermi level to the concentration of electrons in the conduction band by the expression[12]

$$n_c = N_c \, exp\left(-\frac{E_c - E_F}{kT}\right) \tag{2.15}$$

where N_c, as described above, is the effective density of states of electrons in the conduction band, E_c is the conduction band energy and E_F is the Fermi energy level in the oxide.

In the dark, electrons in the oxide (n_c^0) are in equilibrium with the electrolyte and the Fermi level in the oxide equals the redox potential, $E_{F,redox}$[7] (**Figure 2.2**). The redox potential of the electrolyte solution is given by the Nernst equation

$$E_{F,redox} = E^0 + \frac{RT}{nF} ln \frac{[I_3^-]}{[I^-]} \tag{2.16}$$

where R, T, n and F are the ideal gas constant, the temperature, the number of transferred electrons (n = 2 in this case (**Equation 2.4**)) and the Faraday constant, respectively, and E^0 the standard reduction potential of the I^-/I_3^- redox couple.

Under illumination (or externally applied bias), electrons in the oxide are no longer in equilibrium with the redox system and the electron density in the conduction band rises to a steady-state value. This steady-state electron concentration is determined by the balance between electron injection and electron transfer to I_3^- and the oxidized dye[13] and it defines the quasi-Fermi level ($_nE_F$) of electrons [10] (**Figure 2.2**).

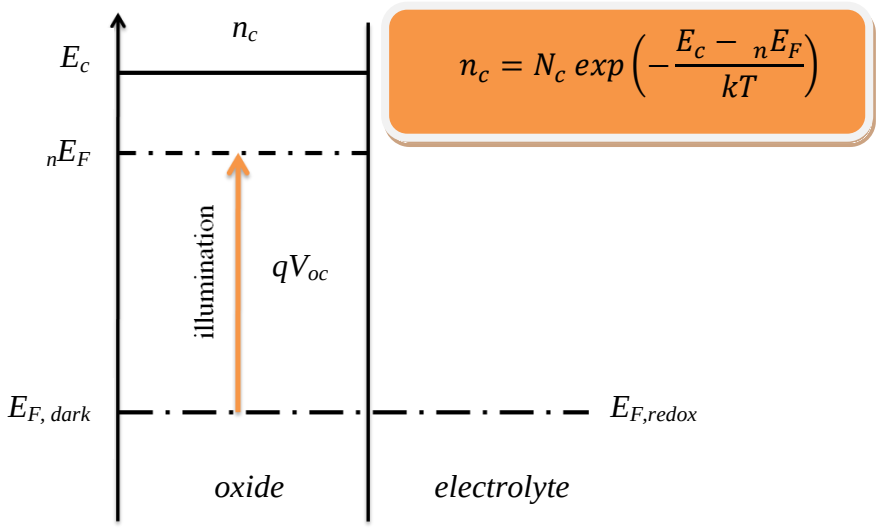

Figure 2.2 Energy level diagram of a DSC under illumination at open circuit.

The open circuit photovoltage of the solar cell is then defined as the difference between the Fermi level in the dark and under illumination[14]

$$V_{oc} = {}_nE_F - E_{F,redox} = \frac{kT}{q} ln\left(\frac{n_c}{n_c^0}\right) \tag{2.17}$$

Thanks to the previous equation, the free electron concentration can be defined in terms of the open circuit voltage

$$n_c = n_c^0\ exp\left(\frac{qV_{oc}}{kT}\right) \tag{2.18}$$

At open circuit conditions and under illumination, all injected electrons will recombine. Therefore

$$G = U_n \tag{2.19}$$

where G is the generation rate, describing the rate of injection of electrons into the oxide (in units of electrons cm^{-3} s^{-1}). This generation rate, as will be shown in following sections, is proportional to the intensity of the incident light (I_0). If we assume linear recombination kinetics, from **Equations 2.6** ($U_n = k_r n_c$), **2.17** and **2.19** we get the following relation between photovoltage and light intensity

$$V_{oc} \propto \frac{kT}{q}\ lnI_0 \tag{2.20}$$

This approximation predicts, therefore, that DSCs should behave as an ideal diode[10], and a semilogarithmic plot of V_{oc} versus light intensity should give a linear response with a slope of 26 mV at room temperature. However, usually DSC photovoltage varies with a slope higher than 26 mV and the empirical non-ideality factor *m* (**Equation 2.2**) accounts for this non ideality:

$$V_{oc} \propto \frac{mkT}{q}\, lnI_0 \tag{2.21}$$

Taking into account sublinear recombination kinetics, the reaction order β would be related to the non ideality factor *m* by its inverse ($m=1/\beta$), as can be obtained by combining **Equations 2.11** ($U_n = kr\, n_c^{\beta}$), **2.19** and **2.21** above.

As commented before, the reasons for the non-ideality are not completely clear in the current literature. Apart from a reaction order different from one, it can arise from the fact that the relationship between the free electron concentration and the cell voltage as described in **Equation 2.18** is only approximate. Some authors[3] have recently proposed an additional non-ideality parameter to describe the dependence of the conduction band electrons with Fermi level. This could be interpreted as a parameter modifying the effective concentration of free electrons in the conduction band (via an electron activity[15]), or a parameter shifting the TiO_2 conduction band with electron concentration[16].

2.3. Photocurrent and incident photon-to-current efficiency

The short circuit photocurrent J_{sc} of a dye-sensitized solar cell is determined by the overlap between its spectral incident photon-to-current efficiency (IPCE) and the spectral photon flux (I_0) of the incident illumination on the cell[17]

$$J_{sc} = q \int_{\lambda_{min}}^{\lambda_{max}} I_0(\lambda) IPCE(\lambda) d\lambda \tag{2.22}$$

where λ_{min} and λ_{max} define a wavelength range. The IPCE can be calculated from the efficiencies of the processes that determine the electrical conversion in DSCs (**Figure 2.3**) by

$$IPCE\ (\lambda) = \eta_{lh}(\lambda)\, \eta_{inj}(\lambda)\, \eta_{col}(\lambda) \tag{2.23}$$

where $\eta_{lh}(\lambda)$ is the light-harvesting efficiency (or absorptance) of the sensitized oxide layer, $\eta_{inj}(\lambda)$ is the electron injection efficiency from the sensitizer into the oxide (**Section 1.2.2**) and $\eta_{col}(\lambda)$ is the electron collection efficiency.

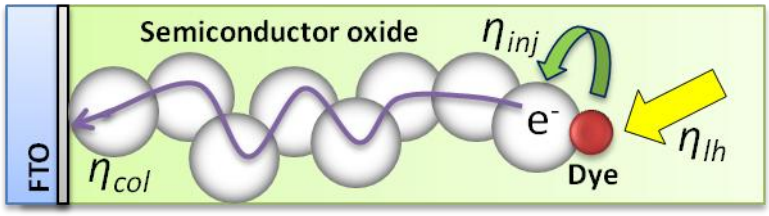

Figure 2.3 Scheme of the processes, which determine the incident photon-to-current efficiency of DSCs.

The light harvesting efficiency or absorptance of the sensitized films indicates how efficiently the adsorbed dye molecules harvest the incident light. The electron injection efficiency (or injection quantum yield) corresponds to the probability that a dye molecule in the excited electronic state injects an electron to the conduction band of the semiconductor. It thus determines how IPCE depends on charge separation at the dye/semiconductor interface. The charge separation depends, as explained in **Section 1.2.2**, on the driving force for electron injection from the LUMO of the dye to the conduction band of the semiconductor oxide, but also, as recently reported[18], on the populations of the acceptor and donor levels in the injection process and the corresponding back process (electron dye-recombination). Finally, the electron collection efficiency is an indication of the probability that a photogenerated electron reaches the collecting substrate contact before it is lost by recombination[17]. The collection efficiency thus depends on the average distance that electrons travel before recombination, which is expressed by a key parameter known as the electron diffusion length (L)[19]. The photogenerated electron collection efficiency can be predicted by solving a continuity equation for electrons where generation, transport and recombination are taken into account simultaneously. This will be described in detail in the next section.

To mark the division of the IPCE into its optical and electrical parts, the absorbed photon-to-current-conversion efficiency (APCE) can be defined. The APCE defines how efficiently absorbed photons are converted to electrons collected at the TCO substrate. The APCE is obtained by

$$APCE\ (\lambda) = \frac{IPCE(\lambda)}{\eta_{lh}(\lambda)} \tag{2.24}$$

For state-of-the-art DSCs, the APCE reaches typically up to 100 % and the IPCE about 85% depending on reflection losses at the DSC substrate[7].

2.4. Continuity equation for electron transport in a dye-sensitized solar cell

The standard model of electron generation, transport and recombination at the nanostructured photoelectrode in a DSC was introduced originally by Södergren et al.[20]. It is based on solving the continuity equation for free electrons. In a general form, the continuity equation for the electron density can be expressed as

$$\frac{\partial n_c}{\partial t} = G + \frac{1}{q}\nabla J_n - U_n \tag{2.25}$$

where n_c is the free electron concentration, J_n is the electron current density (C cm^{-2} s^{-1}), G is the electron generation rate (in electrons cm^{-3} s^{-1}) and U_n is the recombination rate (in electrons cm^{-3} s^{-1}).

Features related to illumination, light-harvesting and electron injection are included in the generation term. This term is expressed by the electron injection efficiency η_{inj} and the Lambert-Beer law for absorption as a function of distance

$$G(x) = \eta_{inj} I_0 \alpha_{abs}\ \exp(-\alpha_{abs} x) \tag{2.26}$$

where α_{abs} is the wavelength-dependent absorption coefficient of the dye-sensitized layer, x is the distance to the anode (also called collecting or *working* electrode) and I_0 is the incident photon flux.

The mesoporous semiconductor electrode, which is the main component of a dye-sensitized solar cell, consists of numerous interconnected nanocrystals. The transport in mesoporous electrodes is quite different compared with their compact analogues and the exact transport mechanisms that take place in DSCs are still under active debate even today. The two major mechanisms that govern electron current density J_n in a semiconductor are drift and diffusion[11]. Drift is charge particle motion in response to an applied electrical field. In contrast, if carriers diffuse, they move from regions of high

concentrations to regions of low concentration until the concentration gradient is zero. This can be expressed as:

$$J_n = \underbrace{nq\mu E}_{\text{Drift}} + \underbrace{qD\frac{dn}{dx}}_{\text{Diffusion}} \tag{2.27}$$

where *n* is the electron concentration, μ the electron mobility, *E* the electrical field and *D* the electron diffusion coefficient. The nanostructure of the semiconductor and also the presence of an electrolyte introduce profound changes in its photoelectrochemical properties. Of great importance is the fact that there is no significant local electric field to assist in the separation of photogenerated electron–hole pairs. This is a consequence of three factors that are typical for nanostructured solar cells: (1) the particles are too small[21], (2) TiO_2 colloids have usually a low carrier concentration[22] and (3) the nanoparticles are surrounded by an electrolyte with a high ionic strength. As a result, a depletion layer cannot be formed in the solid and the nanoparticles will not display any significant band bending. Transport occurs then mainly by diffusion, based on the gradient in electron concentration in the mesoporous oxide. Therefore, **Equation 2.27** is reduced to its diffusion term. In addition, this diffusion will be an ambipolar process, where both electrons and holes (excess of ionic positive charge in the electrolyte) contribute to the total current and the motion of both kinds of carriers is inseparable due to electrical neutrality[23]. The ambipolar diffusion coefficient is defined as

$$D_{amb} = \frac{(n+p)}{\left(\frac{n}{D_{holes}}\right) + \left(\frac{p}{D_{electrons}}\right)} \tag{2.28}$$

where *n* and $D_{electrons}$ are the density and diffusion coefficient of electrons, respectively, and *p* and D_{holes} are the density and diffusion coefficient of holes. If the density of holes (ions in DSCs) *p* vastly exceeds the density of electrons *n*, the previous equation can be simplified to $D_{amb} = D_{electrons}$.

Therefore, the ambipolar diffusion model and the absence of electrical fields lead directly to the conclusion that electron diffusion in the semiconductor oxide controls the current density in electrolyte filled cells. Transport is dominated by an electron density gradient or, in terms of energetics, by a gradient in the quasi-Fermi level for

electrons[10,24]. The second term in the continuity equation accounting for the diffusion current density of electrons can be expressed by Fick´s law in terms of free electrons

$$J_n = qD_0 \frac{\partial n_c}{\partial x} \tag{2.29}$$

where D_0 is the diffusion coefficient of free electrons. From the generalized Einstein relation the conductivity related to the electron diffusion process can be obtained[25]

$$\sigma_n = q^2 \frac{\partial n_c}{\partial \mu_n} D_0 \tag{2.30}$$

where μ_n is the electron mobility. From **Equations 2.29** and **2.18** ($n_c = n_c^0 \, exp(qV/kT)$) and assuming a constant mobility, an expression for the transport resistance (R_t) in the semiconductor can be obtained

$$R_t = R_{t,0} exp\left(-\frac{qV}{kT}\right) \tag{2.31}$$

where $R_{t,0}$ is a constant for all the samples provided that their geometrical dimensions are similar. **Equation 2.31** predicts an exponential behavior of the transport resistance with a slope of 26 mV.

Recombination is usually expressed in terms of the lifetime of electrons, which is defined as the inverse of the recombination constant

$$\tau_0 = \frac{1}{k_r} \tag{2.32}$$

The recombination term (U_n) in the continuity equation expressed in terms of the electron lifetime is then given by

$$U_n = \frac{(n_{c-} n_{eq})^\beta}{\tau_0} \tag{2.33}$$

According to the previous descriptions of the different terms of the continuity equation, time-dependent free electron density $n_c(x,t)$ can be written as:

$$\frac{\partial n_c(x,t)}{\partial t} = \alpha I_0 \exp(-\alpha x) + D_0 \frac{\partial^2 n_c(x,t)}{\partial x^2} - \frac{(n_c(x,t) - n_{eq})^\beta}{\tau_0} \tag{2.34}$$

The steady state solution to this equation assuming linear recombination ($\beta = 1$) yields the free electron concentration distribution through the semiconductor film. **Figure 2.4** illustrates the steady-state profiles of conduction band electrons for short circuit and open circuit.

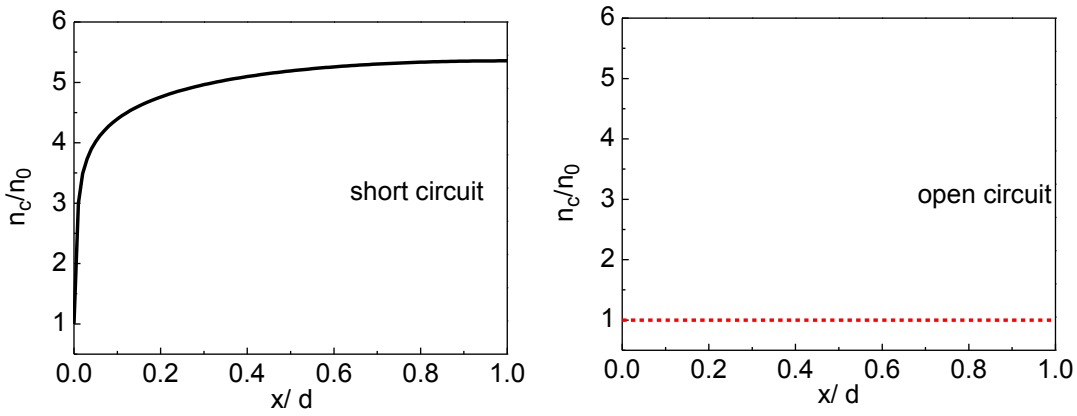

Figure 2.4 Typical concentration profile of free electrons in the DSC under short circuit and open circuit conditions as obtained from the solution of the continuity equation.

Since electron transport occurs by diffusion, an electron density gradient must be present within the nanostructured semiconductor electrode at conditions different from open circuit (**Figure 2.4**). This is related to a *spatial variation* of the quasi-Fermi level within the semiconductor electrode[3].

The electron collection efficiency can be described by this standard diffusion model, solving the continuity equation for the free electron density n_c. Assuming that electron recombination is linear with n_c, at steady-state conditions with no generation (dark conditions) the continuity equation is reduced to

$$D_0 \frac{\partial^2 n_c(x,t)}{\partial x^2} - \frac{(n_c(x,t) - n_{eq})}{\tau_0} = 0 \qquad (2.35)$$

The general solution of this differential equation is an exponential function for n_c where the diffusion length is the decay parameter, which can be defined as[7,19,26,27,44,45]

$$L = \sqrt{D_0 \tau_0} \qquad (2.36)$$

As the average value of an exponential function coincides with the decay parameter, this result demonstrates that **Equation 2.36** describes the diffusion length of electrons. Besides, as D_0 and τ_0 are constants, the diffusion length should be constant under the assumptions of simple diffusion of free electrons and linear recombination.

2.5. Electron traps in dye-sensitized solar cells

It is well known that relaxation times associated with electron transport and electron transfer to I_3^- in nanostructured TiO_2, as measured by small amplitude time or frequency domain techniques, are density-dependent[23,28-30]. All of these techniques measure the *effective* values of the diffusion coefficient and the lifetime (D_n and τ_n, respectively) rather than D_0 and τ_0, as will be explained in this section. Effective diffusion coefficients for electrons in nanostructured TiO_2 electrodes are around 10^{-8} to 10^{-4} cm^2 s^{-1} [31], orders of magnitude lower than those determined for single crystalline anatase TiO_2 (~0.4 cm^2 s^{-1} [32]). On the other hand, values for electron lifetimes in DSCs measured by kinetic techniques typically lie in the millisecond range, which is much longer than the conduction band electron lifetime (tens of microseconds[33]). As mentioned before, the effective values of both magnitudes are density-dependent and the electron diffusion coefficient has been observed to increase with intensity and forward bias, while the electron lifetime decreases. As a consequence, transport becomes more rapid at higher light intensities[24] as well as recombination.

The behaviour of the relaxation times described above is usually explained using a multiple trapping (MT) model[34-36]. This model assumes that TiO_2 electrodes are an effective medium with a distribution of localized energy states (traps) bellow the conduction band edge[37] (**Figure 2.5**).

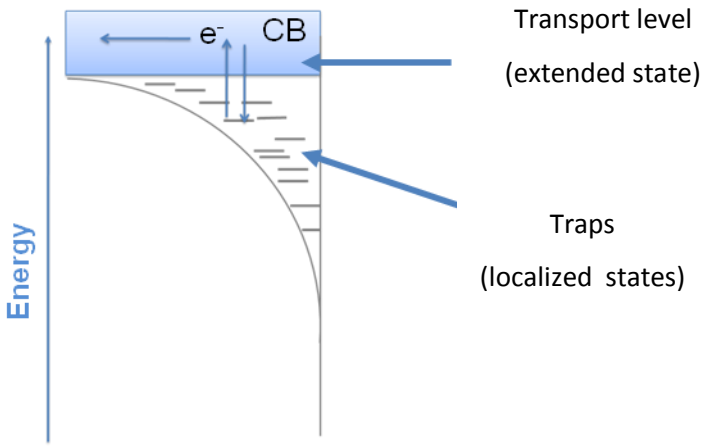

Figure 2.5 Schematic diagram of the multiple-trapping description of electrons in mesoporous oxide electrodes.

Electronic states are composed of a transport state (usually identified with the lower edge of the conduction band) at the energy level E_c with a diffusion coefficient D_0, and a density of localized states $g(E)$ distributed in the band gap[7,25] (**Figure 2.5**). The key feature of multiple trapping is that only free electrons contribute to the diffusion current but transport is slowed down by trapping and detrapping events to and from the localized states (**Figure 2.5**). Trapped electrons can be thermally excited to the conduction band and move freely before they are trapped again. The trapping/detrapping process strongly increases the transport time for the electrons hence explaining the low value of the effective diffusion coefficient with respect to its bulk value. In addition, the variation of trap occupancy with illumination explains the light-intensity dependence of the transport. A clear experimental confirmation of the existence of a high density of electron traps in mesoporous TiO_2 comes from charge extraction experiments[38]. By means of this technique the amount of stored electronic charge in the semiconductor as a function of the voltage is measured. Charge extraction measurements confirm that the density of trapped electrons greatly exceeds the calculated density of conduction band electrons[10,33]. The density and energetic location of traps bellow the conduction band are usually described by an exponential distribution (**Figure 2.5**) of the form[30,39-41]

$$g(E) = \frac{\alpha N_t}{kT} exp\left(\frac{-\alpha(E_c - E)}{kT}\right) \tag{2.37}$$

where E is the energy of the trap, N_t is the total trap density (typically 10^{19}-10^{20} cm^{-3} for TiO_2)[7] and α is a parameter that reflects the average energy of the distribution of trap states below the conduction band. Commonly the trap distribution parameter α is related to temperature via $\alpha = T/T_0$ where T_0 is the characteristic temperature of the distribution (typically T_0 = 600-1500 K for TiO_2[7]). The precise nature and location of the traps in mesoporous TiO_2 is nowadays a subject of discussion. The traps that are involved in electron transport in DSCs can be located either in the bulk, at grain boundaries, or at the TiO_2/electrolyte interface, and their origin, among others, could be defects in the mesoporous oxide.

The potential dependence of the stored charge defines a chemical capacitance of electron accumulation in a DSC. The chemical capacitance C_μ is a thermodynamic quantity that reflects the capability of a system to accept or release additional carriers due to a change in the electrochemical potential. For conduction band electrons, taking

into account **Equation 2.15** ($n_c = N_c\, exp(-(E_c-E_F/kT)$), the chemical capacitance can be obtained by

$$C_\mu^{CB} = q^2 \frac{\partial n_{CB}}{\partial\, {}_nE_F} = \frac{N_c q^2}{kT} exp\left(-\frac{(E_c - {}_nE_F)}{kT}\right) \tag{2.38}$$

This equation defines the capacitance associated with delocalized states or transport states. The presence of band gap states introduces additional possibilities for loading the semiconductor with charges[7]. Most of the electrons in the oxide are located in trap states. In **Section 2.2** the free electron concentration, n_c, was defined. In the same way, the density of localized electrons in traps, n_t, can also be defined as a function of the quasi-Fermi level. The occupancy of the traps will be given by the product of the density of states and the Fermi-Dirac function. Using again the Boltzmann approximation to the Fermi-Dirac distribution, we obtain that at zero temperature the occupied trap density as a function of the quasi-Fermi level is given by

$$n_t = \int_{-\infty}^{+\infty} f(E) g\,(E) dE = \int_{-\infty}^{{}^nE_F} \frac{\alpha N_t}{kT} exp\left(\frac{-\alpha(E_c - E)}{kT}\right) = N_t \exp\left(\frac{-\alpha(E_c - {}_nE_F)}{kT}\right) \tag{2.39}$$

If *g(E)* (**Equation 2.37**) is the distribution of traps, the chemical capacitance is obtained by integrating all the contributions through the band gap

$$C_\mu^{traps} = \frac{\alpha N_t q^2}{kT} exp\left(\frac{-\alpha(E_c - {}_nE_F)}{kT}\right) \tag{2.40}$$

The capacitance can also be expressed as a function of voltage

$$C_\mu^{traps} = \frac{N_t q^2}{kT_0} exp\left(\frac{-\alpha(E_{F,redox} - {}_nE_F)}{kT}\right) exp\left(\frac{-\alpha(E_c - E_{F,redox})}{kT}\right) = C_0 ex\, p\left(\frac{\alpha q V}{kT}\right) \tag{2.41}$$

where C_0 is a constant. Therefore, for the density of trapped carriers (which is the most important contribution to the total electron density), the capacitance gives a slope of $\alpha q/kT$ in a log-linear representation with respect to the applied voltage.

In the context of multiple trapping the increase of the diffusion coefficient with light intensity is easy to rationalize: as the Fermi level raises, the rate of detrapping to the

transport level is enhanced[19]. Concerning the decrease of lifetime with a raise of the Fermi level, two different interpretations can be found in literature. From the perspective of a *dynamic* or transport-limited model[42-45], if recombination is considered a chemical reaction between electrons and acceptors, there is a higher probability per unit time that electrons will encounter recombination sites if they move faster. Therefore, an increase of light intensity (and a consequent progressive filling of deep traps) results in a faster diffusion and hence in faster recombination[29]. In contrast, from the perspective of a *quasi-static* model, increasing the photocarrier density would raise the Fermi level and consequently the concentration of electrons in the conduction band[46]. The quasi-static approximation proposed by Bisquert and Vikhrenko[47] demonstrates that a dynamic, transport limited mechanism is not necessary to explain the behaviour of lifetime. This approach reduces the general multiple trapping to simple diffusion formalism. The Fermi level dependence of the time constants is associated to trapping and detrapping of free carriers, and this process can be expressed by a single trapping factor, $\partial n_c / \partial n_t$. This term accounts for the change of the time constants due to the fraction of time that free carriers spend in traps[19]. If the trapping and detrapping processes are very fast with respect to the free carrier relaxation processes, an approximate equilibrium (quasi-static conditions) between free and trapped carriers is maintained even when the system is perturbed away from equilibrium. This approximation has been verified by random walk simulation with a realistic number and distribution of traps by González-Vázquez et al.[19].

The existence of trapping and detrapping of free electrons makes the determination of the electron diffusion coefficient and the lifetime from time or frequency domain measurements more complicated with respect to the trap-free case. For example, when a DSC is perturbed away from equilibrium the relaxation of free carriers is not only determined by the value of D_0, but also by trapping and detrapping. However, the quasi-static approximation allows the reduction of the multiple trapping framework to the conventional diffusion equations. Under quasi-static conditions[47], local electron transport can still be described by Fickean diffusion. An *effective* diffusion coefficient of electrons is defined, that takes into account the effect of trapping and detrapping by defining a chemical diffusion coefficient

$$D_n = \frac{1}{1 + \frac{\partial n_t}{\partial n_c}} D_0 \tag{2.42}$$

where n_c is the concentration of free (conduction band) electrons, D_0 is the diffusion coefficient in the trap-free system and n_t is the total density of localized electrons in traps. As mentioned before, the derivative $\partial n_c / \partial n_t$ is the trapping factor and expresses the relationship of free to trapped electron concentration for a small variation of the Fermi level. The effect of trapping in the chemical diffusion coefficient is dominant when $\partial n_t / \partial n_c \gg 1$. In this case the equation can be simplified to:

$$D_n = \frac{\partial n_c}{\partial n_t} D_0 \tag{2.43}$$

The trapping term is unavoidable when measuring the chemical diffusion coefficient by any transient technique and it describes the delay of response of the *effective* diffusion coefficient with respect to the diffusion coefficient of free electrons[25,47]. Therefore, D_n provides the time for restoring equilibrium by transport when an excess of carriers is injected, whereas D_0 determines (together with the carrier density) the carrier flux at steady state.

A similar approach can be made to define an *effective* lifetime:

$$\tau_n = \left(1 + \frac{\partial n_t}{\partial n_c}\right) \tau_0 \approx \tau_n = \left(\frac{\partial n_t}{\partial n_c}\right) \tau_0 \tag{2.44}$$

In the quasi-static approximation the trapping factor can be calculated by means of the common equilibrium of traps and delocalized states with respect to the Fermi level[47]. Since the conduction band density of electrons is given by **Equation 2.15**, a change of the Fermi level for free electrons $\partial n_c / \partial E_F$ will be expressed by

$$\frac{\partial n_c}{\partial E_F} = \frac{N_c}{kT} \exp\left(-\frac{E_c - E_F}{kT}\right) \tag{2.45}$$

On the other hand, from the trap density expressed in **Equation 2.39** one obtains

$$\frac{\partial n_t}{\partial E_F} = \frac{\alpha N_t}{kT} \exp\left(-\frac{\alpha(E_c - E_F)}{kT}\right) \tag{2.46}$$

The density of trapped electrons and free electrons can be related thanks to the Fermi level

$$\frac{\partial n_t}{\partial n_c} = \alpha \frac{N_t}{n_c} exp\left(-\frac{\alpha(E_c - E_F)}{kT}\right) \quad (2.47)$$

The *effective* diffusion coefficient and the *effective* lifetime as a function of voltage ($_nE_F$-$E_{F,redox}$) can be calculated from **Equations 2.18** ($n_c = n_c^0\ exp(qV/kT)$), **2.42**, **2.43** and **2.46**

$$D_n = D^0 exp\left(\frac{(1-\alpha)(\ _nE_F - E_{F,redox})}{kT}\right) \quad (2.48)$$

$$\tau_n = \tau^0\ exp\left(\frac{(\alpha-1)(\ _nE_F - E_{F,redox})}{kT}\right) \quad (2.49)$$

where D^0 and τ^0 are the electron diffusion coefficient and the electron lifetime in the dark, respectively. Therefore, the effect of electron trapping kinetics is completely described in terms of electron densities. Furthermore, the exponential dependence on illumination intensity, which is observed experimentally, is correctly described.

As mentioned in **Section 2.4**, the square root of the product of diffusion coefficient and lifetime gives a key parameter known as diffusion length. Bisquert et al.[47], demonstrated that using the quasi-static approximation it is possible to determine a *small amplitude* diffusion length from separate measurements of the effective diffusion coefficient and the effective lifetime, provided that both parameters are measured at the same quasi-Fermi level position. In that case, the derivative of the trapping factor is equal for both parameters and

$$L_n = \sqrt{\tau_n D_n} = \sqrt{\tau_0 D_0} \quad (2.50)$$

As both parameters (τ_n and D_n) vary in opposite sense with illumination intensity and with power law exponents slightly different[33](**Equations 2.48** and **2.49**), Peter and co-workers[48] claimed that in some cases the product of electron lifetime and diffusion coefficient compensates to a large extent, forming a nearly constant electron diffusion length. If so, the diffusion length is independent of light intensity and electron trapping would not reduce the performance of the cells. The theoretical description based on the

quasi-static approximation demonstrates nicely this compensation effect commonly observed in experiments.

However, recent reports indicate that the electron diffusion length is not strictly constant, but increases with the light intensity[48-55]. Some authors have attributed this density dependence to non-linear recombination[6,56]. The physical reason is that in a non-linear model, the recombination rate depends strongly on the local carrier concentration[6] and the light intensity dependence for D_n and τ_n will no longer be the same. In this case the effective lifetime can be formulated as

$$\tau_n = \left(\frac{\partial n_t}{\partial n_c}\right) \tau_f \tag{2.51}$$

where τ_f is a free electron lifetime, which will depend on the specific recombination mechanism. If the recombination is linear with the free electron concentration, τ_f will be constant. However, in the case of sublinear recombination kinetics, the recombination rate will be expressed by **Equation 2.11** ($U_n = k_r n_c^{\beta}$), with a reaction order β lower than one. In that case, the free carrier lifetime shows a dependence with the Fermi level given by[6,19]

$$\tau_f = \frac{{n_0}^{1-\beta}}{\beta k_r} \, exp\left(\frac{(1-\beta)}{k_B T} \, ({}_nE_F - E_{F,redox)}\right) \tag{2.52}$$

According to this, the electron lifetime decreases more slowly with the Fermi level in a non-linear case, and, therefore, the diffusion length is expected to increase with illumination.

An important fact that must be taken into account is that according to the quasi-static approximation electron trapping does not affect steady state cell performance, but only the dynamic electron transport and recombination characteristics. Therefore, steady-state measurements as IPCE, IV curves or conductivity are not affected by trapping.

The diffusion transport model expressed by the continuity equation described in **Section 2.4** is valid as long as it is defined under steady-state conditions. However, for non-steady state conditions, trapping needs to be taken into account in the formulation of the continuity equation, as will be seen in the following section.

2.6. Continuity equation under non-steady state conditions

A physical model that can reproduce both the experimental steady state and dynamic characteristics of DSCs needs to incorporate into an unique continuity equation for electrons the steady-state and transient behaviour of the device. Several approaches towards the solution of the continuity equation under non-steady conditions have been made. In a first approach, some authors[48,57] solved analytically the continuity equation for small amplitude perturbations using intensity dependent effective values of the electron diffusion coefficient (D_n) and electron lifetime (τ_n) rather than the corresponding free electron values D_0 and τ_0 and the trapping term was omitted.

The effect of traps present in the semiconductor can be introduced in the continuity equation by two different ways. On one hand, a continuity equation can be defined, which explicitly considers the influence of trap states on the change of free electron concentration[33,58]

$$\frac{\partial n_c(x,t)}{\partial t} = \alpha I_0 \exp(-\alpha x) + D_0 \frac{\partial^2 n_c(x,t)}{\partial x^2} - \frac{(n_c(x,t) - n_{eq})}{\tau_0} - N_{t,0} < \frac{\partial f}{\partial t} > \quad (2.53)$$

where $N_{t,0}$ is the trap density and f is the probability of trap occupancy..

On the other hand, some authors[23,29,59,] define the continuity equation based on a total electron concentration dominated by trapped electrons. The total electron density is the sum of electron densities in the conduction band (n_c) and in localized states (n_t)

$$n = n_c + n_t \quad (2.54)$$

As already mentioned, the majority of electrons are localized in traps so $n \approx n_t$. Using the Boltzmann approximation, it is obtained that at zero temperature the total density of electrons corresponds to the integral of the distribution of traps between -∞ and the quasi-Fermi level

$$n = \int_{-\infty}^{{}^{n}E_F} f(E) g\,(E) dE = \int_{-\infty}^{{}^{n}E_F} \frac{\alpha N_t}{kT} exp\left(\frac{-\alpha E}{kT}\right) \quad (2.55)$$

The total density can be related to the voltage (${}_nE_F$-$E_{F,redox}$) via

$$n(x) = n_0 \exp\left(\frac{\alpha\,({}_nE_F(x) - E_{F,redox})}{kT}\right) \quad (2.56)$$

The continuity equation in terms of the total density is then written as

$$\frac{\partial n(x,t)}{\partial t} = G(x) + \frac{\partial}{\partial x}\left(D(n)\frac{\partial n(x,t)}{\partial x}\right) - k_r(n)(n_c(x,t) - n_{eq}) \quad (2.57)$$

where $n(x,t)$ is the total density of electrons in the film as a function of distance to the front contact (x) and time (t). The continuity equation is solved for a density dependent diffusion coefficient $D(n)$ and a *pseudo* first order kinetic recombination constant $k_r(n)$, also function of the total density. The density dependence of the diffusion coefficient is obtained from **Equation 2.48**. The kinetic recombination constant, $k_r(n)$, related to the inverse of the electron lifetime, can be obtained from **Equations 2.49** and **2.52** and is defined by

$$k_r\big(n(x)\big) = k_r^0 \; exp\left(\frac{(\beta - \alpha)(\,_nE_F(x) - E_{F,redox})}{kT}\right) \quad (2.58)$$

where k_r^0 is the recombination constant at zero bias. Note that $k_r(n)$ includes the non-linear dependence of the recombination rate on the free electron density. In this approximation both the trapping effects and the non-ideality are included in the model formulation.

2.7. References to Chapter 2

1. Nelson, J. *The Physics of Solar Cells*. (Imperial College Press: 2003).
2. Huang, S.Y., Schlichthörl, G., Nozik, A.J., Grätzel, M. & Frank, A.J. Charge Recombination in Dye-Sensitized Nanocrystalline TiO_2 Solar Cells. *The Journal of Physical Chemistry B* **101**, 2576-2582 (1997).
3. Barnes, P.R.F., Anderson, A.Y., Durrant, J.R. & O'Regan, B. Simulation and measurement of complete dye sensitised solar cells: including the influence of trapping, electrolyte, oxidised dyes and light intensity on steady state and transient device behaviour. *Physical Chemistry Chemical Physics.* **13**, 5798-5816 (2011).
4. Barnes, P.F., Liu, L., Li., X., Anderson, A.Y., Kisserwan, H., Ghaddar, T. H., Durrant, J. & O´Regan, B. Re-evaluation of Recombination Losses in Dye-Sensitized Cells: The Failure of Dynamic Relaxation Methods to Correctly Predict Diffusion Length in Nanoporous Photoelectrodes. *Nano Letters* **9**, 3532–3538 (2009).
5. Södergren, S., Hagfeldt, A., Olsson, J. & Lindquist, S.E. Theoretical-Models for the Action Spectrum and the Current-Voltage Characteristics of Microporous Semiconductor-Films in Photoelectrochemical Cells. *Journal of Physical Chemistry* **98**, 5552–5556 (1994).
6. Bisquert, J. & Mora-Seró, I. Simulation of Steady-State Characteristics of Dye-Sensitized Solar Cells and the Interpretation of the Diffusion Length. *The Journal of Physical Chemistry Letters* **1**, 450–456 (2010).

7. *Dye-Sensitized Solar Cells*. Edited by K. Kalyanasundaram (EPFL Press: 2010).
8. Bisquert, J., Zaban, A. & Salvador, P. Analysis of the mechanisms of electron recombination in nanoporous TiO_2 dye-sensitized solar cells. Nonequilibrium steady-state statistics and interfacial electron transfer via surface states. *Journal of Physical Chemistry B* **106**, 8774–8782 (2002).
9. Salvador, P., Hidalgo, M.G., Zaban, A. & Bisquert, J. Illumination intensity dependence of the photovoltage in nanostructured TiO_2 dye-sensitized solar cells. *Journal of Physical Chemistry B* **109**, 15915–15926 (2005).
10. Peter, L.M. Characterization and Modeling of Dye-Sensitized Solar Cells. *The Journal of Physical Chemistry C* **111**, 6601-6612 (2007).
11. *Nanostructured Materials for Solar Energy Conversion*. Edited by Soga, T. (Elsevier: 2006).
12. Rüdiger Memming *Semiconductor Electrochemistry*. (Wiley: 2001).
13. Peter, L. "Sticky Electrons" Transport and Interfacial Transfer of Electrons in the Dye-Sensitized Solar Cell. *Accounts of Chemical Research* **42**, 1839-1847 (2009).
14. Barnes, P. R. F., Andersson, A.Y., Juozapavicius, M., Liu, L., Li, X., Palomares, E., Forneli, A. & O´Regan, B. Factors controlling charge recombination under dark and light conditions in dye sensitised solar cells. *Physical Chemistry Chemical Physics* **13**, 3547-3558 (2011).
15. Jennings, J.R., Ghicov, A., Peter, L.M., Schmuki, P. & Walker, A.B. Dye-sensitized solar cells based on oriented TiO_2 nanotube arrays: Transport, trapping, and transfer of electrons. *Journal of the American Chemical Society* **130**, 13364–13372 (2008).
16. O'Regan, B.C. & Durrant, J.R. Kinetic and Energetic Paradigms for Dye-Sensitized Solar Cells: Moving from the Ideal to the Real. *Accounts of Chemical Research* **42**, 1799-1808 (2009).
17. Halme, J., Vahermaa, P., Miettunen, K. & Lund, P. Device Physics of Dye Solar Cells. *Advanced Materials* **22**, E210-E234 (2010).
18. Cai, J., Satoh, N. & Han, L. Injection Efficiency in Dye-Sensitized Solar Cells within a Two-Band Model. *The Journal of Physical Chemistry C* **115**, 6033-6039 (2011).
19. Gónzalez-Vázquez, J.P., Anta, J.A. & Bisquert, J. Determination of the Electron Diffusion Length in Dye-Sensitized Solar Cells by Random Walk Simulation: Compensation Effects and Voltage Dependence. *The Journal of Physical Chemistry C* **114**, 8552–8558 (2010).
20. Södergren, S., Hagfeldt, A., Olsson, J. & Lindquist, S. Theoretical Models for the Action Spectrum and the Current-Voltage Characteristics of Microporous Semiconductor Films in Photoelectrochemical Cells. *The Journal of Physical Chemistry* **98**, 5552-5556 (1994).
21. Grätzel, M. Photoelectrochemical cells. *Nature* **414**, 338-344 (2001).
22. Boschloo, G.K., Goossens, A. & Schoonman, J. Photoelectrochemical Study of Thin Anatase TiO_2 Films Prepared by Metallorganic Chemical Vapor Deposition. *Journal of The Electrochemical Society* **144**, 1311-1317 (1997).
23. Kopidakis, N., Schiff, E.A., Park, N., van de Lagemaat, J. & Frank, A.J. Ambipolar Diffusion of Photocarriers in Electrolyte-Filled, Nanoporous TiO_2. *The Journal of Physical Chemistry B* **104**, 3930-3936 (2000).
24. Cao, F., Oskam, G., Meyer, G.J. & Searson, P.C. Electron Transport in Porous Nanocrystalline TiO_2 Photoelectrochemical Cells. *The Journal of Physical Chemistry* **100**, 17021-17027 (1996).
25. Bisquert, J. Physical electrochemistry of nanostructured devices. *Physical Chemistry Chemical Physics* **10**, 49–72 (2008).

26. Bisquert, J. Theory of the Impedance of Electron Diffusion and Recombination in a Thin Layer. *The Journal of Physical Chemistry B* **106**, 325–333 (2002).
27. Harrick, N.J. Lifetime Measurements of Excess Carriers in Semiconductors. *Journal of Applied Physics* **27**, 1439–1442 (1956).
28. Peter, L.M. & Wijayantha, K.G.U. Intensity dependence of the electron diffusion length in dye-sensitised nanocrystalline TiO_2 photovoltaic cells. *Electrochemistry Communications* **1**, 576-580 (1999).
29. J. Frank, A., Kopidakis, N. & Lagemaat, J.V.D. Electrons in nanostructured TiO_2 solar cells: transport, recombination and photovoltaic properties. *Coordination Chemistry Reviews* **248**, 1165-1179 (2004).
30. Anta, J.A., Mora-Seró, I., Dittrich, T. & Bisquert, J. Interpretation of diffusion coefficients in nanostructured materials from random walk numerical simulation. *Physical Chemistry Chemical Physics* **10**, 4478-4485 (2008).
31. Boschloo, G. & Hagfeldt, A. Activation Energy of Electron Transport in Dye-Sensitized TiO_2 Solar Cells. *The Journal of Physical Chemistry B* **109**, 12093-12098 (2005).
32. Forro, L., Chauvet, O., Emin, D., Zuppiroli, L., Berger, H. & Levy, F. High mobility n-type charge carriers in large single crystals of anatase (TiO_2). *Journal of Applied Physics* **75**, 633-635 (1994).
33. Walker, A.B., Peter, L.M., Lobato, K. & Cameron, P.J. Analysis of Photovoltage Decay Transients in Dye-Sensitized Solar Cells. *The Journal of Physical Chemistry B* **110**, 25504-25507 (2006).
34. Schmidlin, F.W. Theory of Trap Controlled Transient Photoconduction. *Bulletin of the American Physical Society* **22**, 346–346 (1977).
35. Tiedje, T. & Rose, A. A physical interpretation of dispersive transport in disordered semiconductors. *Solid State Communications* **37**, 49-52 (1981).
36. Vanmaekelbergh, D. & de Jongh, P.E. Electron transport in disordered semiconductors studied by a small harmonic modulation of the steady state. *Physical Review B* **61**, 4699 (2000).
37. de Jongh, P.E. & Vanmaekelbergh, D. Trap-limited electronic transport in assemblies of nanometer-size TiO_2 particles. *Physical Review Letters* **77**, 3427–3430 (1996).
38. Duffy, N.W., Peter, L.M., Rajapakse, R.M.G. & Wijayantha, K.G.U. A novel charge extraction method for the study of electron transport and interfacial transfer in dye sensitised nanocrystalline solar cells. *Electrochemistry Communications* **2**, 658-662 (2000).
39. Anta, J.A., Mora-Seró, I., Dittrich, T. & Bisquert, J. Dynamics of Charge Separation and Trap-Limited Electron Transport in TiO_2 Nanostructures. *The Journal of Physical Chemistry C* **111**, 13997-14000 (2007).
40. van de Lagemaat, J. & Frank, A.J. Effect of the Surface-State Distribution on Electron Transport in Dye-Sensitized TiO_2 Solar Cells: Nonlinear Electron-Transport Kinetics. *The Journal of Physical Chemistry B* **104**, 4292-4294 (2000).
41. Bisquert, J., Fabregat-Santiago, F., Mora-Sero, I., Garcia-Belmonte, G., Barea, E. M. & Palomares, E. A review of recent results on electrochemical determination of the density of electronic states of nanostructured metal-oxide semiconductors and organic hole conductors. *Inorganica Chimica Acta* **361**, 684–698 (2008).
42. Nelson, J., Haque, S.A., Klug, D.R. & Durrant, J.R. Trap-limited recombination in dye-sensitized nanocrystalline metal oxide electrodes. *Physical Review B* **6320**, (2001).
43. Kopidakis, N., Benkstein, K.D., Lagemaat, J.V.D. & Frank, A.J. Transport-limited

recombination of photocarriers in dye-sensitized nanocrystalline TiO_2 solar cells. *Journal of Physical Chemistry B* **107**, 11307–11315 (2003).
44. Anta, J.A., Casanueva, F. & Oskam, G. A numerical model for charge transport and recombination in dye-sensitized solar cells. *Journal of Physical Chemistry B* **110**, 5372–5378 (2006).
45. Villanueva-Cab, J., Oskam, G. & Anta, J.A. A simple numerical model for the charge transport and recombination properties of dye-sensitized solar cells: A comparison of transport-limited and transfer-limited recombination. *Solar Energy Materials and Solar Cells* **94**, 45–50 (2010).
46. Bisquert, J. & Vikhrenko, V.S. Interpretation of the Time Constants Measured by Kinetic Techniques in Nanostructured Semiconductor Electrodes and Dye-Sensitized Solar Cells. *The Journal of Physical Chemistry B* **108**, 2313-2322 (2004).
47. Bisquert, J. & Vikhrenko, V.S. Interpretation of the Time Constants Measured by Kinetic Techniques in Nanostructured Semiconductor Electrodes and Dye-Sensitized Solar Cells. *The Journal of Physical Chemistry B* **108**, 2313-2322 (2004).
48. Fisher, A.C., Peter, L.M., Ponomarev, E.A., Walker, A.B. & Wijayantha, K.G.U. Intensity Dependence of the Back Reaction and Transport of Electrons in Dye-Sensitized Nanocrystalline TiO_2 Solar Cells. *The Journal of Physical Chemistry B* **104**, 949-958 (2000).
49. Fabregat-Santiago, F., Bisquert, J., Le, C., Peter, C., Wang, M., Zakeeruddin, S. & Grätzel, M. Electron Transport and Recombination in Solid-State Dye Solar Cell with Spiro-OMeTAD as Hole Conductor. *Journal of the American Chemical Society* **131**, 558–562 (2009).
50. Wang, H. & Peter, L.M. A Comparison of Different Methods To Determine the Electron Diffusion Length in Dye-Sensitized Solar Cells. *The Journal of Physical Chemistry C* **113**, 18125–18133 (2009).
51. Barnes, P.R.F., Anderson, A.Y., Koops, S.E., Durrant, J.R. & O'Regan, B.C. Electron Injection Efficiency and Diffusion Length in Dye-Sensitized Solar Cells Derived from Incident Photon Conversion Efficiency Measurements. *The Journal of Physical Chemistry C* **113**, 1126–1136 (2009).
52. Bisquert, J., Fabregat-Santiago, F., Mora-Seró, I., Garcia-Belmonte, G. & Giménez, S. Electron Lifetime in Dye-Sensitized Solar Cells: Theory and Interpretation of Measurements. *The Journal of Physical Chemistry C* **113**, 17278–17290 (2009).
53. Nissfolk, J., Fredin, K., Hagfeldt, A. & Boschloo, G. Recombination and Transport Processes in Dye-Sensitized Solar Cells Investigated under Working Conditions. *The Journal of Physical Chemistry B* **110**, 17715-17718 (2006).
54. Kruger, J., Plass, R., Grätzel, M., Cameron, P.J. & Peter, L.M. Charge transport and back reaction in solid-state dye-sensitized solar cells: A study using intensity-modulated photovoltage and photocurrent spectroscopy. *Journal of Physical Chemistry B* **107**, 7536–7539 (2003).
55. Dunn, H.K. & Peter, L.M. How Efficient Is Electron Collection in Dye-Sensitized Solar Cells? Comparison of Different Dynamic Methods for the Determination of the Electron Diffusion Length. *Journal of Physical Chemistry C* **113**, 4726–4731 (2009).
56. Villanueva-Cab, J., Wang, H., Oskam, G. & Peter, L.M. Electron Diffusion and Back Reaction in Dye-Sensitized Solar Cells: The Effect of Nonlinear Recombination Kinetics. *The Journal of Physical Chemistry Letters* **1**, 748-751 (2010).
57. Dloczik, L., Ileperuma, O., Lauermann, I., Peter, L.M., Ponomarev, E.A., Redmond, G., Shaw, N.J. & Uhlendorf, I. Dynamic Response of Dye-Sensitized

Nanocrystalline Solar Cells: Characterization by Intensity-Modulated Photocurrent Spectroscopy. *The Journal of Physical Chemistry B* **101**, 10281-10289 (1997).

58. Kambili, A., Walker, A.B., Qiu, F.L., Fisher, A.C., Savin, A.D. & Peter, L.M. Electron transport in the dye sensitized nanocrystalline cell. *Physica E-Low-Dimensional Systems & Nanostructures* **14**, 203–209 (2002).
59. Villanueva, J., Anta, J.A., Guillén, E. & Oskam, G. Numerical Simulation of the Current−Voltage Curve in Dye-Sensitized Solar Cells. *The Journal of Physical Chemistry C* **113**, 19722–19731 (2009).

Chapter 3

Characterization Methods of Dye-Sensitized Solar Cells

3. Characterization methods of dye-sensitized solar cells

3.1. Standard solar spectrum and solar irradiation

The efficiency of a solar cell is sensitive to variations of the intensity and the energy distribution of the incident light. Solar radiation reaching the Earth's surface varies significantly with location, atmospheric conditions, time of the day, Earth/Sun distance and solar rotation and activity. Since the solar spectrum depends on so many variables, it is necessary to define a standard spectrum and power density in order to allow for an accurate comparison among different solar devices. The Sun emits light resembling the spectrum of a blackbody at a temperature of 5670K (**Figure 3.1**).

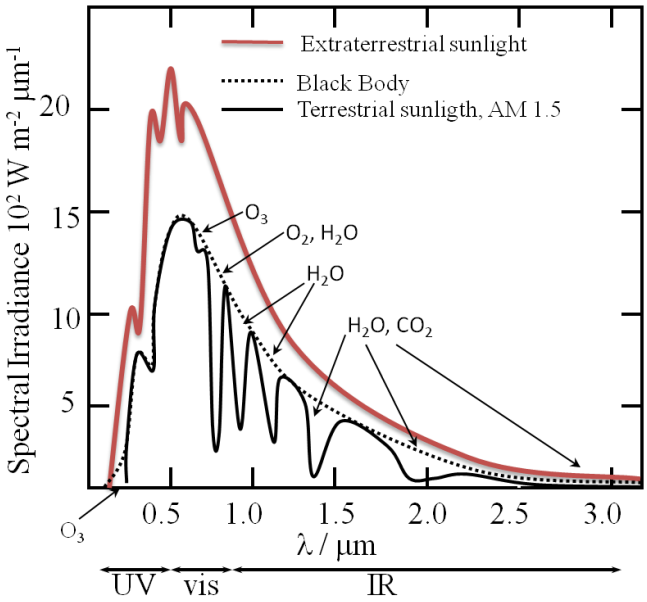

Figure 3.1 Spectra of a black body at 5670 K, extraterrestial sunlight and terrestrial sunlight (AM1.5). Ultraviolet light is filtered out by ozone. Water and CO_2 absorb mainly in the infrared.

The power density at the surface of the Sun is 62 MW m^{-2} and it is reduced to 1353 W m^{-2} at the point just above the Earth's atmosphere[1]. The latter value is the so-called solar constant, which describes the amount of incoming perpendicular solar radiation measured on the outer surface of Earth's atmosphere, when the Sun and Earth are spaced 149,597,890 km (one astronomical unit, AU). Before reaching the ground, the radiation passes through the atmosphere, which modifies the solar spectrum, both intensity and energetic distribution (**Figure 3.1**). The irradiation that finally reaches the ground will depend on the length of the path the radiation must pass. This optical path is defined as *Air Mass* (AM), which takes into account the attenuation radiation suffers due to

atmospheric absorption and depends on the position of the Sun. The Air Mass is defined as

$$AM = \frac{1}{cos\ (\theta)} \tag{3.1}$$

where θ is the angle of elevation of the Sun (**Figure 3.2)**. When the Sun is directly overhead the Air Mass is 1 (AM 1) and the irradiance reaching the Earth's surface is maximum.

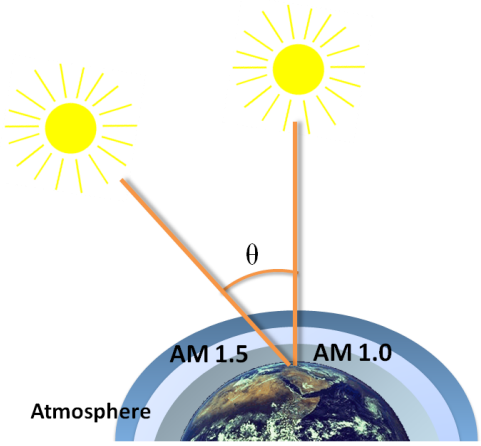

Figure 3.2 Schematic representation of AM 1.5, AM 1.0 and angle of elevation of the Sun.

The standard spectral distribution of the light used for efficiency measurements of solar cells is AM 1.5 G[2], according to θ = 48.2º and an optical path 1.5 times longer than in the case of AM 1 light. This atmosphere thickness should attenuate the solar spectrum to a mean irradiance of around 900 W m^{-2} [1]. However, for convenience the standard spectrum is normalized so that the integrated irradiance of this spectrum per unit area and unit time is 1000 W m^{-2} (known as 1 sun illumination). This light intensity is used for standard testing conditions. The "G" in AM 1.5 G stands for global, as it can be differentiated between direct radiation and global radiation, which takes into account also the diffuse light. DSCs, thanks to their rough surfaces, are better suited for diffuse light than flat surfaces[3]. They are, also, less sensitive to movements of the Sun. In **Figure 3.1** a comparison between the spectrum of a black body at 5670 K and the AM 1.5 spectrum is shown.

3.2. Illumination sources

In this section the different sources of illumination and ways of calibration used in the course of this thesis are summarized. One of the sources used to measure current-voltage characteristics was a Thermo Oriel Xenon 450 W arc lamp coupled to a water filter to remove IR radiation and a 325 nm UV blocking filter. The xenon lamp spectrum differs from the solar spectrum mainly due to the intense line output in the 800-1100 nm region. The objective of using filters was to adjust the lamp spectrum as much as possible to that of AM 1.5. For the same reason, an infrared filter KG5 (Schott) was added in some cases. In some experiments an ABET sun 2000 solar simulator was used as illumination source to measure current-voltage characteristics. The light source in this solar simulator is a xenon lamp as well, but it incorporates an AM 1.5 filter modifying the spectrum for a better match to the standard solar spectrum.

The light intensity was calibrated to the standard value of 1 sun (100 mW cm^{-2}) using a reference solar cell (Oriel, 91150). In general, a reference solar cell with a comparable sensitivity to the sample under test should be employed to adjust the output of the illumination source[4]. For this reason, in some cases the calibration is made with an IR filter (KG5 Schott). The use of KG5 for calibration provides a closer match of the reference cell to the DSC spectral response[4]. The illumination source employed for each test and the calibration procedure will be specified in the corresponding Results sections.

The illumination source for the frequency response techniques described below was provided by a 530 nm light emitting diode (LED). The light intensity of the LED was calibrated using a TiO_2 dye solar cell with known photocurrent response.

3.3. Measurement of the incident photon-to-current efficiency

For incident photon-to-current efficiency (IPCE) measurements the samples were illuminated with monochromatic light using a xenon arc lamp and a grating monochromator. The incident photon flux was measured with a calibrated photodiode. Two monochromators were used: TMc300 monochromator (Bentham) and 1/8 m monochromator (Oriel). The IPCE spectra were measured with a spectral resolution of 10 nm.

3.4. "Short circuit voltage" measurements

This method, first introduced by Boschloo et al.[5], is used to estimate the electron quasi-Fermi level of electrons in the dye-sensitized semiconductor film when the cell is illuminated under short circuit conditions. In a first step, the cell is illuminated under short circuit (SC) conditions until a constant photocurrent is obtained. Then, the illumination is stopped and simultaneously the cell is switched to open circuit (OC) and the voltage is monitored. An example of this measurement is shown in **Figure 3.3**.

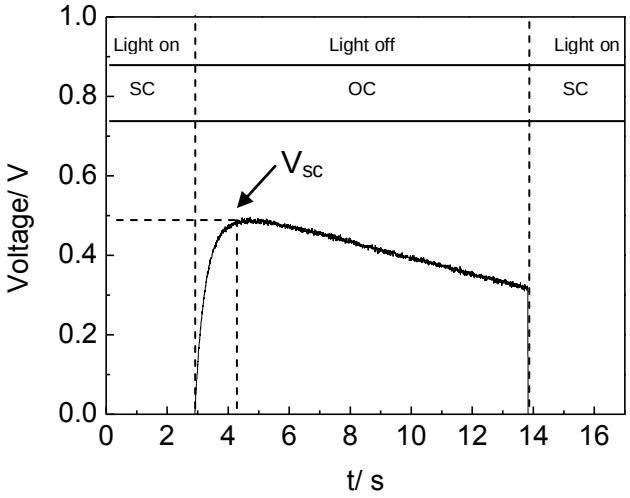

Figure 3.3 Example of a short circuit voltage measurement.

The maximum voltage, which is measured after switching to open circuit, is known as short circuit voltage (V_{sc}) and gives a good estimation of the average electron quasi-Fermi level under short circuit conditions. In a plot of the short circuit voltage and the open circuit voltage versus light intensity a shift between both parameters can be observed, which is almost constant at all light intensities. Typically V_{sc} is 200-250 mV lower than V_{oc}.

3.5. Open circuit voltage decay

During open circuit voltage decay (OCVD) measurements, the cell is first illuminated under open circuit conditions to establish a steady-state photovoltage. Then, the illumination is turned off and the subsequent voltage decay is monitored. The voltage decay is a consequence of the recombination of electrons in the semiconductor film. As can be seen in **Figure 3.4**, the decay is very rapid at the beginning, and then it slows down considerably. This slow-down is due to a slower detrapping of electrons as the quasi-Fermi level falls[6].

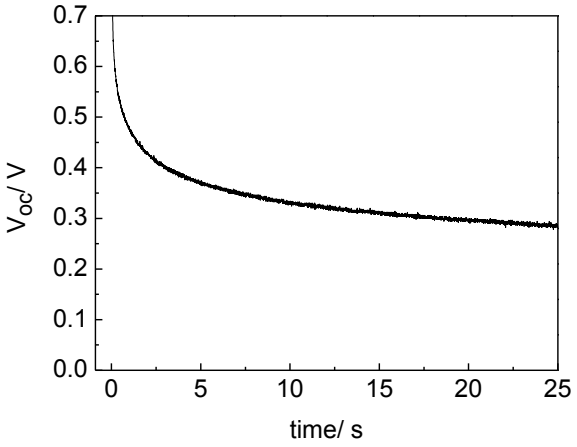

Figure 3.4 Open circuit voltage decay measurement.

Zaban et al.[7] demonstrated the validity of this method to measure the effective electron lifetime as a function of the open circuit voltage. The electron lifetime can be obtained from the inverse of the derivative of the voltage decay transient normalized by the thermal voltage[7] (see **Equations 2.6** and **2.18**):

$$\tau_n^{OCVD} = \frac{k_B T}{q} \left(\frac{dV_{oc}}{dt}\right)^{-1} \tag{3.1}$$

The advantage of this method with respect to alternative methods based on small perturbations in the time or frequency domain is that the lifetime can be determined in a wide potential range with one single measurement, with as much resolution along the Fermi level axis as desired.

For OCVD measurements, a light pulse of 2 seconds duration is used to generate a photovoltage and the subsequent decay is recorded on an oscilloscope via a SR 560 pre-amplifier, which removes high frequency noise.

3.6. Frequency response analysis techniques

Frequency-domain techniques are very useful tools for the characterization of DSCs. In these techniques, a sinusoidal modulation in light intensity or voltage is superimposed on a dc component and the phase and magnitude of the response relative to the input is measured. The modulation amplitude is small enough to ensure a linear response of the system[8,9]. The measurement comprises a wide range of frequencies (mHz to MHz), corresponding to timescales relevant for processes occurring within DSCs.

3.6.1. Electrochemical impedance spectroscopy

Electrochemical impedance spectroscopy (EIS) is a powerful technique for the characterization of electrochemical systems. Regarding DSCs it is one of the most useful experimental techniques as it permits a simultaneous characterization of the different processes taking place in the cell[10,11]. In EIS measurements the potential applied to the solar cell is perturbed by a small amplitude sinusoidal modulation and the resulting sinusoidal current response is measured as a function of the modulation frequency[3].

The meaning of electrical impedance can be understood starting from the concept of resistance. The electrical resistance is the ability of a circuit element to resist the flow of electrical current. The well known Ohm's law defines resistance (*R*) in terms of the ratio between voltage (*V)* and current (*I)*

$$R = \frac{V}{I} \tag{3.2}$$

This relationship is limited to only one circuit element, an ideal resistor. But usually the systems under study contain circuit elements that exhibit a much more complex behaviour. The simple concept of resistance needs to be replaced by a more general parameter: the impedance, which includes not only the relative amplitudes of the voltage and the current (**Equation 3.2**), but also the relative phases. Like resistance, impedance is a measure of the ability of a circuit to resist the flow of electrical current[12].

Electrochemical impedance is normally measured using a small excitation signal in order to obtain a linear response of the cell. The electrical current response is measured when a certain sinusoidal voltage is applied to the system. This current response will be a sinusoid at the same frequency, but shifted in phase (**Figure 3.5**).

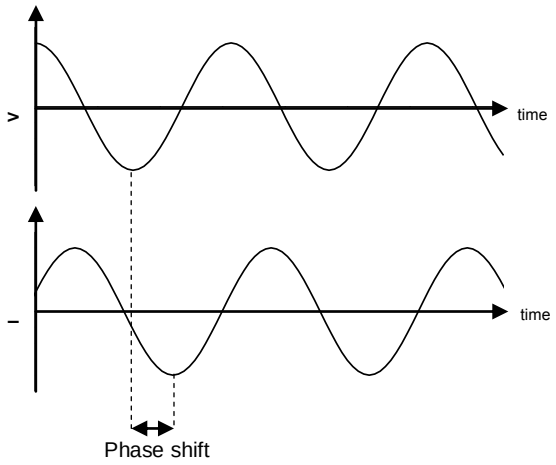

Figure 3.5 Sinusoidal current response in a linear system.

The excitation signal can be written as

$$V(\omega) = V_0 \cos \omega t \tag{3.3}$$

where *V(ω)* is the ac potential applied to the system, V_0 is the amplitude signal and ω is the angular frequency ($\omega = 2\pi f$ rad s^{-1}). The current response will be shifted with respect to the applied potential

$$I(\omega) = I_0 \cos(\omega t + \phi) \tag{3.4}$$

where *I(ω)* is the ac electrical current response signal, I_0 the amplitude and ϕ the phase shift. The phase factor contains the current lag with respect to the voltage. An expression analogous to Ohm´s Law allows for calculating the impedance of the system as

$$Z(\omega) = \frac{V(\omega)}{I(\omega)} = \frac{V_0 \cos \omega t}{I_0 \cos(\omega t + \phi)} \tag{3.5}$$

Usually, it is convenient to use complex exponentials to express the impedance. Complex numbers allow for a simpler representation of the relative magnitude and phase of the input and output signal. Besides, it is a more powerful representation for circuit analysis purposes. Taking into account Euler's relationship,

$$e^{jx} = \cos(x) + j \sin(x) \tag{3.6}$$

it is possible to express the potential as

$$V(\omega) = V_0 e^{j\omega t} \tag{3.7}$$

and the current response can be described as

$$I(\omega) = I_0 e^{j(\omega t+\phi)} \tag{3.8}$$

Since $Z(\omega) = V(\omega)/ I(\omega)$ the exponential $exp\ (j\omega t)$ terms cancel out, so that

$$Z = \frac{V_0}{I_0} e^{-j\phi} = Z_0 e^{-j\phi} \tag{3.9}$$

The impedance is, therefore, expressed in terms of a magnitude Z_0 (ratio of the voltage amplitude to the current amplitude) and a phase shift ϕ. Using **Equation 3.6**, it is possible to separate the real part and the imaginary part of the impedance

$$Z_0 e^{-j\phi} = \underbrace{Z_0\, cos(\phi)}_{real\ (Z)} - \underbrace{Z_0\, j\, sin(\phi)}_{imaginary\ (Z)} \tag{3.10}$$

By varying the frequency of the applied signal, one can get the impedance of the system as a function of frequency. The recorded data can either be represented as magnitude and phase vs. frequency (Bode plot) or on a complex plane (Nyquist plot) (**Figure 3.6**). In a Nyquist plot the real part of the impedance (Z') is plotted on the X-axis and the imaginary part (Z'') is plotted on the Y-axis.

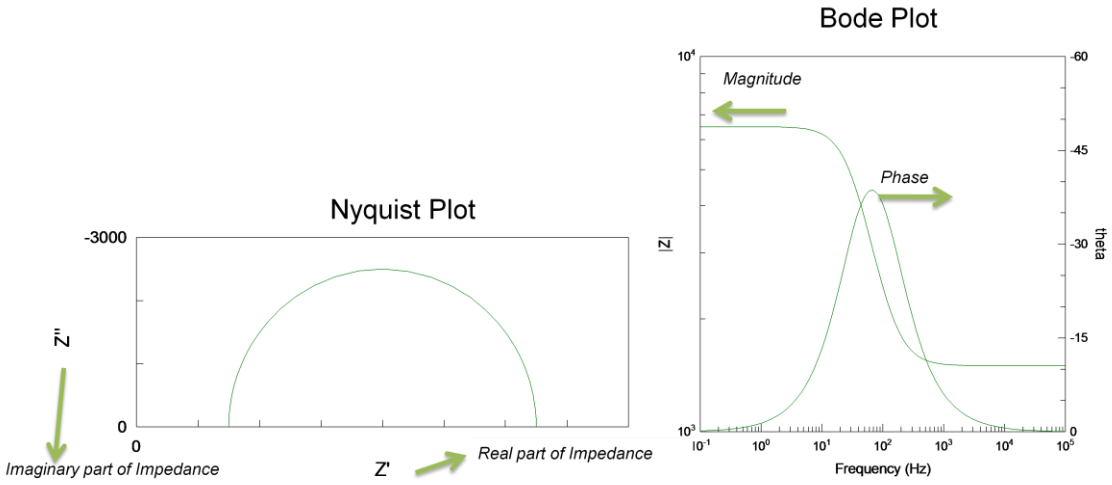

Figure 3.6 Nyquist plot and Bode plot.

EIS data are commonly analyzed in terms of an equivalent circuit model. Most of the circuit elements in the model are common electrical elements such as resistors,

capacitors and inductors. These elements can be combined in series and in parallel to give complex equivalent circuits. For example, the spectra shown in **Figure 3.6** are the result of a resistance in series with a *RC* element (a resistance and a capacitance in parallel). A certain physical meaning must be then assigned to the different elements of the equivalent circuit. The main disadvantage of EIS is primarily associated with possible ambiguities in this assignment and in the interpretation of results[13].

The most common cell model for electrochemical systems is the Randles Circuit (**Figure 3.7a**). This circuit models a cell where polarization is due to a combination of kinetic and diffusion processes. It includes a series resistance (R_s), a double layer capacitor (C_{dl}), a charge transfer resistance (R_{ct}) and a Warburg diffusion impedance (W). The Nyquist Plot for this circuit is shown in **Figure 3.7b**. The double layer capacitance and the charge transfer resistance in parallel define the time constant ($\tau = RC$) or relaxation time of the system[13]. The Nyquist plot for a *RC* combination is always a semicircle as the one indicated in **Figure 3.7b**. The series resistance is expressed by the real intercept at high frequencies of this semicircle. Finally, the Warburg diffusion impedance appears as a straight line with a slope of 45° (**Figure 3.7b**).

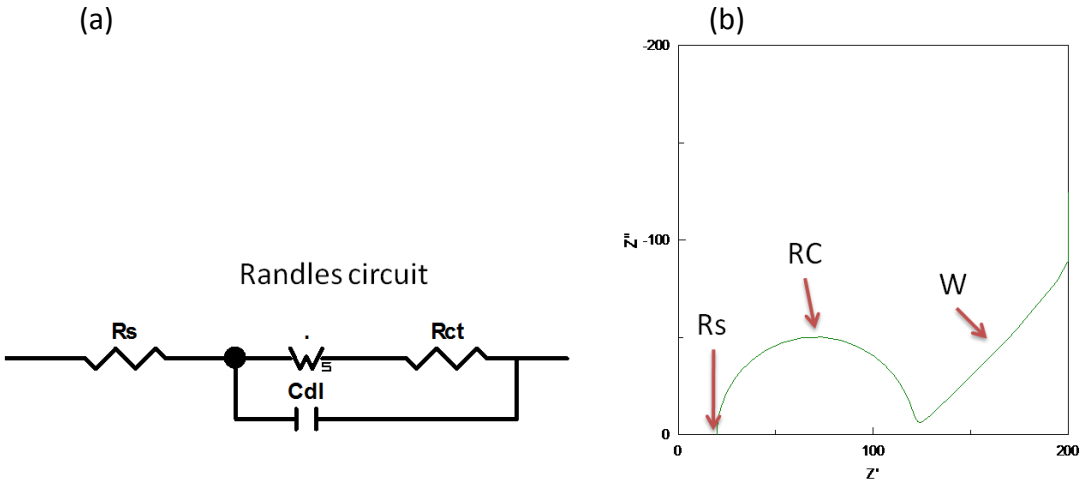

Figure 3.7 (a) Randles circuit, (b) Nyquist plot of Randles circuit.

In addition to being a useful model in its own right, the Randles circuit is the starting point for other more complex models. A dye-sensitized solar cell is a very complex system and its impedance response will be related to the response of the different components of the device. Generally, a transmission line model is used to describe the system, as shown in **Figure 3.8**.

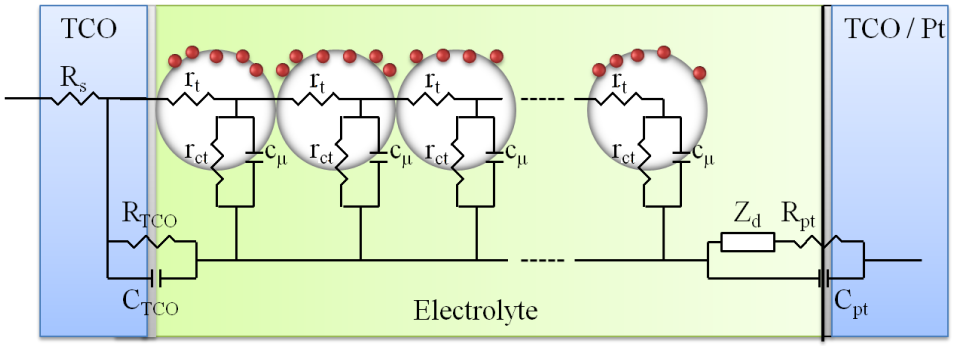

Figure 3.8 Transmission line model for DSC.

Different circuit elements are attributed to the different processes taking place in the cell. The processes occurring in the mesoporous oxide film are usually modeled by a diffusion-recombination transmission line. Its application to DSCs was first proposed by Bisquert[14]. This transmission line is composed of a network of resistive and capacitive elements, which describe the transport and interfacial transfer of electrons that take place in the oxide (**Figure 3.8**). The mesoporous oxide film has two main contributions in the impedance spectrum (**Figure 3.9**). One feature is the intermediate frequency arc, which accounts for the parallel connection of the charge transfer resistance R_{ct} ($R_{ct} = r_{ct}/d$, being d the thickness of the film) and the capacitance of the film C_μ ($C_\mu = c_\mu\ d$). The other feature is a Warburg-like diffusion element, a 45º phase shift at high frequencies related to the electron transport resistance R_t ($R_t = r_t\ d$) in the mesoporous layer. The diffusion impedance of redox species in the electrolyte (Z_d) is usually modeled using a finite-length Warburg element of the type used for thin layer electrochemical cells[6]. Generally, Z_d in DSCs is small and it is difficult to identify it in the overall impedance solar cell response. However, it is clearly visible when electrolytes based on ionic liquids are used. In that case, a semicircle at low frequencies can be distinguished in the spectra. A cathodic impedance due to the platinised electrode is also present in the spectra and it is expressed as a parallel combination of the charge transfer resistance R_{pt} (characterizing electron transfer to and from the redox system) and a double layer capacitance, (C_{pt}). In the spectra, this feature is represented by a semicircle at high frequencies. R_{TCO} and C_{TCO} stand for the charge transfer resistance and the capacitance at the interface TCO/electrolyte. Finally, R_s accounts for the series resistance of the conducting glass plus any other element that might be considered to be in series with the rest of the circuit. The different features are represented in **Figure 3.9**,

where an example of a typical electrochemical impedance spectrum of a dye solar cell is shown.

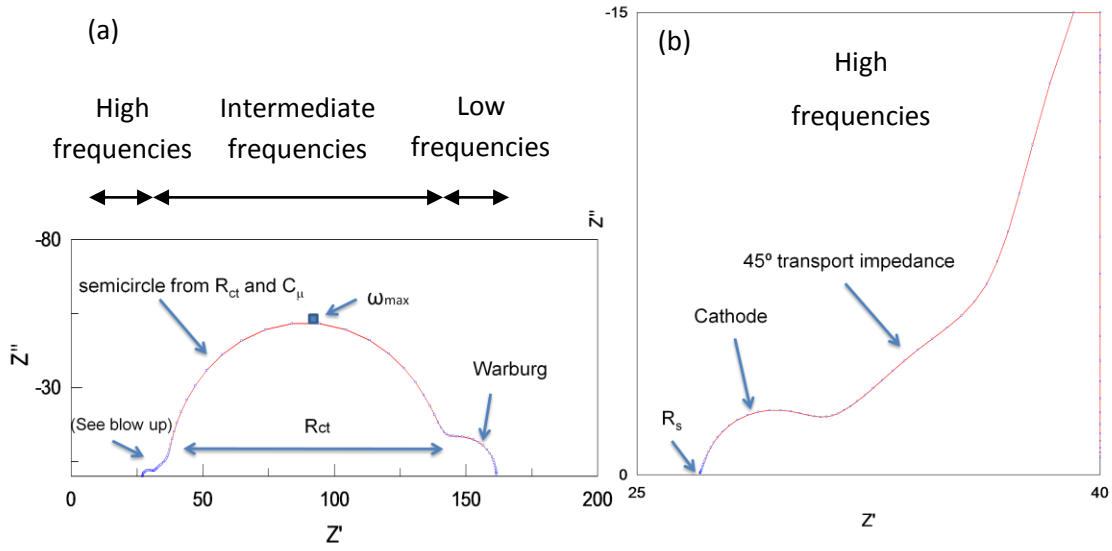

Figure 3.9 (a) Nyquist impedance spectrum of a typical DSC. (b) Blow up of high frequency region showing the semicircle from cathode and 45° transport impedance (transmission line).

It must be pointed out that in many cases the contribution of the different components is not seen as clearly as in the example in **Figure 3.9**. This depends, for example, on the voltage at which the measurement is done or on the semiconductor used, as will be seen in the following Chapters.

The electrochemical impedance spectra were fitted using the Zview software (Scribner) by means of one of the two equivalent circuits shown in **Figure 3.10**,

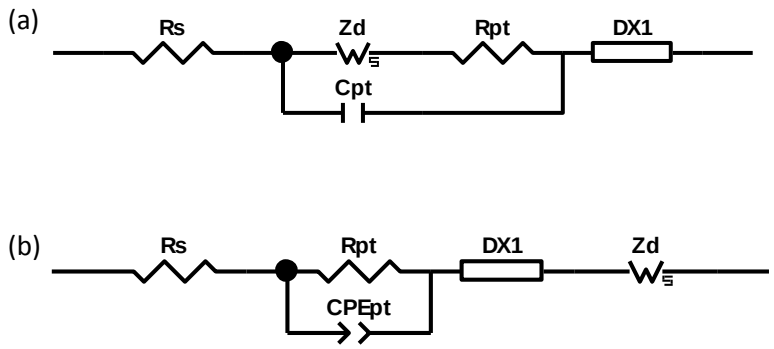

Figure 3.10 Equivalent circuit model used to fit impedance spectra.

where DX1 is the distributed element accounting for the diffusion-recombination transmission line. In model (b) a constant phase element (CPE) is used instead of a

capacitor for the counter electrode. The other parameters were described above. The processes occurring at the TCO/electrolyte interface have been neglected in the fitting. A comparison between fitting to circuit (a) and (b) can be found in the **Appendix 11.1.**

Apart from the parameters directly extracted from the impedance fitting, as for example the charge transfer resistance (R_{ct}), we can obtain some basic electron transport and recombination parameters[6] via the following relations:

- The time constant of the intermediate frequency semicircle can be used to determine the effective electron lifetime defined in **Chapter 2**[15]

$$\tau_n^{EIS} = R_{ct}C_{\mu} = {\omega_{max}}^{-1} \tag{3.11}$$

- The small amplitude diffusion length can be defined from the transport and transfer resistances and taking into account the thickness of the films (d)

$$\frac{L_n}{d} = \sqrt{\frac{\mathrm{R_{ct}}}{\mathrm{R_t}}} \tag{3.12}$$

In this work, the measurements were carried out in three different ways:

- In the dark varying the applied dc voltage
- At open circuit under illumination
- Under illumination (fixed at 1 sun) varying the applied dc voltage

Electrochemical impedance spectroscopy measurements were performed using a 10 mV perturbation in the 10^{-2}-10^{5} Hz range.

3.6.2. Intensity-modulated spectroscopy

Frequency-domain techniques known as intensity modulated spectroscopy comprise intensity modulated photocurrent spectroscopy (IMPS) and intensity modulated photovoltage spectroscopy (IMVS). These techniques involve small amplitude modulation of the photon flux incident on the cell[16]. In the IMVS measurement, the sample is illuminated at open circuit and in the IMPS, at short circuit. Superimposed on a steady-state illumination level, a small sinusoidal modulation of the illumination intensity is applied. The magnitude of the photovoltage or photocurrent response to the

modulation as well as the phase-shift of this response with respect to the modulated illumination is recorded. As already mentioned, the ac modulation must be sufficiently small so that a linear response of the system is obtained.

For both techniques, the simplest analysis of the results involves the determination of a time constant for the photocurrent or photovoltage response. IMVS is typically used to characterize the recombination process in DSCs, and the time constant for this process is the effective electron lifetime described in **Chapter 2**[8]. The IMVS response in the frequency domain is a semicircle in the lower complex plane (**Figure 3.11**). The effective electron lifetime can be obtained from the experimental spectra, taking into account that the minimum of the semicircle is located at an angular frequency that is equal to

$$\omega_{min} = \frac{1}{\tau_n^{IMVS}} \tag{3.13}$$

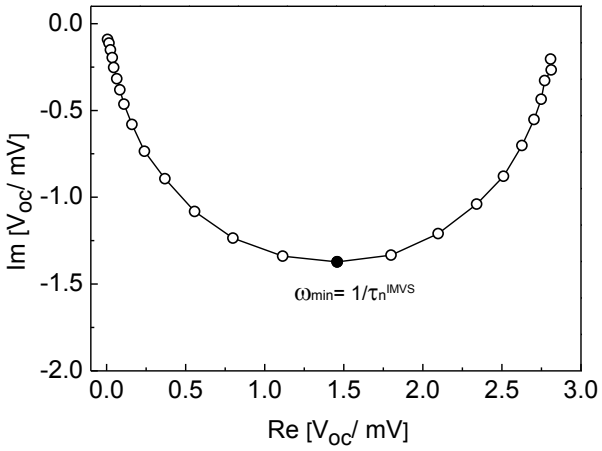

Figure 3.11 IMVS response in the complex plane.

The time constant for the photocurrent response depends on both electron transport and electron recombination[17]. Under short circuit conditions, the electron lifetime is assumed to be much larger than the electron transport time, so the measured photocurrent response is nearly equal to the transport time[3].

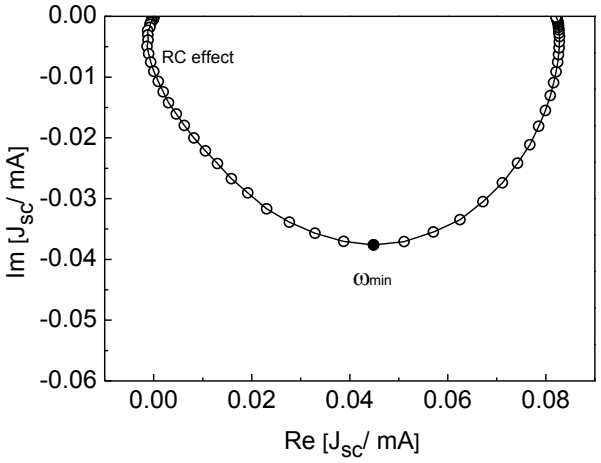

Figure 3.12 IMPS response.

The time constant τ_{IMPS} obtained from the inverse of the minimum angular frequency (ω_{min}) in an IMPS plot (**Figure 3.12**), can be related to the effective diffusion coefficient, D_n by[18,19]

$$\tau_{IMPS} = \frac{d^2}{\gamma D_n} \tag{3.14}$$

where γ is a numerical factor, which depends on layer thickness *(d)*, absorption coefficient (α_{abs}) and illumination direction[20-23].

At low frequencies, the IMPS plots converge to a point on the real axis that corresponds to the steady-state photocurrent. At high frequencies, the modulating frequency is faster than the relaxation of the charge carrier density by transport to the contacts and the modulated photocurrent tends to zero. An additional phase shift is observed at high frequencies, due to the attenuation of the IMPS response by the series resistance and capacitance of the anode[24].

For IMVS and IMPS measurements, the dc level and the modulation of the light intensity were provided by a light emitting diode. The background illumination intensity is set using a dial on the LED driver and the modulation depth and frequency are controlled by a Solartron 1260 Frequency Response Analyser (FRA), which also records the cell response. For IMVS measurements a high impedance buffer amplifier between the sample and the FRA is used and for IMPS a current amplifier. The FRA is controlled using the Zplot program (Zview software package, Scribner Associated) and

the data analysis is carried out using the Zview program. The measurements were carried out with a 530 nm LED over a wide range of dc light intensities. The amplitude of the sinusoidal modulation was 10% of the dc illumination.

3.7. References to Chapter 3

1. Nelson, J. *The Physics of Solar Cells*. (Imperial College Press: 2003).
2. Solar Spectral Irradiance: Air Mass 1.5 http://rredc.nrel.gov/solar/spectra/am1.5/.
3. Hagfeldt, A., Boschloo, G., Sun, L., Kloo, L. & Pettersson, H. Dye-sensitized solar cells. *Chemical Reviews* **110**, 6595-6663 (2010).
4. Ito, S., Matsui, H., Okada, K., Kusano, S., Kitamura, T., Wada, Y. & Yanagida, S. Calibration of solar simulator for evaluation of dye-sensitized solar cells. *Solar Energy Materials and Solar Cells* **82**, 421-429 (2004).
5. Boschloo, G. & Hagfeldt, A. Activation Energy of Electron Transport in Dye-Sensitized TiO_2 Solar Cells. *The Journal of Physical Chemistry B* **109**, 12093-12098 (2005).
6. *Dye-Sensitized Solar Cells*. Edited by K. Kalyanasundaram. (EPFL Press: 2010).
7. Zaban, A., Greenstein, M. & Bisquert, J. Determination of the Electron Lifetime in Nanocrystalline Dye Solar Cells by Open-Circuit Voltage Decay Measurements. *ChemPhysChem* **4**, 859-864 (2003).
8. Bisquert, J. & Vikhrenko, V.S. Interpretation of the Time Constants Measured by Kinetic Techniques in Nanostructured Semiconductor Electrodes and Dye-Sensitized Solar Cells. *The Journal of Physical Chemistry B* **108**, 2313-2322 (2004).
9. Bisquert, J. & Mora-Seró, I. Simulation of Steady-State Characteristics of Dye-Sensitized Solar Cells and the Interpretation of the Diffusion Length. *The Journal of Physical Chemistry Letters* **1**, 450–456 (2010).
10. van de Lagemaat, J. & Frank, A.J. Effect of the Surface-State Distribution on Electron Transport in Dye-Sensitized TiO_2 Solar Cells: Nonlinear Electron-Transport Kinetics. *The Journal of Physical Chemistry B* **104**, 4292-4294 (2000).
11. Fabregat-Santiago, F., Bisquert, J., Garcia-Belmonte, G., Boschloo, G. & Hagfeldt, A. Influence of electrolyte in transport and recombination in dye-sensitized solar cells studied by impedance spectroscopy. *Solar Energy Materials and Solar Cells* **87**, 117-131 (2005).
12. Basics of Electrochemical Impedance Spectroscopy. Application Note. Gamry Instruments. http://www.gamry.com.
13. *Impedance Spectroscopy : Theory, Experiment, and Applications (2nd Edition)*. Edited by Macdonald, J.R. (Wiley: 2005).
14. Bisquert, J. Theory of the Impedance of Electron Diffusion and Recombination in a Thin Layer. *The Journal of Physical Chemistry B* **106**, 325–333 (2002).
15. Bisquert, J., Fabregat-Santiago, F., Mora-Seró, I., García-Belmonte, G. & Giménez, S. Electron Lifetime in Dye-Sensitized Solar Cells: Theory and Interpretation of Measurements. *The Journal of Physical Chemistry C* **113**, 17278–17290 (2009).
16. Peter, L.M. Dynamic aspects of semiconductor photoelectrochemistry. *Chemical Reviews* **90**, 753-769 (1990).
17. Schlichthörl, G., Park, N.G. & Frank, A.J. Evaluation of the Charge-Collection Efficiency of Dye-Sensitized Nanocrystalline TiO_2 Solar Cells. *The Journal of Physical Chemistry B* **103**, 782-791 (1999).
18. Dloczik, L., Ileperuma, O., Lauermann, I., Peter, L.M., Ponomarev, E.A., Redmond, G., Shaw, N.J. & Uhlendorf, I. Dynamic Response of Dye-Sensitized

Nanocrystalline Solar Cells: Characterization by Intensity-Modulated Photocurrent Spectroscopy. *The Journal of Physical Chemistry B* **101**, 10281-10289 (1997).
19. J. Frank, A., Kopidakis, N. & Lagemaat, J.V.D. Electrons in nanostructured TiO_2 solar cells: transport, recombination and photovoltaic properties. *Coordination Chemistry Reviews* **248**, 1165-1179 (2004).
20. Nakade, S., Kanzaki, T., Wada, Y. & Yanagida, S. Stepped Light-Induced Transient Measurements of Photocurrent and Voltage in Dye-Sensitized Solar Cells: Application for Highly Viscous Electrolyte Systems. *Langmuir* **21**, 10803-10807 (2005).
21. Lagemaat, J.V.D. & Frank, A.J. Nonthermalized electron transport in dye-sensitized nanocrystalline TiO_2 films: Transient photocurrent and random-walk modeling studies. *Journal of Physical Chemistry B* **105**, 11194–11205 (2001).
22. Jennings, J.R., Ghicov, A., Peter, L.M., Schmuki, P. & Walker, A.B. Dye-sensitized solar cells based on oriented TiO_2 nanotube arrays: Transport, trapping, and transfer of electrons. *Journal of the American Chemical Society* **130**, 13364–13372 (2008).
23. Barnes, P.R.F., Anderson, A.Y., Koops, S.E., Durrant, J.R. & O'Regan, B.C. Electron Injection Efficiency and Diffusion Length in Dye-Sensitised Solar Cells Derived from Incident Photon Conversion Efficiency Measurements. *The Journal of Physical Chemistry C* **113**, 1126-1136 (2009).
24. Peter, L.M. & Vanmaekelbergh, D. *Time and Frequency Resolved Studies of Photoelectrochemical Kinetics*. (Wiley-VCH Verlag GmbH: 2008).

Chapter 4

Fabrication of Dye-Sensitized Solar Cells

4. Fabrication of dye-sensitized solar cells

In this Chapter, the materials and the fabrication method employed for the fabrication of ZnO dye-sensitized solar cells are described. Deviation from the standard procedure described here will be detailed in the corresponding Results Chapter.

4.1. Substrates

Fluorine-doped tin oxide (SnO_2:F) conducting glass has been used as substrate. The choice of FTO glass substrates is a compromise between optical transmittance and sheet resistance: the higher the conductance the lower the transmittance and vice versa. For this reason, TEC15 substrate (Pilkington, resistance 15 Ω/square, 82-84.5% visible transmittance) has been used for semiconductor film deposition and TEC8 substrate (Pilkington, resistance 8 Ω/square, 80-81.5% visible transmittance) for the counter electrode. By this way, light absorption by dye molecules and fast charge transfer at the counter electrode are favoured.

The substrate cleaning is believed to be a key process that influences the final performance of the devices. A significant effect on the photovoltage behaviour can be observed experimentally depending on the extent of cleaning[1]. For this reason, FTO substrates have been thoroughly cleaned before film deposition. The glass cleaning protocol was the following:

- Sonication in 5% Deconex solution for 15 minutes and subsequent rinsing in MilliQ water. This process is repeated two times
- Sonication in MilliQ water for 15 minutes and subsequent rinsing with Milli Q water
- Sonication in isopropanol for 15 minutes
- Sonication in ethanol for 15 minutes

4.2. Deposition of ZnO films

Colloidal suspensions of 30 wt% were prepared by mixing commercial ZnO nanopowders with water and ethanol (30:70) and stirred for 12 hours. Along this thesis, two different suspensions were used: one based on pure Evonik ZnO nanopowder (VP

AdNano®ZnO20) and the other based on a 1:1 mixture of Evonik ZnO with PIKEM ZnO nanopowder. The oxide powder used for the preparation of the respective cells will be specified in the corresponding Results Chapter.

The approximate nanoparticle size is 20 nm for the Evonik sample (**Figure 4.1**) and 50 nm for the PI-KEM sample. The surface area of these powders as determined by nitrogen physisorption at 77 K (Micromeritics, model ASAP2010) after thermal activation at 150 ºC is 20 m^2/g and 12 m^2/g, for Evonik and PIKEM nanopowders, respectively.

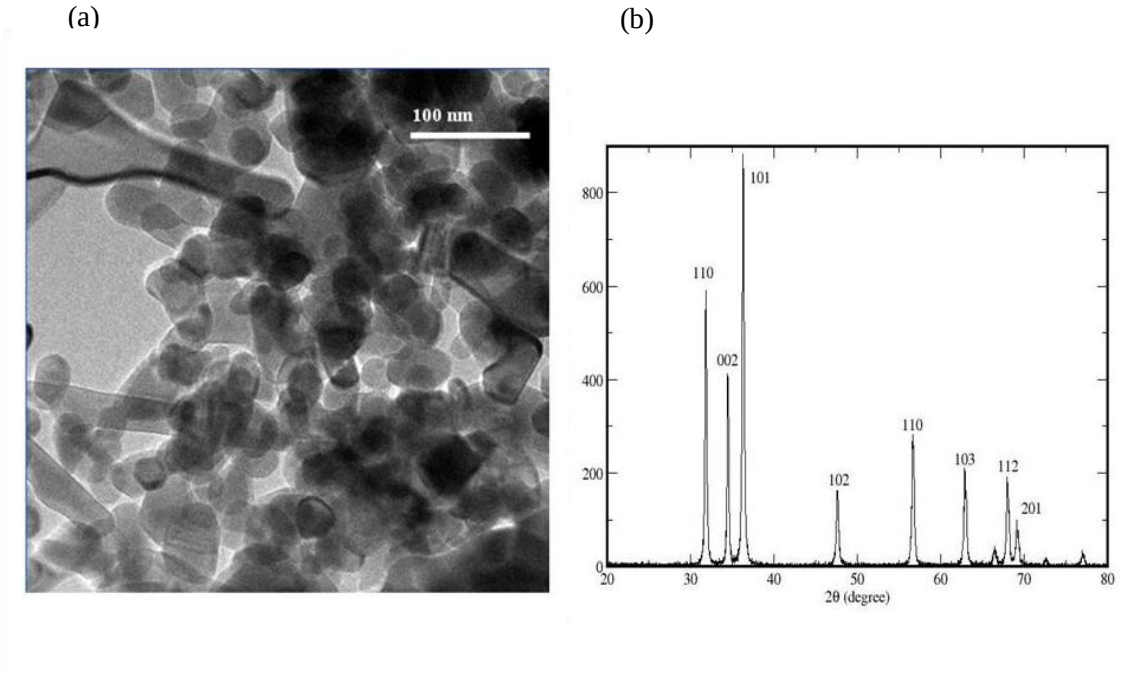

Figure 4.1 TEM micrograph (a) and XRD pattern (b) of the Evonik ZnO nanopowder. The particle size was calculated from the width of the (102) peak using the Scherrer equation. A particle size of ~ 20 nm for Evonik nanopowder is confirmed.

For thin film preparation the suspensions were spread onto the FTO substrate with a glass rod using Scotch tape as spacer (*Doctor Blade* deposition). The resulting films were then heated at 420 ºC for 30 minutes. In **Figure 4.2** SEM images of a film prepared from a colloidal mixture of Evonik and PIKEM nanopowders are shown. The films are composed of a random mixture of large (100 to 200 nm) and small (20–50 nm) particles. Similar size dispersion was found also in films prepared from pure Evonik nanopowder suspensions, but better cell performance was obtained when the nanopowder mixture was used. The active surface areas of the cells were 0.64 or 1 cm^2. The thickness of the films was estimated by SEM analysis and optical profilometry

measurements (**Appendix 11.2**). The thickness of the films ranged between 8 and 10 μm after sintering.

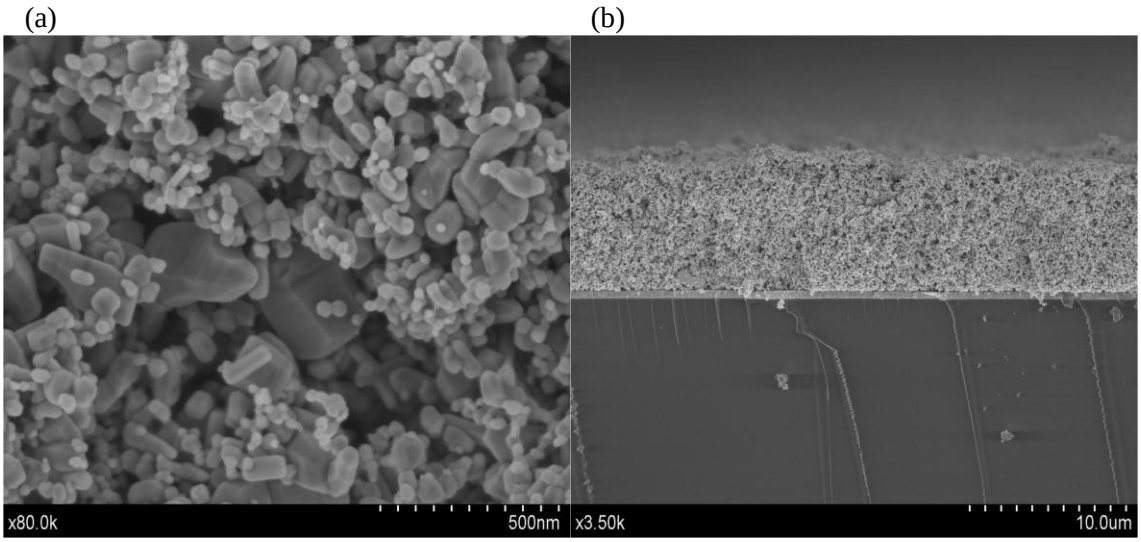

Figure 4.2 SEM images (top view (a) and side view (b)) of a thin film prepared from a mixture of PIKEM and Evonik ZnO nanopowders.

In some of the experiments, a thin continuous ZnO layer was deposited on the FTO substrates before spreading the colloidal ZnO nanoparticle suspension. This compact layer acts as a blocking layer[2] and was deposited from a zinc acetate solution (0.1 M Zn $[C_2H_3O_2]\cdot 2H_2O$, 0.2 M $C_2H_4O_6$ in 25:75 (v/v) water/etanol mixture) by spraying. During deposition the substrate was hold at ~ 350 °C. The spraying process was cycled at 2 seconds with spray and 8 seconds without spray and the number of cycles was 15[3].

Nanowire array samples were prepared by Dr. Ramón Tena and Eneko Azaceta (Department of New Materials, CIDETEC, San Sebastián). The nanowires were electrodeposited by the reduction of dissolved molecular oxygen in zinc chloride solutions[4-6]. The electrolyte was a $5\cdot10^{-4}$ M $ZnCl_2$ (>98.0 %), 2 M KCl (>99.5 %) ultrapure aqueous solution, saturated by bubbling oxygen. Two different nanowire lengths (2.5 and 5 μm) were prepared by varying the charge density (10 and 20 C cm^{-2}). Before sensitization, the nanowire samples were immersed in acetone (15 minutes) and then in isopropanol (15 minutes) and subsequently annealed to 450 ºC for 30 minutes.

4.3. Electrode sensitization

Organic and ruthenium-complex dyes were used for electrode sensitization in the course of this thesis. Before immersion in the dye solution, films were warmed up to

80 ºC to minimize the water vapour content inside the pores of the semiconductor electrode[7]. The sensitization was always performed at room temperature. The concentration and solvent employed for the dye solution depended on the sensitizer. Dipping time did not exceed 2 hours in the majority of the cases, unless a dye sensitization study was performed. After sensitization, the films were rinsed in the same solvent as employed in the dye solution. Dye solutions are systematically kept in the dark trying to avoid evaporation of the solvents. It was observed that a careful control of dye concentration and dipping time is crucial for the performance and reproducibility of the ZnO-based dye-sensitized solar cells.

4.4. Electrolyte solutions

Two types of electrolytes were employed in the course of this thesis: electrolytes based on organic solvents and *solvent free* electrolytes. In the first case, the redox couple is dissolved in an organic solvent as, for example, acetonitrile or methoxypropionitrile. Solvent free electrolytes are based on a room temperature ionic liquid (RTIL), which acts as a highly viscous solvent and at the same time as the source of iodide. In both cases, the redox couple consists of iodine I^- and triiodide I_3^-.

4.5. Platinized counter electrodes

Deposition of platinum films on FTO substrates was performed by two different ways:

- Spreading a drop of hexachloroplatinic acid (0.01 M in isopropanol) over the FTO substrate and subsequent annealing at 380 ºC for 10 minutes
- Spreading 15 µl of *Platisol* (*Solaronix*) over the FTO substrate and subsequent annealing at 400 ºC for 5 min

Platisol is an alcohol-based paint containing a chemical platinum precursor (*Solaronix*). To prepare sealed cells, two holes positioned on opposite corners of the cell are drilled through the FTO substrate before platinum deposition.

4.6. Assembly of dye-sensitized solar sells

Open cells[8] were fabricated by pressing together the electrode and counter electrode using paper binders (**Figure 4.3a**). The electrolyte is introduced in the resulting stack by capillary effect. To prepare sealed cells (**Figure 4.3b**), the two electrodes are sealed

together with a hot-melt polymer film frame around the zinc oxide area. Electrolyte was introduced via the holes drilled through the counter electrode by vacuum filling. The holes were finally sealed using microscope glass slides and a hot-melt polymer. Two different polymers have been used: Surlyn® (60μm) and SX1170-25, Solaronix (25 μm). Silver paint was applied on the exposed areas of FTO substrates on each electrode after cell assembly to extend the contact area of the current collector.

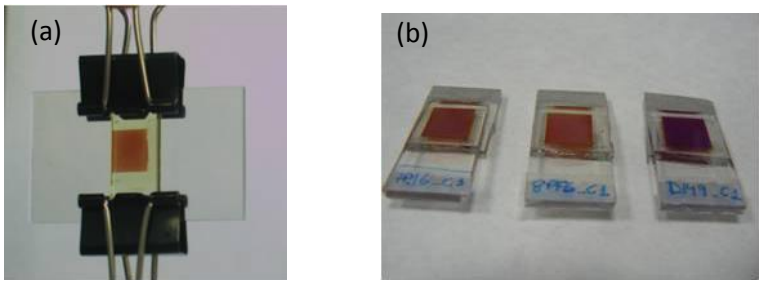

Figure 4.3 Open cell (a) and sealed cells (b).

4.7. References to Chapter 4

1. Cameron, P.J., Peter, L.M. & Hore, S. How Important is the Back Reaction of Electrons via the Substrate in Dye-Sensitized Nanocrystalline Solar Cells? *The Journal of Physical Chemistry B* **109**, 930-936 (2005).
2. Elias, J., Tena-Zaera, R. & Levy-Clement, C. Effect of the chemical nature of the anions on the electrodeposition of ZnO nanowire arrays. *Journal of Physical Chemistry C* **112**, 5736–5741 (2008).
3. Elias, J., Tena-Zaera, R. & Lévy-Clément, C. Electrodeposition of ZnO nanowires with controlled dimensions for photovoltaic applications: Role of buffer layer. *Thin Solid Films* **515**, 8553-8557 (2007).
4. Peulon, S. & Lincot, D. Mechanistic study of cathodic electrodeposition of zinc oxide and zinc hydroxychloride films from oxygenated aqueous zinc chloride solutions. *Journal of The Electrochemical Society* **145**, 864–874 (1998).
5. Tena-Zaera, R., Elías, J., Lévy-Clément, C., Mora-Seró, I., Luo, Y. & Bisquert, J. Electrodeposition and impedance spectroscopy characterization of ZnO nanowire arrays. *Physica Status Solidi a-Applications and Materials Science* **205**, 2345–2350 (2008).
6. Guillén, E., Azaceta, E., Peter, L.M., Arnost, Z., Tena-Zaera, R. & Anta, J.A. ZnO solar cells with an indoline sensitizer: a comparison between nanoparticulate films and electrodeposited nanowire arrays. *Energy & Environmenta Science* (2011). DOI: 10.1039/C0EE00500B
7. Hagfeldt., A., Didriksson, B., Pamqvist, T., Linström, H, Södergren, S., Rensmo, H. & Lindquist, S. Verification of high efficiencies for the Grätzel-cell. A 7% efficient solar cell based on dye-sensitized colloidal TiO_2 films. *Solar Energy Materials and Solar Cells* **31**, 481-488 (1994).
8. Hosono, E., Mitsui, Y. & Zhou, H. Metal-free organic dye sensitized solar cell based on perpendicular zinc oxide nanosheet thick films with high conversion efficiency. *Dalton Transactions* 5439–5441 (2008).

Chapter 5

Zinc Oxide Sensitized with Xanthene Dyes

5. Zinc oxide sensitized with xanthene dyes

In this Chapter a comparative study of the photovoltaic performance of nanostructured ZnO electrodes sensitized with xanthene dyes and the more common ruthenium dye N719 is described.

As mentioned in **Chapter 1**, ruthenium-complex dyes are the most frequently employed sensitizers for DSCs. They have some essential characteristics of a good sensitizer for this kind of devices, such as an adequate anchoring group to the semiconductor, an efficient metal-to-ligand charge transfer (MLCT) and a wide absorption spectrum, which ranges from the visible to the near-IR (especially for the one known as "black dye"). However, ruthenium-based dyes also present some limitations for their use in DSCs. They do not meet the mass production requirements needed for industrial applications. Apart from being based on a precious metal, the fabrication of metal complexes requires careful synthesis and tricky purification steps[1]. This aspect has been very controversial, as the key factors of this new technology are the low cost and high availability of materials and the simple fabrication procedures. Besides, molar extinction coefficients of ruthenium-complex dyes are moderate. This limitation, as will be seen in the following Chapters, can be a key factor for cell configurations different from the standard, as for example cells based on ionic liquid electrolytes or composed of one-dimensional nanostructured electrodes.

When working with ZnO as semiconductor, ruthenium-based dyes have an additional disadvantage: the instability of this semiconductor when sensitized with acidic dyes. The low performance of ZnO cells has been ascribed to poor sensitization with the most common ruthenium-based dyes[2-7]. In a work published in 2000, Keis et al.[7] performed a study of the sensitization procedure of ZnO with ruthenium-complex dyes. They found that the dye solutions lead to a partial dissolution of the oxide and to the formation of dye-ZnO aggregates. Several approaches have been made to overcome these sensitization problems. In a later work Keis et al.[4] obtained 5% of efficiency[i] adding KOH to the acidic dye-loading solutions and shortening the loading time. Other authors[8,9] claimed that an improvement of dye-loading can be achieved by changing the microstructure of the ZnO films thus avoiding complex formation without the need of

[i] The irradiance was 10 $mWcm^{-2}$ and the active surface area of the cell was 0.5 cm^2.

basic dye solutions. Up to now the best performing ZnO-based solar cell has been obtained with the N719 dye[9]. Nevertheless, it is generally accepted that ruthenium-complexes are not appropriate dyes for ZnO.

The development of new types of photosensitizers for their use in ZnO DSCs is a subject that has been widely investigated. In the same year as Keis et al.[7] highlighted the problems of the interaction between ZnO and ruthenium dyes, Hara et al.[10] reported on a highly efficient photon-to-electron conversion of ZnO solar cells sensitized with an organic dye. Organic dyes as alternative to ruthenium-complex sensitizers exhibit many advantages, including low cost and environmental-friendly properties. Besides, they can be prepared rather inexpensively by following established design strategies. In contrast to ruthenium-complexes, different light absorbing groups can be incorporated into the organic framework to tune the absorption over a broad spectral range[1]. Finally, the molar extinction coefficients of organic dyes are usually higher than those of Ru-complexes[11].

It has been reported that ZnO performs particularly well when sensitized with organic dyes. Some organic dyes do not precipitate in the presence of Zn^{2+} ions and can, therefore, be used more easily in combination with ZnO[12]. However, after ten years of research, an appropriate dye for ZnO, which can lead to efficiencies comparable to that of TiO_2, has not been described yet. Looking for an appropriate dye for ZnO has been one of the aims of this thesis and results of the sensitization of the ZnO films used in this work with several dyes can be found in the **Appendix 11.3**. In this Chapter, a study of xanthene derivative organic dyes will be described, making a comparison of their performance with the most frequently used ruthenium dye N719. The objective of this work is to study the suitability of alternative dyes as sensitizers for ZnO, as well as to weigh up the advantages and disadvantages of organic dyes with respect to ruthenium-based dyes. The results presented in this Chapter served as benchmark for the work presented in subsequent Chapters, where a fully organic dye of high efficiency (D149) is used to sensitize ZnO electrodes.

5.1. Xanthene dyes

Xanthene is a yellow, heterocyclic compound **(Figure 5.1)**, which is the fundamental structure of several chromopohores. Derivatives of xanthene are commonly referred to collectively as xanthenes and include fluoresceins, eosins and rhodamines. Xanthenes

are very cheap dyes. They are frequently used as chromophores in biology and laser physics.

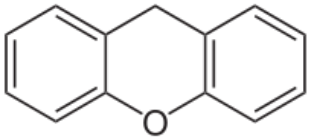

Figure 5.1 Molecular structure of xanthene.

Early work[13-15] in dye sensitization of wide band gap semiconductors was based on this type of dyes. Sensitizers as for example Eosin Y[16-19], Mercurochrome[10,20] or Rose Bengal[21] have been successfully employed. In this work, several xanthenes have been tested as sensitizers for ZnO: Eosin Y (salt and acid form), Eosin Blue, Mercurochrome, Rose Bengal and Rhodamine. The best performances were obtained for Mercurochrome and Eosin Y in the acid form (Eosin Y from now on). Therefore, these two dyes were chosen for the comparative study with the ruthenium dye N719. A comparison between three different Eosins can also be found in the **Appendix 11.3.1**.

There are several reports on the sensitization of ZnO with Eosin Y for application in DSCs. In **Table 5.1** best results for ZnO dye-sensitized solar cells sensitized with this dye are summarized.

Table 5.1 Summary of the performance data of DSCs based on ZnO sensitized with Eosin Y.

ZnO film	Cell area (cm^2)	Ref.	J_{sc} ($mA\ cm^{-2}$)	V_{oc} (V)	FF	Efficiency (%)
Nanoparticles	1	[22]	3.63	0.539	0.57	1.11 %
Nanoparticles	1	[17]	~7	~0.6	-	2.40 %
Nanoparticles	0.25	[23]	3.66	0.65	0.7	1.69 %
Micro-nanotextured ZnO films	0.25	[24]	6.12	0.549	0.59	2.00 %
ZnO/Eosin Y Hybrid films	-	[25]	6.1	0.59	0.63	2.30 %

Eosin Y has also proved to be a suitable dye for electrodeposition of ZnO in the presence of dye[16,23,25,26]. This combined approach represents a new synthetic route for

photoelectrode materials and involves the cathodic electrodeposition of ZnO/dye hybrid films from aqueous mixed solution of Zn salts and dye molecules. Using this method high surface area mesoporous ZnO films with high cristallinity are successfully obtained. The performance of these photoelectrodes in DSC applications was found to improve when Eosin molecules were desorbed after film deposition and the electrodes, afterwards, sensitized again[25,26].

The benchmark study on Mercurochrome as sensitizer for DSCs is the work by Hara et al.[10]. They studied several nanoporous semiconductor oxides and found that Mercurochrome performs especially well with ZnO. An efficiency of 2.5% was obtained for DSCs based on Mercurochrome-sensitized ZnO cells. Despite being a very promising dye there are only a few works on ZnO-sensitization with Mercurochrome[10,27-29].

Figure 5.2 shows the approximate energy levels as well as the chemical structures of the three dyes, which were compared in the present study.

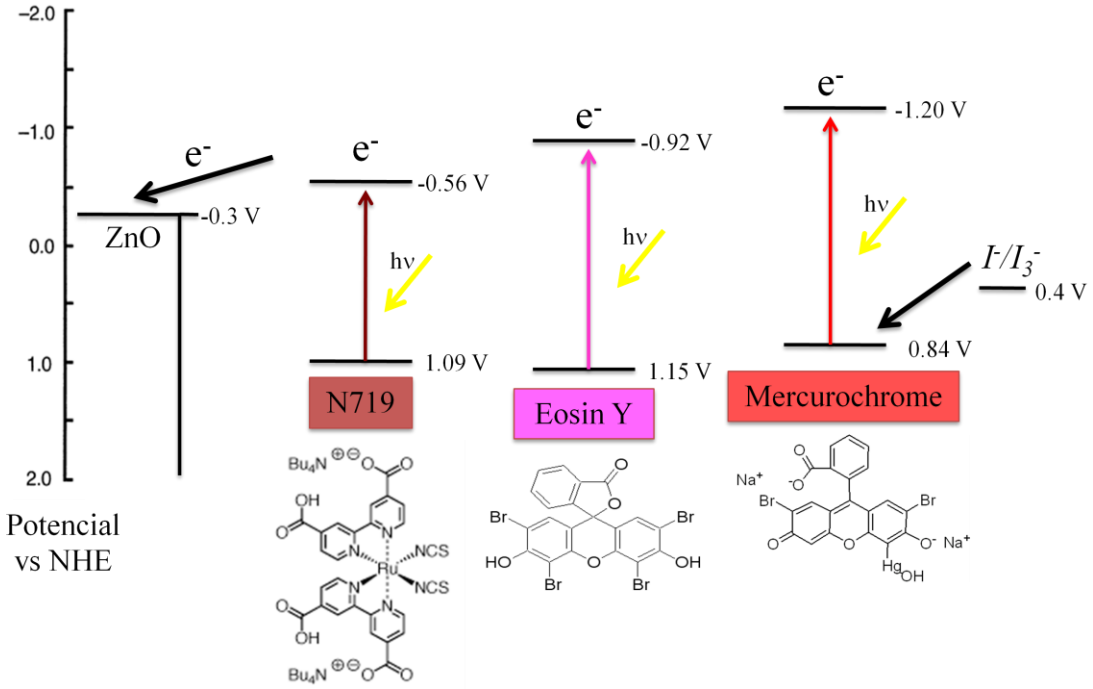

Figure 5.2 Approximate energy diagram and molecular structures of the dyes compared in this work.

Their molecular structures contain adequate anchoring groups to be adsorbed onto the oxide surface, specifically carboxylate groups. Besides, the HOMO and LUMO levels of the dyes are adequate for electron injection to ZnO and for regeneration by the redox

couple. The oxidation potential for mercurochrome is more negative than those for N719 and Eosin Y[10].

5.2. Fabrication and characterization of the devices

The materials used for the fabrication of the cells are summarized in **Table 5.2** and the parameters of the illumination source used for photovoltaic characterization in **Table 5.3**.

Table 5.2 Summary of the materials employed in the fabrication of the cells.

ZnO	Dyes	Electrolyte	Counter Electrode
Evonik VP AdNano®ZnO20 Cell area: 1 cm^2	**Mercurochrome** 0.5 mM dye in ethanol	0.5 M TBAI, 0.05 M I_2, 0.5 M 4-tert-butylpyridine (TBP) in Propylene Carbonate	Hexachloroplatinic acid (0.01 M in isopropanol)
	N719 0.5 mM dye in ethanol		
	Eosin Y 32 mM dye in ethanol	0.5 M TBAI, 0.05 M I_2, 0.5 M TBP in Propylene Carbonate	

Table 5.3 Illumination set-up used for DSC testing.

Illumination source	Filters	Calibration
Xenon 450W arc lamp	Water filter and 325 nm UV blocking filter	Reference solar cell (Oriel, 91150) 100 mW cm^{-2}

The ZnO films were deposited in a rectangular arrangement with an active area of 1 cm^2. The tests were performed in open cells except for the stability tests. In that case, the cells were sealed with Surlyn film (60 μm) heated to 180ºC after sensitization. Short circuit currents, open circuit voltages and current-voltage curves were obtained by applying an input voltage to the cell from zero to open circuit voltage through a Direct Current Accuracy Operational Amplifier. Incident photon-to-current efficiencies (IPCE) were measured by means of a 1/8 m monochromator (Oriel). The light intensity was determined as a function of wavelength using a calibrated silicon photodiode (Thorlabs). Laser Beam Induced Current (LBIC) measurements were carried out by the group of Dr. Joaquín Martín Calleja in the Department of Physical Chemistry of the University of Cadiz. The LBIC system is based on an optomechanical device to obtain a

very small laser spot and minimal geometric distortions in conjunction with a set of mathematical algorithms based on internal properties of the samples to perform automatic focalization[30]. In this work, measurements with micrometric resolution were carried out using this versatile computer controlled high-resolution LBIC system. Two different wavelengths were used: 532 nm and 632.8 nm. The LBIC experiments were performed on sealed cells and the scanned area was 300 × 300 μm. The laser was focused on a surface area of $2 \cdot 10^{-12}$ m^2.

5.3. Dye sensitization of the semiconductor films

Dye concentration and immersion time in the dye solution greatly influence the dye adsorption and the resultant overall light conversion efficiency of ZnO films[3,31]. Moreover, the sensitization depends to a great extent on the characteristics of the photoelectrodes. Therefore, when working with ZnO a careful control of the dye adsorption conditions is crucial. For this reason, first of all, an optimization of the dye loading has been carried out for the ZnO-based DSCs. In **Figure 5.3**, the photocurrent response versus the immersion time in dye solution is plotted for Mercurochrome, N719 and Eosin Y in acid form and Eosin B.

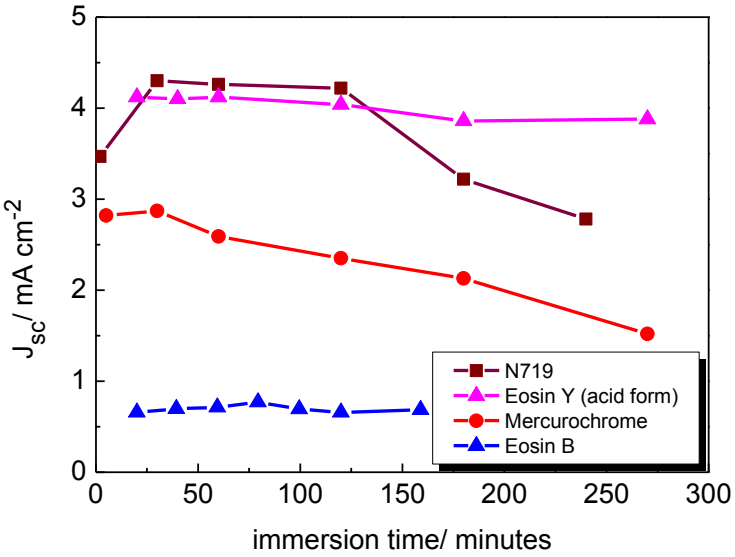

Figure 5.3 Short-circuit photocurrent as a function of sensitization time for the dyes studied in this work. Irradiance: 100 mW cm^{-2}.

During the process of sensitization with N719 dye, the photocurrent increases at short immersion times, reaches a plateau and after a critical time, it decreases. Mercurochrome dye is rapidly adsorbed and upon longer immersion a systematic decay

of the current is observed. On the contrary, Eosin Y produces currents that do not depend much on immersion time. Results for Eosin B are also plotted to show that this behaviour is shared for other Eosin dyes. Based on these results, the immersion time was set to 1 hour for the N719 dye, 80 minutes for the Eosin dyes and 40 minutes for Mercurochrome.

The immersion time also affects the shape of the IV curve (see **Figure 5.4**). It is observed that the fill factor in the N719 cells decreases with sensitization time whereas it remains unaffected when the organic dyes are used. In the case of Mercurochrome-sensitized cells, longer immersion times reduce only the short circuit current but the fill factor and open circuit voltage are not altered. When using Eosin Y the current-voltage curve is virtually independent of the immersion time used to sensitize the films. The same behaviour was found for all forms of Eosin.

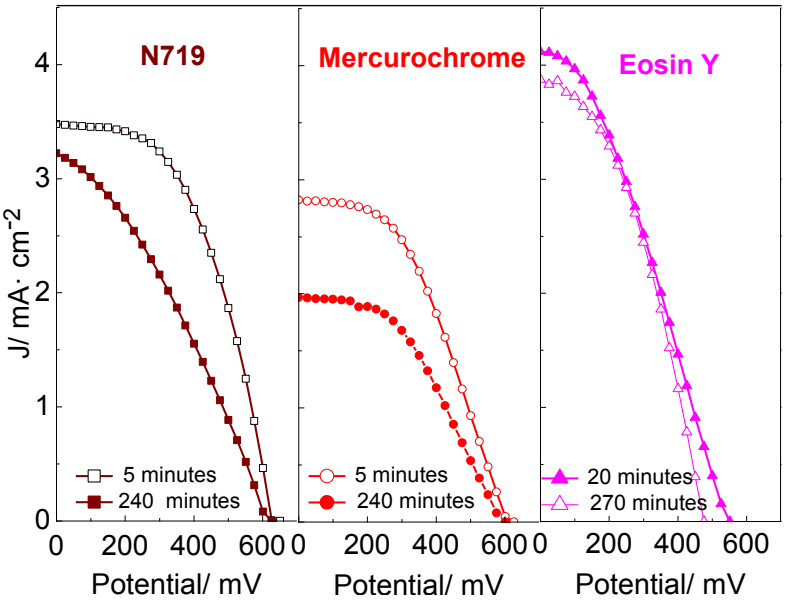

Figure 5.4 Current-voltage characteristics of ZnO DSCs prepared with different dyes for two immersion times in the dye solution.

Keis et al.[3,4,7] studied in detail the sensitization process of ZnO with the more common ruthenium dyes N719 and N3. They found that the IPCE values decreased when electrodes were left in the dye-bath for long times. Protons derived from the ruthenium-complexes make the dye solution relatively acidic (**Figure 5.5** (1)). The pH for the dye-sensitization process (pH~5) is much lower than the point of zero charge of ZnO (~9). It has been demonstrated that titration with acid leads to the dissolution of the ZnO colloid already below pH 7.4[32]. The low local pH at the surface of ZnO during dye sensitization

provokes the dissolution of Zn^{2+} ions from the ZnO surface (**Figure 5.5** (2)). These Zn^{2+} ions form complexes with the dye (**Figure 5.5** (3)), which accumulate in the pores of the semiconductor film. It is assumed that only dye molecules directly attached to the ZnO surface can inject efficiently electrons and contribute to the photocurrent[33]. Therefore, Zn^{2+}/dye complexes, in spite of absorbing light, do not inject electrons.

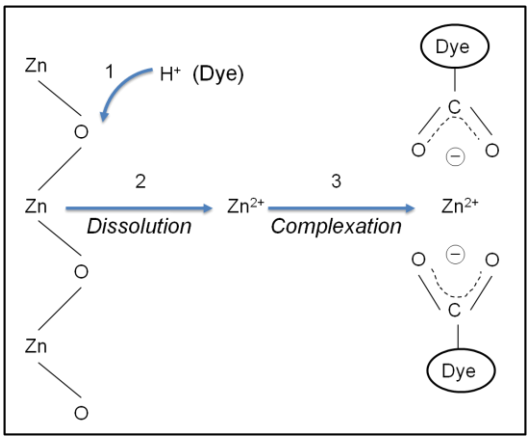

Figure 5.5 A schematic drawing of the problems associated with the dye-sensitization process of ZnO with dyes containing protonated anchoring groups.

The different point of zero charge of TiO_2 (similar to the pH of the dye solution) and its higher chemical stability explain the different behaviour found for this oxide with ruthenium dyes[31].

The plateau in the photocurrent observed for N719 at intermediate sensitization times can be due to the competition between complete coverage and aggregation. The dye must diffuse through the semiconductor film to achieve full sensitization by forming a complete monolayer. This is a common feature of all dyes. However, in the case of N719, whereas some parts of the film are on the way to increase efficiency (dye monolayer adsorption), other parts can be in the phase of decreasing efficiency (formation of complexes)[3,11]. The lower fill factor found for long sensitization times can be a consequence of both the deterioration of the semiconducting film and the presence of aggregates in the pores.

Wu et al.[20] found that Mercurochrome could provide ZnO DSCs with a fill factor significantly larger than that obtained with the ruthenium N3 dye. In contrast to N719, when Mercurochrome is used as the dye, the fill factor is insensitive to immersion time (**Figure 5.4**). The pH of the ethanolic solution of Mercurochrome is 7.65, consequently the degradation of ZnO in the course of sensitization is expected to be lower than in the

case of N719. However, the decrease of the photocurrent at prolonged immersion times suggests that deterioration of ZnO takes place to some extent also during sensitization with Mercurochrome. The formation of aggregates in ZnO films sensitized with Mercurochrome was reported by Hara et al[10].

The pH of the Eosin Y solution is ~ 6. Neither the photocurrent (**Figure 5.3**), nor the fill factor (**Figure 5.4**) is found to change significantly with immersion time.

It must be kept in mind that both Eosin and Mercurochrome dyes have a carboxylic group in their molecular structures. Although a direct relation between acidity and number of carboxylic groups cannot be established, the fact that the xanthene dyes have only one carboxylic group (**Figure 5.2**) may explain their lower reactivity with ZnO. Nguyen et al.[34] designed a ruthenium-complex with only one carboxylated bipyridyl ligand and found much reduced dye precipitation onto the ZnO electrode compared to the ruthenium-complex dye N3 (with two carboxylic groups in its molecular structure). They obtained a solar cell efficiency of 4.0% and no aggregation was observed after 24 hours of immersion in the dye solution. Therefore, it may be expected that the carboxylic acid group will cause some dissolution of ZnO in the dye bath containing Eosin Y and Mercurochrome, but it seems that the deposition of ineffective dye/oxide aggregates on the ZnO electrode is not as critical as for N719.

5.4. UV-vis absorption and IPCE spectra

In **Figure 5.6** the absorption spectra of the three dyes in ethanol are shown. Organic dyes exhibit rather sharp absorption peaks compared to the ruthenium dye. They absorb mainly in the range between 450-550 nm, with the maximum absorption peak at ~ 517 nm for Mercurochrome and at ~ 530 nm for Eosin Y, matching up with the maximum of the solar spectrum. N719 shows a much broader absorption with a maximum lying between the one of Mercurochrome and of Eosin. In both xanthene dyes a shoulder at wavelengths below the absorption maximum is observed. This shoulder is commonly seen in xanthene dyes and is attributed to the absorption of a dimer[10,15,35].

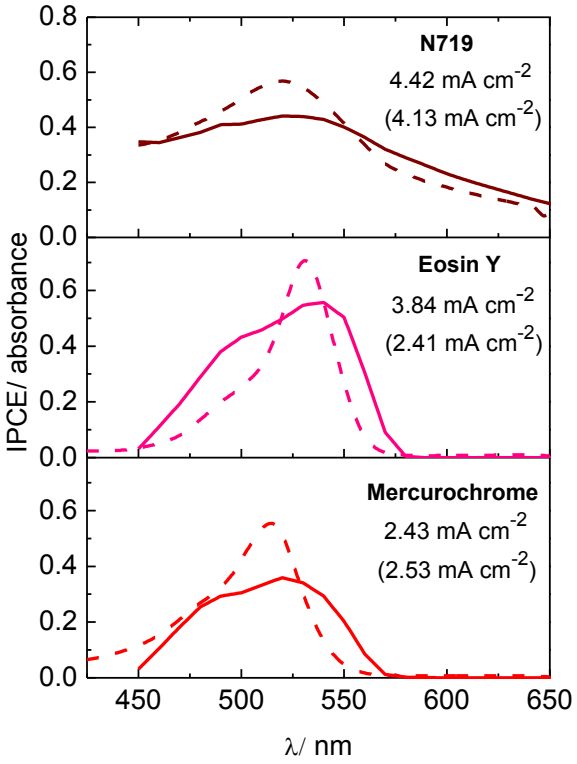

Figure 5.6. IPCE (solid lines) and absorbance spectra (dashed lines) in ethanolic solution for Mercurochrome, Eosin Y and N719. The values of the photocurrent is obtained from the convolution of the IPCE curve integrated between 450 and 700 nm, with the AM 1.5 photon flux at 100 mW cm^{-2}. In parenthesis, the result of cell illumination with white light (using a 400 nm blocking filter) is indicated.

The incident photon-to-current efficiency (IPCE) spectra of ZnO electrodes sensitized with the three dyes are also represented as a function of wavelength in **Figure 5.6**. The IPCE spectra of the organic dyes adsorbed on the ZnO electrodes are broader than the absorption curves of the dyes in solution. For Mercurochrome and Eosin Y, the absorption intensity of the shoulder at lower wavelengths increases compared to that in ethanol, indicating that dimers of dye molecules are formed on the ZnO surface[10]. Aggregation of dye molecules can lead to a broadening and an enhancement of absorption at shorter wavelengths when compared to the monomers[35]. Sayama et al.[36] found for TiO_2 cells sensitized with Eosin Y that both, dimers and monomers, are adsorbed on the surface. They also claimed that dimers were more efficient than monomers for photocurrent generation.

For both organic dyes the onset of the IPCE spectrum is red-shifted as compared to the absorption onset of the dyes in solution. As a consequence, most of the visible range is covered. Hara et al.[10] attributed the broadening of the IPCE spectrum of Mercurochrome to the interaction of ZnO with the dye molecules, which results in the appearance of additional energy levels in the electronic spectrum of the dye. This "doubling" of the original HOMO and LUMO levels allows for a broadening of the

optical absorption spectrum and the IPCE spectrum of the adsorbed dye as compared to the absorption spectrum of the isolated dye. Additionally, as will be described in **Chapter 8**, internal scattering might also contribute to the broadening of the spectrum of the adsorbed dye and the IPCE. Theoretical calculations by Labat et al.[37] also pointed to a significant modification of the absorption properties of the Eosin Y dye by the interaction with the semiconductor surface. It is worth mentioning that the shape of the absorption and IPCE spectra for N719 are very similar, which indicates that the transition energy for electron transfer from the Ru-center to the bpy-ligands is relatively insensitive to the establishment of a linkage between the carboxyl group and the ZnO surface.

A mismatch between the spectrum of the illumination source (Xenon lamp + water filter + UV filter) used for cell characterization and AM 1.5 light has to be taken into account. For this reason, the IPCE spectra were convoluted with the AM 1.5 standard photon flux normalized to 100 mW cm^{-2} and then integrated between 450 and 700 nm to test the accuracy of the illumination set-up. The result for the photocurrent is then compared with the value obtained under white light illumination with a 400 nm blocking filter (**Figure 5.6**). In general, the calculated value is higher than the one observed experimentally, although the results are within the statistical uncertainty found in the fabrication of the cells. Note also that the photoconversion in the interval 400-450 nm is not considered and this introduces some error that can be important for N719. In any case, these results are in agreement with the observation that the cells perform better under real solar illumination, resulting in short circuit current densities around 10-25% higher than obtained with the combination of Xe lamp and filters used here for cell characterization.

5.5. Photovoltaic performance

A number of cells using the different dyes were fabricated and characterized. In **Table 5.4** the photovoltaic parameters for the best performing cells are summarized for each dye.

Table 5.4 Best results for overall efficiencies of 1 cm^2 ZnO-based DSCs.

ZnO film	J_{sc} (mA cm^{-2})	V_{oc} (V)	FF	Efficiency (%)
N719	6.0	0.701	0.42	1.8
Eosin Y	4.5	0.551	0.47	1.2
Mercurochrome	3.1	0.626	0.56	1.1

Reproducibility was not optimal, both for photocurrent and photovoltage. However, it must be noted that working with a relatively large cell area (1 cm^2) makes achieving good reproducibility more cumbersome. As shown below in the LBIC experiments (described in **Section 5.7**), there is at least 10-15% variability in the local photocurrent at different points of the film. This variability becomes important when working with large cells. On the other hand, the critical sensitization process makes the reproducibility difficult. Little changes of the dye concentration or the residence time of the nanostructured film in the dye solution have large effects on the photoelectrochemical output of sensitized ZnO[31,38]. These effects are not so dramatic for sensitized TiO_2 films[31]. Furthermore, it turned out to be critical to use freshly prepared dye solutions in order to obtain a better reproducibility of the performance of ZnO dye solar cells.

It is generally observed that N719 dye produces the best-performing cells. Mercurochrome cells give photovoltage values close to those of the Ru-based dye cells, but lower photocurrents. Cells prepared with Eosin Y provide competitive photocurrents although photovoltages are generally lower. This is most probably due to the absence of tert-butylpyridine (TBP) in the electrolyte in those cells, as it was found that the presence of TBP results in the desorption of Eosin from the ZnO surface. This compound, as will be shown in the following Chapters, improves the photovoltage of the cells. Fill factors are in the range 0.4-0.6 for most cells and the efficiencies range between 0.4 and 1.2% for the organic dyes and 1.0-1.8% for N719 cells.

In a recent report[23] the performance of ZnO electrodes sensitized with different organic dyes was compared with the performance of ZnO electrodes sensitized with N719. The authors reached similar conclusions to the ones found in this study.

Concretely, the efficiency for Eosin Y-sensitized ZnO solar cells was found to be about 40% lower than for N719-based cells.

5.6. Light intensity dependence of the photovoltage and the photocurrent

In **Figure 5.7** the short circuit currents and the open circuit voltages are shown as a function of light intensity (I_0) for sealed cells with the N-719, Eosin Y and Mercurochrome dyes.

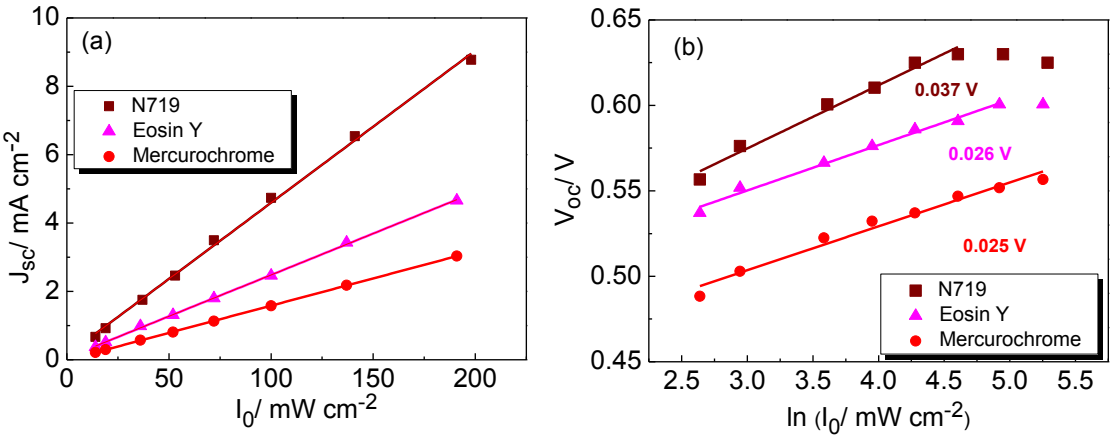

Figure 5.7 (a) Light intensity dependence of the short circuit photocurrent and (b) open circuit photovoltage for N719, Mercurochrome and Eosin Y. In the case of the open circuit voltage, the slopes of the respective linear fits are indicated as well.

The short circuit photocurrent is linearly proportional to light intensity up to 200 mW cm^{-2} for the three dyes. On the other hand, the open circuit photovoltage increases approximately linearly with the logarithm of the light intensity for all the samples. ZnO films sensitized with organic sensitizers exhibit nearly ideal diode behaviour with an approximate slope of 26 mV (**Equation 2.20,** $V_{oc} \propto kT/q\ lnI_0$). Hara et al.[10] also found an ideal behaviour in the open circuit voltage versus light intensity plots (slope ~ 25 mV) of Mercurochrome-sensitized ZnO cells. As described in the following Chapters, ideal behaviour is not a common characteristic of ZnO dye solar cells. Non-ideal slopes as those found for N719 (slope ~ 37 mV), are usually found in the V_{oc} versus ln(I_0) plots. However, the recombination mechanism in the case of Mercurochrome and Eosin Y might be substantially different, with a possible important contribution of electron recombination with the oxidized dye molecules.

5.7. Local energy conversion performance

The spatial dependence of the cell efficiency was evaluated by means of the Laser Beam Induced Current (LBIC) technique[30] in combination with transmittance measurements. The LBIC mapping technique permits to study simultaneously the local performance of the cells, the dye degradation and the efficacy of the oxide sensitization. Results for photoconversion data obtained from LBIC measurements are presented in **Table 5.5**.

Table 5.5 Photoconversion data as extracted from LBIC experiments.

Wavelength (nm)	Dye	Max IPCE (%)	Min IPCE (%)	Mean IPCE (%)	St. dev. (%)
532.0 (4.15μW)	**N719**	24.4	13.1	19.2	1.24
	Eosin Y	29.1	15.5	20.3	1.20
	Mercurochrome	19.7	9.8	15.1	0.90
632.8 (5.1 μW for N719, 515 μW for organic dyes)	**N719**	4.30	2.87	3.30	0.111
	Eosin Y	0.033	0.024	0.027	0.001
	Mercurochrome	0.159	0.067	0.102	0.014

The intensity of the 532 nm laser was fixed at 4.15 μW whereas the 632.8 nm laser was set to 5.10 μW for N719 cells and 515.0 μW for Mercurochrome and Eosin Y cells. Higher light intensity was needed to obtain similar currents due to the lower absorption of these organic dyes in the red as compared to that of N719. As expected from their absorption spectra, the IPCE for organic dyes is negligible compared to N719 dye cells at 635 nm. However, the quantum efficiency of the organic dyes is impressive at 532 nm, especially for Eosin Y. These results clearly show that the main reason for the decrease of the overall efficiency for DSCs with the organic dyes as compared to the standard N719 is the poor absorption at wavelengths beyond 600 nm.

Transmittance measurements were performed simultaneously to the LBIC experiment (**Table 5.6**). Transmittance values for a non-sensitized ZnO cell are also shown for comparison.

Table 5.6 Transmittance (T) corresponding to the LBIC scans reported on **Table 5.5**.

Wavelength (nm)	Dye	Max T (%)	Min T (%)	Mean T (%)	St. deviation (%)
532.0 (4.15μW)	**N719**	6.4	0.2	1.9	0.8
	Eosin Y	3.7	0.2	1.5	0.5
	Mercurochrome	3.3	0.2	0.9	0.4
	No Dye	22.9	1.4	7.9	3.1
632.8 (5.1 μW for N719 515 μW for organic dyes)	**N719**	47.4	1.7	16.6	7.2
	Eosin Y	59.3	2.5	17.3	6.9
	Mercurochrome	56.2	3.4	16.5	7.4
	No Dye	50.2	2.6	20.8	7.8

The lower light harvesting of organic dyes with respect to N719 is confirmed by the high value of the transmittance for Eosin Y and Mercurochrome cells at 633 nm. The transmittance at 532 nm is lower for organic dyes, indicating good light harvesting properties of these dyes at the maximum of the solar spectrum. Neither light absorption, nor photoconversion is homogeneous throughout the film.

In **Figure 5.8** the photoconversion and transmittance maps obtained for the different cells are shown. In this figure, the surface distribution of the local photoconversion performance can be easily distinguished.

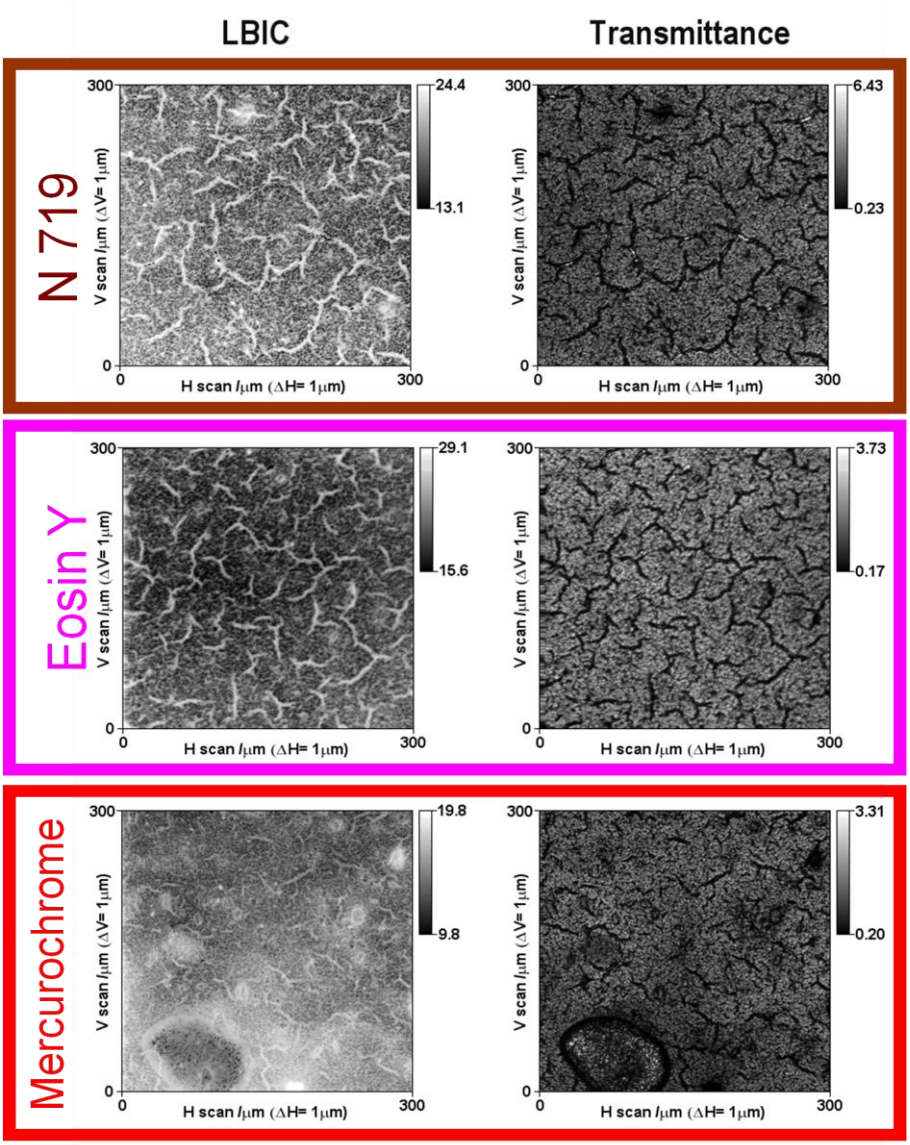

Figure 5.8 LBIC and transmittance maps for sealed cells, using the 532 nm laser line. Photoconversion efficiencies (%) and transmittance (%) are coded using a scale of grey, the white being the maximum value in the selected interval.

Regions of larger photoconversion efficiency (bright regions in left graph) correlate well with regions where a stronger light harvesting is detected (dark regions in right graph) and vice versa. This is another indication that the light harvesting efficiency is the main factor that controls the performance of the cells.

In **Figure 5.9** IPCE values are plotted versus transmittance along a straight line in the LBIC scan. An overall linear dependence is found for the three dyes. Similar results are obtained if the scan is performed along different lines or directions or using a different excitation wavelength.

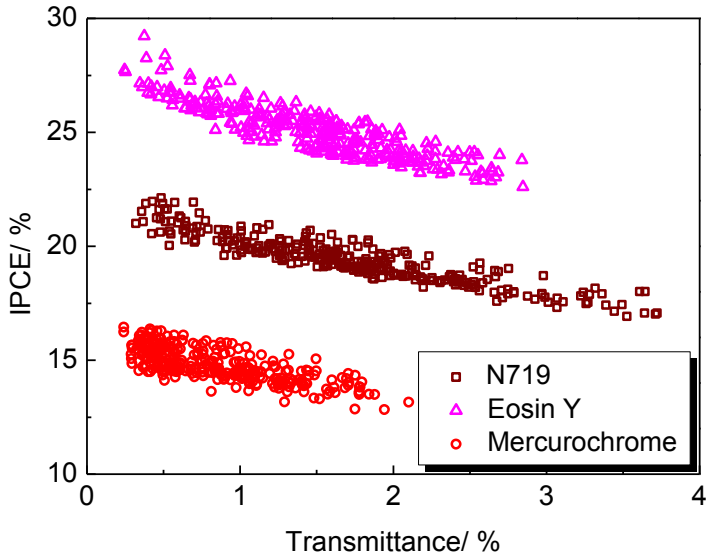

Figure 5.9 Quantum efficiency versus transmittance along a single line in a LBIC-transmittance scan with the 532 nm laser. Eosin data are shifted upward by a 5% for clearer presentation.

As described in **Chapter 2,** the incident photon-to-current efficiency (IPCE) can be defined as the product of the light harvesting efficiency $\eta_{lh}(\lambda)$, the injection efficiency $\eta_{inj}(\lambda)$ and the electron collection efficiency $\eta_{col}(\lambda)$ (**Section 2.3**). The results in **Figure 5.9** can be interpreted using the following expression for the light harvesting efficiency:

$$\eta_{lh}(\lambda) = (1 - T(\lambda) - R) \tag{5.1}$$

where T is the transmittance and R the reflectance. When the other factors are constant ($\eta_{inj}(\lambda)$ and $\eta_{col}(\lambda)$), a plot of the IPCE versus the transmittance should give a straight line with a negative slope. This is what is actually found for the LBIC-transmittance data obtained in this study. Furthermore, the slope is observed to be roughly the same for the three dyes, indicating that the injection quantum yield (provided that collection efficiency is constant) is very similar for the organic dyes and the N719 dye. Note that the reflectance term will introduce a constant shift of the IPCE-transmittance data if it is assumed that there are no significant differences in the reflectance properties of the film from one point to another. These results confirm that the lower light absorption of the organic dyes due to the narrower absorption spectrum is the reason for the lower efficiencies obtained with respect to the N719 dye.

5.8. Stability tests

Organic dyes are considered to be less stable than metal complexes. It is, therefore, fundamental to check the viability of this type of dyes by performing stability tests. The

cells have been illuminated at an intensity of 200 mW cm^{-2} for several hours and the photocurrent densities have been monitored along time. It must be borne in mind that an intensity of 200 mW cm^{-2} corresponds to twice the standard solar light intensity. The reason for using this illumination condition was that at higher intensity, the turn-over rate of the dye is higher and possible degradation mechanisms can be accelerated. The results are shown in **Figure 5.10**.

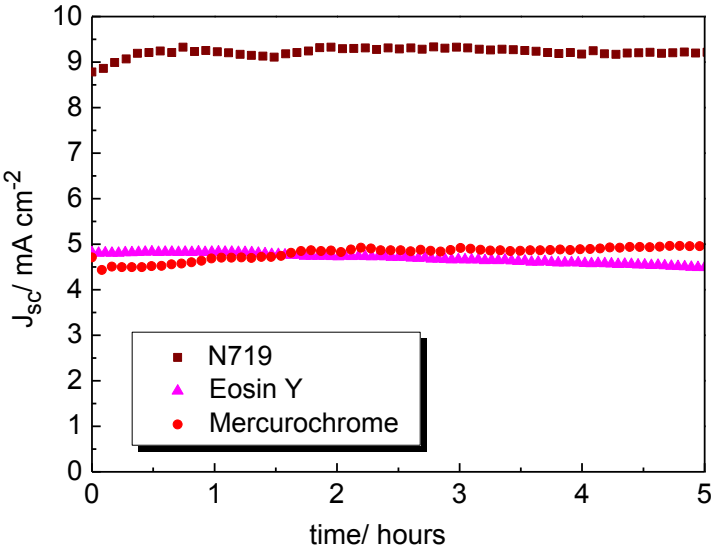

Figure 5.10 Photocurrent at short circuit for sealed cells with different dyes. The illumination intensity was set to 200 mW cm^{-2}.

The stability tests were carried out with sealed cells. No apparent degradation of the organic dyes is observed as a result of the thermal treatment (180°C). The test revealed that the three dyes studied (N719, Mercurochrome and Eosin Y) produce short circuit photocurrents that are virtually constant. This has been verified for at least 5-8 hours and no visible decay is observed over this time span. It should be noted that the continuous illumination test implies that the cell is heated to approximately 80^{o}C. In spite of this, the cells remain stable and provide a constant current under continuous illumination.

5.9. Conclusions

In this Chapter the performance of ZnO DSCs sensitized with xanthene dyes and with the N719 reference dye has been compared. It was found that organic dyes such as Mercurochrome and Eosin Y can be used to successfully fabricate DSCs based on the semiconductor ZnO. It was observed that the sensitization process is crucial for

optimizing the efficiency of DSCs based on N719 and Mercurochrome, but not for Eosin Y cells. In addition, the fill factors of N719 cells deteriorate with sensitization time. On the contrary, the organic sensitizers appear more robust in this aspect, indicating a favourable interaction between the dye and the ZnO semiconductor film. Local photocurrent and transmittance measurements at two different wavelengths confirm the good performance of xanthene dyes in their absorption maxima. It was found that the main factor that limits the efficiencies of the organic dyes with respect to the N719 reference dye is their relatively narrow absorption spectrum. Sealed cells with xanthene dyes show good stability even at high illumination intensities.

In the light of these results, the efficiency of cells with organic dyes might be optimized by tailoring the dye absorption in the red. The sensitization of ZnO with organic dyes seems very promising even if the ideal dye is not available yet.

5.10. References to Chapter 5

1. Mishra, A., Fischer, M. & Bäuerle, P. Metal-free organic dyes for dye-sensitized solar cells: from structure:property relationships to design rules. *Angewandte Chemie International Edition* **48**, 2474-2499 (2009).
2. Quintana, M., Edvinsson, T., Hagfeldt, A. & Boschloo, G. Comparison of dye-sensitized ZnO and TiO_2 solar cells: studies of charge transport and carrier lifetime. *The Journal of Physical Chemistry C* **111**, 1035-1041 (2007).
3. Keis, K., Bauer, C., Boschloo,G., Westermark, K. & Siegbahn, H. Nanostructured ZnO electrodes for dye-sensitized solar cell applications. *Journal of Photochemistry and Photobiology A: Chemistry* **148**, 57-64 (2002).
4. Keis, K., Magnusson, E., Lindstrom, H., Lindquist, S.E. & Hagfeldt, A. A 5% efficient photo electrochemical solar cell based on nanostructured ZnO electrodes. *Solar Energy Materials and Solar Cells* **73**, 51–58 (2002).
5. Zeng, L.Y., Dai, S.Y., Xu, W.W. & Wang, K.J. Dye-sensitized solar cells based on ZnO films. *Plasma Science & Technology* **8**, 172–175 (2006).
6. Guillén, E., Idigoras, J. & Anta, J.A. Solvent-Free ZnO dye-sensitised solar cells. *ECS Transactions* **25**, 111-122 (2010).
7. Keis, K., Lindgren, J., Lindquist, S.E. & Hagfeldt, A. Studies of the adsorption process of Ru complexes in nanoporous ZnO electrodes. *Langmuir* **16**, 4688–4694 (2000).
8. Kakiuchi, K., Hosono, E. & Fujihara, S. Enhanced photoelectrochemical performance of ZnO electrodes sensitized with N-719. *Journal of Photochemistry and Photobiology A: Chemistry* **179**, 81-86 (2006).
9. Saito, M. & Fujihara, S. Large photocurrent generation in dye-sensitized ZnO solar cells. *Energy & Environmental Science* **1**, 280-283 (2008).
10. Hara, K., Horiguchi, T., Kinoshita, T. & Sugihara, H. Highly efficient photon-to-electron conversion with mercurochrome-sensitized nanoporous oxide semiconductor solar cells. *Solar Energy Materials and Solar Cells* **64**, 115–134 (2000).

11. Hagfeldt, A., Boschloo, G., Sun, L., Kloo, L. & Pettersson, H. Dye-sensitized solar cells. *Chemical Reviews* **110**, 6595-6663 (2010).
12. Quintana, M., Marinado, T., Nonomura, K., Boschloo, G. & Hagfeldt, A. Organic chromophore-sensitized ZnO solar cells: Electrolyte-dependent dye desorption and band-edge shifts. *Journal of Photochemistry and Photobiology A: Chemistry* **202**, 159-163 (2009).
13. Gerischer, H., Michel-Beyerle, M., Rebentrost, F. & Tributsch, H. Sensitization of charge injection into semiconductors with large band gap. *Electrochimica Acta* **13**, 1509-1515 (1968).
14. Tsubomura, H., Matsumura, M., Nomunara, Y. & Amamiya, T. Dye sensitised zinc oxide: aqueous electrolyte: platinum photocell. *Nature* **261**, 402-403 (1976).
15. Moser, J. & Grätzel, M. Photosensitized electron injection in colloidal semiconductors. *Journal of the American Chemical Society* **106**, 6557-6564 (1984).
16. Yoshida, T., Terada, K., Schlettwein, D. & Sugiura, T. Electrochemical self-assembly of nanoporous ZnO/eosin Y thin films and their sensitized photoelectrochemical performance. *Advanced Materials* **12**, 1214–1217 (2000).
17. Lee, W.J., Okada, H., Wakahara, A. & Yoshida, A. Structural and photoelectrochemical characteristics of nanocrystalline ZnO electrode with Eosin-Y. *Ceramics International* **32**, 495–498 (2006).
18. Suri, P., Panwar, M. & Mehra, R.M. Photovoltaic performance of dye-sensitized ZnO solar cell based on Eosin-Y photosensitizer. *Materials Science-Poland* **25**, 137–144 (2007).
19. Suri, P. & Mehra, R.M. Effect of electrolytes on the photovoltaic performance of a hybrid dye sensitized ZnO solar cell. *Solar Energy Materials and Solar Cells* **91**, 518–524 (2007).
20. Wu, J., Chen, G., Yang, H., Ku, C. & Lai, J. Effects of dye adsorption on the electron transport properties in ZnO-nanowire dye-sensitized solar cells. *Applied Physics Letters* **90**, 213109 (2007).
21. Matsumura, M., Matsudaira, S., Tsubomura, H., Takata, M. & Yanagida, H. Dye sensitization and surface-structures of semiconductor electrodes. *Industrial & Engineering Chemistry Product Research and Development* **19**, 415–421 (1980).
22. Rani, S., Suri, P., Shishodia, P.K. & Mehra, R.M. Synthesis of nanocrystalline ZnO powder via sol-gel route for dye-sensitized solar cells. *Solar Energy Materials and Solar Cells* **92**, 1639–1645 (2008).
23. Guerin, V.M., Magne, C., Pauporté, T., Le Bahers, T. & Rathousky, J. Electrodeposited nanoporous versus nanoparticulate ZnO films of similar roughness for dye-sensitized solar cell applications. *ACS Applied Materials & Interfaces* **2**, 3677-3685 (2010).
24. Hosono, E., Fujihara, S. & Kimura, T. Synthesis, structure and photoelectrochemical performance of micro/nano-textured ZnO/eosin Y electrodes. *Electrochimica Acta* **49**, 2287–2293 (2004).
25. Yoshida, T., Ando, H., Kazuteru Nonomura, Wohrle, D. & Minoura, H. Improved photoelectrochemical performance of electrodeposited ZnO/EosinY hybrid thin films by dye re-adsorption. *Chemistry Communications.* 400-401 (2004).
26. Minoura, H. & Yoshida, T. Electrodeposition of ZnO/dye hybrid thin films for dye-sensitized solar cells. *Electrochemistry* **76**, 109–117 (2008).
27. Ku, C. & Wu, J. Electron transport properties in ZnO nanowire array/nanoparticle composite dye-sensitized solar cells. *Applied Physics Letters* **91**, 093117 (2007).
28. Hara, K., Horiguchi, T., Kinoshita, T., Sayama, K., Sugihara, H. & Arakawa, H. Highly efficient photon-to-electron conversion of mercurochrome-sensitized

Nanoporous ZnO solar cells. *Chemistry Letters* **29**, 316 (2000).
29. Liu, Z., Pan, K., Zhang, Q., Wang, D., & Li, T. The performances of the mercurochrome-sensitized composite semiconductor photoelectrochemical cells based on TiO_2/SnO_2 and ZnO/SnO_2 composites. *Thin Solid Films* **468**, 291-297 (2004).
30. Fernandez-Lorenzo, C., Poce-Fatou, J.A., Alcantara, R., Navas, J. & Martín-Calleja, J. High resolution laser beam induced current focusing for photoactive surface characterization. *Applied Surface Science* **253**, 2179–2188 (2006).
31. Chou, T.P., Zhang, Q.F. & Cao, G.Z. Effects of dye loading conditions on the energy conversion efficiency of ZnO and TiO_2 dye-sensitized solar cells. *Journal of Physical Chemistry C* **111**, 18804–18811 (2007).
32. Boschloo, G., Edvinsson, T. & Hagfeldt, A. Dye-sensitized nanostructured ZnO electrodes for solar cell applications. *Nanostructured Materials for Solar Energy Conversion* 227-254 (2006).
33. Horiuchi, H., Katoh, R., Hara, K., Murata, S., & Tachiya, M. Electron injection efficiency from excited N3 into nanocrystalline ZnO films: effect of $(N3{-}Zn^{2+})$ aggregate formation. *The Journal of Physical Chemistry B* **107**, 2570-2574 (2003).
34. Nguyen, H., Mane, R.S., Ganesh, T., Han, S. & Kim, N. Aggregation-free ZnO nanocrystals coupled HMP-2 dye of higher extinction coefficient for enhancing energy conversion efficiency. *The Journal of Physical Chemistry C* **113**, 9206-9209 (2009).
35. Sirimanne, P.M., Senevirathna, M.K.I., Premalal, E.V.A. & Pitigala, P.K.D.D.P A solid-state solar cell sensitized with mercurochrome. *Current Science Association, Indian Academy of Sciences* **90**, 639-640 (2006).
36. Sayama, K., Sugino, M., Sugihara, H., Abe, Y. & Arakawa, H. Photosensitization of porous TiO_2 semiconductor electrode with xanthene dyes. *Chemistry Letters* **27**, 753 (2000).
37. Frédéric Labat, Ciofini, I. & Raghavachari, K. First principles modeling of Eosin-loaded ZnO films: a step toward the understanding of dye-sensitized solar cell performances. *Journal of the American Chemical Society* **131**, 14290-14298 (2009).
38. Zhang, Q., Dandeneau, C.S., Zhou, X. & Cao, G. ZnO nanostructures for dye-sensitized solar cells. *Advanced Materials.* **21**, 4087-4108 (2009).

Chapter 6

Electrolytes based on Room Temperature Ionic Liquids for ZnO-based Dye-Sensitized Solar Cells

6. Electrolytes based on room temperature ionic liquids for ZnO-based dye-sensitized solar cells

In this Chapter, a study of dye-sensitized solar cells based on nanostructured zinc oxide combined with imidazolium-based room temperature ionic liquid electrolytes is presented.

Due to concerns about the long-term stability of a solid-liquid junction solar cell, there has been a great interest in finding a substitute for volatile electrolytes based on organic solvents. One approach, as mentioned in **Section 1.2.3**, has been the development of solid state devices based on hole conductors such as inorganic p-type semiconductors like e.g. CuSCN[1] and CuI[2] or organic hole-transporters as the Spiro-MeOTAD[3,4]. However, incomplete pore filling, high recombination rates and low hole conductivity limit the performance of this type of devices.

Room temperature ionic liquids (RTILs) represent an interesting compromise between organic solvent-based electrolytes and a solid hole conductor. As they are liquid, they can penetrate easily into the semiconductor pores. At the same time they have a negligible vapour pressure, so that evaporation problems are avoided. In addition, they can be used in flexible plastic cells because, in contrast to organic solvents, they do not permeate the plastic cell walls[5,6].

The concept of a liquid salt is usually associated to high temperatures due to the strong electrostatic attraction ionic compounds usually exhibit (e.g. NaCl). However RTILs are composed of very asymmetric and large ions, so that attractive forces are weak. The consequences are a low melting point (they are liquid at room temperature) and a negligible vapour pressure (they are practically non-volatile). Besides non-volatility, RTILs possess unique physicochemical properties, which make them very distinct from conventional molecular liquids such as non-flammability, high ionic conductivity and high thermal, chemical and electrochemical stability[7].

Ionic liquids were first discovered in the 1940s and since then their potential applications have not stopped increasing. Their main application is as solvents in the field known as *green chemistry*. RTILs are good solvents for a wide range of both inorganic and organic materials and, in contrast to organic solvents, they are non-volatile an easily recyclable[8], avoiding costs and environmental problems. On the other

hand, since the ionic liquids are essentially ionic conductors with high conductivities[9], their utilization as novel electrolytes for electrochemical devices such as lithium secondary batteries, electric double layer capacitors, dye-sensitized solar cells, fuel cells and actuators has also been the subject of intense studies.

RTILs are typically comprised of combinations of organic cations, such as imidazolium, pyridinium, ammonium, sulfonium and phosphonium derivatives and a wide range of anions, from simple halides to inorganic anions such as tetrafluoroborate or large organic anions like triflate. Physical and chemical properties such as viscosity, density and solubility can vary in a wide range depending on the cation-anion combination of the ionic liquid. This high versatility allows for the design of different ionic liquids for each application and the number of existing RTILs is immense.

RTIL-based electrolytes (solvent free electrolytes) have been widely used in dye-sensitized solar cells[6,10-13]. However, the viscosity of typical RTILs is about 100 times higher than that of acetonitrile at room temperature. As a consequence, mass transport limitations[10,14] as well as high recombination rates[11] have been reported for this kind of electrolytes, leading to lower efficiencies with respect to the cells based on organic solvent electrolytes. Nevertheless, conversion efficiencies of around 9%[i] have been reported for ionic-liquid-based DSCs[15] and devices with high long-term stability can be obtained. As will be discussed in **Chapter 7**, the key factor for this high efficiency is the combination of RTIL electrolytes with strongly absorbing sensitizers (i.e. dyes with high extinction coefficients).

Among the huge variety of ionic liquids available, the best results for DSCs have been obtained with imidazolium based salts. Wang et al.[13] obtained an efficiency over 7%[ii] with the low-viscosity ionic liquid 1-ethyl-3-methylimidazolium selenocyanate, replacing the common iodide/triiodide redox couple by $SeCN^-$/ $(SeCN)_3^-$, although this electrolyte has proved to be unstable. However, apart from this reference, the best efficiencies have been obtained with iodide imidazolium melts. Among the iodide imidazolium salts that are room temperature ionic liquids, PMII (1-propyl-3-methyl-imidazolium iodide) has the lowest viscosity[6] and the highest conductivity[16]. This ionic liquid very often constitutes the main component of a solvent free electrolyte acting at

[i] Cell active area: 0.158 cm^2
[ii] Cell active area: 0.152 cm^2

the same time as solvent and as iodide source. A remarkable 6%[iii] efficiency has been obtained with pure PMII based electrolytes[17]. However, due to the large size of the counter ion it has a very high viscosity. This limits its applicability as electrolyte for solvent free cells. Additionally, in DSCs with an electrolyte containing a high concentration of iodide, a reductive quenching of the sensitizer has been observed: excited dye molecules accept an electron from I^- thus forming a reduced dye species (D^-), which no longer injects electrons in the semiconductor[6,18,19].

In order to overcome the limitations associated with iodide imidazolium salts, without renouncing their proved favourable properties, electrolytes based on mixtures of PMII and ionic liquids of low viscosity have been explored[18,20,21]. The nature of anions, e.g. their geometry and charge distribution, determines the strength of the cation-anion interactions and eventually the viscosity of an ionic liquid[22,23]. Imidazolium salts containing non-electroactive anions such as thiocyanate[6,21], dicyanamide[24], tricyanomethide, tetracyanoborate[15,19,20] or selenocyanate[13] have a much lower viscosity than the iodide based PMII. It has been proved that the addition of imidazolium salts containing non-electroactive anions to pure PMII decreases the viscosity of the electrolyte and improves the power conversion efficiencies of DSCs[6].

The substitution of organic solvents by RTILs in ZnO-based solar cells, which has not been studied up to now, is discussed in this Chapter. PMII was chosen as the basic component of the electrolyte, and its combination with other imidazolium-based ionic liquids of lower viscosity is analyzed. In **Table 6.1** the viscosity of the ionic liquids tested in this study is summarized and in **Figure 6.1** the molecular structures are shown.

Table 6.1 Viscosity of the ionic liquids tested in this study.

RTIL	Viscosity (cP)	Ref.
PMII	776.0 (298 K)	[25]
EMIDCN	21.0 (298 K)	[26]
EMIBCN	19.8 (293K)	[19]
EMITFSI	44.4 (298 K)	[19]

[iii] Cell active area: 0.152 cm^2

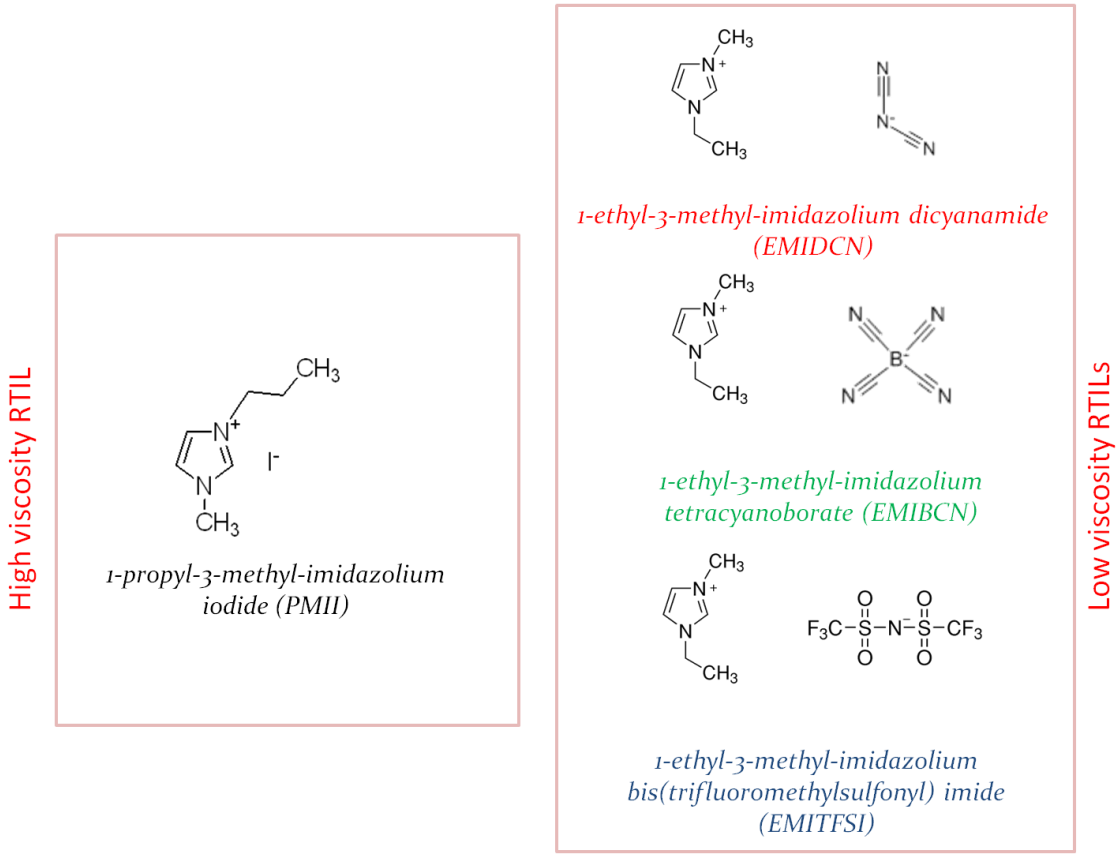

Figure 6.1 Molecular structures of the room temperature ionic liquids used in this study.

The first step of this study was the optimization of the iodine and iodide concentration of the ionic liquid electrolytes for ZnO solar cells. EMIDCN was chosen as "solvent RTIL". The effects of the redox couple concentration, I^-/I_3^- ratios, light intensity and additives (4-tert-butylpyridine (TBP) and LiI) on the performance of the DSCs were explored. EMIDCN is an ionic liquid with promising features for DSCs[27] due to its high electrochemical stability, low viscosity and broad liquid range[28] as well as its relatively low price. In addition, good efficiencies have been obtained for TiO_2 cells based on ionic liquid mixtures of EMIDCN and PMII[23]. The combination of PMII with two additional ionic liquids has been also studied in order to investigate the effect of different RTIL anions in the performance of the cells.

6.1. Fabrication and characterization of the devices

The materials used for the fabrication of the cells are summarized in **Table 6.2** and the parameters of the illumination source used for photovoltaic characterization in **Table 6.3**.

Table 6.2 Summary of the materials employed in the fabrication of the cells

ZnO	Dyes	Electrolytes	Additives	Counter electrode
Degussa VP AdNano®ZnO20 Cell area: 0.64 cm^2	N719 0.5 mM in ethanol (2 hours)	PMIMI + I_2 • EMIDCN • EMITFSI • $EMIB(CN)_4$	LiI (0.1 M) TBP (0.8 M)	Hexachloroplatinic acid (0.01 M in isopropanol)

Table 6.3 Illumination set-up used for DSC testing

Illumination source	Filters	Calibration
Xenon 450W arc lamp	• Water filter • 325 nm UV • KG5 IR filter	Reference solar cell (Oriel, 91150) 100 mW cm^{-2}

The electrodes were sealed at 180°C using a Surlyn film (60 μm). The electrolyte was introduced via two channels in the Surlyn seal frame. Before characterization, the cells were stored in the dark overnight to allow the electrolyte to penetrate the ZnO pores. The white light illumination intensity was varied between 10 and 200 mW cm^{-2} at room temperature using neutral density filters. Additionally, in some measurements a green laser (532 nm) was used as light source. Photocurrents, photovoltages, current-voltage curves, open circuit photovoltage decays and impedance spectra were measured with an Autolab/PGSTAT302N station (Ecochemie) coupled with a FRA2 frequency generator module. Circuit (b) (**Figure 3.10**) has been used to fit the impedance data. Dye-sensitized solar cells were illuminated until constant values of J_{sc} were reached. Using RTIL as electrolyte, this procedure can take up to 20 minutes, especially for the most viscous compositions. This long stabilisation times can be explained by the slow mass transport associated with RTILs and hence, a longer time required to reach the final concentration gradients for the charge carriers and charge compensating ions in the DSC. The heating of the cell, as will be described in **Section 6.4**, also plays an important role in this process.

6.2. Optimization of the iodine concentration

The optimization of the iodine concentration is one of the most important variables in the performance optimization of DSCs. As seen in **Chapter 1**, triiodide plays a fundamental role in the functioning of the dye solar cell. Its optimization is crucial as equilibrium between fast reduction to iodide and slow recombination with the injected electrons must be achieved. In the case of ionic liquid electrolytes, another factor that must be taken into account is a possible diffusion limitation of the species forming the redox couple. This is a consequence of the higher viscosity of this kind of solvents. It is expected that the optimal iodine concentration will depend on the respective electrolyte composition[29]. However, we limit our analysis on the optimization of the iodine concentration in the pure PMII. The optimization is thus made for the most viscous electrolyte used in this work, so that photocurrent losses due to mass transport limitation of triiodide are minimized[6].

To compensate for the slow diffusion in ionic liquid electrolytes, the need for a higher concentration of triiodide with respect to the one used in organic electrolytes has been reported[10,30]. However, the increment of the concentration of I_3^- can lead to a lower performance of the cell. On the one hand, it must be born in mind that iodine absorbs light[10,26], which can provoke a diminution of the photocurrent. In addition, an increase in the iodine concentration can accelerate recombination since more triiodide ions are available for accepting electrons (**Equation 2.5**). Hence, maximum of the cell performance is expected at intermediate triiodide concentrations.

In **Figure 6.2**, the photocurrent obtained under white light illumination (without KG5 filter) is plotted versus the iodine concentration in the electrolyte. The short circuit current density increases initially with iodine concentration and reaches a maximum at around 0.05 M. Upon a further increase of the iodine concentration the photocurrent decreases steadily. The initial increase of the photocurrent could be a consequence of diffusion limitation in the electrolyte associated to the low triodide concentration. Furthermore, it was observed that the addition of iodine to a RTIL decreases its viscosity[10,26,30]. This could also contribute to the initial improvement.

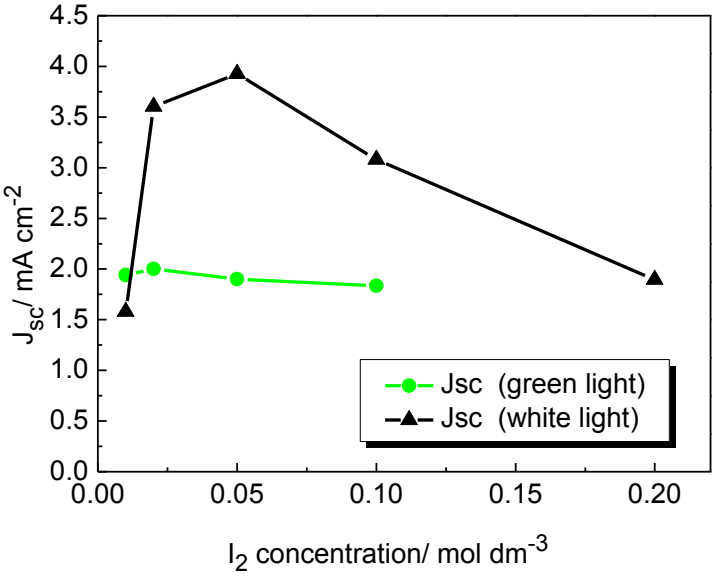

Figure 6.2 Short circuit photocurrent for PMII-based ZnO dye-sensitized solar cells versus I_2 molar concentration. White light illumination with UV filter (100 mW cm^{-2}) and green light (laser at 532 nm) were used to photoexcite the devices.

The influence of the iodine concentration on the photocurrent when using a green laser as light source is also highlighted in **Figure 6.2.** In contrast to experiments with a white light source, no photocurrent maximum is observed in this case. This different behaviour points to the fact that light absorption by triiodide is very important in the case of white light illumination. It is observed that the PMII/I_2 electrolyte absorbs strongly between 350 and 450 nm (**Appendix 11.4**). The decrease of the photocurrent at high iodine concentrations can, therefore, be assigned mainly to the absorption of light by triiodide.

In ionic liquid electrolytes with a high iodide concentration the measured triiodide diffusion coefficient is observed to be much higher than expected on the basis of viscosity data[26,31]. A mechanism for triiodide transport in ionic liquids has been suggested to explain this non-Stokesian behaviour [26,30,32]. It is believed that apart from the normal physical diffusion, the triiodide transport is determined by a Grotthuss-type charge-exchange mechanism[6,30,31,33]. A scheme of the underlying mechanism is shown in **Figure 6.3**. The triiodide approaches iodide from one end, forming an encounter complex, from which triiodide is released at the other end. As a result, the triiodide is displaced by the length of one I–I bond (2.9 Å[34]) without having to cross that distance. The Grotthuss mechanism describes, therefore, charge transport rather than real mass transport. This is manifested, however, as an apparent acceleration of the triiodide diffusion and can explain the abnormally high diffusion coefficients determined experimentally[6].

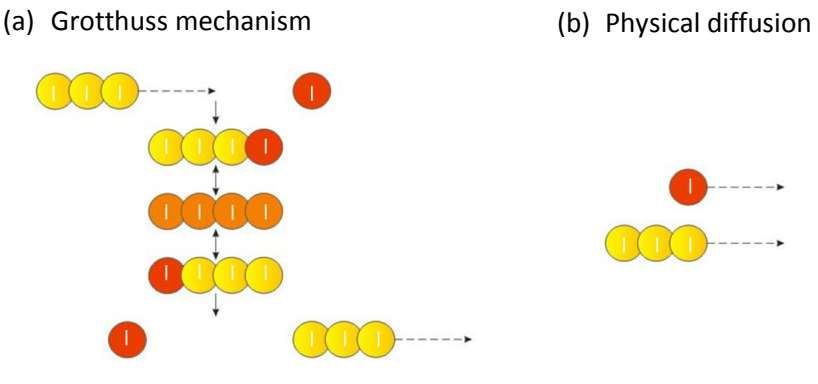

Figure 6.3 a) Grotthuss mechanism of transport for triiodide in ionic liquids with high iodide concentration. Iodide (red), triiodide (yellow), encountering complex (orange). b) Physical diffusion.

Watanabe et al.[35] confirmed by a microelectrode study that when the concentration of the redox species is high, and [I^-] and [I_3^-] are comparable, the contribution from the exchange reaction dominates the charge transport in this system. This mechanism can contribute to an increase in the charge transport process when the iodine concentration is high. However, the results presented in **Figure 6.2** point to the fact that in this case light absorption of triiodide overcompensates for the possible improvement of diffusion at high iodine concentrations[23].

The open circuit voltage dependence on iodine concentration is shown in **Figure 6.4**. According to **Equation 2.5** an increment of the iodine concentration leads to a higher recombination rate[26]. As a consequence of the higher recombination rate and, therefore, the shorter lifetime, the photovoltage is found to decrease with iodine concentration.

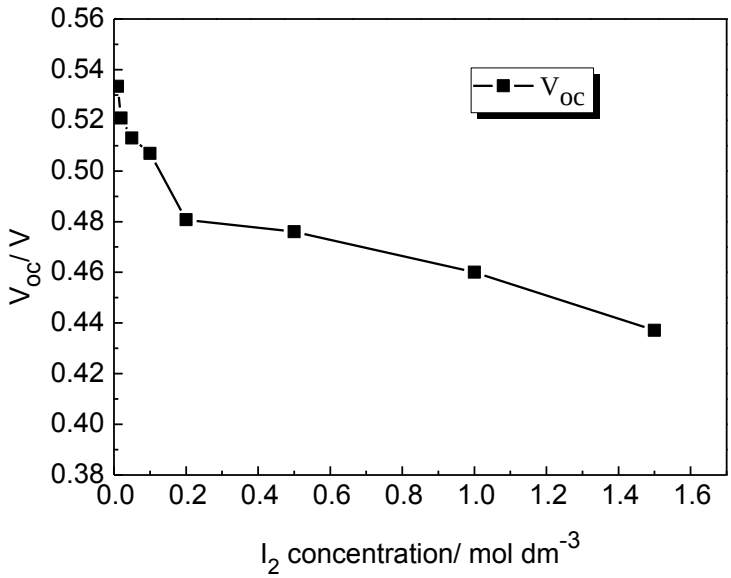

Figure 6.4 Open circuit voltage as a function of the iodine concentration. White light illumination with UV filter (100 mW cm^{-2}).

In order to maximize the device performance, an optimal iodine concentration of 0.05 M can be deduced from the photocurrent (**Figure 6.2**) and photovoltage (**Figure 6.4**) profiles. This concentration is very similar to those utilized in volatile standard electrolytes[36].

6.3. Optimization of the iodide concentration

Electrolyte composition is also optimized with respect to the iodide concentration. As mentioned in **Section 6.1**, the photovoltaic performance of the cells can be strongly improved by mixing PMII with less viscous ionic liquids. For this purpose PMII was mixed with 1-ethyl-3-methyl-imidazolium dicyanamide (EMIDCN, **Figure 6.1**) in the present study. A summary of the photovoltaic parameters as a function of the PMII/EMIDCN mixing ratio is shown in **Table 6.4**.

Table 6.4 Photovoltaic parameters as a function of PMII/EMIDCN mixing ratio. Illumination intensity: 100 mW cm^{-2}. Mean values and deviations are derived from independent measurements of several devices for each electrolyte composition.

Mol% PMII	J_{sc} (mA cm^{-2})	V_{oc} (mV)	FF	η (%)
20%	2.83 ± 1.09	645 ± 4.24	0.56 ± 0.01	1.03 ± 0.39
40%	7.78 ± 1,30	620 ± 1.41	0.50 ± 0.01	2.43 ± 0.38
60%	7.74 ± 0,32	580 ± 2.12	0.48 ± 0.01	2.17 ± 0.13
100%	5.70 ± 0.43	528 ± 2.12	0.48 ± 0.01	1.46 ± 0.08

An optimal mixing ratio of 40% PMII and 60% EMIDCN is found. All the photovoltaic parameters of the cells are clearly affected by PMII/EMIDCN mixing ratio. The first factor that must be taken into account to explain the behaviour of cells with different electrolyte compositions is the viscosity. We must bear in mind that EMIDCN is much less viscous than PMII (**Table 6.1**). According to Wachter et al.[26,27], reducing the PMII content from 100% to 80% by mixing this ionic liquid with EMIDCN results in a viscosity-decrease of about 75%. A further reduction of the PMII content down to 40% yields an overall viscosity-decrease of about 95%. Therefore, larger triiodide diffusion coefficients are expected for the ionic liquid blends compared to the pure PMII electrolyte. In fact, it is observed that the initial reduction of PMII from 100% to 60 % induces a significant improvement of the photocurrent (**Figure 6.5**).

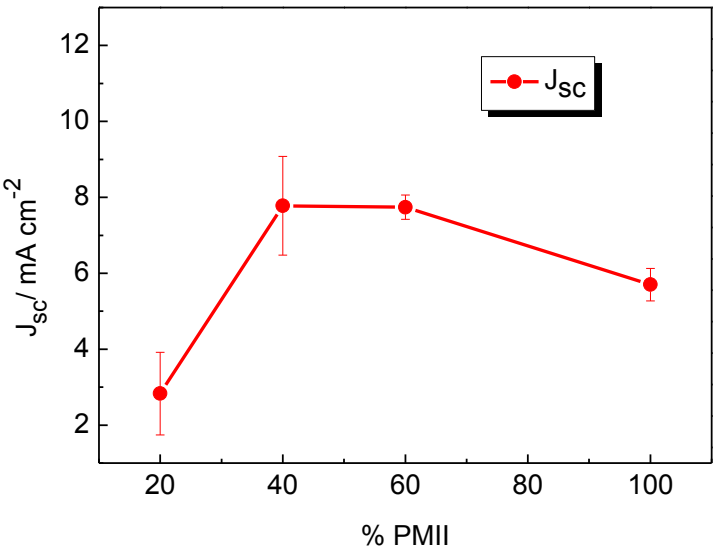

Figure 6.5 Photocurrent versus PMII content.

However, although the reduction of the PMII ratio initially provokes an increase of the photocurrent, it is observed that it reaches a plateau and even decreases strongly at low PMII concentrations. In terms of charge transport via the Grotthuss mechanism in ionic liquids (as described in **Section 6.2**), a high iodide concentration would promote exchange transport of triiodide. Therefore, lowering the PMII/EMIDCN mixing ratio not only would induce an increase of physical diffusion as a consequence of viscosity decrease, but also a slow-down of the exchange reaction due to the diminution of iodide concentration (**Figure 6.3**).

Very recently, Hao et al.[37] reported on the performance of TiO_2 cells using the same binary electrolyte system as the one studied in this work. They explain the observed dependence of the photocurrent on the PMII/EMIDCN ratio by the change of the relative contributions from physical diffusion and exchange reaction to the overall charge transport. However, Wanatabe et al.[35,38] have proved that the contribution of the exchange reaction mechanism to the transport of triiodide is small with respect to physical diffusion for high iodide/triiodide concentration ratios, that is, when there is a large excess of iodide in the electrolyte[38]. The low iodine concentration employed for the fabrication of the cells (0.05 M), together with the fact that physical diffusion is greatly enhanced by the low viscosity ionic liquid EMIDCN, seem to indicate that the charge transfer mechanism does not have a major impact[39] on the overall performance of the cells studied in this work.

Zhang et al.[38] attributed the decrease of the photocurrent at low PMII content in ionic liquid-based TiO_2 cells to incomplete dye regeneration at PMII concentrations lower than 1 M. In addition, the strong photocurrent deterioration observed in **Figure 6.5** is probably due to the instability of the sensitized films when the EMIDCN content in the electrolyte is high. Dye desorption may take place at high concentrations of dicyanamide anions, a process that is more critical on ZnO than on TiO_2 due to the lower chemical stability of this oxide and the problematic dye-oxide interaction described in **Chapter 5**. This instability is furthermore reflected in a lower reproducibility of the short circuit photocurrent measured for cells with high EMIDCN contents (**Figure 6.5**). Therefore, a low proportion of dicyanamide is desirable to avoid desorption of the dye and to optimize cell performance. Although a certain instability has been reported under light soaking for TiO_2 cells using EMIDCN as well[21], it must be pointed out that a remarkable efficiency (>6%) has been obtained with solvent free electrolytes based on PMII and EMIDCN.

The mixing ratio affects the photovoltage as well (**Figure 6.6**). It is found that the photovoltage is incremented by more than 100 mV when the PMII content is decreased from 100% to 20%.

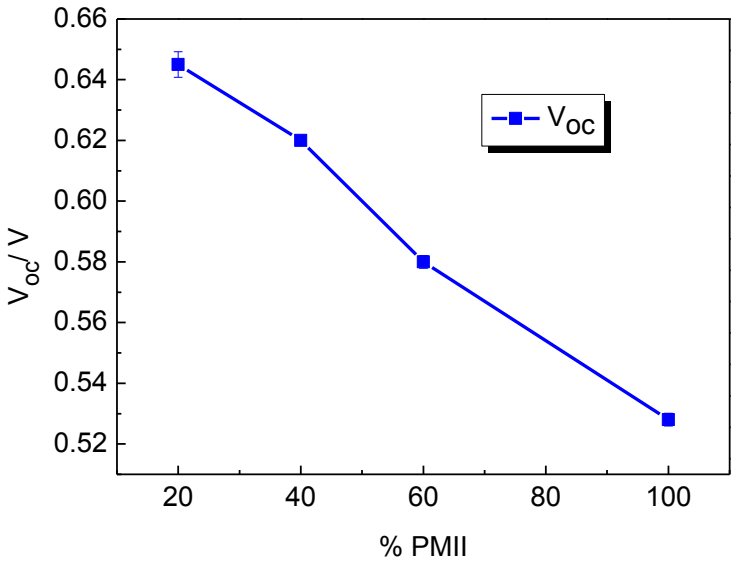

Figure 6.6 Photovoltage versus PMII ratio.

An improvement of the photovoltage is expected with a reduction of the iodide content in the electrolyte[19] due to the displacement of the equilibrium redox potential of the I^-/I_3^- couple according to the Nernst equation (**Equation 2.16**). If the Fermi level in the semiconductor is fixed, as expected for constant illumination intensity, this

displacement will lead to a higher photovoltage. However, **Equation 2.16** can only account for an increment of around 21 mV upon a decrease of the iodide concentration by a factor of 5.

Electrochemical impedance spectroscopy (EIS) measurements can be used to study in detail the processes determining the overall cell performance. In **Figure 6.7** EIS spectra measured in the dark at an applied voltage of 0.55 V are shown for cells with different PMII/EMIDCN mixing ratios. As discussed in **Chapter 3**, the arc at intermediate frequencies (middle arcs in **Figure 6.7**) corresponds to the charge-transfer resistance of the electron recombination at the oxide/electrolyte interface.

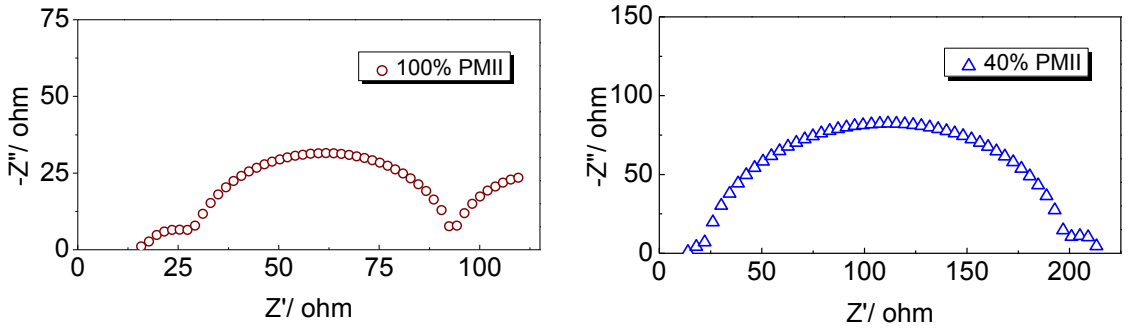

Figure 6.7 Impedance spectra for different PMII/EMIDCN mixing ratios at 550 mV in the dark.

The value of the charge-transfer resistance strongly increases as the concentration of iodide ions decreases. The fitting of the impedance spectra yields for the charge transfer resistance R_{ct} = 65.1 Ω and 215 Ω for pure PMII and 40% PMII, respectively. On the other hand, the lifetimes (**Equation 3.11** $\tau_n = R_{ct} C_\mu$) extracted from the fits were 0.0075 s and 0.015 s for pure PMII and 40% PMII, respectively. The increase of the recombination resistance and of the lifetime when the PMII/EMIDCN mixing ratio is reduced explains the improvement of the photovoltage with respect to pure PMII. These results point to a blocking of electron recombination with triiodide when dicyanamide anions are present at the ZnO/electrolyte interface. Examples of EIS spectra for each of the four mixing ratios can be found in the **Appendix 11.5**.

The improvement of the photovoltage and the increase of the recombination resistance at low PMII/EMIDCN mixing ratios may also be the consequence of a negative displacement[40] of the ZnO conduction band upon EMIDCN addition. To ascertain this point we have carried out impedance spectra at different bias voltages. The dependence of the transport resistance and the chemical capacitance of the ZnO/electrolyte interface

on the applied voltage provides information on this kind of band displacement [41] as will be explained in more detail in **Chapter 9**. Both magnitudes, transport resistance and chemical capacitance, are presented in **Figure 6.8** as a function of the applied voltage.

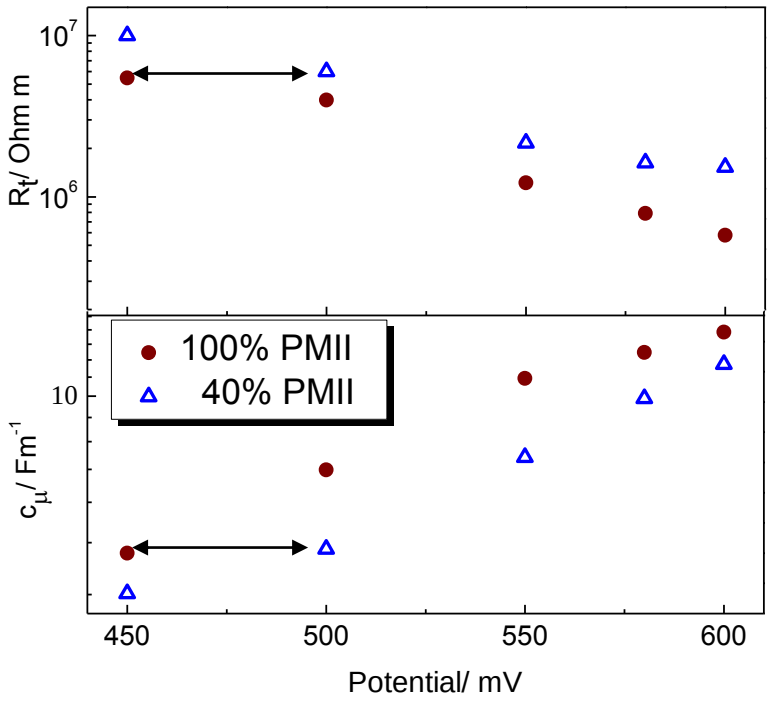

Figure 6.8 Variation of the transport resistance (upper panel) and of the chemical capacitance (lower panel) with the applied voltage for two electrolyte compositions.

The capacitance is related to the difference between the Fermi level and the conduction band edge by **Equation 2.40**. Therefore, if we assume the same trap distribution for all our samples, data in **Figure 6.8** reveal a negative displacement of the ZnO conduction band of around 50 mV in the PMII/EMIDCN (40% PMII) cell with respect to the one containing pure PMII. The same conclusion is reached from the analysis of the resistance data in **Figure 6.8**.

A deviation from linearity at high voltages is observed for both capacitance and transport resistance (**Figure 6.8**). In the case of ZnO cells, the fitting of the transport resistance turns out to be problematic and as a consequence a flattening at high voltages is often observed. This matter will be discussed in detail in **Chapter 9**, together with a procedure to overcome this problem. Small deviations from linearity both in capacitance and transport resistance can be also produced by a potential drop through the film due to series resistance[42]. A similar observation has been reported for solvent free TiO_2 solar cells sensitized with N719 dye[11].

Recently[43,44], a quantum-mechanical study of dicyanamide anions has proved that the nitrogen atom of the cyano groups virtually carries more negative charge than the central nitrogen. This fact makes the adsorption on the oxide more favourable. The dipole, which points from the electrolyte toward the oxide, probably causes the conduction band edge elevation (**Figure 6.9**).

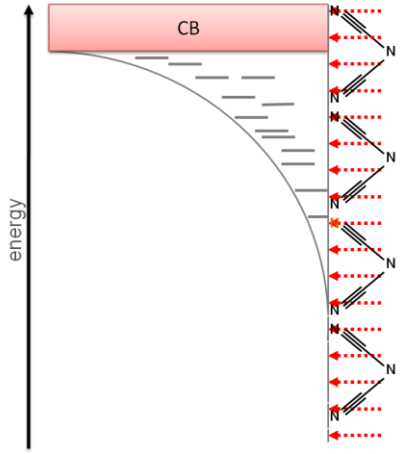

Figure 6.9 Schematic presentation of the dipole effect on the conduction band edge. The red arrows indicate the dipole direction.

The displacement of the band edge leads to a lower density of states at the same Fermi level position. As a consequence lower recombination and longer lifetimes are observed for the dicyanamide containing electrolyte with respect to the pure PMII at the same applied voltage. In addition, it has been recently reported[45] that highly viscous solvents might lead to higher recombination losses due to poor dye regeneration during solar cell operation.

Very recently, Hao et al.[37] have carried out a similar study to the one described here for TiO_2 cells in combination with PMII and EMIDCN. They also found an improvement in the photovoltage when the EMIDCN content was increased, but this improvement (68 mV) is less pronounced than the one observed in this study (117 mV, **Figure 6.6** and **Table 6.4**). This may be a consequence of dye desorption in the presence of EMIDCN, which is expected to be more pronounced for ZnO thus providing more adsorption sites for the dicyanamide anion.

It must be pointed out that negative conduction band shifts are reported to provoke a diminution of the injection quantum yield due to a lower driving force, and this can affect also to the photocurrent measured as a function of the PMII ratio.

The viscosity of the electrolyte also affects the fill factor of the cells[6,19,25]. The charge transfer resistance of the counter electrode (high frequencies, left semicircle) and the diffusion resistance of the electrolyte (low frequencies, right semicircle) increase with PMII concentration (**Figure 6.7** and **Appendix 11.5**). This illustrates that the viscosity of the ionic liquid is a key property not only for the diffusion of ions in the electrolyte, but also for the kinetics of electron transfer at the counter electrode of the DSC[46].

6.4. Light intensity dependence and diffusion limitations

Transport limitations in viscous electrolytes are commonly detected by measuring the photocurrent at short circuit (J_{sc}) as a function of light intensity (I_0). A non-linear response indicates that ionic transport in the electrolyte is neither fast enough to regenerate the dye nor to transport the holes towards the counterelectrode[10,11]. Bearing this in mind we have measured the short circuit photocurrent as a function of light intensity (**Figure 6.10**) for the most viscous composition (i.e. pure PMII).

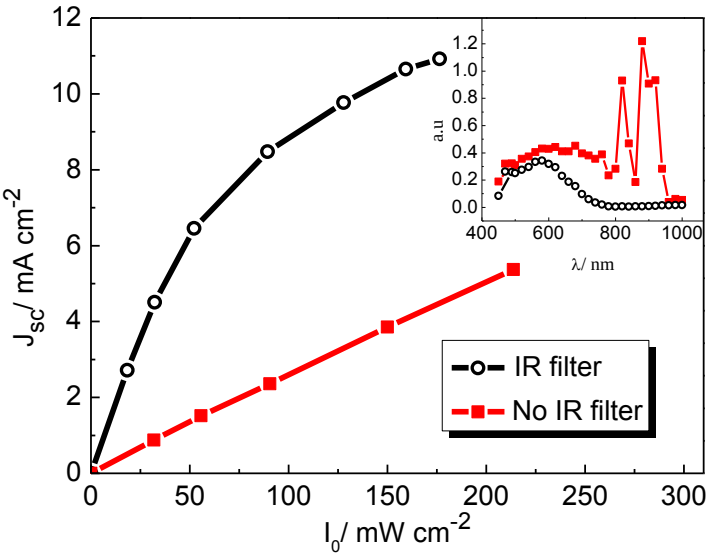

Figure 6.10 Short-circuit photocurrent as a function of light intensity for PMII-based ZnO dye solar cells with and without IR filter. The inset shows the incident illumination spectra with and without IR filter.

The measurements were carried out up to an intensity of 200 mW cm^{-2} (yielding photocurrents of up to 11 mA cm^{-2}) with (circles) and without (squares) the IR filter KG5 (**Chapter 4**). When using the IR filter the photocurrent shows a clear deviation from linearity at intensities above 7 mA cm^{-2} (**Figure 6.10**). This observation reveals that there is indeed a certain diffusion limitation due to the high viscosity of the pure PMII electrolyte.

The diffusion limitation observed in **Figure 6.10** can be compared to an estimation of the saturation current density of triiodide ions within the cells, as the main limitation is expected to be the transport of triiodide to the counter electrode[10]. Assuming an homogeneous electrode we can estimate the saturation current using the approximate formula[10,47]

$$j_{sat} = \frac{2nF[I_3^-]D_{I_3^-}}{\delta} \tag{6.1}$$

where n is the number of electrons involved in the reaction, $D_{I_3^-}$ is the diffusion coefficient of the triiodide ions and δ is the diffusion layer. Taking 2 10^{-7} cm^2 s^{-1} for the diffusion coefficient as reported in Ref. [11], $[I_3^-]$ = 0.05 M, n = 2 and δ ~ 30 μm (half the thickness of the spacer) we obtain j_{sat} = 1.29 mA cm^{-2} at room temperature. According to **Figure 6.10**, the mass limitation appears at much higher photocurrent densities. However, it must be pointed out that the cell becomes heated when the illumination intensity is increased (up to 80ºC can be reached at working conditions[48]) and there is a strong increase of the triiodide diffusion coefficient with increasing temperature and decreasing viscosity[27]. Wachter et al.[32] found that the diffusion coefficient of triiodide in PMII increased by a factor of 8 upon a temperature increase from 25 ºC to 60 ºC. This would lead to a saturation current close to the one observed in **Figure 6.10**.

To confirm the temperature effect, the dependence of the photocurrent with the light intensity was also measured without the IR filter (**Figure 6.10**). In this case the photocurrent increases linearly with light intensity. Hence, heating of the cell can indeed help to avoid diffusion limitations in this kind of systems. It must be mentioned that the photocurrents obtained without the IR filter were lower than those obtained when this filter is used in the illumination set-up. Both illumination configurations were calibrated using the same reference photodiode. When the light intensity is adjusted to the same value for both set-ups (using appropriate neutral density filters), the source spectrum contains a lower amount of visible light in the absence of the IR filter. Since dye absorption is produced in the visible region, this makes the photocurrent to be reduced at the same irradiance value when the IR filter is removed. From the inset in **Figure 6.10** it can be seen, furthermore, that the presence of the KG5 filter is useful to approximate the lamp spectrum to the standard AM 1.5 spectrum.

In **Figure 6.11** impedance spectra of cells with pure PMII electrolyte at different illumination intensities are represented.

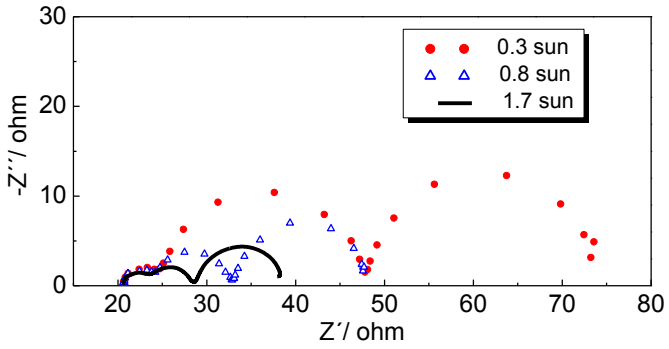

Figure 6.11 Impedance spectra of PMII-based ZnO solar cells under various illumination intensities**.**

It can be seen that the two main arcs (accounting for recombination charge transfer and diffusion of ions in the electrolyte) reduce their sizes when the light intensity is increased. This is a consequence of the drop in the charge transfer and diffusion resistances[11]. The heating, as described above, contributes to the decrease of the diffusion resistance of the triiodide in the electrolyte. But at the same time, the charge transfer is favoured by the increment of the triodide diffusion coefficient upon heating and as a consequence the recombination current increases. Therefore, although the diffusion limitations could be avoided by heating the cells, this would also provoke a decrease in the electron lifetime.

6.5. Effect of additives

It is well known that the presence of some additives in the electrolyte can lead to a significant improvement of the photovoltaic performance of DSCs. Two of the most used additives for organic liquid electrolytes are tert-butyl pyridine (TBP) and lithium cations (Li^+). After the study of the iodide and iodine concentration effect in the binary blend EMIDCN/PMII, the influence of TBP and Li^+ on the performance of the optimized blend (60/40 EMIDCN/PMII) is analyzed. In **Table 6.5** the photovoltaic performance of a reference cell with no additives and cells with LiI and TBP added can be found.

Table 6.5 Photovoltaic parameters under white light illumination at 100 mW cm^{-2}. Mean values and deviations are derived from independent measurements of several devices for each electrolyte composition.

Cell	J_{sc} (mA cm^{-2})	V_{oc} (mV)	FF	η (%)
no additive	8.13 ± 0.84	607 ± 11.5	0.50 ± 0.01	2.64 ± 0.06
+ LiI (0.1M)	9.28 ± 0.82	656 ± 9.19	0.53 ± 0.01	3.28 ± 0.17
+ TBP (0.8M)	7.79 ± 0.23	637 ± 9.89	0.57 ± 0.01	2.81 ± 0.03

These two additives are found to improve the overall performance of the cells. Both are responsible for a significant improvement of the photovoltage, and Li^+ also increases the photocurrent of the devices. The device with the best performance yields a photoconversion rate of 3.4% under 1 sun with this illumination set-up (**Section 6.1**). In **Figure 6.12** representative IV curves for each configuration are shown.

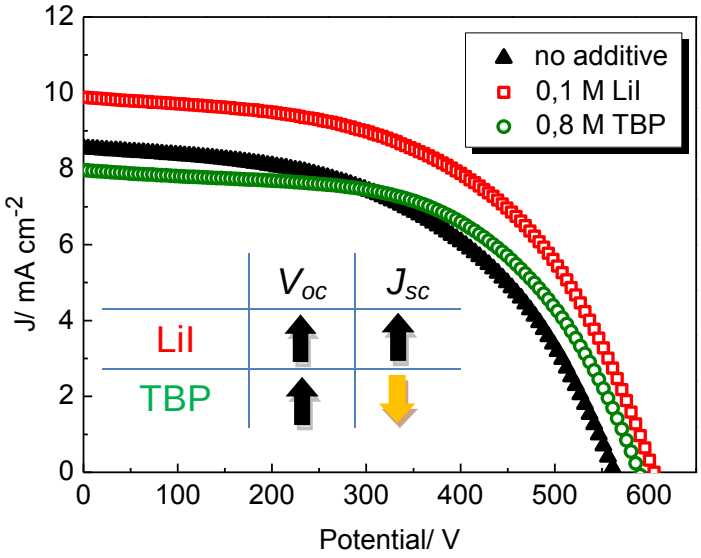

Figure 6.12 Current-voltage curves for ZnO solar cells with optimized electrolyte composition.

To ascertain the origin of the effect of additives on the performance of the cells we have carried out open circuit voltage decay (OCVD) measurements and impedance spectroscopy measurements of cells with the different electrolyte configurations. In **Figure 6.13** the lifetimes obtained from OCVD measurements (**Equation 3.1**) are plotted versus the open circuit voltage[49].

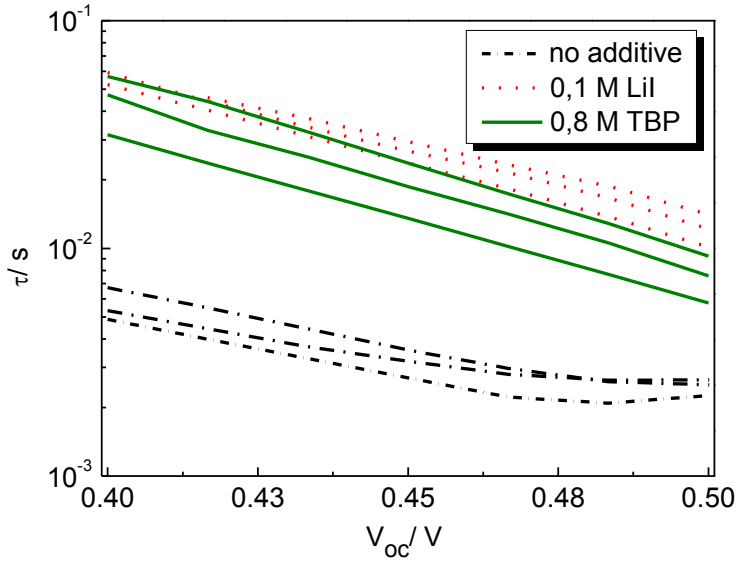

Figure 6.13 Electron lifetimes as obtained from OCVD measurements.

In the OCVD measurements the light intensity is adjusted so that the initial value of the voltage (i.e. the quasi-Fermi level within the semiconductor) is the same for all cases[50]. Furthermore, 3 cells of each cell type have been prepared to determine the reproducibility of the results and they are all plotted in **Figure 6.13**.

The results show that both TBP and Li^+ ions decrease the recombination rate, which explains the enhancement in the open circuit photovoltage. These results are confirmed by the impedance spectra, for which the size of the intermediate-frequency arc is observed to increase in the presence of LiI and TBP with respect to the reference cells (**Figure 6.14**). The effect is more pronounced in the case of TBP.

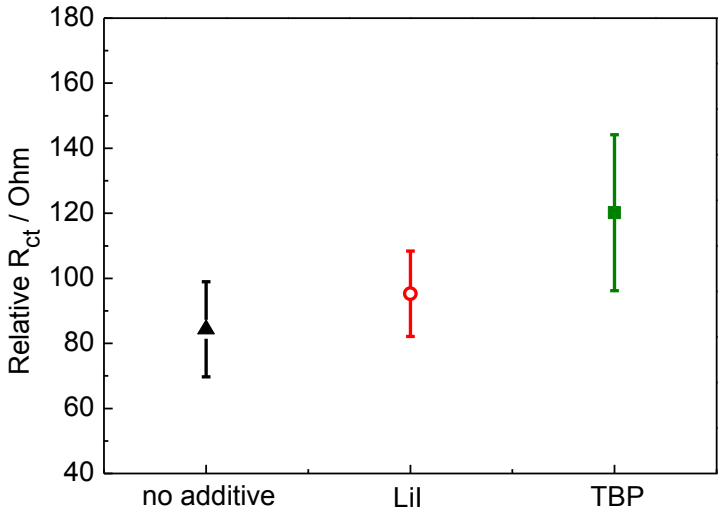

Figure 6.14 Size of the intermediate frequency arc as extracted from EIS measurements in the dark at an applied voltage of 590 mV for different electrolyte compositions.

The improvement of the photovoltage in the presence of TBP is well documented in the literature for cells based on organic electrolytes[50,51] including ZnO-based solar cells[52] and also for TiO_2 cells with ionic-liquid-based electrolytes[23,53]. This improvement is explained by the inhibition of recombination and by the negative shift of the conduction band due to TBP adsorption on the oxide surface. Therefore, the addition of TBP to the electrolyte provokes an effect, which is similar to the one described above for dicyanamide anions (**Section 6.3**). At the same time, TBP usually leads to a decrease of the photocurrent due to a lower driving force for injection associated to the band displacement. As can be seen in **Figure 6.12** and **Table 6.5**, TBP containing cells show lower photocurrent with respect to reference cells. However, this is only a minor effect, which could be the result of the competition between a less favourable driving force and the decrease of the viscosity of the electrolyte by the addition of TBP.

In the case of TiO_2-based dye-sensitized solar cells, Li^+ ions are known to infiltrate the TiO_2 structure and to adsorb at the oxide surface, thus affecting surface charge and lowering the energy of the conduction band edge (positive band shift). This band displacement leads to the enhancement of electron injection and at the same time, to the decrease of the open circuit voltage of the cells[54]. These effects are well documented in the literature[50,55-57]. The positive effect on the photocurrent in the presence of Li^+ (**Figure 6.12** and **Table 6.5**) can be associated to the band displacement described above. However, an improvement of the photovoltage is also observed. Furthermore, Li^+ ions seem to decrease the recombination rate as can be deduced from the OCVD and impedance measurements. The effect of lithium in these systems is not fully understood up to now.

Kawano et al.[23] observed in an ionic-liquid-based electrolyte an improvement of the photovoltage with Li^+ concentration up to 0.1 M, which they attributed to an enhancement of electron injection. Quintana et al.[58] claimed that the effect of Li^+ ions in ZnO-based DSCs appeared to be very different to the one in TiO_2-based cells. They also observed an increment of the photovoltage upon addition of Li^+ although this improvement was accompanied with a better photocurrent only when the lithium concentration was very small. Kamat et al.[59] observed a significant decrease in the recombination rate of accumulated electrons upon Li^+ intercalation in TiO_2 nanotubes due to the blocking of recombination centres. Very recently, Wang et al.[60] compared a

standard organic electrolyte with and without lithium ions added and found that, in fact, the presence of lithium decreases the charge recombination rate, which could yield a higher cell voltage. They claimed, however, that the positive shift of the conduction band upon Li^+ adsorption overcompensated the advantageous influence on charge recombination, resulting in an overall photovoltage decrease. The effect of lithium must be studied in more detail in order to explain its behaviour in solvent free ZnO solar cells, although its positive effect is clear.

6.6. Alternative blends of ionic liquids

To study the influence of the anionic structure of the RTIL on the performance of ZnO-solvent free solar cells, other imidazolium-based ionic liquids have been studied in combination with PMII. The two ionic liquids studied are 1-ethyl-3-methyl-imidazolium tetracyanoborate (EMIBCN) and 1-ethyl-3-methyl-imidazolium bis(trifluoromethylsulfonyl) imide (EMITFSI) (**Figure 6.1**), both with a much lower viscosity than PMII (**Table 6.1**). In **Figure 6.15** the short circuit photocurrent is plotted as a function of the respective mixing ratio of ionic liquids.

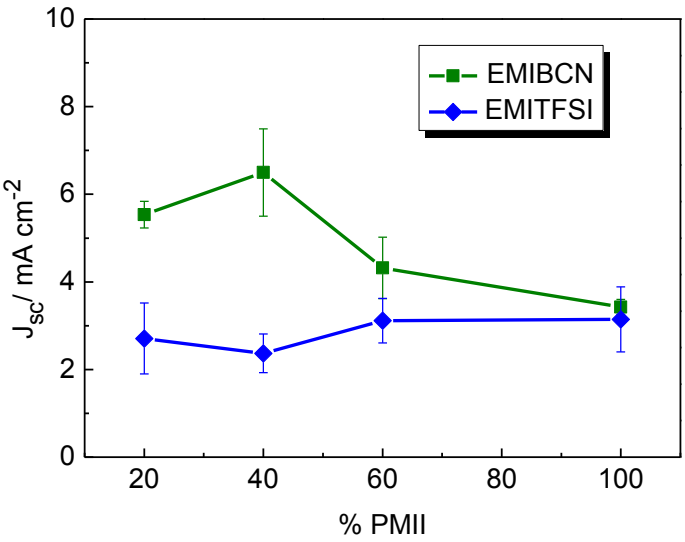

Figure 6.15 Short circuit photocurrent as a function of the mixing ratio of ionic liquids.

No clear trend is observed in the photocurrent profile for EMITFSI based electrolytes. The insignificant variation of the photocurrent could be related to the higher viscosity of EMITFSI as compared to the other solvents used (EMIDCN, EMIBCN)[26] (**Table 6.1**). For the low viscosity ionic liquid based on tetracyanoborate (EMIBCN), a trend similar to EMIDCN is observed. The initial increment with decreasing PMII content can be attributed, like in the case of EMIDCN, to the lowering of viscosity. However, in this

case the strong decrease in the photocurrent at low PMII contents is not observed. This seems to indicate that, in the case of EMITFSI and EMIBCN, dye desorption is not critical. The most interesting result is related to the photovoltage trend shown in **Figure 6.16**.

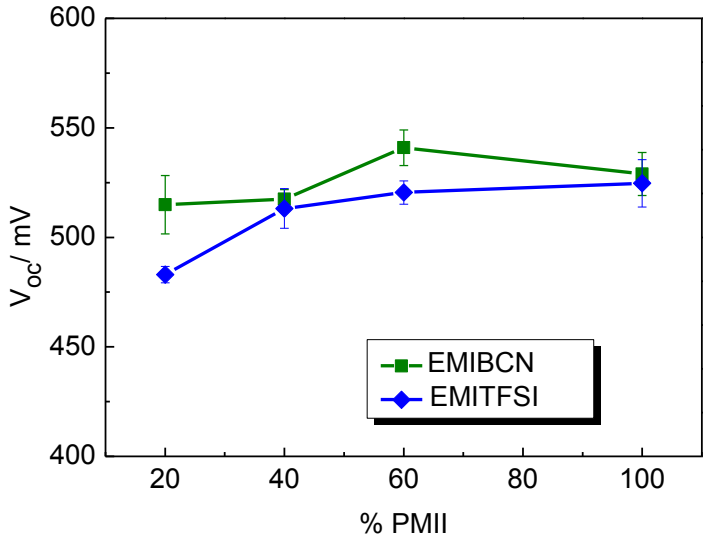

Figure 6.16 Photovoltages as a function of the mixing ratio of ionic liquids.

In contrast to the behaviour observed in the presence of dicyanamide anions, the photovoltage of the cells is not improved when the PMII content is decreased. It seems that these anions do not provoke a displacement of the conduction band edge of ZnO. This indicates that the nature of the interaction between the oxide surface and the anion influences crucially the recombination kinetics. The fact that tetracyanoborate and bis(trifluoromethylsulfonyl)imide anions do not interact significantly with the ZnO surface has a negative effect on the photovoltage with respect to dicyanamide, but at the same time, it improves the stability of the ZnO cells because dye desorption is not observed.

6.7. Conclusions

In this Chapter, the performance of ZnO solvent free solar cells has been analyzed. Binary mixtures of the most frequently used ionic liquid PMII with low viscosity ionic liquids have proved to have a positive effect on the performance of the cells. However, it has been observed that low viscosity is not the exclusive crucial factor to optimize the performance of ZnO solvent free cells. The nature of the non-electroactive anion in these binary mixtures is found to be also important. A specific improvement of the

photovoltage has been observed for dicyanamide anions whereas no such behaviour was observed for tetracyanoborate and bis(trifluoromethylsulfonyl)imide anions. The improvement has been associated to the adsorption of dicyanamide anions on the ZnO surface and to a negative displacement of the conduction band. However, the interaction of dicyanamide with the ZnO surface provokes, on the other hand, dye desorption. As a consequence an optimal dicyanamide content in the electrolyte has to be determined to maximize cell performance. Lower photovoltages are observed with non-interacting anions such as bis(trifluoromethylsulfonyl)imide and tetracyanoborate anions, which do not cause band displacements, and do not induce dye desorption. The weak interaction dye-oxide for ZnO-based solar cells will be discussed in **Chapter 7**.

The behaviour of the photocurrent as a function of light intensity is observed to be quite sensitive to mass transport limitations. These limitations are due to the viscosity of the electrolyte and depend strongly on cell heating. The positive effect of common additives in DSCs such as lithium and TBP is confirmed for this combination of nanocrystalline ZnO and solvent free electrolytes.

6.8. References to Chapter 6

1. O'Regan, B. & Schwartz, D.T. Large enhancement in photocurrent efficiency caused by UV illumination of the dye-sensitized heterojunction TiO_2/RuLL ' NCS/CuSCN: Initiation and potential mechanisms. *Chemistry of Materials* **10**, 1501–1509 (1998).
2. Kumara, G.R.A., Kaneko, S., Okuya, M. & Tennakone, K. Fabrication of Dye-Sensitized Solar Cells Using Triethylamine Hydrothiocyanate as a CuI Crystal Growth Inhibitor. *Langmuir* **18**, 10493-10495 (2002).
3. Howie, W.H., Harris, J.E., Jennings, J.R. & Peter, L.M. Solid-state dye-sensitized solar cells based on spiro-MeOTAD. *Solar Energy Materials and Solar Cells* **91**, 424–426 (2007).
4. Fabregat-Santiago, F., Bisquert, J., Le, C., Peter, C., Wang, M., Zakeeruddin, S. & Grätzel, M. Electron Transport and Recombination in Solid-State Dye Solar Cell with Spiro-OMeTAD as Hole Conductor. *Journal of the American Chemical Society* **131**, 558–562 (2009).
5. Zakeeruddin, S.M. & Grätzel, M. Solvent-Free Ionic Liquid Electrolytes for Mesoscopic Dye-Sensitized Solar Cells. *Advanced Functional Materials* **19**, 2187–2202 (2009).
6. Cao, Y.M., Zhang, J., Bai,Y., Li, R.Z., Zakeeruddin, S.M., Grätzel, M. & Wang, P. Dye-sensitized solar cells with solvent-free ionic liquid electrolytes. *Journal of Physical Chemistry C* **112**, 13775–13781 (2008).
7. Wasserscheid, P. & Welton, T. Ionic liquids in Synthesis. (*Wiley-VCH, Weinheim, Germany*: 2003).
8. Welton, T. Room-Temperature Ionic Liquids. Solvents for Synthesis and Catalysis. *Chemical Reviews* **99**, 2071-2084 (1999).

9. Welton, T. Room-temperature ionic liquids. Solvents for synthesis and catalysis. *Chemical Reviews* **99**, 2071–2083 (1999).
10. Kubo, W., Kambe, S., Nakade, S., Kitamura, T., Hanabusa, K., Wada, Y. & Yanagida, S. Photocurrent-determining processes in quasi-solid-state dye-sensitized solar cells using ionic gel electrolytes. *Journal of Physical Chemistry B* **107**, 4374–4381 (2003).
11. Fabregat-Santiago, F., Bisquert, F., Palomares, E., Oter, L., Kuang, D.B., Zakeeruddin, S.M. & Grätzel, M. Correlation between photovoltaic performance and impedance spectroscopy of dye-sensitized solar cells based on ionic liquids. *Journal of Physical Chemistry C* **111**, 6550–6560 (2007).
12. N. Yamanaka, Kubo, W., Watanabe, M. & Yanagida, S. Dye-sensitized TiO_2 solar cells using imidazolium-type ionic liquid crystal systems as effective electrolytes. *Journal of Physical Chemistry B* **111**, 4763–4769 (2007).
13. Wang, P., Zakeeruddin, S.M., Moser, J., Humphry-Baker, R. & Grätzel, M. A Solvent-Free, $SeCN^-/(SeCN)_3^-$ Based Ionic Liquid Electrolyte for High-Efficiency Dye-Sensitized Nanocrystalline Solar Cells. *Journal of the American Chemical Society* **126**, 7164-7165 (2004).
14. Kuang, D. B., Klein, C., Ito, S. Moser, J.E., Humphry-Baker, R., Evans, N., Duriaux, F., Grätzel, C., Zakeeruddin, S.M. & Grätzel, M. High-efficiency and stable mesoscopic dye-sensitized solar cells based on a high molar extinction coefficient ruthenium sensitizer and nonvolatile electrolyte. *Advanced Materials* **19**, 1133–1137 (2007).
15. Shi, D., Pootrakulchote, N., Li, R.Z., Guo, J., Wang, Y., Zakkeruddin, S.M., Grätzel, M. & Wang, P. New Efficiency Records for Stable Dye-Sensitized Solar Cells with Low-Volatility and Ionic Liquid Electrolytes. *Journal of Physical Chemistry C* **112**, 17046–17050 (2008).
16. *Dye-Sensitized Solar Cells*. (EPFL Press: 2010).
17. Wang, P., Zakeeruddin, S.M., Comte, P., Exnar, I. & Grätzel, M. Gelation of ionic liquid-based electrolytes with silica nanoparticles for quasi-solid-state dye-sensitized solar cells. *Journal of the American Chemical Society* **125**, 1166–1167 (2003).
18. Wang, P., Wenger, B., Humphry-Baker, R., Moser, J.E., Teuscher, J., Kantlehner, W., Mezger, J., Stoyanov, E. V., Zakeeruddin, S.M. & Grätzel, M. Charge separation and efficient light energy conversion in sensitized mesoscopic solar cells based on binary ionic liquids. *Journal of the American Chemical Society* **127**, 6850–6856 (2005).
19. Kuang, D.B., Klein, C., Zhang, Z.P., Ito, S., Moser, J.E., Zakeeruddin, S.M. & Grätzel, M. Stable, high-efficiency ionic-liquid-based mesoscopic dye-sensitized solar cells. *Small* **3**, 2094–2102 (2007).
20. Kuang, D., Wang, P., Ito, S., Zakeeruddin, S.M. & Grätzel, M. Stable Mesoscopic Dye-Sensitized Solar Cells Based on Tetracyanoborate Ionic Liquid Electrolyte. *Journal of the American Chemical Society* **128**, 7732-7733 (2006).
21. Wang, P., Zakeeruddin, S.M., Humphry-Baker, R. & Grätzel, M. A Binary Ionic Liquid Electrolyte to Achieve ≥ 7% Power Conversion Efficiencies in Dye-Sensitized Solar Cells. *Chemistry of Materials* **16**, 2694–2696 (2004).
22. Fredin, K., Gorlov, M., Petterson, H., Hagfeldt, A., Kloo, L. & Boschloo, G. On the influence of anions in binary ionic liquid electrolytes for monolithic dye-sensitized solar cells. *Journal of Physical Chemistry C* **111**, 13261–13266 (2007).
23. Kawano, R. High performance dye-sensitized solar cells using ionic liquids as their electrolytes. *Journal of Photochemistry and Photobiology A-Chemistry* **164**, 87–92

(2004).
24. Yoshida, Y., Baba, O., Larriba, C. & Saito, G. Imidazolium-Based Ionic Liquids Formed with Dicyanamide Anion: Influence of Cationic Structure on Ionic Conductivity. *The Journal of Physical Chemistry B* **111**, 12204-12210 (2007).
25. Hao, F., Lin, H., Liu, Y. & Li, J. Anionic structure-dependent photoelectrochemical responses of dye-sensitized solar cells based on a binary ionic liquid electrolyte. *Physical Chemistry Chemical Physics.* **13**, 6416-6422 (2011).
26. Wachter, P., Schreiner, C., Zistler, M., Gerhard, D., Wassercheid, P. and Gores, H.J. A microelectrode study of triiodide diffusion coefficients in mixtures of room temperature ionic liquids, useful for dye-sensitised solar cells. *Microchimica Acta* **160**, 125–133 (2008).
27. Wachter, P., Zistler, M., Schreiner, C., Berginc, M., Krasovec, U.O., Gerhard, D., Wasserheid, P., Hinsch., A. & Gores, H. Characterisation of DSSC-electrolytes based on 1-ethyl-3-methylimidazolium dicyanamide: Measurement of triiodide diffusion coefficient, viscosity, and photovoltaic performance. *Journal of Photochemistry and Photobiology A: Chemistry* **197**, 25–33 (2008).
28. MacFarlane, D.R., Golding, J., Forsyth, S., Forsyth, M. & Deacon, G.B. Low viscosity ionic liquids based on organic salts of the dicyanamide anion. *Chemistry Communications.* 1430-1431 (2001).
29. Berginc, M., Opara Krasovec, U., Hocevar, M. & Topic, M. Performance of dye-sensitized solar cells based on Ionic liquids: Effect of temperature and iodine concentration. *Thin Solid Films* **516**, 7155-7159 (2008).
30. Papageorgiou, N., Athanassov, Y., Armand, M., Bonhote, P., Petterson, H., Azam, A & Grätzel, M. The Performance and Stability of Ambient Temperature Molten Salts for Solar Cell Applications. *Journal of The Electrochemical Society* **143**, 3099–3108 (1996).
31. Zistler. M., Wachter, P., Wasserscheid, P., Gerhard, D., Hinsch, A., Satrawan, R. & Gores, H.J. Comparison of electrochemical methods for triiodide diffusion coefficient measurements and observation of non-Stokesian diffusion behaviour in binary mixtures of two ionic liquids. *Electrochimica Acta* **52**, 161–169 (2006).
32. Wachter, P., Zistler, M., Schreiner, C., Fleischmann, M., Gerhard, D., Wasserscheid, P., Barthel, J. & Gores, H.J. Temperature Dependence of the Non-Stokesian Charge Transport in Binary Blends of Ionic Liquids. *Journal of Chemical and Engineering Data* **54**, 491–497 (2009).
33. Kawano, R. & Watanabe, M. Anomaly of charge transport of an iodide/tri-iodide redox couple in an ionic liquid and its importance in dye-sensitized solar cells. *Chemistry Communications.* 2107-2109 (2005).
34. Said, F.F., Bazinet, P., Ong, T., Yap, G.P.A. & Richeson, D.S. Hydrogen Bonding Motifs of N,N‘,N‘ ‘-Trisubstituted Guanidinium Cations with Spherical and Rodlike Monoanions: Syntheses and Structures of I^-, I_3^-, and SCN^- Salts. *Crystal Growth & Design* **6**, 258-266 (2006).
35. Kawano, R. & Watanabe, M. Equilibrium potentials and charge transport of an I^-/I_3^- redox couple in an ionic liquid. *Chemistry Communications.* 330-331 (2003).
36. Wang, Q. Characteristics of high efficiency dye-sensitized solar cells. *Journal of Physical Chemistry B* **110**, 25210–25221 (2006).
37. Hao, F., Lin, H., Zhang, J. & Li, J. Balance between the physical diffusion and the exchange reaction on binary ionic liquid electrolyte for dye-sensitized solar cells. *Journal of Power Sources* **196**, 1645-1650 (2011).
38. Zhang, Z., Ito, S., Moser, J., Zakeeruddin, S.M. & Grätzel, M. Influence of Iodide Concentration on the Efficiency and Stability of Dye-Sensitized Solar Cell

Containing Non-Volatile Electrolyte. *ChemPhysChem* **10**, 1834-1838 (2009).
39. Zistler, M., Wachter, P., Schreiner, C. & Gores, H.J. Electrochemical measurement of triiodide diffusion coefficients in blends of ionic liquids: Results for improving a critical parameter of dye-sensitized solar cells. *Journal of Molecular Liquids* **156**, 52–57 (2010).
40. Fabregat-Santiago, F., Zaban, A., Garcia-Canadas, J., Garcia-Belmonte, G., Bisquert, J. Chemical capacitance of nanoporous-nanocrystalline TiO_2 in a room temperature ionic liquid. *Physical Chemistry Chemical Physics* **8**, 1827–1833 (2006).
41. Fabregat-Santiago, F., Bisquert, J., Garcia-Belmonte, G., Boschloo, G. & Hagfeldt, A. Influence of electrolyte in transport and recombination in dye-sensitized solar cells studied by impedance spectroscopy. *Solar Energy Materials and Solar Cells* **87**, 117–131 (2005).
42. González-Pedro, V., Xu, X., Mora-Seró, I. & Bisquert, J. Modeling High-Efficiency Quantum Dot Sensitized Solar Cells. *ACS Nano* **4**, 5783-5790 (2010).
43. Zhou, D., Bai, Y., Zhang, J., Cai, N., Su, M., Wang, Y., Zhang, M. & Wang, P. Anion Effects in Organic Dye-Sensitized Mesoscopic Solar Cells with Ionic Liquid Electrolytes: Tetracyanoborate vs Dicyanamide. *The Journal of Physical Chemistry C* **115**, 816-822 (2011).
44. Zhang, M., Zhang, J., Bai, Y., Wang, Y., Su, M. & Wang, P. Anion-correlated conduction band edge shifts and charge transfer kinetics in dye-sensitized solar cells with ionic liquid electrolytes. *Physical Chemistry Chemical Physics.* **13**, 3788-3794 (2011).
45. Barnes, P.R.F., Anderson, A. Y., Juozapavicius, M., Liu, L., Palomares, E., Forneli, A. & O´Reagan, B. Factors controlling charge recombination under dark and light conditions in dye sensitised solar cells. *Physical Chemistry Chemical Physics*. **13**, 3547-3558 (2011).
46. Cheng, P., Wang, W., Lan, T., Chen, R., Wang, J., Yu, J., Wu, H., Yang, H. Deng, C. & Guo, S. Electrochemical characterization and photovoltaic performance of the binary ionic liquid electrolyte of 1-methyl-3-propylimidazolium iodide and 1-ethyl-3-methylimidazolium tetrafluoroborate for dye-sensitized solar cells. *Journal of Photochemistry and Photobiology A: Chemistry* **212**, 147-152 (2010).
47. Papageorgiou, N., Grätzel, M. & Infelta, P.P. On the relevance of mass transport in thin layer nanocrystalline photoelectrochemical solar cells. *Solar Energy Materials and Solar Cells* **44**, 405-438 (1996).
48. Grätzel, M. The advent of mesoscopic injection solar cells. *Progress in Photovoltaics* **14**, 429–442 (2006).
49. Bisquert, J., Zaban, A., Greenshtein, M. & Mora-Seró, I. Determination of Rate Constants for Charge Transfer and the Distribution of Semiconductor and Electrolyte Electronic Energy Levels in Dye-Sensitized Solar Cells by Open-Circuit Photovoltage Decay Method. *Journal of the American Chemical Society* **126**, 13550-13559 (2004).
50. Peter, L.M. Characterization and Modeling of Dye-Sensitized Solar Cells. *The Journal of Physical Chemistry C* **111**, 6601-6612 (2007).
51. Boschloo, G., Haggman, L. & Hagfeldt, A. Quantification of the effect of 4-tert-butylpyridine addition to I^-/I_3^- redox electrolytes in dye-sensitized nanostructured TiO_2 solar cells. *Journal of Physical Chemistry B* **110**, 13144–13150 (2006).
52. Keis, K., Magnusson, E., Lindstrom, H., Lindquist, S.E. & Hagfeldt, A. A 5% efficient photo electrochemical solar cell based on nanostructured ZnO electrodes. *Solar Energy Materials and Solar Cells* **73**, 51–58 (2002).

53. Wang, P., Zakeeruddin, S.M., Moser, J. & Grätzel, M. A New Ionic Liquid Electrolyte Enhances the Conversion Efficiency of Dye-Sensitized Solar Cells. *The Journal of Physical Chemistry B* **107**, 13280-13285 (2003).
54. Nakade, S., Kanzai, T., Kubo, W., Kitamura, T., Wada, Y. & Yanagida, S. Role of electrolytes on charge recombination in dye-sensitized TiO_2 solar cell (1): The case of solar cells using the I^-/I_3^- redox couple. *Journal of Physical Chemistry B* **109**, 3480–3487 (2005).
55. Haque, S.A., Tachibana, Y., Willis, R.L., Moser, J.E., Grätzel, M., Klug, D.R. & Durrant, J.R. Parameters influencing charge recombination kinetics in dye-sensitized nanocrystalline titanium dioxide films. *Journal of Physical Chemistry B* **104**, 538–547 (2000).
56. Wang, Y., Sun, Y., Song, B. & Xi, J. Ionic liquid electrolytes based on 1-vinyl-3-alkylimidazolium iodides for dye-sensitized solar cells. *Solar Energy Materials and Solar Cells* **92**, 660–666 (2008).
57. Hoshikawa, T., Ikebe, T., Kikuchi, R. & Eguchi, K. Effects of electrolyte in dye-sensitized solar cells and evaluation by impedance spectroscopy. *Electrochimica Acta* **51**, 5286–5294 (2006).
58. Quintana, M., Marinado, T., Nonomura, K., Boschloo, G. & Hagfeldt, A. Organic chromophore-sensitized ZnO solar cells: Electrolyte-dependent dye desorption and band-edge shifts. *Journal of Photochemistry and Photobiology A: Chemistry* **202**, 159-163 (2009).
59. Meekins, B.H. & Kamat, P.V. Got TiO_2 Nanotubes? Lithium Ion Intercalation Can Boost Their Photoelectrochemical Performance. *ACS Nano* **3**, 3437-3446 (2009).
60. Quingjiang, Y., Wang, Y., Zu, N,, Zhang, J., Zhang, M. & Wang, P. High-Efficiency Dye-Sensitized Solar Cells: The Influence of Lithium Ions on Exciton Dissociation, Charge Recombination, and Surface States. *ACS Nano* **4**, 6032-6038 (2010).

Chapter 7

ZnO-based Dye-Sensitized Solar Cells with Pure Ionic Liquid Electrolyte and Organic Sensitizer

7. ZnO-based dye-sensitized solar cells with pure ionic-liquid electrolyte and organic sensitizer

In this Chapter a study of the performance of ZnO-based DSCs sensitized with an organic dye in the presence of a pure ionic-liquid electrolyte is presented. Following the previous studies about organic sensitizers as alternatives to ruthenium-complex dyes and solvent-free electrolytes, the aim of this work was to connect the knowledge obtained in the two previous Chapters.

The use of non-volatile electrolytes in combination with fully organic dyes is a key issue in the development of stable dye-sensitized solar cells (DSCs). The combination of a solvent-free electrolyte with highly absorptive sensitizers is interesting since the poor transport properties and high recombination losses in RTIL-based devices[1,2] produce short electron diffusion lengths and require very thin devices. The lower surface area can be compensated by using a highly absorbing organic dye. As shown in **Chapter 5**, organic dyes, as e.g. xanthene derivatives, have been successfully used since the beginning of DSC development. In the last years, new types of highly absorbing, fully organic dyes have been explored with very promising results for TiO_2 and they are now approaching record efficiencies typical of ruthenium dyes[3].

Among the wide new varieties of organic dyes tested, some of the most efficient ones are those based on indoline derivatives[4]. These dyes have absorption coefficients several times higher than the common N719 dye at the maximum of the solar spectrum[5,6]. Besides, the colour of the indoline dyes is tunable by changing their orbital system[7]. These stimulating features encourage research on these dyes. An impressive 9.5% efficiency has been obtained with an indoline dye and an organic electrolyte[8], which is one of the best efficiencies reported for DSCs with an organic dye. The efficiencies are also remarkable for solvent free solar cells sensitized with this type of dyes, reaching more than 7%[9i].

As discussed in **Chapter 5**, conversion efficiency in ZnO-based DSCs is generally limited due to the reaction of acidic dyes with the oxide surface. Indoline derivatives are known to be less acidic[10] than ruthenium complexes and therefore they are not expected

[i] Cell active area: 0.158 cm^2

to react with the ZnO surface and to produce undesirable species that reduce the performance of the devices. Only recently, these dyes have been used as sensitizers for ZnO solar cells[5,6,11-14]. The group of Yoshida has reported efficiencies of ZnO-based solar cells above 5%[15].

Due to the especially good performances reported for ZnO with indoline dyes and considering that the xanthene derivatives explored in **Chapter 5** were totally unstable in the presence of ionic liquids, this study has been focused on the performance of an indoline derivative coded D149. The D149 dye has an absorption coefficient five times higher than the common N719 at the maximum of the solar spectrum. Cheng and Hsieh[14] have obtained 4.95% of efficiency for ZnO solar cells sensitized with this dye. The purpose of this study is to analyse the main features of the ZnO/indoline dye/ionic-liquid electrolyte combination. The electrolytes are based on a combination of imidazolium salts studied in **Chapter 6**. Ionic liquids with dicyanamide anions are found to strongly desorb D149 molecules from the surface of ZnO. Therefore, the study is based on the combination of PMII with the other two low viscosity ionic liquids tested in **Chapter 6**: 1-ethyl-3-methyl-imidazolium tetracyanoborate (EMIBCN) and 1-ethyl-3-methyl-imidazolium bis(trifluoromethylsulfonyl) imide (EMITFSI) (**Figure 6.1**). The viscosity of the blends is expected to be much lower than the one of the pure ionic liquid electrolyte (**Table 6.1**). Stability will be a key issue in this context, since it may hinder the applicability of organic dyes in ZnO DSCs in combination with an ionic liquid. For this reason, the main objective of this study is to analyse carefully the chemical interactions between dye, oxide and electrolyte, as well as to highlight the drawbacks of this cell configuration.

7.1. Fabrication and characterization of the devices

The materials used for the fabrication of the cells are summarized in **Table 7.1** and the parameters of the illumination source used for photovoltaic characterization in **Table 7.2**.

Table 7.1 Summary of the materials employed in the fabrication of the cells.

ZnO	Dyes	Electrolytes	Counter electrode
Degussa VP AdNano®ZnO20 / PI-KEM 1:1 Cell area 0.64 cm^2	D149 0.5 mM/ chenodeoxycholic acid 0.7 mM tert-butyl alcohol-acetonitrile (1:1) 30 minutes	• **(A)** PMII • **(B)** PMII/EMIBCN (2:3 volume fraction) • **(C)** PMII/EMIBCN/ EMITFSI (2:1:1 volume fraction) + 0.05 M I_2	Hexachloroplatinic acid (0.01 M in isopropanol)

Table 7.2 Illumination set-up used for DSC testing.

Illumination source	Filters	Calibration
Solar Simulator ABET	AM 1.5 filter	Reference solar cell (Oriel, 91150) 100 mW cm^{-2}
Xenon 450W arc lamp	• Water filter • 325 nm UV • KG-5 IR filter	

The two electrodes were clamped together to form a sandwich-type open cell[40]. A Bruker IFS 66/S FTIR spectrometer was used to obtain IR spectra of the neat dye and the sensitized oxide particles in KBr. For this purpose 0.14 mg of dye were mixed with KBr and pressed into pellets. In order to measure the IR spectra of the adsorbed dye, part of the oxide film was detached mechanically from the conducting glass substrate after the sensitization step. 5 mg of the sensitized ZnO powder was then mixed with KBr and pressed. Spectra were obtained by averaging 100 scans at a resolution of 2.5 cm^{-1}.

Photocurrents, photovoltages, current-voltage curves and impedance spectra were measured using an Autolab/PGSTAT302N station (Ecochemie) coupled with a FRA2 frequency generator module. The EIS spectra were fitted to the equivalent circuit (b)

(**Figure 3.10**). The absorption spectrum of the dye adsorbed on the oxide film was measured using an integrating sphere coupled to a UV-vis detector (Ocean Optics). The amount of dye adsorbed on the semiconductor film was evaluated from the absorbance of the solution after dye desorption in alkaline solution (1 mM KOH in ethanol/Mili-Q water (50:50) solution).

7.2. Sensitization of ZnO films with the indoline dye D149

In **Figure 7.1**, the UV-vis absorption spectrum of the D149 dye is shown in solution and adsorbed onto the ZnO film. The dye exhibits strong absorption around 530 nm, close to the maximum irradiance of the solar spectrum[16] and it shows a broader absorption than the xanthene dyes studied in **Chapter 5**. Its chemical structure is also shown in the figure.

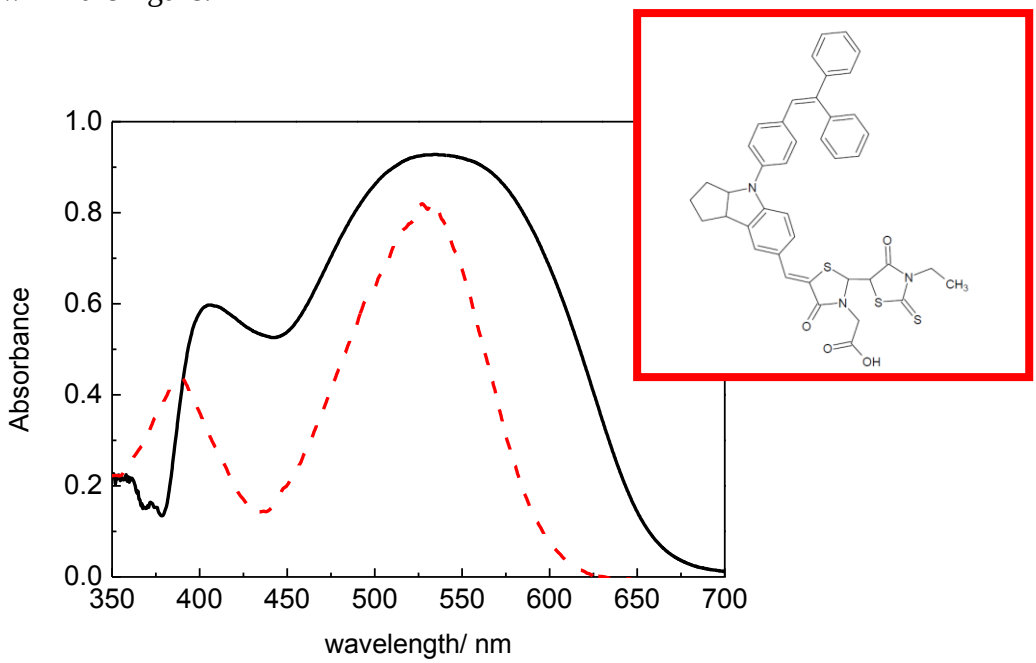

Figure 7.1 Red dashed line: UV-vis absorption spectrum of D149 in solution (5.16 10^{-3} mM in tert-butanol/acetonitrile). Black thick line: D149 adsorbed on ZnO. The inset shows the molecular structure of D149.

The absorbance (A) of the dye adsorbed to the ZnO surface was measured by means of an integrating sphere and by analogy with the usual definition of the transmission absorbance, it is defined as $A = log(R_0/R)$, where R and R_0 are the reflectance of the sample and the reference, respectively. As observed for xanthene dyes and as reported also for indoline dyes[4], the spectrum gets broadened with respect to the free dye in solution. A red shift of the absorption maximum is often found for indoline dyes

adsorbed on TiO_2, which is usually associated to the formation of aggregates of the dye[4,6,16,17]. However, there is no significant shift of the absorption maximum upon adsorption of D149 on ZnO and dye aggregation is, therefore, assumed to have only a minor effect in this case. This result is somehow expected since chenodeoxycholic acid is added to the sensitizing solution. This additive is known to prevent dye aggregation[8].

In **Figure 7.2** the FT-IR spectra of the pure D149 dye is compared with that of dye-sensitized ZnO powder.

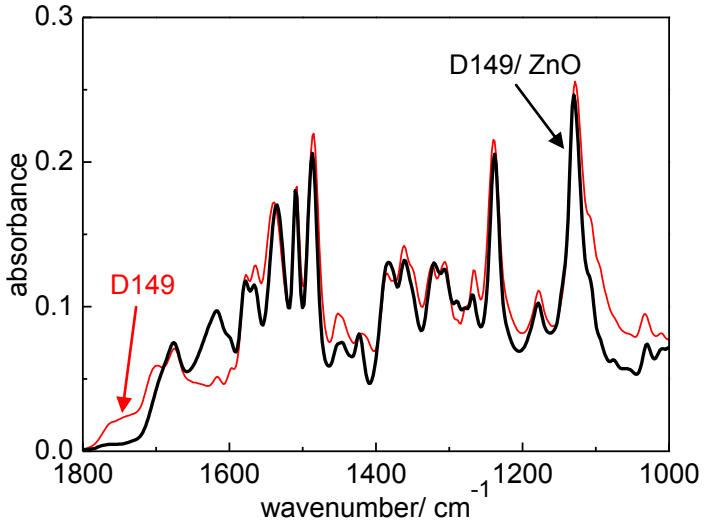

Figure 7.2 FT-IR spectra of pure D149 dye and D149 adsorbed onto ZnO.

Upon dye adsorption two peaks at 1700 and 1750 cm^{-1} (attributed to carbonyl groups) disappear and a new peak at 1600 cm^{-1} (corresponding to the COO asymmetric stretching) is observed. This observation is compatible to bidentate adsorption of the dye to the ZnO surface via the carboxylate group[10,18,19].

The adsorption process of the D149 dye on ZnO is analyzed in **Figure 7.3**, where the short circuit photocurrent for electrolyte composition A (pure PMII, **Table 7.1**) under white light illumination is plotted versus the immersion time of the ZnO film in the dye solution. D149 behaviour is similar to the results obtained for Eosin adsorption onto ZnO (**Section 5.3**). In contrast to ruthenium-based dyes, no deterioration of the current at long immersion times is observed. This indicates that there are no undesirable chemical reactions[20] between the dye and the oxide in this case.

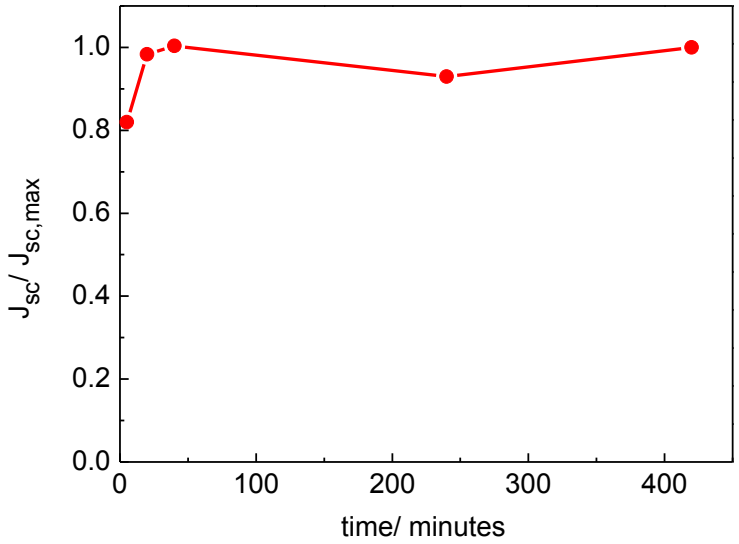

Figure 7.3 Short circuit photocurrent as a function of immersion time for ZnO cells sensitized with D149 and electrolyte composition A under white light illumination (Xenon lamp with UV and IR filters).

Based on the results shown in the plot, a sensitizing time of 30 minutes was utilized for the cell fabrication.

7.3. Photovoltaic performance

Photovoltaic parameters of the devices can be found in **Table 7.3.** The good absorption properties of the dye together with the large surface area of the semiconductor films lead to short circuit photocurrents between 7 and 10 mA cm^{-2} under simulated solar light conditions (AM 1.5G, 1 sun), with best results obtained for the less viscous compositions B and C (**Table 7.3**).

Table 7.3. Photovoltaic parameters of solvent-free ZnO-based DSCs under AM 1.5 illumination (100 mW cm^{-2}). Mean values and deviations are derived from independent measurements of several devices for each electrolyte composition.

Electrolyte	J_{SC} (mA cm^{-2})	V_{OC} (mV)	FF	η (%)
A	7.7 ± 0.5	489 ± 14	0.52 ± 0.04	2.0 ± 0.1
B	9.1 ± 0.9	505 ± 13	0.55 ± 0.05	2.5 ± 0.4
C	8.8 ± 1.4	507 ± 16	0.56 ± 0.04	2.5 ± 0.3

Reproducibility of around ±1 mA cm^{-2} is achieved in all cases. In spite of the good performance at short circuit the cells show low open circuit photovoltages of around 480-520 mV. In addition, although an improvement of the fill factors with the decrease

of viscosity is observed[21], they hardly exceed 0.55. The low open circuit voltages and low fill factors limit the photoconversion efficiency to 2-3% (2.9% for the best cell). The fact that similar performances are obtained for the binary (B) and ternary (C) ionic liquid blends indicates that the main factor that causes improved performance with respect to pure PMII is the decrease of the viscosity and not the anion structure of the ionic liquids. In **Figure 7.4** current-voltage curves of the solar cells with best performances are presented.

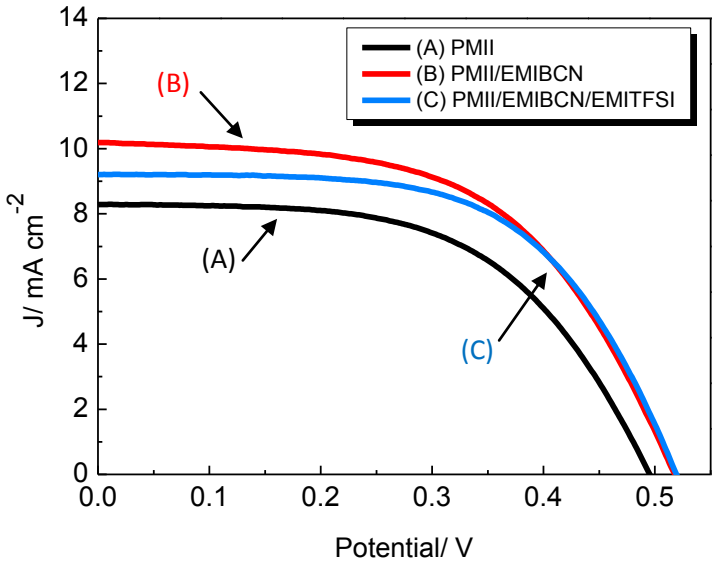

Figure 7.4 Best results for the current–voltage curve of solvent-free ZnO solar cells sensitized with D149 under simulated solar light (AM 1.5G) at 1 sun (100 mW cm^{-2}), for the three electrolyte compositions considered in this work.

Based on the analysis of solvent free solar cells carried out in **Chapter 6**, the origin of the low photovoltage observed for cells in **Figure 7.4** can be related to several factors. The high iodide concentration makes the redox potential of the iodide/triiodide couple more positive with respect to organic-based electrolytes, which typically contain much lower iodide concentrations[22]. The high viscosity may cause slower regeneration of the dye[23] and stronger recombination[1,21,22]. Finally, the low photovoltage is related to the absence of species that produce negative band displacements of the semiconductor oxide[24]. The mean value of the photovoltage is slightly improved for electrolytes B and C, and this is likely due to a positive displacement of the redox potential of the iodide/triiodide redox couple when the concentration of iodide is reduced. According to the Nernst equation (**Equation 2.16**) the shift expected from reducing the concentration of iodide would be in the range of 10 mV for a two-electron redox reaction at room

temperature. This calculated shift is quite close to the displacements actually observed for the photovoltage in the three electrolytes.

On the other hand, there is a clear correlation between the viscosity of the electrolyte and the photocurrent. The impedance spectroscopy study described in the following section will cast light on the origin of the different performance for cells with electrolytes A, B and C.

7.4. Electrochemical impedance spectroscopy studies

Electrochemical impedance measurements were carried out in the dark at various applied voltages. In **Figure 7.5** impedance spectra for cells with electrolyte A at different applied voltages are shown. The spectra show the characteristic shape of DSCs based on ionic liquid electrolytes described in **Chapter 6**.

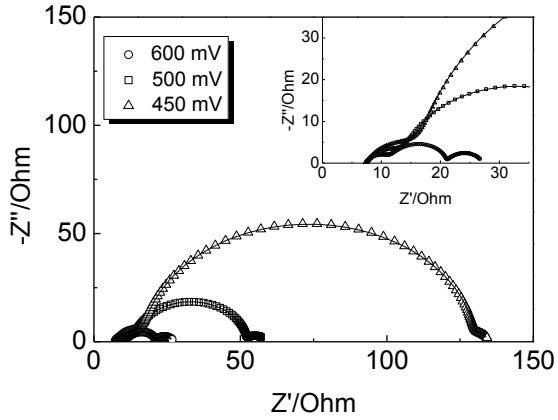

Figure 7.5 Impedance spectra of a ZnO dye solar cell sensitized with D149 and PMII electrolyte at different applied potentials in the dark. The dots represent the measured data points and the straight lines are the fitting results based on the equivalent circuit (transmission-line) model described in **Chapter 3.**

Results for the charge-transfer resistance R_{ct}, the chemical capacitance C_{μ} and the lifetime τ as a function of the applied bias are presented in **Figure 7.6.**

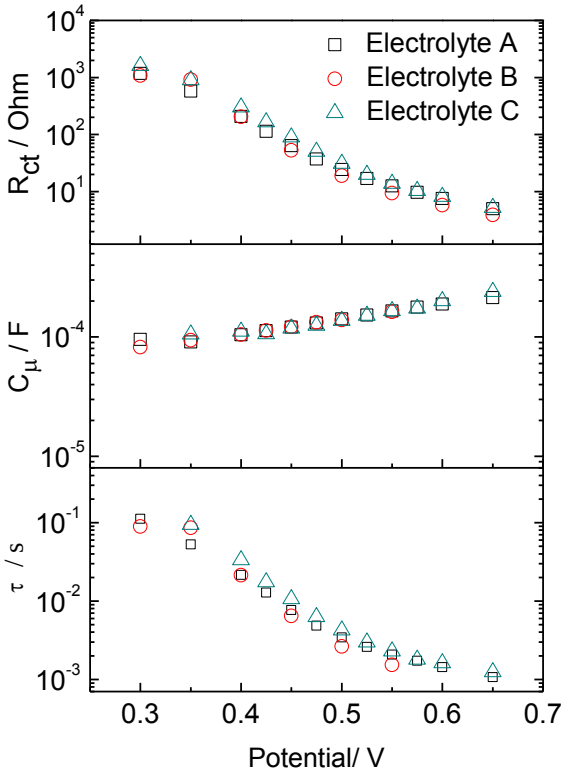

Figure 7.6 Results from impedance measurements in the dark: charge transfer resistance (R_{ct}), chemical capacitance (C_μ) and lifetime (τ) for D149-sensitized ZnO solar cells as a function of applied voltage.

The charge transfer resistance exhibits approximate exponential behaviour within the studied range of potentials, with a slight change of slope in the log-lin-representation as the potential is increased. This, as mentioned in **Chapter 6**, can be related to a potential drop through the films. This drop is due to series resistance of the cell that becomes of the same order of magnitude as the charge transfer resistance. Correction for the potential drop produced by the series resistance of the cell permits to refer the measured magnitudes to the real voltages applied to the film. However, in this case, in the vicinity of the open circuit potential of the cell (0.5V) the charge-transfer resistance maintains the exponential behaviour. This is probably due to the low current running through the devices, which makes the voltage drop due to series resistance very small. Similar recombination behaviour is found for the three electrolytes. Fitting the experimental data to **Equation 2.10** ($R_{ct} = R_{ct,0}\, exp(-\beta qV/kT)$) yields values for the transfer parameter close to $\beta = 0.5$ for the three studied electrolyte compositions. The chemical capacitance C_μ shows also exponential behaviour except at low voltages. Here again, there is a change in the slope. Fitting of the experimental data to **Equation 2.41** ($C_\mu = C_0\, exp(\alpha V/kT)$) yields values close to $\alpha \sim 0.1$ for the three electrolytes. The meaning and implications of these β and α parameters will be discussed in detail in **Chapter 9**, where

a study of the electronic and the recombination properties of ZnO-based solar cells with different configurations, including RTIL electrolytes is presented.

The product of the charge transfer resistance and the chemical capacitance yields the electron lifetime at each applied voltage (**Equation 3.11** $\tau_n = R_{ct} C_\mu$). These results are also shown in **Figure 7.6**. As expected from the similar capacitance and charge transfer resistance, all the samples have approximately the same lifetime at the different applied voltages. The value of the lifetime at an applied voltage of 0.55 V is ~ 0.002 seconds, which is shorter than lifetimes obtained for ZnO sensitized with D149 and organic solvent electrolyte[14]. According to the results presented in **Chapter 6**, at the same applied potential the lifetime for a ZnO solar cell sensitized with N719 and with a pure PMII electrolyte is 0.0075 seconds. This difference could be related to the dye, which is believed to have a crucial effect on the performance of cells with ionic liquid electrolytes[25-28].

The much higher viscosity of the pure PMII electrolyte does not lead to a higher recombination. In addition, the recombination behaviour is basically the same for the three electrolytes studied. This indicates that there are no specific interactions between the constituent ions of the three electrolytes and the oxide and that the electrolyte composition does not affect the recombination rate. These results explain the different behaviour found in **Section 6.6** for the sulfonyl- and tetracyanoborate-based ionic liquids (EMITFSI and EMIBCN) with respect to the dicyanamide-based one (EMIDCN). The fact that the different electrolyte compositions do not modify the recombination rate explains why the open-circuit photovoltage varies only by a few millivolts (due to the small redox potential shift, as discussed above).

The diffusion resistance for the transport of triiodide in the electrolyte can be extracted from the impedance measurements[1]. The third semicircle accounting for the transport in the electrolytes is observed in all the samples in the range of studied voltages (results not shown). In **Figure 7.7** results for diffusion resistance (R_D, extracted from the Warburg diffusion impedance Z_d described in **Chapter 3**) for electrolytes A and C are presented.

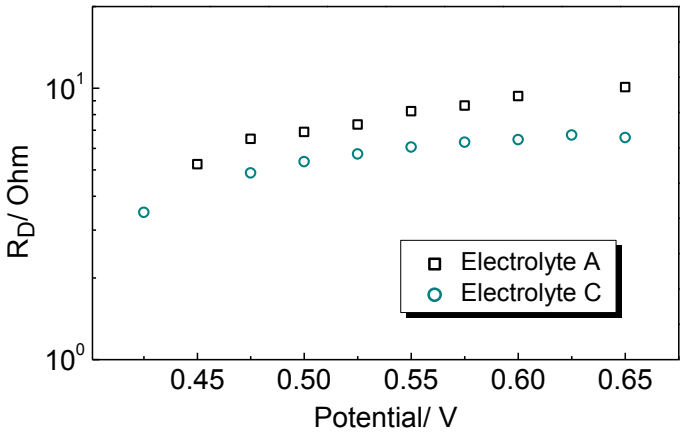

Figure 7.7 Diffusion resistance (R_D) as a function of applied voltage for the D149-sensitized ZnO solar cells with different electrolyte compositions studied in this work.

The diffusion resistance increases with the applied voltage and as expected, it is larger for pure PMII (electrolyte A).

7.5. Stability Test

As mentioned in previous Chapters, DSCs with ionic-liquid-based electrolytes are interesting because they do not present evaporation losses and, as a consequence, they are considered good candidates for fabricating stable devices. The long term stability of the devices studied in this Chapter, was, therefore, tested. The results for a device with electrolyte composition A (pure PMII) without any sealing are presented in **Figure 7.8**.

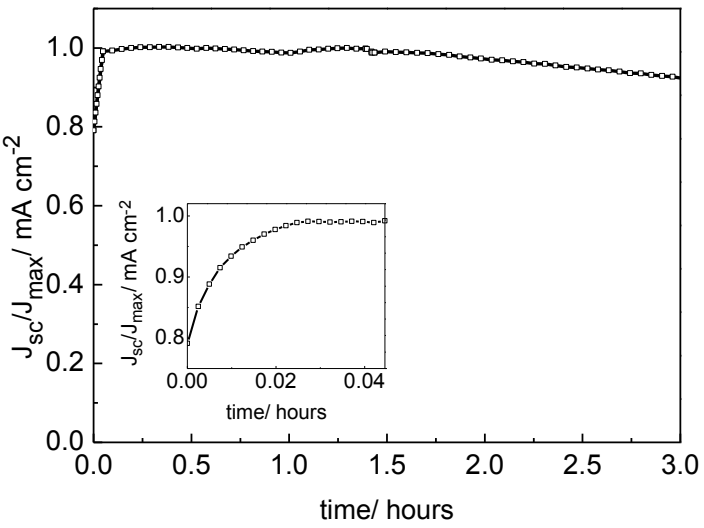

Figure 7.8 Photocurrent evolution of a D149-sensitized ZnO solar cell with electrolyte composition A and without sealing under continuous light soaking using a Xenon lamp with UV and IR filters. The inset shows the behaviour at short times.

The cell was illuminated with a Xenon lamp coupled to UV and IR filters. It must be pointed out that this illumination set-up presents a higher intensity, with respect to AM 1.5, in the spectral zone where the dye absorbs and it is used here to test the cell at more extreme conditions. At short times the photocurrent increases steadily due to the heating of the device, which reduces the viscosity of the electrolyte[1]. However, after this initial stage, the short circuit photocurrent diminishes in a 6% in three hours of exposition to white light. Stability tests with the solar simulator (AM 1.5, 100 mW cm^{-2}) exhibit a much slower degradation.

As mentioned in the Introduction, one of the mayor aims of this work is the study of the interaction between the dye and the ionic liquid electrolyte. In this context, the instability observed in **Figure 7.8** could be a consequence of dye desorption in the presence of electrolyte, as observed already for other ZnO systems (**Chapter 6**). To elucidate the origin of the photocurrent decay, the interaction dye-electrolyte has been analyzed. A D149-sensitized film was left in contact with 50 µl of pure PMII (without I_2) for 12 hours. The ionic liquid was then diluted in tert-butanol/acetonitrile and an UV/vis spectrum of the solution was recorded. On the other hand, the spectrum of pure PMII diluted in the same proportion using the same solvents was also recorded. Both spectra are shown in **Figure 7.9**.

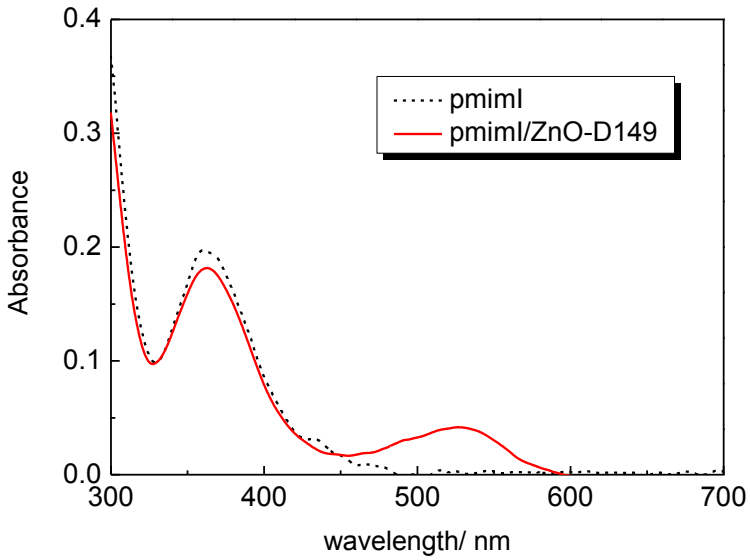

Figure 7.9 UV-Vis absorption spectra of PMII in tert-butanol/acetonitrile (1:1) (dashed black line) and PMII diluted in tert-butanol/acetonitrile (1:1) after contact in the dark with a D149-sensitized ZnO film (thin red line).

The presence of the characteristic D149 absorption peak at 530 nm in the PMII sample that had been brought in contact with the sensitized film reveals that small amounts of dye get detached from the ZnO surface in the presence of PMII. Dye desorption was studied only in the dark, however, it is expected to be stronger under illumination[29]. Therefore, the deterioration of the photocurrent observed in **Figure 7.8** is attributed to dye desorption. Cell degradation due to dye desorption has been reported before for indoline dyes[7]. Kubo et al.[30] observed desorption of the dye from the surface of TiO_2 during stability tests with ionic liquid electrolytes. In addition, it has been reported that a high iodide concentration is detrimental to stability. In line with this, Zhang et al.[31] found poor stability with electrolytes containing a high PMII concentration. Bahers et al.[32] also reported on dye desorption for D149-sensitized ZnO cells.

7.6. Conclusions

In this Chapter, the performance of ZnO solvent free solar cells sensitized with the organic dye D149 has been analyzed. The good absorption properties of the dye, together with the large surface area of the mixture of commercial powders used, leads to short-circuit photocurrents between 7 and 10 mA cm^{-2} under AM 1.5G (1 sun) conditions, with best results obtained for the less viscous ionic-liquid compositions. The maximum energy conversion efficiency achieved was 2.9% at 1 sun.

The devices yield open circuit photovoltages of 480-520 mV, which is much lower than best-performing cells based on organic solvent electrolytes. Impedance data show that they have a high recombination rate, similar to other devices based on pure ionic liquid electrolytes[1], and much larger than those characteristic of organic solvent electrolytes. The addition of an ionic liquid of lower viscosity is found to improve the photocurrent of the cells, but it does not have a major effect on the photovoltage. In fact, the recombination rate is similar for the three electrolytes studied. At this point, it is worth comparing these new results with the ones previously reported in **Chapter 6**. In that case, N719 was used in combination with the low viscosity ionic-liquid 1-ethyl-3-methylimidazolium dicyanamide. This ionic liquid was found to reduce the recombination rate due to a band displacement, which has been attributed to the adsorption of dicyanamide anions to the ZnO surface. When the same ionic liquid is employed in combination with the D149 sensitizer, complete desorption of the dye is observed. The same is true when using the common additive tert-butylpyridine (TBP).

This indicates that species that tend to attach strongly to the oxide surface and that are helpful to reduce recombination and, thus, to improve performance, may have detrimental effects when the dye-oxide interaction is weak. PMII, the imidazolium salt most frequently used in solvent free TiO_2 cells, is found to induce desorption of the indoline dye from the ZnO surface, hence limiting the long-term stability. Exploration of alternative ionic-liquid electrolyte compositions or modification of the ZnO surface is, therefore, required for fabricating stable devices based on ZnO films sensitized with this organic dye.

7.7. References to Chapter 7

1. Fabregat-Santiago, F., Bisquert, F., Palomares, E., Oter, L., Kuang, D.B., Zakeeruddin, S.M. & Grätzel, M. Correlation between photovoltaic performance and impedance spectroscopy of dye-sensitized solar cells based on ionic liquids. *Journal of Physical Chemistry C* **111**, 6550–6560 (2007).
2. Shi, D., Cao, Y., Pootrakulchote, N., Yi., Z., Xu, M., Zakeeruddin, S., Grätzel, M & Peng, W. New Organic Sensitizer for Stable Dye-Sensitized Solar Cells with Solvent-Free Ionic Liquid Electrolytes. *Journal of Physical Chemistry C* **112**, 17478–17485 (2008).
3. Zeng, W.D., Cao, Y.M., Bai, Y., Wang, Y.H., Shi, Y.S., Zhang, M. Wang, F.F., Pan, C.Y. & Wang, P. Efficient Dye-Sensitized Solar Cells with an Organic Photosensitizer Featuring Orderly Conjugated Ethylenedioxythiophene and Dithienosilole Blocks. *Chemistry of Materials* **22**, 1915–1925 (2010).
4. Horiuchi, T., Miura, H., Sumioka, K. & Uchida, S. High Efficiency of Dye-Sensitized Solar Cells Based on Metal-Free Indoline Dyes. *Journal of the American Chemical Society* **126**, 12218–12219 (2004).
5. Chiu, W.H., Lee, C.H., Cheng, H.M., Lin, H.F., Liao, S.C., Wu, J.M. & Hsieh, W.F. et al. Efficient electron transport in tetrapod-like ZnO metal-free dye-sensitized solar cells. *Energy & Environmental Science* **2**, 694–698 (2009).
6. Jose, R., Kumar, A., Thavasi, V. & Ramakrishna, S. Conversion efficiency versus sensitizer for electrospun TiO_2 nanorod electrodes in dye-sensitized solar cells. *Nanotechnology* **19**, (2008).
7. Tanaka, H., Takeichi, A., Higuchi, K., Motohiro, T., Takata, M., Hirota, N., Nkajima, J. & Toyoda, T. Long-term durability and degradation mechanism of dye-sensitized solar cells sensitized with indoline dyes. *Solar Energy Materials and Solar Cells* **93**, 1143–1148 (2009).
8. Ito, S., Miura, H., Uchida, S., Takata, M., Sumiota, K., Liska, P., Comte, P., Pechy, P. & Grätzel, M. High-conversion-efficiency organic dye-sensitized solar cells with a novel indoline dye. *Chemical Communications* 5194–5196 (2008).
9. Kuang, D., Uchida, S., Humphry-Baker, R., Zakeeruddin, S. & Grätzel, M. Organic Dye-Sensitized Ionic Liquid Based Solar Cells: Remarkable Enhancement in Performance through Molecular Design of Indoline Sensitizers. *Angewandte Chemie International Edition* **47**, 1923-1927 (2008).
10. Chen, G., Zheng, K., Mo, X., Sun, D., Meng, Q. & Chen, G. Metal-free indoline dye sensitized zinc oxide nanowires solar cell. *Materials Letters* **64**, 1336–1339

(2010).
11. Plank, N., Howard, I., Rao, A., Wilsin, M., Ducati, C., Mane, R. S., Louca, R.R.M., Bendall, J., Greenham, N.C., Miura, H., Friend, R.H., Snaith, H.J. &Welland, M.E. Efficient ZnO Nanowire Solid-State Dye-Sensitized Solar Cells Using Organic Dyes and Core−shell Nanostructures. *The Journal of Physical Chemistry C* **113**, 18515–18522 (2009).
12. Hosono, E., Mitsui, Y. & Zhou, H. Metal-free organic dye sensitized solar cell based on perpendicular zinc oxide nanosheet thick films with high conversion efficiency. *Dalton Transactions* 5439–5441 (2008).
13. Wu, J., Chen, G., Yang, H., Ku, C. & Lai, J. Effects of dye adsorption on the electron transport properties in ZnO-nanowire dye-sensitized solar cells. *Applied Physics Letters* **90**, 213109 (2007).
14. Cheng, H. & Hsieh, W. High-efficiency metal-free organic-dye-sensitized solar cells with hierarchical ZnO photoelectrode. *Energy & Environmental Science* **3**, 442 (2010).
15. Yoshida, T., Zhang, J.B., Komatsu, D., Sawatani, S., Minoura, H., Pauporte, T., Lincot, D., Oekermann, T., Schlettwein, D., Tada, H., Wohrle, D., Funabiki, K., Matsui, M., Miura, H., & Yanagi, H. Electrodeposition of Inorganic/Organic Hybrid Thin Films. *Advanced Functional Materials* **19**, 17–43 (2009).
16. Horiuchi, T., Miura, H. & Uchida, S. Highly-efficient metal-free organic dyes for dye-sensitized solar cells. *Chemical Communications* 3036-3037 (2003).
17. Horiuchi, T., Miura, H. & Uchida, S. Highly efficient metal-free organic dyes for dye-sensitized solar cells. *Journal of Photochemistry and Photobiology A: Chemistry* **164**, 29-32 (2004).
18. Dentani, T., Yasuhiro, K., Funabiki, K., Jin, J., Yoshida, T., Minoura, H., Miura, H. & Matsui, M. Novel thiophene-conjugated indoline dyes for zinc oxide solar cells. *New Journal of Chemistry* **33**, 93–101 (2009).
19. Qin, P., Yand, X., Chen, R., Sun, L., Marinado, T., Edvinsson, T., Boschloo, G. & Hagfeldt, A. Influence of π-Conjugation Units in Organic Dyes for Dye-Sensitized Solar Cells. *The Journal of Physical Chemistry C* **111**, 1853–1860 (2007).
20. Chou, T.P., Zhang, Q.F. & Cao, G.Z. Effects of dye loading conditions on the energy conversion efficiency of ZnO and TiO_2 dye-sensitized solar cells. *Journal of Physical Chemistry C* **111**, 18804–18811 (2007).
21. Hao, F., Lin, H., Liu, Y. & Li, J. Anionic structure-dependent photoelectrochemical responses of dye-sensitized solar cells based on a binary ionic liquid electrolyte. *Physical Chemistry Chemical Physics* **13**, 6416-6422 (2011).
22. Kuang, D.B., Klein, C., Zhang, Z.P., Ito, S., Moser, J.E., Zakeeruddin, S.M. & Grätzel, M. et al. Stable, high-efficiency ionic-liquid-based mesoscopic dye-sensitized solar cells. *Small* **3**, 2094–2102 (2007).
23. Barnes, P. R. F., Andersson, A.Y., Juozapavicius, M., Liu, L., Li, X., Palomares, E., Forneli, A. & O´Regan, B. Factors controlling charge recombination under dark and light conditions in dye sensitised solar cells. *Physical Chemistry Chemical Physics* **13**, 3547-3558 (2011).
24. Guillén, E., Fernández-Lorenzo, C., Alcántara, R., Martín-Calleja, J. & Anta, J. Solvent-free ZnO dye-sensitised solar cells. *Solar Energy Materials and Solar Cells* **93**, 1846-1852 (2009).
25. Zakeeruddin, S.M. & Grätzel, M. Solvent-Free Ionic Liquid Electrolytes for Mesoscopic Dye-Sensitized Solar Cells. *Advanced Functional Materials* **19**, 2187–2202 (2009).
26. Cheng, P., Wang, W., Lan, T., Chen, R., Wang, J., Yu, J., Wu, H., Yand, H.,Deng,

C. & Guo, S. Electrochemical characterization and photovoltaic performance of the binary ionic liquid electrolyte of 1-methyl-3-propylimidazolium iodide and 1-ethyl-3-methylimidazolium tetrafluoroborate for dye-sensitized solar cells. *Journal of Photochemistry and Photobiology A: Chemistry* **212**, 147-152 (2010).

27. Wang, P., Zakeeruddin, S.M., Moser, J. & Grätzel, M. A New Ionic Liquid Electrolyte Enhances the Conversion Efficiency of Dye-Sensitized Solar Cells. *The Journal of Physical Chemistry B* **107**, 13280-13285 (2003).
28. Wang, Z. S., Koumura, N., Cui, Y., Miyashita, M., Mori, S. & Hara, K. Exploitation of Ionic Liquid Electrolyte for Dye-Sensitized Solar Cells by Molecular Modification of Organic-Dye Sensitizers. *Chemistry of Materials* **21**, 2810-2816 (2009).
29. Quintana, M., Marinado, T., Nonomura, K., Boschloo, G. & Hagfeldt, A. Organic chromophore-sensitized ZnO solar cells: Electrolyte-dependent dye desorption and band-edge shifts. *Journal of Photochemistry and Photobiology A: Chemistry* **202**, 159-163 (2009).
30. Kubo, W., Kambe, S., Nakade, S., Kitamura, T., Hanabusa, K., Wada, Y. & Yanagida, S. Photocurrent-determining processes in quasi-solid-state dye-sensitized solar cells using ionic gel electrolytes. *Journal of Physical Chemistry B* **107**, 4374–4381 (2003).
31. Zhang, Z., Ito, S., Moser, J., Zakeeruddin, S.M. & Grätzel, M. Influence of Iodide Concentration on the Efficiency and Stability of Dye-Sensitized Solar Cell Containing Non-Volatile Electrolyte. *ChemPhysChem* **10**, 1834-1838 (2009).
32. Le Bahers, T., Labat, F., Pauporte, T. & Ciofini, I. Effect of solvent and additives on the open-circuit voltage of ZnO-based dye-sensitized solar cells: a combined theoretical and experimental study. *Physical Chemistry Chemical Physics* **12**, 14710-14719 (2010).

Chapter 8

Ordered ZnO nanostructures

8. Ordered ZnO nanostructures

One of the most interesting properties of ZnO is its flexibility in synthesis and morphology. Most of the work made for ZnO in DSCs has been devoted to the exploration of the performance of a wide range of ZnO nanostructures as photoanodes. These nanostructures have exciting transport[1-3] and optical properties [4-6]. Specifically, ZnO photoanodes based on vertically aligned nanostructures such as nanowires, nanorods and nanotubes are often believed to provide a good conducting path towards the external contact, so that electron collection at the photoanode can be enhanced[7,8] . In fact, an increase of the electron lifetime and/or the electron diffusion length with respect to nanoparticulate films has been reported[1,3,9,10] . Photocurrents of up to 4 mA cm^{-2} and an efficiency of 1.7%[i] have been reported for nanowires[11] and an efficiency of 2.3%[ii] for nanotubes with the common N719 and N3 dyes[12]. In comparison to nanoparticle-based DSCs the use of nanowire arrays may result in a significant loss of surface area for supporting the dye. This lower surface area is believed to be the main limitation of one-dimensional (1-D) ZnO nanostructures.

As it was shown in **Chapter 7**, organic dyes such as the indoline derivative D149 have very high extinction coefficients. The enhanced optical absorption can provide a way to compensate for the low surface area of vertically aligned nanostructures. The sensitization of vertically aligned ZnO nanostructures with this kind of dyes shows promising results[13-16]. However, the efficiencies are still much lower than those obtained with nanoparticle-based solar cells.

This Chapter is divided in two main sections. In the first one, a systematic study of the optical, electrochemical and photovoltaic properties of DSCs based on ZnO nanostructures with two different morphologies (nanoparticles and nanowires) both sensitized with the organic dye D149, will be presented. The aim of this study is to clarify the reasons for the lower performance of the one-dimensional ordered nanostructures with respect to randomly oriented nanoparticles. In the second section, a strategy to improve the performance of the ZnO nanowires is proposed: ZnO nanowire arrays with nanoparticles spin-coated onto the surface are fabricated and characterized.

[i] Active surface area of the cell: 0.28 cm^2
[ii] Illumination intensity: 42 mW cm^{-2}

8.1. Comparison between nanoparticulate films and electrodeposited nanowire arrays

The performance of dye sensitized solar cells with two different ZnO photoanodes has been explored: (a) randomly oriented nanocrystalline networks and (b) nanowire arrays. D149 has been the dye employed, on account of its proved good properties as sensitizer for ZnO and its high extinction coefficient. Due to the poor stability of this dye in contact with ionic liquid (**Chapter 8**), this study has been based on organic liquid electrolytes.

8.1.1. Fabrication and characterization of the devices

The materials used for the fabrication of the cells are summarized in **Table 8.1** and the parameters of the illumination source used for photovoltaic characterization in **Table 8.2**.

Table 8.1 Summary of the materials employed in the fabrication of the cells.

<table>
<tr><th>ZnO</th><th>Dyes</th><th>Electrolytes</th><th>Counter electrode</th></tr>
<tr><td>Degussa VP AdNano®ZnO20/ PI-KEM 1:1
Cell area: 0.64 cm^2</td><td>D149 (0.5 mM) chenodeoxycholic acid (0.7 mM) in tert-butyl alcohol/acetonitrile (1:1)
30 minutes</td><td rowspan="3">0.05 mM I_2
0.5 M TBAI in acetonitrile/ ethylencarbonate (1:4)</td><td rowspan="3">*Platisol* (TEC 8)</td></tr>
<tr><td>Nanowire arrays 2.5 μm
Cell area: 0.64 cm^2</td><td rowspan="2">D149 (0.5 mM) chenodeoxycholic acid (0.7 mM) in tert-butyl alcohol/acetonitrile (1:1)
90 minutes</td></tr>
<tr><td>Nanowire arrays 5 μm
Cell area: 0.64 cm^2</td></tr>
</table>

Table 8.2 Illumination set-up used for DSC testing.

Illumination source	Filters	Calibration
Solar Simulator ABET	AM 1.5 filter	Reference solar cell (Oriel, 91150) + KG5 100 mW cm^{-2}

The fabrication and the optical characterization of the ZnO nanowire arrays were carried out by Dr. Ramón Tena and Eneko Azaceta (Department of New Materials, CIDETEC, San Sebastián). The nanowires were electrodeposited by the reduction of dissolved molecular oxygen in zinc chloride solutions. The electrolyte was a $5 \cdot 10^{-4}$ M $ZnCl_2$ (>98.0 %), 2 M KCl (>99.5 %) ultrapure aqueous solution, saturated by bubbling with oxygen. Two different nanowire lengths were prepared by varying the charge density (10 and 20 C cm^{-2}). More details about the electrodeposition can be found in references [17-19]. The nanoparticle and nanowire array films were deposited on TCO substrates previously covered via spray deposition with a thin continuous ZnO layer which acts as blocking layer[5] (**Section 4.2**). Before sensitization, the nanowire samples were immersed in acetone and isopropanol and then annealed at 450ºC for 30 minutes. The working and counter electrodes were sealed together with a thermoplastic (SX1170-25, Solaronix).

To adjust the light intensity to 1 sun (100 mW cm^{-2}) a calibrated silicon solar cell with an IR filter (KG5) has been used. The use of KG5 provides a closer match to the DSC spectral response of the reference cell[20]. Electrochemical impedance spectroscopy measurements under illumination and intensity modulated spectroscopy were carried out using a Solartron 1250 frequency response analyzer (FRA) and a Solartron 1286 electrochemical interface.

In **Figure 8.1** the SEM micrographs of the samples with nanowire (NW) array (a, b) and nanoparticle (NP) network morphology (c, d), are shown. The roughness factor of the different samples was determined from krypton adsorption isotherms using the BET method. Adsorption isotherms were carried out by Arnost Zukal of the Academy of Sciences of the Czech Republic (Prague).

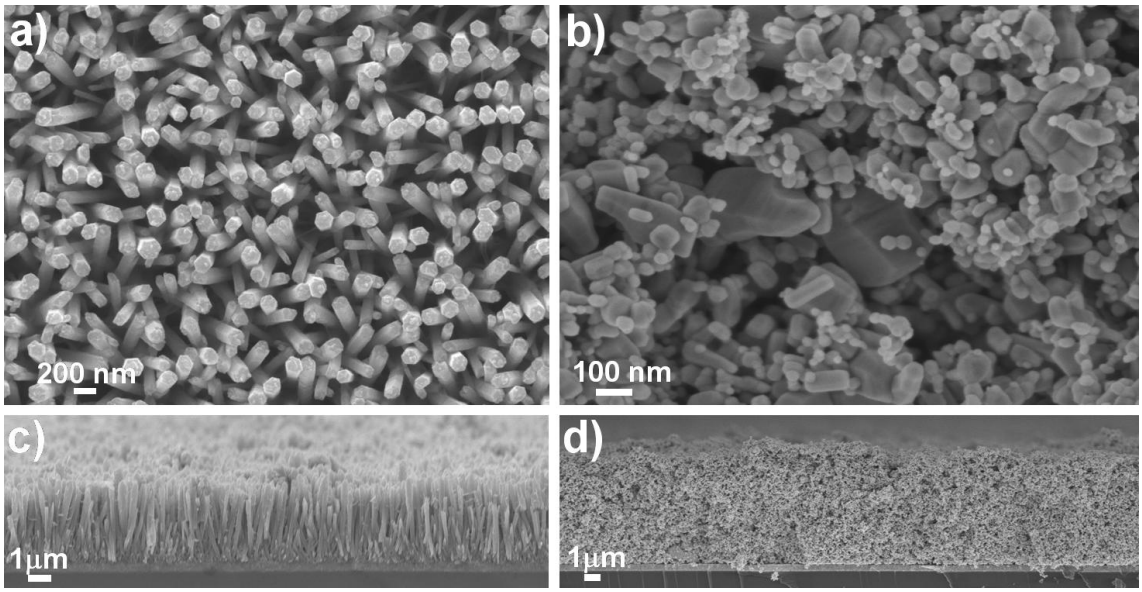

Figure 8.1 SEM micrographs of the different ZnO architectures: a) and c) nanowire arrays and b) and d) randomly oriented nanoparticle network.

ZnO nanowires show diameters of around 200 nm. The nanoparticle anodes are composed of a random mixture of large (~100-200 nm) and small (20-50 nm) particles (**Table 8.3**).

Table 8.3 Nanoparticle (NP) and nanowire (NW) diameter, length of the nanowires and thickness of the nanoparticle film.

Sample	Diameter (nm)	Length/Thickness (μm)
NWs 2.5	~ 200	2.5
NWs 5	~ 200	5
NPs	20-50 + 100-200	~8

8.1.2. Optical characterization

An optical characterization of the different photoanodes has been carried out. In **Figure 8.2** the total reflectance spectra of the ZnO films before sensitization are shown.

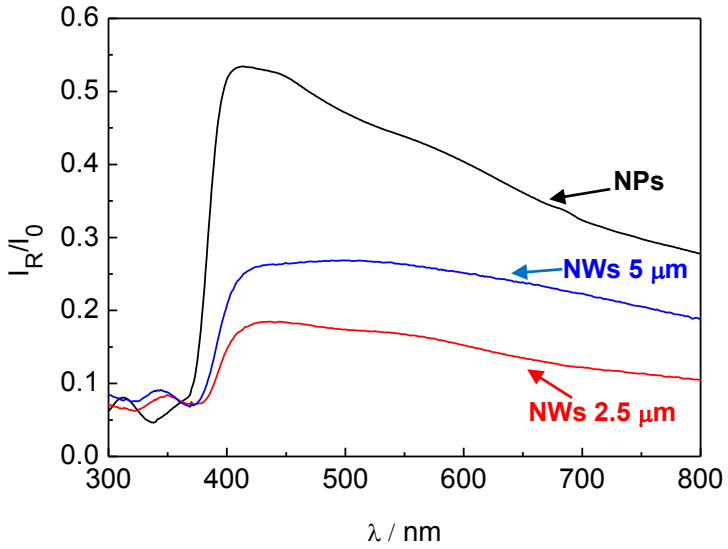

Figure 8.2 Total reflectance spectra of glass/SnO_2:F/ZnO samples constituted of nanoparticles and nanowire arrays (2.5 and 5 μm in length).

Since the total reflectance is related to light scattering[21] these measurements indicate that the nanoparticle substrates produce strong scattering in the visible region. This is likely related to the presence of large particles in the ZnO powder, which act as very efficient light scattering centres in this wavelength region. In **Table 8.4** optical and structural parameters of both kinds of nanostructures are summarized.

Table 8.4 Roughness factor (*RF*), amount of adsorbed dye, dye coverage, effective absorption in the 370-700 nm range (A_E) for samples with different ZnO morphology and maximum theoretical short circuit current density.

Sample	RF	Dye adsorbed* (mol cm^{-2})	Dye coverage** (cm^{-2})	A_E (%)	$J_{sc,max}$ (mA cm^{-2})
NWs (2.5 μm)	20	$3.27\ 10^{-9}$	$9.8\ 10^{13}$	48.9	9.6
NWs (5 μm)	50	$5.62\ 10^{-9}$	$6.8\ 10^{13}$	57. 3	11.3
NPs	300	$3.52\ 10^{-8}$	$7.1\ 10^{13}$	69.3	13.6

*Refers to the projected area. ** Refers to the total surface area.

The roughness factor (*RF*) is defined as the physical surface area of the ZnO film divided by its projected area. The amount of dye adsorbed on the films is defined with respect to the projected area. The dye coverage is defined with respect to the total surface area taking into account the roughness factor of the different samples. The effective absorption (A_E) is the ratio between the amount of absorbed photons and the amount of incident photons (AM 1.5) and is defined as

$$A_E = \frac{\int_{\lambda_1}^{\lambda_2} A(\lambda) I_0(\lambda) d\lambda}{\int_{\lambda_1}^{\lambda_2} I_0(\lambda) d\lambda} \quad (8.1)$$

where A is the absorptance, I_0 is the standard (AM 1.5) solar flux, and λ_1 and λ_2 are 370 and 700 nm respectively. **Table 8.4** also includes an estimation of the maximum photocurrent (assuming 100% quantum yield of charge injection and 100% charge collection efficiency) that can be obtained from the devices under AM 1.5 illumination.

As expected, the surface area is larger for the nanoparticle films than for the nanowires (by a factor of 6 and 15 for the longer and shorter nanowires respectively). This increment in the roughness factor of the nanoparticles with respect to the nanowires is nicely correlated with the amount of dye adsorbed on the films. Hence, the nanoparticles are found to load approximately six times more dye than the longer nanowires. In **Figure 8.3** examples of a sensitized ZnO nanoparticle film and a sensitized nanowire film (5 μm) are shown.

(a) (b)

Figure 8.3 Sensitized ZnO films: (a) nanoparticles and (b) 5 μm length nanowires.

The results for dye coverage are similar for the three kinds of anodes, and close to the theoretical values for monolayer coverage (either monodentate or bidentate) of D149 on TiO_2 electrodes[22]. In **Chapter 7** it was already pointed out that aggregation seems to have only a marginal effect in ZnO films sensitized with D149. The results for dye coverage suggest, furthermore, that the dye molecules form basically a monolayer on the oxide surface.

The effective absorption (A_E) of the samples in the range from 370 to 700 shows that the arrays constituted of nanowires with a length of 5 μm collect light in this wavelength range by a fraction close to 57%, which is slightly smaller than the fraction

absorbed by the nanoparticle film (69%). As the nanoparticle network samples exhibited the strongest scattering for visible light (**Figure 8.2**), the ratio between the effective absorption and the amount of loaded dye is larger for nanoparticle-based anodes than for the nanowire arrays. The transmission of the sensitized nanoparticle network is negligible for wavelengths lower than 600 nm, although 100% absorption is not reached mainly due to reflectance losses[19]. The theoretical maximum photocurrent predicted for the sensitized nanowire arrays (> 11.0 mA cm^{-2}) is comparable to that estimated for nanoparticles (13.6 mA cm^{-2}).

The absorptance spectra of the sensitized electrodes and the optical density of solutions containing the desorbed dye are presented in **Figure 8.4**. The characteristic absorption of the D149 dye near 550 nm is clearly seen in all cases.

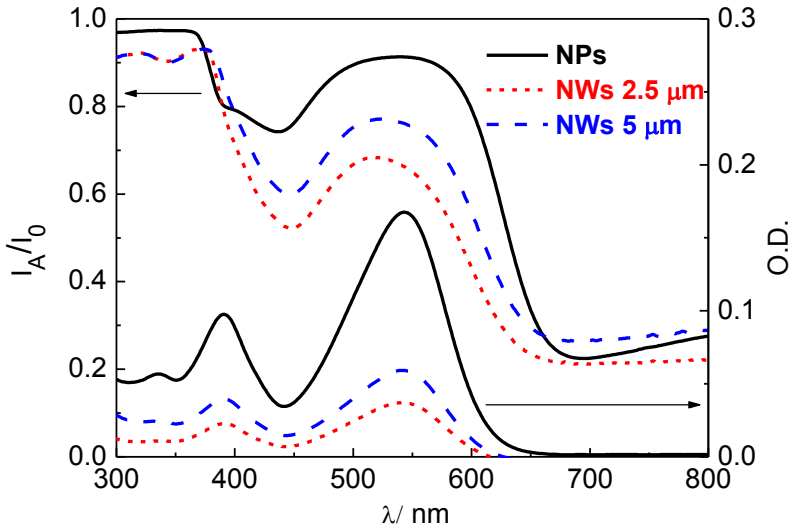

Figure 8.4 Absorptance spectra of glass/SnO_2:F/ZnO/D149 samples (left y-axis) and optical density (absorbance) of solutions containing the desorbed dye (right y-axis).

Again a broadening of the dye spectrum can be observed when adsorbed on the ZnO films with respect to the spectrum in solution. It is worth mentioning that the nanoparticle-based samples, which exhibit a stronger scattering of the visible light, show a broader absorption. This could be an indication that the light scattering effects may also contribute to the absorption broadening.

The optical characterization suggests that the sensitized nanowire arrays show a significant light harvesting capability when compared with the nanoparticle films.

8.1.3. Photovoltaic performance and IPCE measurements

The good light harvesting properties of the ZnO photoanodes sensitized with the D149 dye should be correlated with the photovoltaic performance. In **Table 8.5** the photovoltaic parameters of the DSCs based on the different ZnO architectures are summarized.

Table 8.5: Photovoltaic parameters of the ZnO DSCs under simulated light (100 mW cm^{-2}).

Sample	J_{SC} (mA cm^{-2})	V_{OC} (V)	FF	Efficiency (%)
NWs (2.5 µm)	3.35	0.502	0.34	0.56
NWs (5 µm)	4.25	0.554	0.37	0.88
NPs	9.65	0.635	0.45	2.73

The nanoparticle-based solar cell gives an efficiency of 2.73%, whereas the nanowires lead to efficiencies of 0.88% and 0.56% for the long and the short nanowires respectively. These values are larger than recent literature data[15] for D149-sensitized nanowires of similar length, although they lie below recent results for nanowires deposited on a ZnO nanoparticle layer with the D102 indoline dye[16]. The photovoltages of the devices are found to increase with surface area. This means that the long nanowires lead to a larger value of V_{oc} probably due to the larger dye loading and higher electron injection. This is in contrast with previous results for solar cells constructed with vertically aligned ZnO nanostructures[23]. An example of current-voltage curves of the different kind of samples under standard (1 sun) AM 1.5 illumination can be found in **Figure 8.5**.

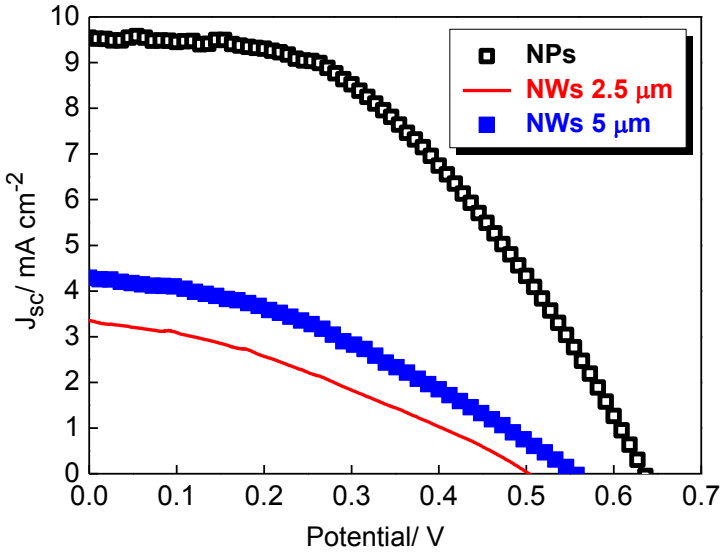

Figure 8.5 Photocurrent–voltage curves of ZnO solar cells sensitized with D149 under simulated solar light (AM 1.5G) at 1 sun (100 mW cm^{-2}), for the nanostructures considered in this work.

Fill factors are low, especially for nanowire samples. Low fill factors are usually found in ZnO ordered nanostructures[24,25]. In **Figure 8.6** the Incident photon-to-current efficiency (IPCE) of the different solar cells is shown.

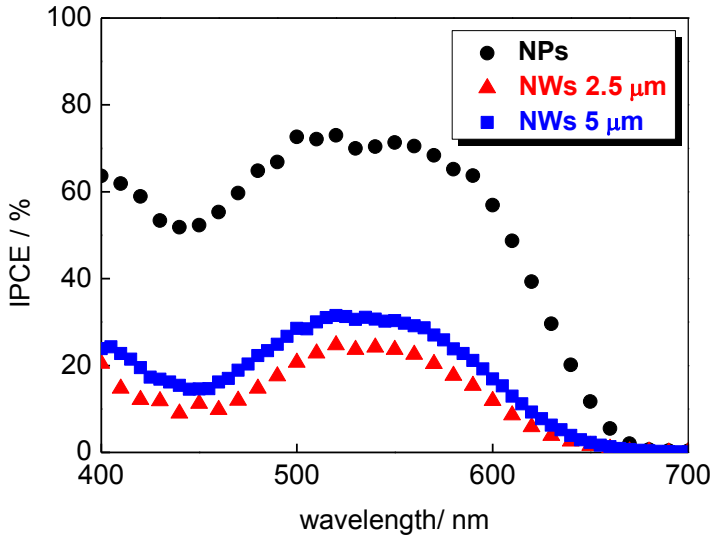

Figure 8.6 Incident-photon-to-current-efficiency (IPCE) of the studied samples

The nanowires exhibit a maximum IPCE close to a 30%, almost half of the maximum value encountered for the nanoparticles. As expected, this is the same reduction factor that it is found when comparing the photocurrents of both kinds of nanostructures

(**Table 8.5**). The quantum efficiency curves are broadened with respect to the spectrum of the isolated dye, as already observed in **Figure 8.4** for the spectrum of the adsorbed dye.

By comparing the measured photocurrent at short circuit (J_{sc}) with the maximum values estimated from the absorptance spectra ($J_{sc,max,}$ **Table 8.4**), it is found that the experimental values are ~70% and ~35% of the predicted maximum values for the nanoparticle and nanowire arrays, respectively. In addition, the photocurrent loss shown by the nanowires arrays does not depend on the length of the nanowire. Therefore, the good light harvesting properties observed for nanowires are not correlated with a good photovoltaic performance for this type of nanostructures. If the same electron injection quantum yield for nanoparticles and nanowires is assumed (as it might be expected for the same dye/oxide combination), the relative ratios obtained for nanowire arrays would indicate that recombination losses are larger for this architecture. The electronic and recombination behaviour of both nanostructures will be treated in detail in following sections.

8.1.4. Light intensity dependence of the open circuit voltage

The semilogarithmic plots in **Figure 8.7** compare the intensity dependence of the open circuit voltage for the different samples. The results indicate that for the two kinds of nanostructures, V_{oc} depends linearly on the logarithm of light intensity. The slopes of the plots are 37 mV for nanoparticle-based solar cells and 63 mV and 56 mV for nanowires 2.5 and 5 microns in length respectively. All these slopes depart from the ideal-diode value of 26 mV. Departure from ideal behaviour can be due to non-linear recombination[26,27], possibly produced by strong influence of recombination via surface localized states, in the ZnO anodes.

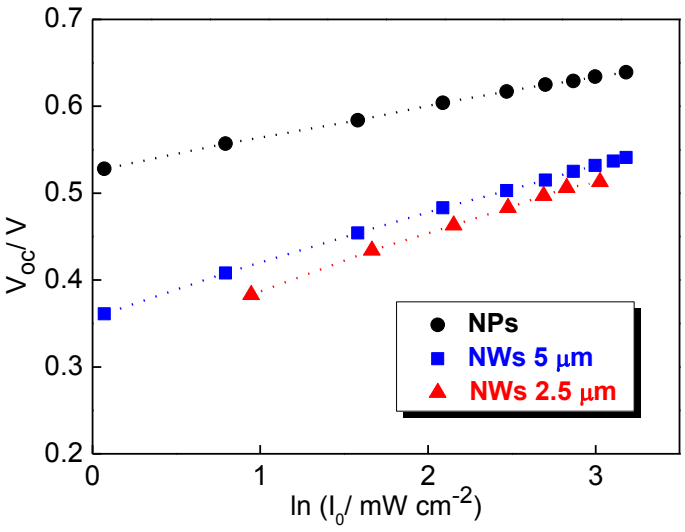

Figure 8.7 Open-circuit voltage as a function of light intensity for cells with nanoparticles and nanowires.

The present results seem thus to indicate that the nanowires exhibit a relatively high density of surface states. This possibility is supported by the fact that the slope in the V_{oc} versus light plot is reduced when the nanowires are annealed at higher temperature (**Appendix 11.6**), as annealing is known to have a significant effect on the mean free carrier density of ZnO nanowires[28].

8.1.5. Open circuit voltage decay

Open circuit voltage decays of the different samples have been measured. In **Figure 8.8** the voltage transients are shown on a logarithmic time scale for nanoparticles and nanowires of 5 μm length. Voltage decays are useful to extract electron lifetimes[29,30] (**Section 3.5**) provided that there is no significant contribution of back-reaction through the substrate[31,32]. Electron leakages from the conducting glass substrate or any compact layers deposited on it produce abnormally rapid decays, especially at longer times.

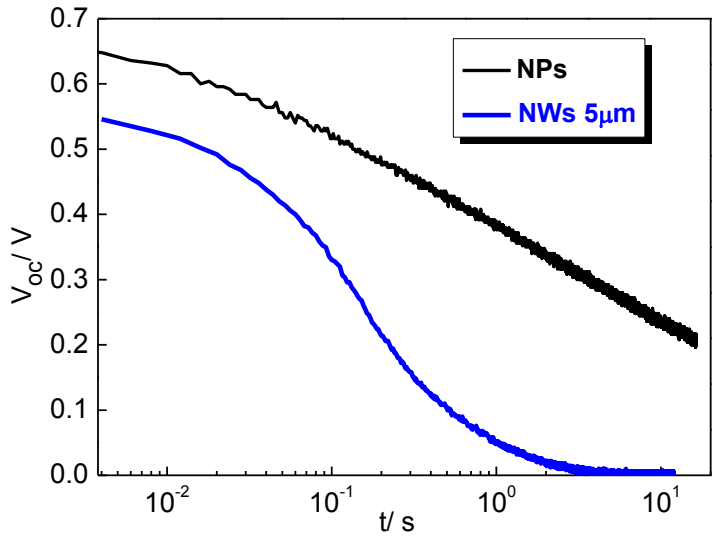

Figure 8.8. Open-circuit voltage decays for D149-sensitized solar cells with ZnO nanoparticles and nanowires of 5 μm length.

In **Figure 8.8** a very different shape is obtained for nanoparticles and nanowires. As a matter of fact the rapid voltage decay in the case of the nanowires strongly suggests that there may be a significant loss of electrons via the substrate[31], the substrate being in this case the sprayed ZnO thin layer used as blocking layer in the nanoparticle-based solar cells and as buffer layer for growing the 1-D nanostructures in the nanowire array solar cells. There is an apparent failure of this thin blocking layer in the nanowire-based solar cells. Two plausible explanations are found for this fact. On the one hand, it could be connected to the n-type doping typically produced in electrodeposition methods in the presence of chloride[28,33]. On the other hand, the thin ZnO layer could undergo etching during the electrodeposition of the nanowires[34] leaving the FTO unprotected. To cast light into this fact, a study of the effect of electrodeposition on the degradation of the thin continuous ZnO layer has been carried out. In fact, it is found that electrodeposition can cause the degradation of the buffer layer, but this deterioration depends strongly on deposition conditions. Results can be found in the **Appendix 11.7**.

It should be noted that sub-linear recombination can also produce a rapid decay, as can be derived from the numerical solution of the continuity equation at open circuit for non-linear kinetics[35]. However, in contrast to the nanoparticles, it was not possible to fit the decays for the nanowires without inclusion of a term accounting for back-reaction through substrate (see Ref [19]).

8.1.6. Electrochemical impedance spectroscopy studies

To gain further insight into the functioning of the devices they have been characterized by electrochemical impedance spectroscopy under illumination. In **Figure 8.9** spectra of a nanoparticle sample and a nanowire sample (nanowire length: 5 µm) are shown.

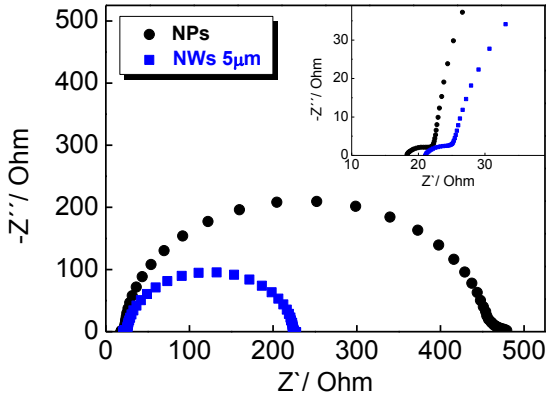

Figure 8.9. Impedance spectra under illumination and at V_{oc} = 0.520 V and 0.525 mV of nanoparticle and nanowire ZnO dye solar cells sensitized with D149.

As mentioned in **Chapter 7**, the transmission-line feature attributed to electron transport in the semiconductor oxide (**Section 4.7.1**) cannot be observed in DSCs based on ZnO nanoparticles. In **Figure 8.9 (inset)** it can be seen, furthermore, that this feature is absent in the case of ZnO nanowire films as well. This is somehow expected, as in nanowires the transport is reported to be faster than in nanoparticles, mainly due to the lack of grain boundaries, which could slow down electron transport[1]. Hence it was not possible to extract reliable transport resistance values from the equivalent circuit fittings and the impedance study was limited to the analysis of the recombination behaviour of both the nanoparticle and the nanowire-based solar cells.

In **Figure 8.10** the capacitance (C_μ) and the charge transfer resistance (R_{ct}) are plotted as a function of voltage for both kinds of nanostructures. Capacitance values are plotted with respect to the total projected area.

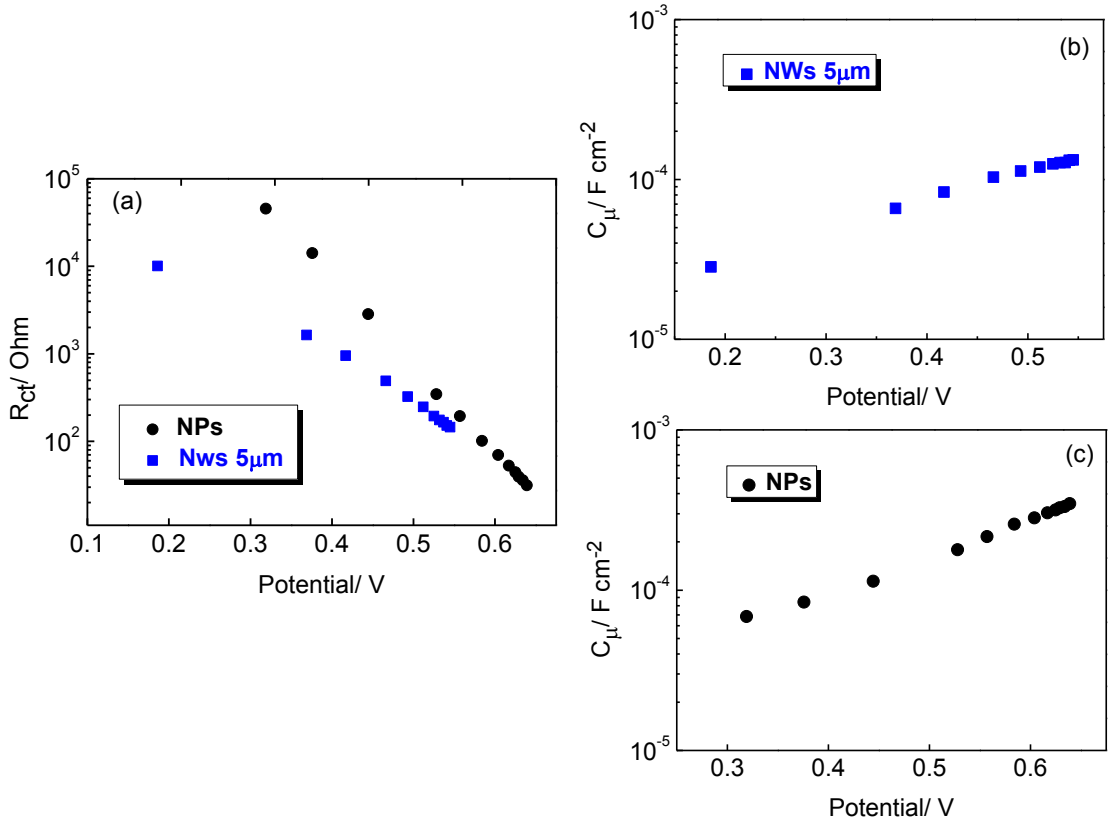

Figure 8.10 Impedance parameters as determined from measurements under illumination: charge transfer resistance (a) and capacitance normalized by the geometrical area for D149-sensitized solar cells with ZnO nanoparticles (b) and nanowires of 5 μm length (c).

Both parameters show the exponential behaviour found typically in dye-sensitized solar cells. From the experimental slopes a smaller transfer parameter (β) (**Equation 2.10** $R_{ct} = R_{ct,0}\, exp(-\beta qV/kT)$) is found for the nanowires. This can be related[26,36] to the lower fill factors encountered for the nanowires (**Table 8.5**) and is connected to the higher non-ideality observed in **Figure 8.7**. In general, the smaller charge transfer resistance found for nanowire-based solar cells implies that the open circuit potential will be reduced for these devices. This holds for both nanowire lengths, with lower photovoltage and lower charge-transfer resistance found for the short nanowires. However, additional effects can be occurring in this case, as discussed below.

The capacitances plotted in **Figure 8.10b** and **Figure 8.10c** show a clear exponential behaviour. However, the weak dependence on the voltage we already observed for nanoparticles ZnO solar cells (**Section 7.4**), is also found for nanowires. A similar behaviour has been already reported for 1-dimensional ZnO nanostructures[9,37,38]. The interpretation of this feature is not straightforward and would require a careful

consideration of the degree of doping[39,40] and the formation of a depletion layer on the surface, especially for the nanowires. The chemical origin of the capacitance can be argued. As discussed in Refs. [2] and [38] the formation of a depletion layer in ZnO nanowires produces a very flat dependence of the capacitance with respect to voltage. The magnitude of this effect depends on the donor density in the oxide. If the depletion mechanism is taking place in the ZnO nanowires, then the capacitance extracted from EIS is not "chemical" so that lifetimes cannot be evaluated from the impedance measurements[41]. On the other hand it was assumed that the contribution of the capacitance of the ZnO blocking layer was negligible (see Ref [19]).

8.1.7. Comparison of different methods to obtain the electron lifetime

The likely influence of space-charge effects (not "chemical") in the capacitance and the contribution of back-reaction through the substrate in the nanowire samples complicate the extraction of electron lifetimes from EIS and OCVD techniques, respectively. To evaluate these effects, in **Figure 8.11** the lifetimes extracted from EIS and from OCVD (**Sections 3.6.1** and **3.5** respectively) are compared.

It can be observed that there is good agreement between the lifetimes extracted from both experimental techniques for the nanoparticle-based solar cells. On the contrary, the nanowire array solar cells yield quite different results, especially at low voltages. This analysis indicates that in the case of the nanoparticle-based solar cells, the measured lifetimes quantify properly the kinetics of the recombination reaction and that the measured capacitance is a true chemical capacitance. In contrast, the determination of the lifetimes in the case of the nanowires is subject to error due to the afore-mentioned effects.

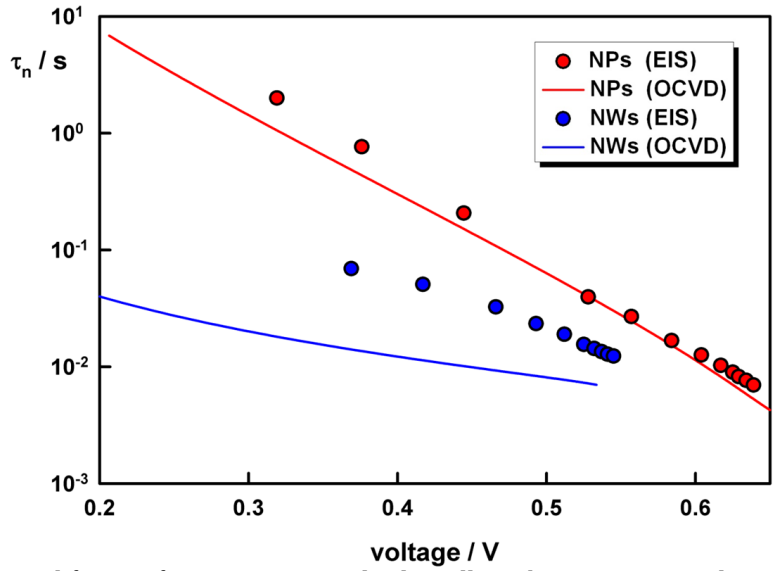

Figure 8.11 Electron lifetimes for D149-sensitized solar cells with ZnO nanoparticles and nanowires of 5 μm length as obtained from open circuit voltage decay experiments and impedance spectroscopy under illumination.

In spite of the uncertainty in the determination of the electron lifetimes in the case of the nanowire-based solar cells, the present results suggest that recombination is indeed more rapid for nanowires and explain why photocurrents are small, in spite of the good light harvesting properties of the sensitized films. It must be borne in mind that shunting through the substrate does not occur at short circuit, so that this cannot be a loss mechanism for the short circuit photocurrent. In addition, space-charge effects in nanowires are more important at low voltages and might not affect the measurement of the lifetime near the open-circuit potential (where a clear exponential behaviour of the capacitance is observed, analogous to that of the nanoparticle-based solar cells).

8.2. ZnO nanowire/nanoparticle (NW-NP) composite solar cells

In this section, a study of dye-sensitized solar cells based on electrodeposited ZnO nanowires (NWs) coated by ZnO nanoparticles (NPs) is presented.

Several studies have tried to increase the performance of one-dimensional nanostructures by combining them with nanoparticles[42] or with hierarchical structures[4]. Baxter et al.[43] first hybridized ZnO NWs and ZnO NPs with the aim of improving the surface area without sacrificing good electron transport properties of the nanowires. ZnO nanowire arrays act as direct pathways for fast electron transport and the nanoparticles dispersed between them provide a high specific surface area for dye adsorption[44]. The ZnO nanowires are usually covered by TiO_2 nanoparticles[45] or by

ZnO nanoparticles[43], which can be deposited by several methods, for instance chemical bath deposition[46] or spin coating[42]. Usually the efficiency of ZnO NW /NP composite DSCs is significantly higher than the efficiency of cells based on ZnO NWs[42,43,47]**.** This improvement is mainly ascribed to a higher photocurrent as a consequence of an enhanced light harvesting [46].

On the other hand, core-shell nanostructures are applied to electrodes in DSCs to reduce the recombination rate at the electrode/electrolyte interface[24]. Usually, core-shell nanoparticle electrodes are formed by the combination of two different oxides[48]. This combination can affect the electrode properties by different mechanisms. The core shell electrodes can slow down the recombination processes by the formation of an energy barrier at the oxide surface based on the different conduction band potential of the shell with respect to the core[24,49,50]. On the other hand, the shell material can shift the conduction band potential of the core, increasing the open circuit photovoltage while reducing the short circuit photocurrent compared to the non-coated oxide electrode[51]. According to this last approach, the coating forms a dipole layer at the electrode/electrolyte interface which shifts the electrode band potentials depending on the dipole intensity and direction. The dipole layer is attributed to either the different electron affinity or different acidity of the two semiconductors[52]. ZnO is often used as the shell in core-shell nanoparticle structures[53].

In the study described in **Section 8.1**, it was found that the main limitation for the one-dimensional electrodeposited nanostructures in combination with a highly absorbing dye is high recombination rather than low surface area. According to these observations, surface modification may constitute an appropriate strategy for improving the performance of one-dimensional nanostructures in dye solar cells by controlling recombination. For this purpose, solar cells based on ZnO nanowires coated by ZnO nanoparticles have been fabricated and characterized. The aim of coating the surface of the nanowires is the same as in conventional core-shell structures: the minimization of the recombination with the electrolyte. However, neither of the two processes explaining the improvement in core-shell structures based on two different oxides is expected as ZnO is used both for the core and for the shell. A high concentration of surface states on the nanowires, which could be a result of the specific deposition method, was considered as a possible reason for the high recombination. In this case,

the surface modification aims at the removal of surface states as a consequence of the coating.

8.2.1. Fabrication and characterization of the devices

The materials used for the fabrication of the cells are summarized in **Table 8.6**, and the parameters of the illumination source used for photovoltaic characterization in **Table 8.7**.

Table 8.6 Summary of the materials employed in the fabrication of the cells

ZnO	Dyes	Electrolytes	Counter electrode
Nanowire arrays 2.5 μm (Blocking layers)/ Spin coated Nanoparticles Cell area: 0.64 cm^2	D149 (0.5 mM) chenodeoxycholic acid (0.7 mM) in tert-butyl alcohol/ acetonitrile (1:1) 20 minutes	0.05 mM I_2 0.5 M TBAI in acetonitrile/ ethylencarbonate (1:4)	*Platisol* (TEC 8)

Table 8.7 Illumination set-up used for DSC testing.

Illumination source	Filters	Calibration
Solar Simulator ABET	AM 1.5 filter	Reference solar cell (Oriel, 91150) 100 mW cm^{-2}

The nanowires were electrodeposited as explained in **Section 8.1.1** and their approximate length was ~ 2.5 μm. The samples were immersed in acetone and isopropanol and then annealed to 450 ºC for 30 minutes. To prepare a ZnO colloidal suspension 0.11 g of zinc acetate dehydrate was dissolved in 50 mL of methanol under vigorous stirring at 60º C. Subsequently, a 0.03 M solution of KOH (25 mL) in methanol was added dropwise at 60ºC. The reaction mixture was stirred for 2 h at 60ºC[54]. The obtained colloidal suspension was spin-coated at 2000 rpm for 30 s on the nanowire substrates. The ZnO deposition process was followed by annealing at 100ºC in air for 5 minutes. Three different kinds of nanowire samples were studied: (a)

reference samples with no nanoparticle deposition, and samples (b) and (c) with 10 and 30 cycles of nanoparticle deposition, respectively. Before immersion in the dye solution, the samples were washed again with acetone and isopropanol.

In this case, no KG5 infrared filter[20] was used to calibrate the solar simulator. Light intensity dependence of the open circuit voltage was measured using a xenon arc lamp coupled to an UV filter and a KG5 infrared filter. Neutral density filters were used to adjust the illumination intensity. Electrochemical impedance spectroscopy measurements were carried out in the dark at different applied voltages. For open circuit voltage decay measurements the initial illumination was provided by the solar simulator.

8.2.2. Photovoltaic performance

In **Figure 8.12** the IV characteristics for DSCs fabricated using D149-sensitized ZnO NWs and hybrid NW-NP ZnO with 10 and 30 nanoparticle deposition cycles are shown. The photovoltaic parameters are summarized in **Table 8.6**. Two cells of each configuration were characterized.

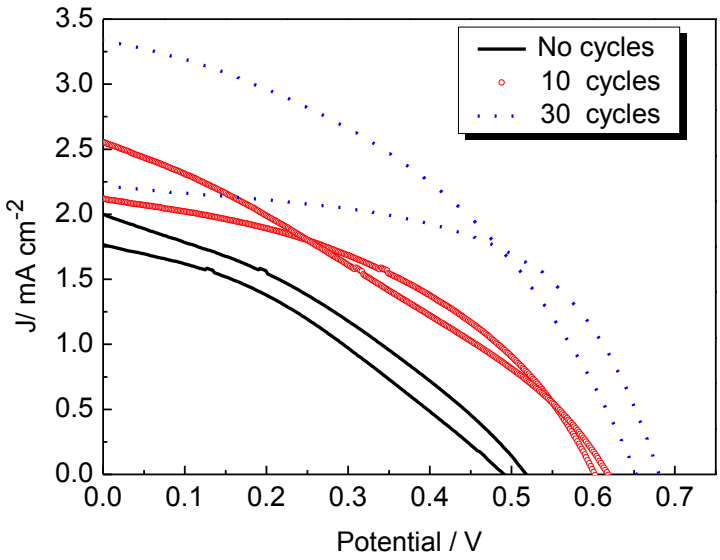

Figure 8.12 IV curves for the three different configurations.

Table 8.6: Photovoltaic parameters of the ZnO DSCs under simulated white light (100 mW cm^{-2}).

Cell	Cycles	J_{sc} (mA cm^{-2})	V_{oc} (V)	FF	Efficiency (%)
1	-	2.01	0.51	0.34	0.4
2	-	1.76	0.48	0.34	0.3
3	10	2.12	0.60	0.43	0.6
4	10	2.54	0.61	0.31	0.5
5	30	2.10	0.66	0.52	0.7
6	30	3.32	650	0.41	0.9

As expected, an improvement of the photocurrent after nanoparticle deposition on the nanowires is observed, either as a consequence of the higher surface area or of a descrease in the recombination rate. However, although there is indeed an improvement, it is not as high as expected according to previous results in literature for composite NW-NP cells[42,47]. In fact, a preliminary study of the absorption properties of nanowires and NWs-NPs films indicates that absorption is not greatly improved by the deposition of the nanoparticles.

As highlighted in **Section 8.1**, the use of a highly absorbing dye (as e.g. D149) can compensate for the low dye loading typically observed for nanowire films with low surface areas. The improvement of the photocurrent upon nanoparticle deposition (**Table 8.6**) could be associated, therefore, to a decrease of the recombination in the NW-NP samples, rather than to the increase of the surface area. This hypothesis is supported by the fact that the photovoltage improves significantly with increasing numbers of deposition cycles. Concretely, the photovoltage increases by more than 100 mV after 30 deposition cycles. In addition, the fill factor also improves upon NP deposition. This improvement can also be related to a decrease of the recombination rate and is usually observed in hybrid NW-NP cells[43].

8.2.3. Recombination losses in ZnO NW-NP composite cells

In **Figure 8.13** the electron lifetime is represented as a function of voltage for each configuration. This parameter was extracted from open circuit voltage decay measurements using in each case the cell with the highest open circuit voltage.

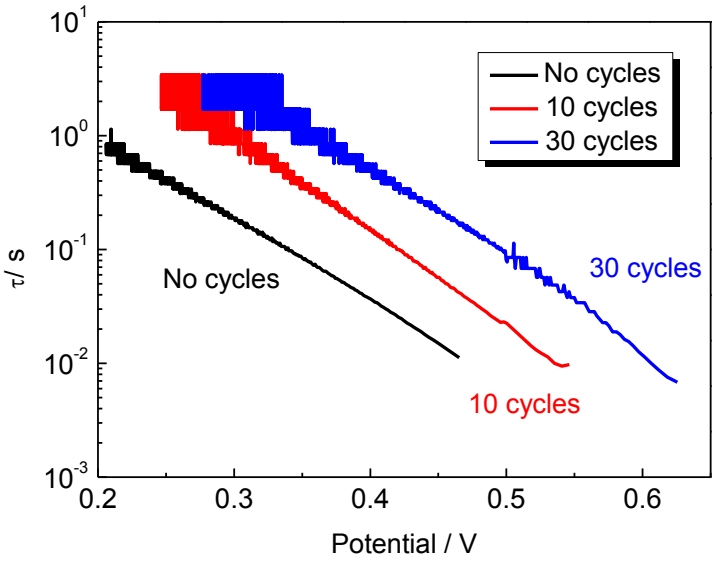

Figure 8.13 Electron lifetime as extracted from open circuit voltage decays. For each configuration the cell with the highest open circuit voltage is plotted.

It is observed that the lifetime increases with the number of deposition cycles. In addition, the open circuit voltage decay profiles show that no significant recombination through the substrate is taking place in any of the spin coated samples. This could be related to the coverage of initially uncovered areas of the FTO substrate by nanoparticle deposition. The recombination properties of the different samples were also analyzed by electrochemical impedance spectroscopy measurements. In **Figure 8.14**, the charge transfer resistance is represented as a function of the applied voltage for each configuration.

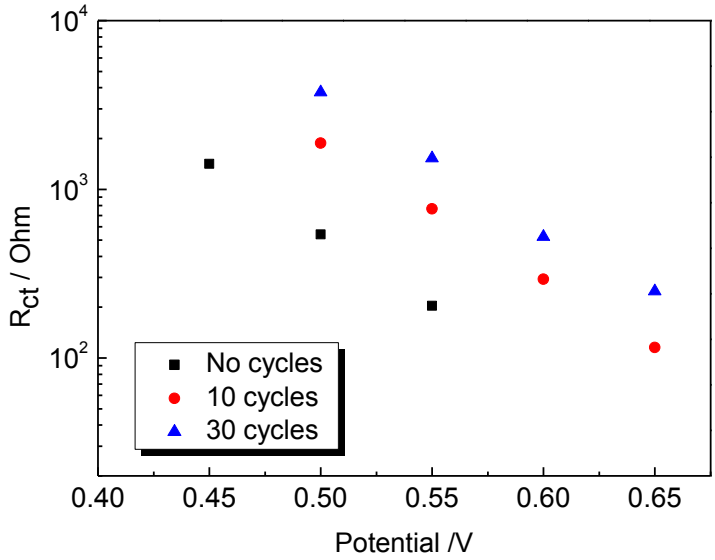

Figure 8.14. Charge transfer resistance versus applied potential for different configurations.

In line with the previous observation, significantly higher values of the charge recombination resistance can be observed after nanoparticle deposition.

8.3. Conclusions

In contrast to previous reports, it was found that vertically aligned ZnO nanowire arrays sensitized with highly absorbing dyes can reach good solar light harvesting. In spite of the lower surface area, effective absorption values for nanowire array films are close to those of nanoparticle-based films. However the photocurrents of the nanowire-based cells are much smaller than expected from the good light absorption. This suggests that either poor injection and/or strong recombination are responsible for the limited performance of the nanowire arrays, rather than a low surface area. Regarding recombination, impedance spectroscopy and open-circuit voltage decays yield shorter lifetimes for nanowires. However the weak voltage dependence of the capacitance and the lifetime may be related to space-charge effects within the nanowires and with electron losses from the substrate, respectively, hence complicating the experimental extraction of the lifetimes. On the other hand, differences in injection yield for the two kinds of nanostructure cannot be completely ruled out since the different synthetic procedures can lead to a different chemical structure of the ZnO surface.

Lower efficiencies than reported in bibliography[1,9,10] have been achieved with the nanowire samples fabricated in this study. However, it is worth mentioning that in those references the ZnO nanostructures were deposited by vapour phase techniques, which might induce an improvement of the ZnO electronic performance. It must not be forgotten that the nanostructures analyzed here (NPs and NWs) are fabricated by different methods. The nanowires were electrodeposited in aqueous media. On the contrary, the commercial powders are synthesized in the gas phase. Therefore, the density of surface states is expected to be lower for nanoparticles with respect nanowires. This fact might complicate the comparison. A recent paper by Guerin et al.[54] reports, in agreement with our results, a shorter lifetime for electrodeposited ZnO mesoporours films with respect to nanoparticle films prepared by the doctor-blade method. This confirms the key contribution of the preparation method on device performance.

The failure of the thin blocking layer in the nanowire-based solar cells has been related to undesired etching during the electrodeposition of the nanowires leaving parts of the FTO substrate unprotected. Therefore, strategies should be applied to minimize recombination as well as electron losses from the substrate.

Nanoparticle deposition on the surface of the nanowires by spin-coating decreases the electron recombination. As a consequence, the photovoltage is greatly improved with respect to bare nanowire samples. In addition, nanoparticle deposition also improves the fill factor of the fabricated cells.

This work provides a significant new insight into the relatively low efficiencies usually obtained in dye-sensitized solar cells based on ZnO nanowires. Furthermore, we present a strategy to improve the performance of this type of cells by surface modification with nanoparticles, which is found to reduce recombination. Besides, further research is required to establish whether poor injection is also contributing to the low performance of the nanowire-based solar cells.

8.4. References to Chapter 8

1. Galoppini, E., Rochford, J., Chen, H., Saraf, H., Lu, Y., Hagfeldt, A., & Boschloo, G. Fast Electron Transport in Metal Organic Vapor Deposition Grown Dye-sensitized ZnO Nanorod Solar Cells. *The Journal of Physical Chemistry B* **110**, 16159-16161 (2006).
2. Mora-Seró, I., Fabregat-Santiago, F., Denier, B., Bisquert, J., Tena-Zaera, R., Elías, J. & Lévy-Clément, C. Determination of carrier density of ZnO nanowires by electrochemical techniques. *Applied Physics Letters* **89**, 203117–203120 (2006).
3. Law, M., Greene, L.E., Johnson, J.C., Saykally, R. & Yang, P. Nanowire dye-sensitized solar cells. *Nature Materials* **4**, 455-459 (2005).
4. Cheng, H., Chiu, W., Lee, C., Tsai, S. & Hsieh, W. Formation of Branched ZnO Nanowires from Solvothermal Method and Dye-Sensitized Solar Cells Applications. *The Journal of Physical Chemistry C* **112**, 16359–16364 (2008).
5. Elías, J., Tena-Zaera, R. & Lévy-Clément, C. Effect of the chemical nature of the anions on the electrodeposition of ZnO nanowire arrays. *Journal of Physical Chemistry C* **112**, 5736–5741 (2008).
6. Konenkamp, R., Dloczik, L., Ernst, K. & Olesch, C. Nano-structures for solar cells with extremely thin absorbers. *Physica E* **14**, 219–223 (2002).
7. Hochbaum, A.I. & Yang, P. Semiconductor Nanowires for Energy Conversion. *Chemical Reviews* **110**, 527–546 (2010).
8. González-Valls, I. & Lira-Cantú, M. Vertically-aligned nanostructures of ZnO for excitonic solar cells: a review. *Energy & Environmental Science.* **2**, 19-34 (2009).
9. Martinson, A.B.F., Góes, M., Fabregat-Santiago, F., Bisquert, J., Pellin, M. & Hupp, J.T. Electron Transport in Dye-Sensitized Solar Cells Based on ZnO Nanotubes: Evidence for Highly Efficient Charge Collection and Exceptionally Rapid Dynamics. *The Journal of Physical Chemistry A* **113**, 4015–4021 (2009).

10. Martinson, A.B.F., McGarrah, J.E., Parpia, M.O.K. & Hupp, J.T. Dynamics of charge transport and recombination in ZnO nanorod array dye-sensitized solar cells. *Physical Chemistry Chemical Physics* **8**, 4655–4659 (2006).
11. Gao, Y., Nagai, M., Chang, T. & Shyue, J. Solution-Derived ZnO Nanowire Array Film as Photoelectrode in Dye-Sensitized Solar Cells. *Crystal Growth & Design* **7**, 2467–2471 (2007).
12. Guo, M., Diao, P. & Cai, S.M. Photoelectrochemical properties of highly oriented ZnO nanotube array films on ITO substrates. *Chinese Chemical Letters* **15**, 1113–1116 (2004).
13. Plank, N., Howard, I., Rao, A., Wilsin, M., Ducati, C., Mane, R. S., Louca, R.R.M., Bendall, J., Greenham, N.C., Miura, H., Friend, R.H., Snaith, H.J. &Welland, M.E. Efficient ZnO Nanowire Solid-State Dye-Sensitized Solar Cells Using Organic Dyes and Core−shell Nanostructures. *The Journal of Physical Chemistry C* **113**, 18515–18522 (2009).
14. Pradhan, B., Batabyal, S.K. & Pal, A.J. Vertically aligned ZnO nanowire arrays in Rose Bengal-based dye-sensitized solar cells. *Solar Energy Materials and Solar Cells* **91**, 769–773 (2007).
15. Lupan, O., Guerin, V.M., Tiginyanu, I.M., Ursaki, V.V., Chow, L., Heinrich, H. & Pauporte, T. Well-aligned arrays of vertically oriented ZnO nanowires electrodeposited on ITO-coated glass and their integration in dye sensitized solar cells. *Journal of Photochemistry and Photobiology A-Chemistry* **211**, 65–73 (2010).
16. Chen, G., Zheng, K., Mo, X., Sun, D., Meng, Q. & Chen, G. Metal-free indoline dye sensitized zinc oxide nanowires solar cell. *Materials Letters* **64**, 1336–1339 (2010).
17. Peulon, S. & Lincot, D. Mechanistic study of cathodic electrodeposition of zinc oxide and zinc hydroxychloride films from oxygenated aqueous zinc chloride solutions. *Journal of The Electrochemical Society* **145**, 864–874 (1998).
18. Tena-Zaera, R., Elías, J., Lévy-Clément, C., Mora-Seró, I., Luo, Y. & Bisquert, J. Electrodeposition and impedance spectroscopy characterization of ZnO nanowire arrays. *Physica Status Solidi a-Applications and Materials Science* **205**, 2345–2350 (2008).
19. Guillén, E., Azaceta, E., Peter, L.M., Arnost, Z., Tena-Zaera, R. & Anta, J.A. ZnO solar cells with an indoline sensitizer: a comparison between nanoparticulate films and electrodeposited nanowire arrays. *Energy & Environmental Science.* (2011). DOI: 10.1039/C0EE00500B.
20. Ito, S., Matsui, H., Okada, K., Kusano, S., Kitamura, T., Wada, Y. & Yanagida, S. Calibration of solar simulator for evaluation of dye-sensitized solar cells. *Solar Energy Materials and Solar Cells* **82**, 421-429 (2004).
21. Tena-Zaera, R., Elías, J. & Lévy-Clément, C. ZnO nanowire arrays: Optical scattering and sensitization to solar light. *Applied Physics Letters* **93**, (2008).
22. Howie, W.H., Harris, J.E., Jennings, J.R. & Peter, L.M. Solid-state dye-sensitized solar cells based on spiro-MeOTAD. *Solar Energy Materials and Solar Cells* **91**, 424–426 (2007).
23. Kieven, D., Dittrich, T., Bladai., A., Tornow, J., Schwarburg, K., Allsop, K. & Lux-Steiner, M. Effect of internal surface area on the performance of ZnO/In_2S_3/CuSCN solar cells with extremely thin absorber. *Applied Physics Letters* **92**, 153107 (2008).
24. Zhang, Q., Dandeneau, C.S., Zhou, X. & Cao, G. ZnO nanostructures for dye-sensitized solar cells. *Advanced Materials.* **21**, 4087-4108 (2009).
25. Hagfeldt, A., Boschloo, G., Sun, L., Kloo, L. & Pettersson, H. Dye-sensitized solar

cells. *Chemical Reviews* **110**, 6595-6663 (2010).
26. Bisquert, J. & Mora-Seró, I. Simulation of Steady-State Characteristics of Dye-Sensitized Solar Cells and the Interpretation of the Diffusion Length. *The Journal of Physical Chemistry Letters* **1**, 450–456 (2010).
27. Villanueva-Cab, J., Wang, H., Oskam, G. & Peter, L.M. Electron Diffusion and Back Reaction in Dye-Sensitized Solar Cells: The Effect of Nonlinear Recombination Kinetics. *The Journal of Physical Chemistry Letters* **1**, 748-751 (2010).
28. Tena-Zaera, R., Lévy-Clément, C., Bekeny, C., Voss, T., Mora-Seró, I. & Bisquert, J. Influence of the Potassium Chloride Concentration on the Physical Properties of Electrodeposited ZnO Nanowire Arrays. *The Journal of Physical Chemistry C* **112**, 16318–16323 (2008).
29. Zaban, A., Greenshtein, M. & Bisquert, J. Determination of the Electron Lifetime in Nanocrystalline Dye Solar Cells by Open-Circuit Voltage Decay Measurements. *ChemPhysChem* **4**, 859-864 (2003).
30. Bisquert, J., Zaban, A., Greenshtein, M. & Mora-Seró, I. Determination of Rate Constants for Charge Transfer and the Distribution of Semiconductor and Electrolyte Electronic Energy Levels in Dye-Sensitized Solar Cells by Open-Circuit Photovoltage Decay Method. *Journal of the American Chemical Society* **126**, 13550-13559 (2004).
31. Cameron, P.J., Peter, L.M. & Hore, S. How Important is the Back Reaction of Electrons via the Substrate in Dye-Sensitized Nanocrystalline Solar Cells? *The Journal of Physical Chemistry B* **109**, 930-936 (2005).
32. Cameron, P.J. & Peter, L.M. How does back-reaction at the conducting glass substrate influence the dynamic photovoltage response of nanocrystalline dye-sensitized solar cells? *Journal of Physical Chemistry B* **109**, 7392–7398 (2005).
33. Rousset, J., Saucedo, E. & Lincot, D. Extrinsic Doping of Electrodeposited Zinc Oxide Films by Chlorine for Transparent Conductive Oxide Applications. *Chemistry of Materials* **21**, 534–540 (2009).
34. Elías, J., Tena-Zaera, R., Wang, G. & Lévy-Clément, C. Conversion of ZnO Nanowires into Nanotubes with Tailored Dimensions. *Chemistry of Materials* **20**, 6633–6637 (2008).
35. Walker, A.B., Peter, L.M., Lobato, K. & Cameron, P.J. Analysis of Photovoltage Decay Transients in Dye-Sensitized Solar Cells. *The Journal of Physical Chemistry B* **110**, 25504-25507 (2006).
36. Villanueva-Cab, J., Oskam, G. & Anta, J. A simple numerical model for the charge transport and recombination properties of dye-sensitized solar cells: A comparison of transport-limited and transfer-limited recombination. *Solar Energy Materials and Solar Cells* **94**, 45-50 (2010).
37. He, C., Zheng, Z., Tang, H., Zhao, L. & Lu, F. Electrochemical Impedance Spectroscopy Characterization of Electron Transport and Recombination in ZnO Nanorod Dye-Sensitized Solar Cells. *The Journal of Physical Chemistry C* **113**, 10322–10325 (2009).
38. Tornow, J., Ellmer, K., Szarko, J. & Schwarzburg, K. Voltage bias dependency of the space charge capacitance of wet chemically grown ZnO nanorods employed in a dye sensitized photovoltaic cell. *Thin Solid Films* **516**, 7139–7143 (2008).
39. Pettinger, B., Schoppel, H.R. & Gerischer, H. Tunnel effects in spectral sensitization on highly doped ZnO electrodes. *Berichte der Bunsen-Gesellschaft - Physical Chemistry Chemical Physics* **77**, 960–966 (1973).
40. Pettinger, B., Schoppel, H.R. & Gerischer, H. Tunneling processes at highly doped

ZnO electrodes in contact with aqueous electrolytes.1. Electron exchange with conduction band. *Berichte der Bunsen-Gesellschaft - Physical Chemistry Chemical Physics* **78**, 450–455 (1974).
41. Bisquert, J., Fabregat-Santiago, F., Mora-Seró, I., Garcia-Belmonte, G. & Giménez, S. Electron Lifetime in Dye-Sensitized Solar Cells: Theory and Interpretation of Measurements. *The Journal of Physical Chemistry C* **113**, 17278–17290 (2009).
42. Yodyingyong, S., Zhang, Q., Park, K., Dandeneau, C., Zhou, X., Triampo, D. & Cao, G. ZnO nanoparticles and nanowire array hybrid photoanodes for dye-sensitized solar cells. *Applied Physics Letters* **96**, 073115 (2010).
43. Baxter, J.B. & Aydil, E.S. Dye-sensitized solar cells based on semiconductor morphologies with ZnO nanowires. *Solar Energy Materials and Solar Cells* **90**, 607-622 (2006).
44. Zhang, Q. & Cao, G. Nanostructured photoelectrodes for dye-sensitized solar cells. *Nano Today* **6**, 91-109 (2011).
45. Gan, X., Li, X., Gao, X., Zhuge, F. & Yu, W. ZnO nanowire/TiO_2 nanoparticle photoanodes prepared by the ultrasonic irradiation assisted dip-coating method. *Thin Solid Films* **518**, 4809-4812 (2010).
46. Ku, C. & Wu, J. Electron transport properties in ZnO nanowire array/nanoparticle composite dye-sensitized solar cells. *Applied Physics Letters* **91**, 093117 (2007).
47. Chen-Hao, K. & Jih-Jen, W. Chemical bath deposition of ZnO nanowire–nanoparticle composite electrodes for use in dye-sensitized solar cells. *Nanotechnology* **18**, 505706 (2007).
48. Park, N.G., Kang, M.G., Kim, K.M., Ryu, K.S., Chang, S.H., Kim, D.K., van de Lagemaat, Benkstein, K.D. & Frank, A.J. Morphological and Photoelectrochemical Characterization of Core−Shell Nanoparticle Films for Dye-Sensitized Solar Cells: Zn−O Type Shell on SnO_2 and TiO_2 Cores. *Langmuir* **20**, 4246-4253 (2004).
49. Chen, S.G., Chappel, S., Diamant, Y. & Zaban, A. Preparation of Nb_2O_5 Coated TiO_2 Nanoporous Electrodes and Their Application in Dye-Sensitized Solar Cells. *Chemistry of Materials* **13**, 4629-4634 (2001).
50. Palomares, E., Clifford, J.N., Haque, S.A., Lutz, T. & Durrant, J.R. Control of Charge Recombination Dynamics in Dye Sensitized Solar Cells by the Use of Conformally Deposited Metal Oxide Blocking Layers. *Journal of the American Chemical Society* **125**, 475-482 (2003).
51. Diamant, Y., Chen, S.G., Melamed, O. & Zaban, A. Core−Shell Nanoporous Electrode for Dye Sensitized Solar Cells: the Effect of the $SrTiO_3$ Shell on the Electronic Properties of the TiO_2 Core. *The Journal of Physical Chemistry B* **107**, 1977-1981 (2003).
52. Diamant, Y., Chappel, S., Chen, S.G., Melamed, O. & Zaban, A. Core-shell nanoporous electrode for dye sensitized solar cells: the effect of shell characteristics on the electronic properties of the electrode. *Coordination Chemistry Reviews* **248**, 1271-1276 (2004).
53. Wang, Z., Huang, C. H., Huang, Y.Y., Hou, Y.J., Xie, P.H., Zhang, B. W. & Cheng, H.M. A Highly Efficient Solar Cell Made from a Dye-Modified ZnO-Covered TiO_2 Nanoporous Electrode. *Chemistry of Materials* **13**, 678-682 (2001).
54. Guerin, V.M., Magne, C., Pauporté, T., Le Bahers, T. & Rathousky, J. Electrodeposited nanoporous versus nanoparticulate ZnO films of similar roughness for dye-sensitized solar cell applications. *ACS Applied Materials & Interfaces* **2**, 3677-3685 (2010).

Chapter 9

Electron Transport and Recombination in ZnO Dye-Sensitized Solar Cells

9. Electron transport and recombination in ZnO dye-sensitized solar cells

The work described in the previous Chapters has been devoted to the study of several ZnO-based DSC systems. Different dyes, electrolytes and ZnO nanostructures have been tested. Taking advantage of the experience gained thanks to these studies, different cell configurations have been fabricated to perform a comprehensive study of the electron transport and recombination in ZnO DSCs.

The performance of ZnO-based dye-sensitized solar cells was studied for three different configurations involving two dyes and two types of electrolytes with the iodide/triiodide couple as redox mediator: ZnO/N719/organic-solvent-electrolyte (C1), ZnO/D149/organic-solvent-electrolyte (C2) and ZnO/N719/ionic-liquid-electrolyte (C3). No combination of D149 dye and ionic-liquid-based electrolyte was considered due to the instability described in **Chapter 7**.

In comparison to TiO_2, very few studies of the electronic behaviour have been carried out on dye-sensitized nanostructured ZnO solar cells[1-4]. The aim of the present study is to get further insight into the behaviour of ZnO-based solar cells, paying special attention to its recombination and transport properties and trying to elucidate if the same theories and approximations formulated for TiO_2 can be applied to ZnO. Furthermore, it is aimed to find the factors, which determine the lower performance of ZnO-based solar cells so that strategies for improvement can be formulated. In this regard, different dyes and electrolytes have been tested in order to check if general characteristics can be found that only depend on the intrinsic properties of the semiconductor oxide, but not on the other components of the cell. As different experimental techniques have been used, the results must be analyzed carefully. To make an accurate comparison, the cells must be tested under similar working conditions. In some cases this is simply achieved by setting a similar experimental condition. In other cases, it is necessary to make appropriate corrections (concerning e.g. band shifts or the position of the Fermi level) when analyzing the data. In this regard, special care has been taken when comparing the different samples analyzed in this study.

9.1. Fabrication and characterization of the devices

The materials used for the fabrication of the cells are summarized in **Table 9.1** and the parameters of the illumination source used for photovoltaic characterization in **Table 9.2**.

Table 9.1 Summary of the materials employed in the fabrication of the cells.

ZnO		Dyes	Electrolytes	Counter electrode
Evonik AdNano ZnO20 / PI-KEM 1:1 Cell area: 0.64 cm^2	**C1**	0.5 mM N719 (1 hour)	0.5M LiI/ 0.05M I_2/ 0.5 M TBP in 3-methoxypropionitrile	*Platisol* (TEC 8)
	C2	D149 (0.5 mM) chenodeoxycholic acid (0.7 mM) in tert-butyl alcohol/acetonitrile (1:1) (30 minutes)	0.05 mM I_2 0.5 M TBAI in acetonitrile/ ethylencarbonate (1:4)	
	C3	0.5 mM N719 (1 hour)	0.05M I_2 in TCNB/PMIMI (35:65 vv)	

Table 9.2 Illumination set-up used for DSC testing.

Illumination source	Filters	Calibration
Xenon Lamp	AM 1.5 filter	Reference solar cell (Oriel, 91150) + KG5 (100 mW cm^{-2})

The nanoparticle films were deposited on TCO substrates previously covered via spray deposition with a thin continuous ZnO layer which acts as blocking layer[5] (**Section 4.2**). Photoanodes and counter electrodes were sealed together in a sandwich configuration using a hot-melt polymer (SX1170-25, Solaronix 25 μm, Solaronix). Electrochemical impedance spectroscopy measurements under illumination at open circuit and intensity-modulated spectroscopy were carried out using a Solartron 1250 frequency response analyzer (FRA) and a Solartron 1286 electrochemical interface. EIS spectra were fitted to equivalent circuit (a) (**Section 3.6.1**).

9.2. Photovoltaic performance

Figure 9.1 shows the current-voltage characteristics (AM 1.5) for one representative cell of each configuration. C2 exhibits the highest photocurrent, due to the large absorption coefficient of the D149 dye compared to N719[5]. In C2 and C3, the same dye (N719) is employed, but for C3 an electrolyte with a higher viscosity is used. The fill factors and the efficiencies obtained for each cell are also shown in the figure.

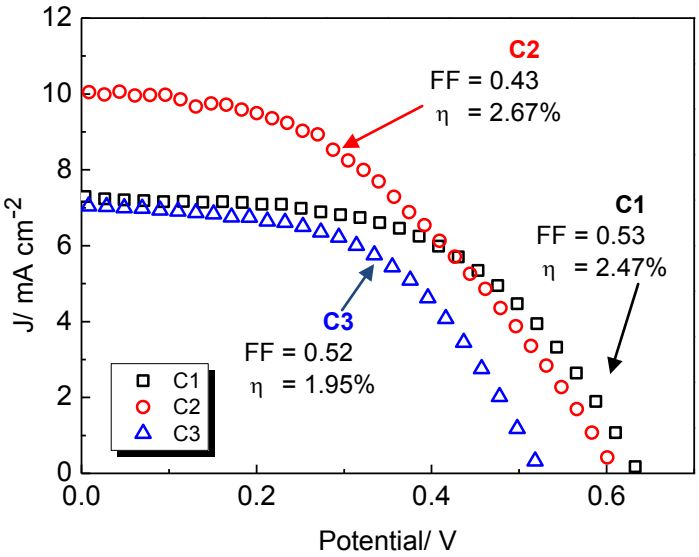

Figure 9.1 Representative IV curves for the different configurations analyzed. Fill factors and efficiencies are also shown in the graph.

As analyzed in **Chapters 6** and **7**, diffusion limitations are usually observed in cells containing pure ionic liquid electrolytes[6]. Therefore, a lower photocurrent was expected for C3 with respect to C1. However, both types of cells exhibit a similar photocurrent, which seems to indicate that slow diffusion in the electrolyte is not a significant limiting factor in C3. This is in agreement with the results discussed in **Section 6.4**, where it was observed that photocurrent limitations for a pure PMII electrolyte do not have a major effect at photocurrent densities below 7 mA cm^{-2} (**Figure 6.10)**.

The highest value of the open circuit voltage is found for cells of configuration C1. This was expected due the presence of tert-butylpyridine (TBP) in the electrolyte (see **Section 6.5**). C2 exhibits similar photovoltage although TBP is not used in the electrolyte. This could be due to a higher injection, and to the use of TBAI instead of LiI. TBA^+ is known to have a positive effect on the photovoltage due to the screening of conduction band electrons from recombination with the triiodide[7,8]. On the other hand, the configuration with pure ionic-liquid-based electrolyte (C3) gives the lowest open

circuit voltage, which is also in agreement with previous observations described in **Chapters 6 and 7**. Fill factors are low, especially for the cell with the highest photocurrent. It must be pointed out that even the most efficient ZnO-based solar cell obtained up to now (reported by Saito and Fujihara in 2008[9]) shows a fill factor of only 0.58. Quintana et al.[1], when comparing TiO_2 and ZnO-based cells with similar characteristics (same particle size, same electrolyte, same dye) found that ZnO cells have considerably lower fill factors (0.49) than TiO_2 cells (0.69). The best performing cell, as a consequence of its high photocurrent, corresponds to configuration C2. The incident photon-to-current efficiencies, IPCE (**Appendix 11.8**) are around 70% for C1, and 30% for C1 and C2 at the maximum of the dye absorption.

9.3. Light intensity dependence of the open circuit voltage

The semilogarithmic plots in **Figure 9.2** show the light intensity (I_0) dependence of the open circuit voltage V_{oc} for the different configurations.

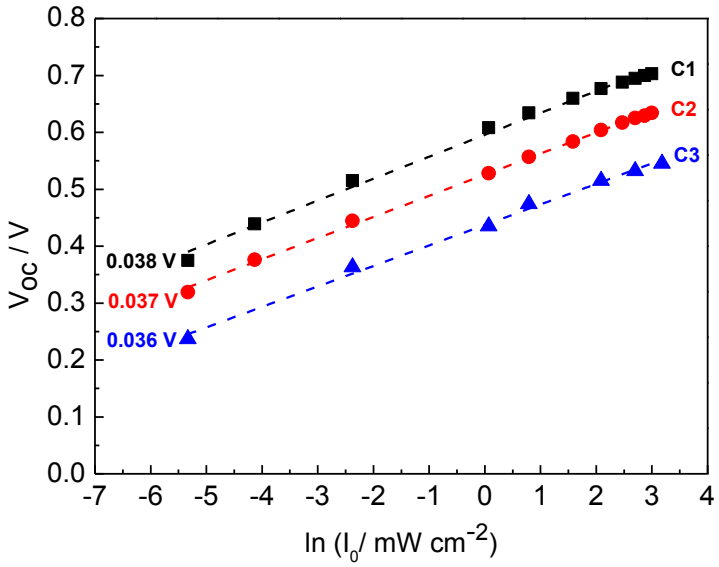

Figure 9.2 Light intensity dependence of the open circuit voltage. Slopes are indicated in the graph.

For all of the samples V_{oc} depends linearly on the logarithm of the light intensity (**Equation 2.21**) and the slopes lie close to 37 mV. All configurations are found to depart from ideal-diode behaviour, with non-ideality factors higher than 1 (**Table 9.3** and **Figure 9.2**).

Table 9.3 Slopes, ideality factors (*m*) and reaction orders (β) obtained from the open circuit voltage plots for the three configurations.

Sample	Slope (V)	m	1/m (β)
C1(ZnO/N719/OLE)	0.038	1.46	0.68
C2(ZnO/D149/OLE)	0.037	1.42	0.70
C3(ZnO/N719/ILE)	0.036	1.38	0.72
Ideal	0.026	1	1

As described in **Chapter 2**, dye-sensitized solar cells usually behave non-ideally[10], although the origin of this non-ideality is not well understood yet. Frequently, this phenomenon is attributed to recombination via surface states[11]. The definition of sublinear recombination kinetics with a reaction order (β) lower than one take into account this non-ideality[10,12]. A high non-ideality is also observed for the ZnO DSCs studied here. Most TiO_2 solar cells, including high efficiency cells, are also non-ideal in response, exhibiting slopes between 30 and 40 mV[13] or even more than 50 mV[14] in the V_{oc} versus ln(I_0) plots. Recently, Jennings et al.[15] have reported an ideal slope for TiO_2 cells in the presence of a high Li^+ concentration in the electrolyte. Cells become more ideal as the Li^+ increases. This ideality seems thus to depend on the electrolyte. In addition, the effect of the dye on the ideality needs to be taken into account. A slightly different slope is found for each configuration. The ideality factor *m* is related to the reaction order through its inverse, $m = 1/\beta$ (**Section 2.2**). In the case of the ZnO solar cells studied here, it is found that $\beta \sim 0.7$ for the three configurations (**Table 9.3**). Alternatively, as it described in **Chapter 2**, according to some authors[10] the reaction order can be estimated from the slope of the charge-transfer resistance versus voltage in an EIS experiment. A more detailed discussion of this approach is included below.

The steady-state electron concentration can be also affected by a possible back reaction via the substrate. The linear behaviour of the V_{oc} in the semilogarithmic plots (**Figure 9.2**) is an indication that recombination through the substrate is negligible over the entire range of measured photon fluxes[16].

9.4. Electrochemical impedance spectroscopy studies

Electrochemical impedance spectroscopy measurements were carried out at open circuit over a wide range of light intensities. In experiments performed in the open circuit mode the voltage corresponds to the V_{oc} observed at the intensity of the incident

light[17]. Hence at this voltage there is no net current flow and no drop in the R_{ct} and C_{ct} plots is observed at high voltages (**Section 6.3** and **Section 7.4)**. An example of spectra for each configuration can be found in **Figure 9.3**.

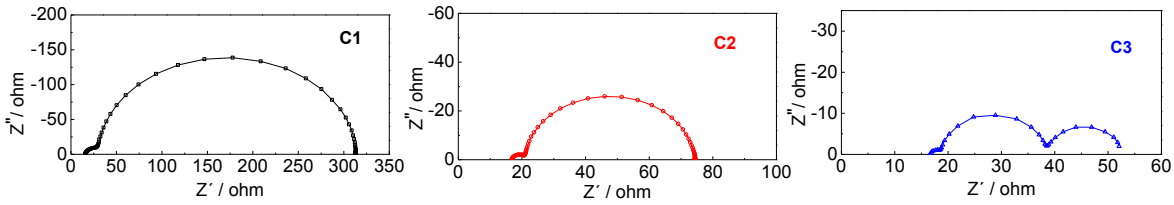

Figure 9.3 Impedance spectra of the devices studied in this work at the open circuit photovoltage (100 mW cm^{-2}) for each configuration.

As was seen in **Chapter 2** the capacitance measured in TiO_2 solar cells by EIS usually shows an exponential variation with potential, corresponding to an exponential trap energy distribution below the conduction band edge[18]. This distribution is governed by the parameter α ($\alpha = T/T_0$) according to **Equation 2.41** ($C_\mu = C_0 \exp(\alpha V/kT)$). The capacitance values obtained for the three configurations of ZnO solar cells show also this exponential behaviour (**Figure 9.4**). However, as already discussed in **Chapters 7** and **8** the capacitance for ZnO solar cells exhibits a very weak dependence on the voltage, with α ranging between 0.11 and 0.13 for the three configurations studied (**Table 9.4**).

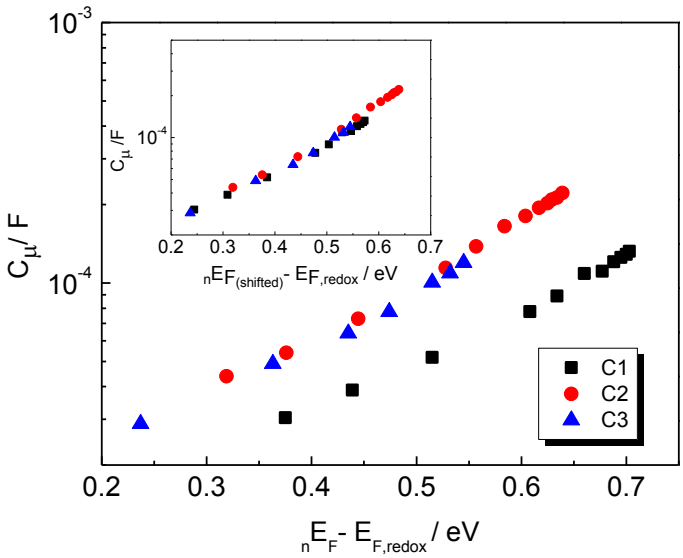

Figure 9.4 Capacitance values obtained from EIS fitting. The inset shows the results after band edge correction for configuration C1 (see text for details).

The results point to an exponential trap energy distribution in ZnO cells with a very high characteristic temperature. TiO_2 cells usually show a much lower characteristic temperature, with α values ranging between 0.2-0.5[19,20]. The distribution parameter is very similar for the three configurations studied here, and in concordance with the one found in previous EIS studies of ZnO-based solar cells (**Chapter 6** and **Chapter 7**). Quintana et al.[1] also reported a similar behaviour of ZnO-based solar cells. From their charge extraction measurements a trap distribution parameter α = 0.13 is obtained.

A comparison between transport and recombination rates for different DSCs can only be made if the ratio of the number of electrons in the conduction band and in traps is the same for all the samples[21] (**Section 2.5**). For cells with similar trap distributions, (as may be assumed for C1, C2 and C3 due to the similarity of α), this condition is fulfilled when the position of the quasi-Fermi level relative to the conduction band edge ($_nE_F$ - E_c) is set to equivalent values in the cells being compared (**Figure 9.5a**). Under open circuit conditions it can be assumed that the electron quasi-Fermi level through the film is approximately uniform (**Figure 2.4 and 9.19**). On the other hand, the energy of the conduction band edge can become shifted as a consequence of oxide/electrolyte interactions (**Figure 9.5.b**). This kind of displacements has been reported a number of times in literature[22] and has been described in **Chapter 6** for an electrolyte containing the dicyanamide anion. When comparing samples with a similar trap distribution, the chemical capacitance data can indicate a possible shift in the conduction band edge[23,24] (**Section 6.6**).

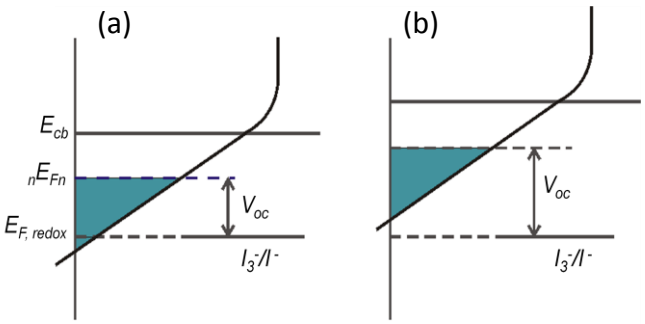

Figure 9.5 Effect of the conduction band-edge position E_{cb} on the open circuit voltage V_{oc} for a given exponential trap density at the same illumination. Band–edge shift from (a) to (b) increases the V_{oc} of cell.

In **Figure 9.4** an upward displacement of the ZnO conduction band is observed for C1. This behaviour can be attributed to the presence of TBP in the electrolyte[25] (**Section 6.5**). Therefore, the data of C1 have been shifted by -0.130 V (see inset **Figure 9.4**), which leads to an overlap of the capacitance values for the three kinds of cells[24]. The

criterion for this modification is that the chemical capacitance is directly related with the difference between the Fermi level and the conduction band edge by **Equation 2.40**[18] and an overlap of the different plots will lead to an E_c-$_nE_F$ difference similar for the three cells. Taking into account this shift for configuration C1, it is possible to compare the three configurations at the same values of E_c-$_nE_F$, so that the electron properties of these solar cells based on different dyes and electrolytes can safely be compared[17].

Consequently, the same shift has been applied to the other recombination and transport parameters (see below), and they are plotted versus $_nE_{F(shifted)}$-$E_{F,redox}$. Additionally, data of the transport resistance can also be used to estimate the band shift[17](**Section 6.3**) if the diffusion coefficient of free electrons is assumed to be constant. As will be shown below, a similar shift is observed for the transport resistance data of C1.

As pointed out several times along this thesis, the transmission-line feature commonly attributed to electron transport in the semiconductor oxide[23,26,27] is not observed in the EIS spectra of the ZnO films (**Figure 9.3**). This is probably due to the higher mobility of electrons in the ZnO material in comparison to TiO_2[28]. Therefore, the reliability of transport resistance values obtained from impedance measurements (**Figure 9.6a**) is questionable.

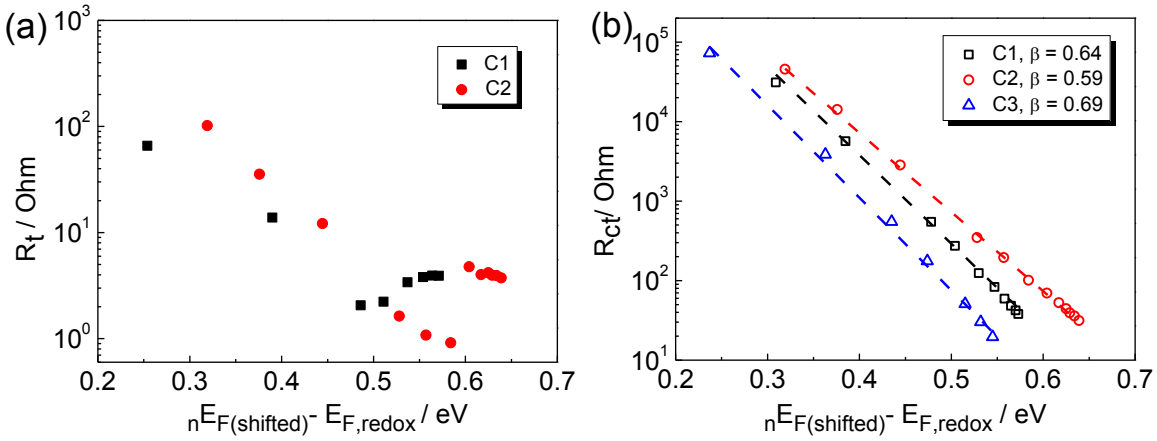

Figure 9.6 Transport resistance (a) and charge transfer resistance (b) obtained from EIS fitting. For the transport resistance only the results of C1 and C2 are shown.

At high voltages the transport resistance versus voltage plot obtained from the fittings is flattened (**Figure 9.6a**). Wang and Peter[29] also found this flattening when fitting the transport resistance from impedance measurements for TiO_2 cells under illumination at

high light intensities. These authors claimed that when the value of R_t becomes lower than the resistance of the cathode, fitting becomes unreliable. For ZnO cells, the transport resistance is not distinguishable from the cathode feature at any bias potential. A suggestion to overcome this problem involving IMPS measurements in the fitting will be described below.

In **Figure 9.6b** the charge transfer resistances for C1, C2 and C3 are plotted versus ${}_nE_{F(shifted)}$-$E_{F,redox}$. C3 exhibits the lowest charge transfer resistance, which explains the difference of more than 100 mV of the photovoltage for this cell with respect to the other two. C1 exhibits slightly faster recombination than C2. The small difference in open circuit voltage between C1 and C2 can be explained by the difference in the position of the conduction band observed in the capacitance measurements as well as by the difference in the recombination resistance.

The charge transfer resistance contains primary information regarding the recombination rate at steady-state[30] and it has been fitted to **Equation 2.10** ($R_{ct} = R_{ct,0}\ exp(-\beta qV/kT)$). Values of the transfer coefficient β are found to be 0.64, 0.59 and 0.69 for C1, C2 and C3, respectively. The transfer coefficient (β) can be considered[10], as discussed in **Chapter 2**, an empirical estimation of the reaction order in sublinear recombination kinetics. As in TiO_2, this transfer parameter is greatly affected by the composition of the electrolyte and the dye. The role of the dye in the recombination of electrons with the oxidized species might be important. It is reported that dyes can influence recombination in two ways: (1) they can prevent electrons in the metal oxide from reacting with acceptor species in the electrolyte, or (2) they can facilitate recombination via an association between the dye and triiodide[20]. The influence of dye structure on charge recombination has been stressed recently[31,32]. It must be pointed out that values of $\beta \sim 0.5$ were obtained in previous EIS studies in the dark for ionic liquid electrolytes (**Chapter 7**), as well as for cells with configuration 2 in the dark (results not shown). This is significantly lower than the values observed under illumination for C1, C2 and C3, respectively. Apart from an influence of different triiodide concentrations in the vicinity of the film, this difference may be a consequence of recombination with the oxidized dye, a recombination path that is usually neglected.

As already mentioned, the reaction order is associated with the non-ideality factor m (**Section 2.2**, $\beta = 1/m$[10]) obtained from the V_{oc} vs. ln(I_0) plots (**Figure 9.2**). As shown in

Table 9.4, this relation is not completely satisfied for any configuration, especially for C2. This could indicate that other factors contribute to the non-ideal behaviour observed in the V_{oc} vs. ln(I_0) plots apart from a non-linear recombination. As mentioned in **Section 2.2**, some authors[32] have recently proposed an additional non-ideality parameter that describes the departure of the concentration of conduction band electrons from ideal (Boltzmann) statistics. According to this, the parameter m and the reaction order β would satisfy a different relation[32] that could account for the results in **Table 9.4**.

Table 9.4 Distribution parameter (α), characteristic temperature (T_0), and charge transfer parameter (β) obtained from EIS measurements under illumination. The reaction orders obtained by the inverse of the ideality factor from V_{oc} versus ln(I_0) plots (**Figure 9.2** and **Table 9.3**) are also indicated.

Sample	α	T_0 (K)	β (from R_{ct} fitting)	$1/m$ (β)
C1 (ZnO/N719/OLE)	0.11	2700	0.64	0.68
C2(ZnO/D149/OLE)	0.13	2300	0.59	0.70
C3(ZnO/N719/ILE)	0.12	2500	0.69	0.72

In addition, the lower V_{oc} obtained for C3 can be a consequence of a displacement of the equilibrium redox potential of the I^-/I_3^- couple[33] (**Equation 2.16**). Taking into account that the molar iodide concentration in configuration C3 is much larger (2.4 M) than in the other two (0.5 M), the redox potential of the electrolyte should be shifted towards more negative values. If the Fermi level in the semiconductor is fixed, this displacement leads to a lower photovoltage. However, using the Nernst equation for a 2-electron redox process, only a 20 mV displacement of the redox equilibrium level is predicted between the organic liquid electrolytes (C1, C2) and the ionic liquid electrolyte (C3).

9.5. Open circuit voltage decay and lifetime measurements

Open circuit voltage decay experiments were carried out to probe the recombination kinetics. **Figure 9.7** shows the photovoltage transients for the three configurations in a semilogarithmic plot.

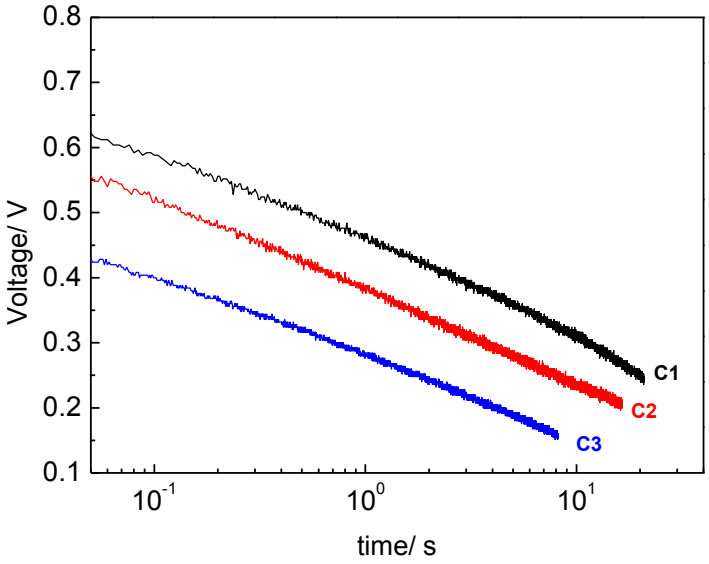

Figure 9.7 Open circuit voltage decays for the three configurations studied.

According to Walker et al.[11], voltage time decay should become logarithmic at longer times if recombination occurs through the semiconductor/electrolyte interface via an exponential distribution of trapping states and the quasistatic approximation holds. The slope in the semilogarithmic plot can be related to the trap distribution parameter α by[11]

$$\frac{dV_{oc}(t)}{d\ln t} \approx -\frac{k_B T/q}{1-\alpha} \tag{9.1}$$

The voltage vs. ln(t) plots yield a similar slope for the three configurations studied (**Figure 9.7**). However, the decay is much steeper than predicted by the trap distribution parameter obtained from the capacitance measurements (**Figure 9.4** and **Table 9.4**). This can be a further indication of non-linear recombination, which can influence the slope in the voltage versus ln(t) plot as shown in the simulations reported in Ref. [34]. The logarithmic behaviour in **Figure 9.7** is also an indication that back reaction via the substrate is negligible[16]. This is consistent with the fact that the illumination dependence of the open circuit voltage (**Figure 9.2**) is linear in the semilogarithmic plot[35].

IMVS measurements were carried out for the three configurations at different intensities of the light. In **Figure 9.8**, examples of IMVS spectra are shown for each of the configurations at the same Fermi level (taking into account the shift for C1).

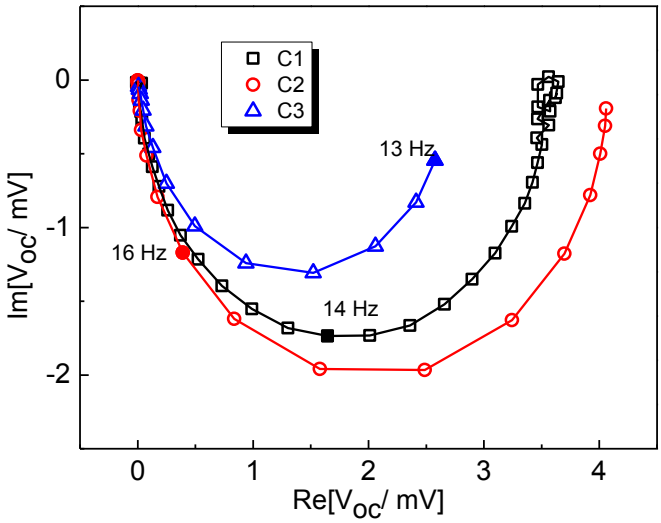

Figure 9.8 IMVS spectra for C1, C2 and C3 at approximately the same Fermi level.

The effective electron lifetime is obtained from three different techniques including OCVD and small perturbation measurements according to:

$$\tau_n^{(OCVD)} = \frac{k_B T}{q} \left(\frac{dV_{oc}}{dt}\right)^{-1} \tag{3.1}$$

$$\tau_n^{(EIS)} = R_{ct} C_\mu \tag{3.11}$$

$$\tau_n^{(IMVS)} = \frac{1}{\omega_{min}} \tag{3.13}$$

The corresponding results can be found in **Figure 9.9.** Once again the voltage has been corrected to account for the band displacement as explained above.

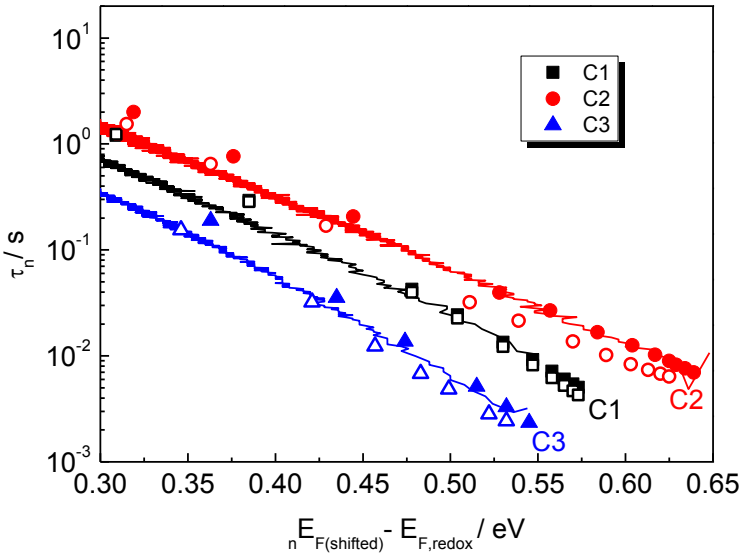

Figure 9.9 Electron lifetimes for the three configurations obtained from EIS, OCVD and IMVS measurements.

There is a very good agreement among the lifetimes extracted from the three techniques. In line with the lower recombination resistance found in **Figure 9.6** for configuration C3, the electron lifetime for C3 is found to be much shorter than for the other configurations. This explains the much lower photovoltage found for this kind of cell. Configuration C2 exhibits the longest lifetime, which explains its similar voltage to C1 despite the lack of TBP in the electrolyte.

The slopes of the log-lin plot of lifetimes versus voltage yield a distribution parameter value that is considerably higher than the value obtained from the capacitance. This is consistent with sub-linear recombination kinetics. In this case, the reaction order needs to be taken into account and the lifetime versus the voltage should give an exponential with a characteristic exponent (with respect to k_BT/q) equal to α-β (**Equations 2.48** and **2.51**). A comparison between the predicted values and the experimental results for each technique are summarized in **Table 9.5**.

Table 9.5 Exponent α-β predicted from capacitance and charge transfer measurements and obtained experimentally from electron lifetime measured by EIS, IMVS and OCVD.

Cell	α	β (from R_{ct} fitting)	α-β predicted	α-β EIS	α-β IMVS	α-β OCVD
C1(ZnO/N719/OLE)	0.11	0.66	-0.55	-0.52	-0.54	-0.43
C2(ZnO/D149/OLE)	0.13	0.59	-0.46	-0.46	-0.46	-0.40
C3(ZnO/N719/ILE)	0.12	0.69	-0.57	-0.57	-0.53	-0.55

The predicted values are consistent with the values obtained from lifetime measurements by EIS and IMVS, but not for OCVD, which shows the largest deviations.

9.6. "Short circuit voltage" measurements

Short Circuit Voltage (V_{sc}) measurements[36] allow to make an estimation of the position of the quasi Fermi level ($_nE_F$) in the mesoporous ZnO film under illumination at short circuit conditions as explained in **Section 3.4**. Examples for configuration C1 at low and high light intensities can be found in **Figure 9.10a** and **9.10b**.

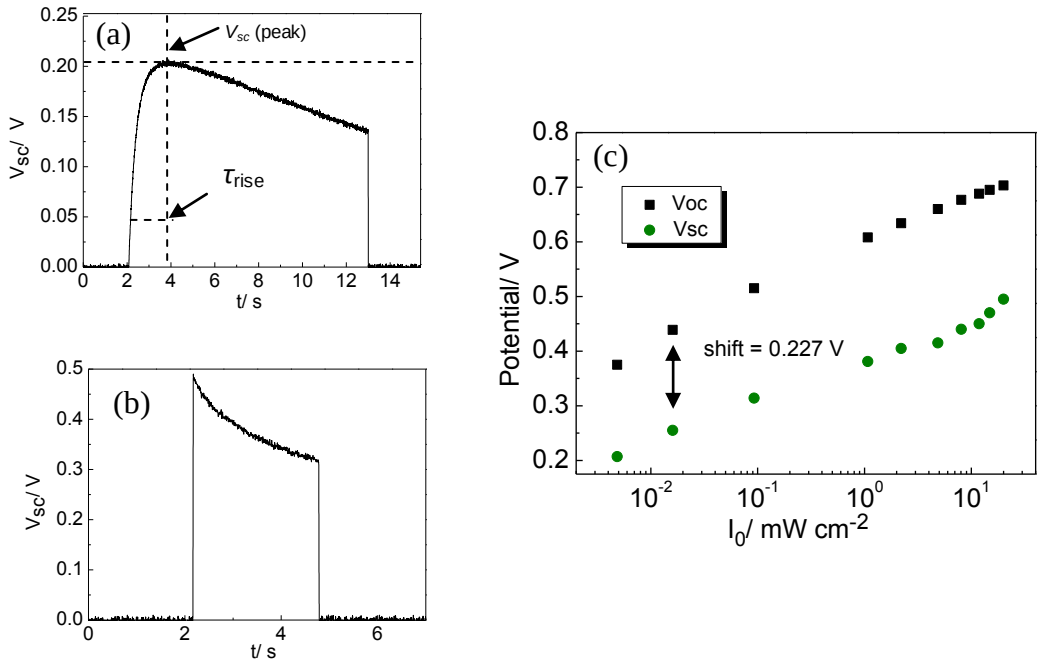

Figure 9.10 Short circuit voltage for configuration C1 (a) at low light intensity ($4.8 \cdot 10^{-3}$ mW cm^{-2}) and (b) at high intensity (20 mW cm^{-2}). V_{oc} and V_{sc} versus light intensity for C1(c).

As can be seen in **Figure 9.10a**, there is a rise time before the voltage reaches its maximum V_{sc}, and afterwards the voltage decays. This rise time is very short for high light intensities (**Figure 9.10b)**. In **Figure 9.10c** the V_{sc} measured at different light intensities is plotted together with the open circuit voltage for C1. From this plot the shift of the quasi-Fermi level between open and short circuit conditions is obtained, accounting for 0.227 V and 0.222 V for configurations C1 and C2 respectively. A similar shift can be found in previous reports for ZnO[1] and TiO_2[36]. The shift for C3 is found to be smaller, 0.150 V, which is consistent with the shorter electron lifetime for this type of cell.

A deviation of the short circuit voltage at high light intensities as the one observed in **Figure 9.10c** was obtained for all the measurements. Since a mechanical switch was used, a non-perfect synchronization between circuit opening and turning off of the light can lead to an overestimation (underestimation) of the voltage measured, due to electron accumulation (extraction). This fact can turn into a problem when making measurements at high light intensity, where the transient responses of the cells can be faster than the switch synchronization. This could explain the deviation found when measuring V_{sc} at high light intensities. On the other hand, at lower intensities, imperfect switch synchronization should not introduce any significant error. Therefore, these

values were used to obtain the voltage shift. Interestingly, this technique was not suitable for measurements of the nanowire samples (**Appendix 11.9**).

9.7. Electron transport in ZnO-based solar cells

Electron transport properties in the nanostructured metal oxide were studied using intensity-modulated photocurrent spectroscopy (IMPS)[37,38] (**Figure 9.11**).

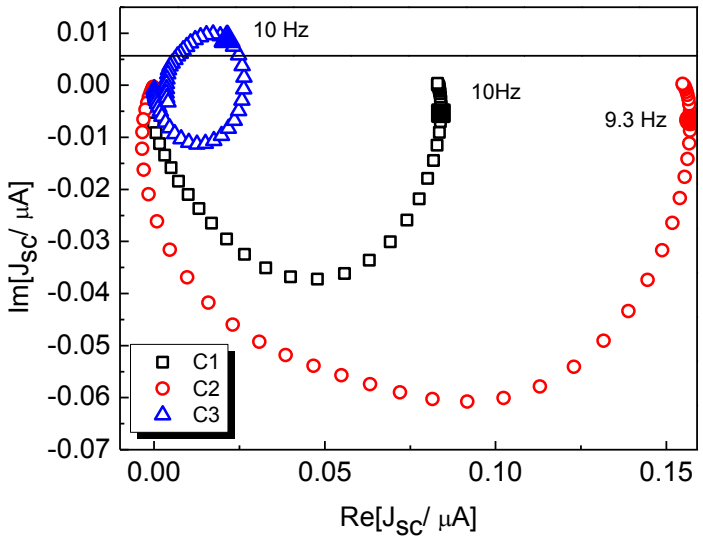

Figure 9.11 IMPS spectra for C1, C2 and C3 measured at the same light intensity.

The spectra show the typical shape of an IMPS response for C1 and C2 over the complete range of intensities studied (**Figure 9.11**). However, for C3 an additional relaxation feature in the upper quadrant of the IMPS response appears at high light intensities. This behaviour has been already reported for dye-sensitized solar cells where the iodide/triiodide redox couple was substituted by a Co(dbbip)$_2$ redox shuttle and was attributed to diffusion limitation in the electrolyte[39].

The double logarithmic plot in **Figure 9.12a** shows how the electron lifetimes τ_n from IMVS measurements and the time constant obtained from the IMPS spectrum τ_{IMPS} depend on the light intensity. We found a slope of -0.8 for the light intensity dependence of τ_{IMPS} and a slope of -0.7 for the light intensity dependence of τ_n. This slope values are in agreement with the ones obtained for dye sensitized TiO_2[37,38] and ZnO[1,2] cells.

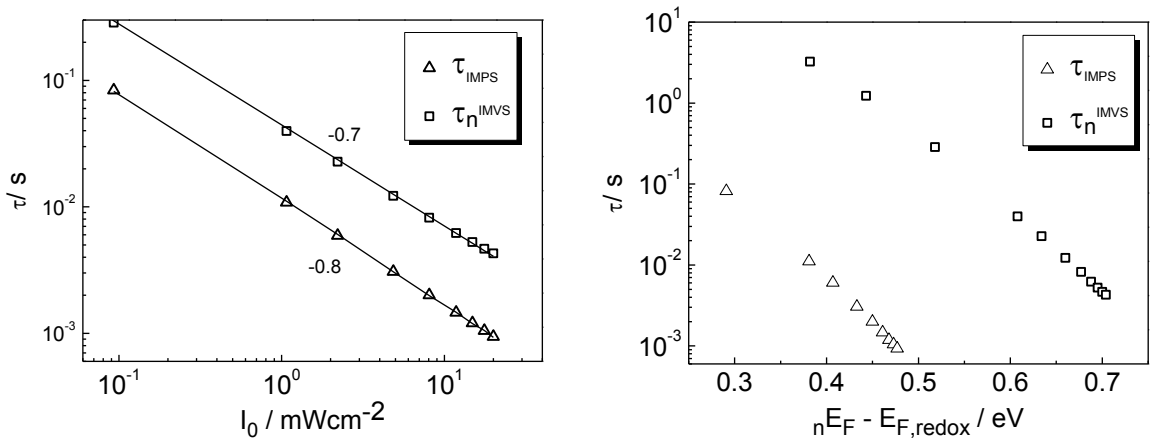

Figure 9.12 IMPS and IMVS time constants for C1 as a function of light intensity (a) and as a function of Fermi level (b).

The time constants from IMPS measurements can be interpreted as the average electron transport time provided that transport time is considerably shorter than the electron lifetime[40]. If this condition is not fulfilled, time constants obtained from IMPS spectra are partially influenced by recombination. In **Figure 9.12b** IMVS and IMPS time constants are plotted versus the Fermi level energy. IMPS time constants are at least two orders of magnitude smaller than the IMVS time constants, suggesting that the effects of recombination on the IMPS response can be neglected. This applies for the three configurations. As introduced already in **Equation 3.14,** in the absence of recombination the IMPS time constant can be related to the effective electron diffusion coefficient (D_n) using an expression of the form[41]

$$\tau^{IMPS} = \frac{d^2}{\gamma D_n} \tag{3.14}$$

where γ is a numerical factor, which depends on layer thickness (d), absorption coefficient (α_{abs}) and illumination direction[42-45]. A plot of this factor γ versus $\alpha_{abs}d$ can be found in the **Appendix 11.10**. According to **Figure 8.3** in the previous Chapter, the absorptance for the ZnO nanoparticulated film sensitized with the D149 dye is 0.9 at 530 nm (the wavelength of the light source used for testing). For a film thickness of 8 μm and taking into account the relation between absorptance and transmittance (neglecting reflectance) expressed in **Equation 5.1**, $\alpha_{abs}d$ is ~1, which corresponds to a numerical factor γ of ~2.61 (**Appendix 11.10**). Note that this factor is obtained for the sample (C2), which exhibits the highest absorptance. For C1 and C3, γ is expected to be different due to the lower absorption coefficient of N719. However, according to the figure in **Appendix 11.10**, no significant change is expected and the validity of this

approximation is assumed. In **Figure 9.20**, the diffusion coefficients for the three configurations with respect to the position of the Fermi level are shown (taking into account the conduction band shift for C1). Similar diffusion coefficients have been reported by Quintana et al.[1] for ZnO solar cells.

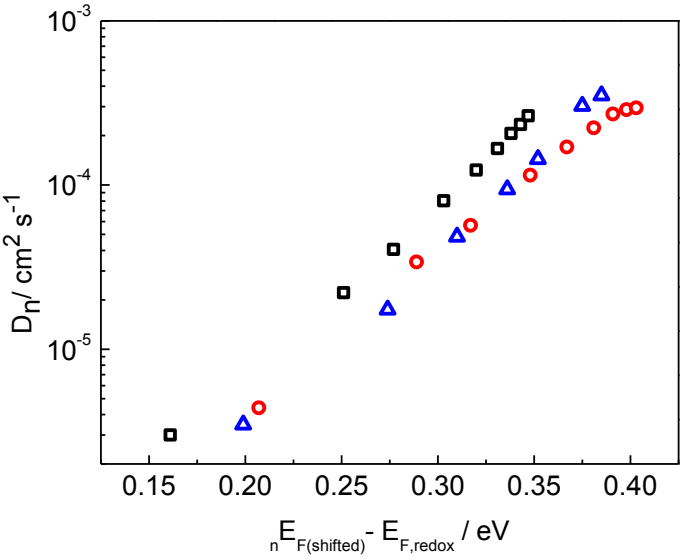

Figure 9.13 Diffusion coefficient obtained from the IMPS response as a function of the Fermi level position. The shift in C1 has been corrected for.

According to the multiple trapping model, the diffusion coefficient D_n must be related to the trap distribution parameter α by **Equation 2.48** ($D_n = D^o \exp((1-\alpha)({}_nE_F - E_{F,redox})/kT)$)[46-48]. Therefore, diffusion coefficients should increase with applied bias with a slope proportional to 1-α. However, D_n values for the three cells exhibit smaller slopes than the ones predicted from the distribution parameter as obtained from the capacitance data (**Table 9.4**). An α value of 0.37, 0.43 and 0.34 is obtained for C1, C2 and C3, respectively. This could be again an indication of the non-ideal behaviour of conduction band electrons as mentioned above.

The time constant measured by IMPS can be expressed as the product of the transport resistance of electrons in the semiconductor film and the film capacitance[26,41,49]

$$\tau_{IMPS} \cdot \gamma = R_t \cdot C_\mu \qquad (9.2)$$

Therefore, a way to obtain the transport resistance is to combine the time constant obtained from the IMPS measurements and the capacitance data obtained from the impedance response. It has to be noted that such a strategy comprises an approximation in so far as it is ignored that IMPS takes into account non-homogeneous illumination

via the IMPS factor whereas the impedance model[49] actually only applies for homogeneous illumination. This could introduce an error in the estimation.

As the first technique is a short circuit measurement and the second is carried out at open circuit, a third measurement, the short circuit voltage V_{sc}[36] is necessary to relate the two parameters to the same trap occupancy (i.e. to the position of the Fermi level relative to the conduction band) (**Section 9.6**). Taking into account this shift between open circuit and short circuit, the IMPS relaxation constant and the capacitance at the same quasi-Fermi level can be related in order to extract R_t according to **Equation 9.2**. In order to obtain a set of values for R_t in the range of interest, the IMPS time constant as a function of voltage is fitted to an exponential, which was extrapolated to obtain values in the range where capacitance data were determined. The resulting transport resistances can be found in **Figure 9.14**. In the inset, data were corrected taking into account the displacement of the conduction band. After this correction, all samples show a similar transport resistance, indicating that the conduction band offset obtained from the capacitance data for C1 (**Figure 9.4**) is consistent with the shift observed in the transport resistance data.

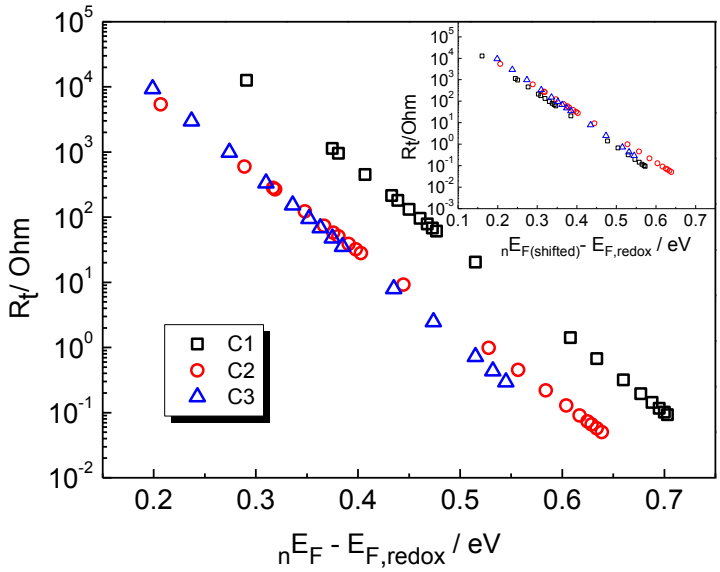

Figure 9.14 Transport resistance for the three configurations obtained from EIS and IMPS data. In the inset, data were corrected taking into account the displacement for the conduction band for C1.

In **Figure 9.15** a comparison between the transport resistances obtained from this method, and those obtained from the impedance fitting is shown for configuration C2.

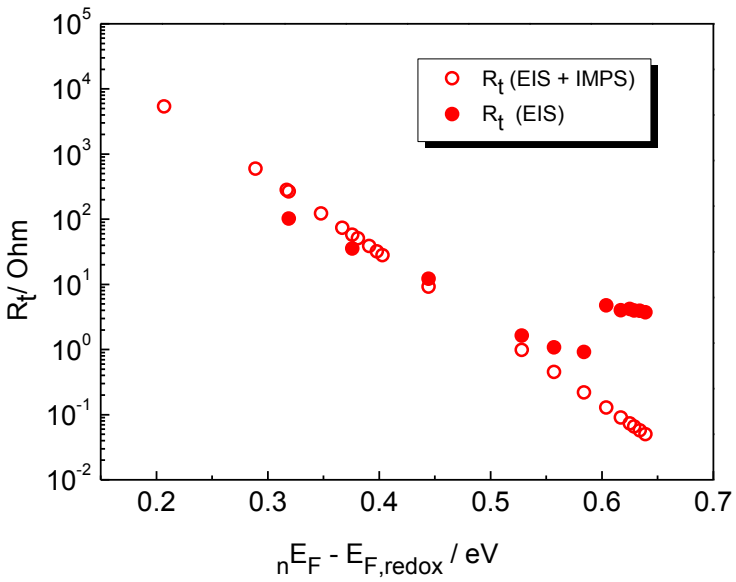

Figure 9.15 Transport resistance for C2 obtained from EIS fitting and from the combination of IMPS and EIS data.

As can be seen in **Figure 9.15** both methods lead to similar transport resistances at low voltages. This seems to indicate that the charge transport resistance extracted from impedance measurements could be considered basically correct even if the Warburg feature is not observed in the plot. On the other hand, the new method proposed here can be very useful to avoid the interferences of the cathode resistance in the fitting of impedance data.

Table 9.7 Slopes obtained from the fitting of the transport resistances plotted in **Figure 9.14**.

Cell	Slope (mV)
C1(ZnO/N719/OLE)	35
C2(ZnO/D149/OLE)	37
C3(ZnO/N719/ILE)	33

In **Table 9.7** the slopes of the corresponding semilogarithmic plots of the transport resistance (**Figure 9.14**) are indicated. Values are considerably higher than the ideal value (**Equation 2.31**), which was found in previous studies on TiO_2 cells[17,23,27]. However, those transport resistances were measured in the dark. Fabregat et al.[23] observed an ideal behaviour of the transport resistance in the dark for TiO_2, but it departed from ideality when impedance measurements were carried out under illumination. Several explanations could be proposed to account for the anomalous behaviour of the transport properties. First of all, it must be borne in mind that non-

ideality can arise from interactions between electrons and these are more likely to be important in ZnO due to its lower dielectric constant with respect to TiO_2. Strong interactions between electrons might lead to a non-constant diffusion coefficient of electrons in the conduction band. In addition, non-ideal transport properties can be a consequence of a non-ideal behaviour of the free electron concentration with respect to the Fermi level energy (i.e. n_c might not be equal to $N_c \, exp \, (E_c\text{-}E_f/kT)$ as expected for an ideal system, **Equation 2.15**)[32,44]. All these factors are likely to influence in the non-ideal behaviour of diffusion coefficient and transport resistance observed here.

9.8. Small amplitude electron diffusion length

For conditions of small perturbations with respect to an uniform background density, the electron diffusion length can be obtained from the effective values of the electron lifetime and the electron diffusion coefficient measured at coincident positions of the Fermi level[10,12,50] ($L_n = (\tau_n \, D_n)^{1/2}$, **Equation 2.50**). As the diffusion coefficient is obtained from IMPS (short circuit) and the lifetime is obtained from IMVS (open circuit measurement), it is necessary again to take into account the displacement of the Fermi level at short circuit with respect to open circuit. A fit line to the data was used to extrapolate and obtain a continuous function describing the relationship of D_n and τ_n with the electron quasi Fermi level along all the energy range of interest (**Figure 9.16a**).

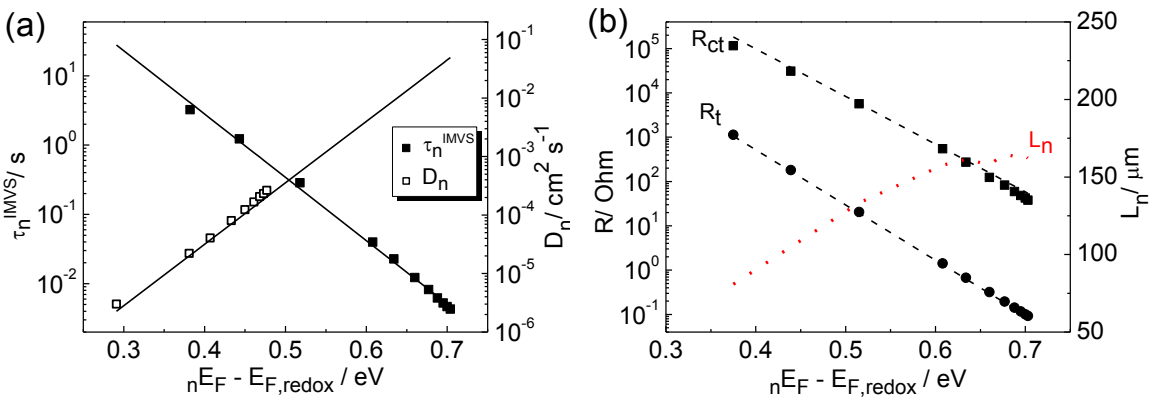

Figure 9.16 (a) Experimental data (symbols) and fit (line) of the diffusion coefficient and electron lifetime for C1 as a function of the Fermi level energy. (b) Charge transfer resistance (R_{ct}), transport resistance (R_t) and resulting diffusion length (L_n) for C1. A similar approach has been made for the rest of configurations.

On the other hand, the electron diffusion length can also be estimated from the EIS and IMPS data according to **Equation 3.12** ($L_n/d = (R_{ct}/R_t)^{1/2}$)[23,26] where R_{ct} is the charge transfer resistance obtained from EIS measurements and R_t is the electron

transport resistance obtained by combining capacitance data and transport times from IMPS, as explained above **(Figure 9.16b)**. The small amplitude diffusion lengths obtained from both methods are plotted in **Figure 9.17** for the three types of cells. It has to be noted that a correction accounting for the band shift was made in the case of configuration C1.

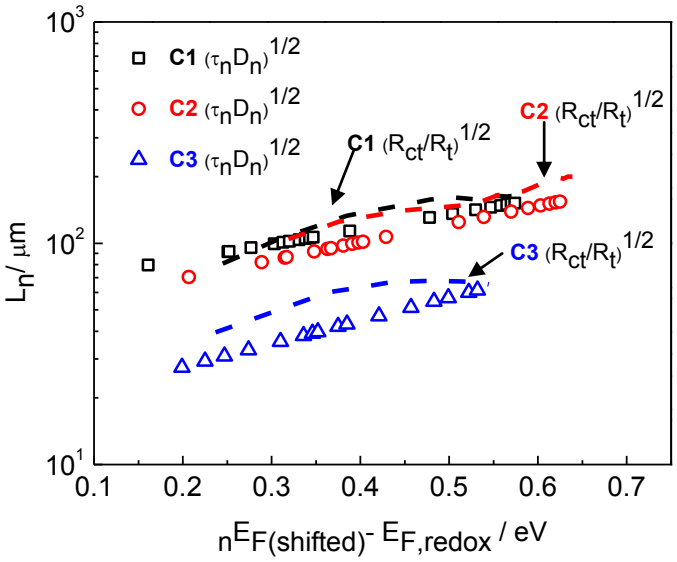

Figure 9.17 Small-perturbation electron diffusion lengths for the solar cells studied in this work from EIS (lines) and EIS + IMPS (symbols).

The agreement between both techniques is good, especially for C1 and C2. Regardless of the method used, the diffusion length is found to increase with applied voltage as expected from a non-linear recombination mechanism[10,12,50] (**Section 2.5**). More interestingly, the diffusion lengths are found to be much longer than the film thickness, suggesting 100% collection efficiency. For the ionic-liquid configuration (C3), the stronger recombination pointed out in **Sections 9.4** and **9.5**, reduces the diffusion length significantly, but it is still considerably larger than the film thickness.

9.9. Simulation of the IV curve

The determination of transport and recombination parameters makes it possible to attempt the simulation of the IV curves for the three configurations studied by solving the continuity equation for electrons in the semiconductor film[51-53](**Section 2.6**). The continuity equation is solved for a density dependent diffusion coefficient $D(n)$ and a *pseudo* first order kinetic recombination constant $k_r(n)$. The density dependence of these magnitudes is related to their Fermi level dependence according to the experimental

measurements in **Figures 9.13** and **9.9** for the diffusion coefficient and the electron lifetime, respectively. The diffusion coefficient is modelled according to **Equation 2.48**, whereas $k_r(n)$ (related to the inverse of the electron lifetime), is modelled via **Equation 2.58**. This equation implies that the recombination rate is non-linear in electron concentration, as was recently discussed in Refs. [10,12] and as inferred from our experimental results.

The continuity equation is solved in the space and time domain and the photocurrent is obtained from the gradient of the total density profile at $x = 0$ (**Appendix 11.13**). The IV curve is simulated by solving the equation at various applied voltages at $x = 0$, from V = 0 (short circuit) to open circuit conditions, these defined as the situation for which the photocurrent becomes zero (the parameter k_r^0 is adjusted to give zero current at the experimental open circuit voltage). To compute the density-dependent diffusion coefficient, the parameter D^0 in **Equation 2.48** represents the diffusion coefficient in the dark, when $E_F = E_{F,redox}$. The photocurrent is obtained once the steady-state condition is reached. The experimental short circuit photocurrent is matched by adjusting the dye loading in the film (assuming 100% injection quantum yield). The voltage drop due to series resistance is introduced by modifying the applied voltages by $V \rightarrow V + JR_sA$, where R_s is the series resistance of the cell and A is the active area of the cell.

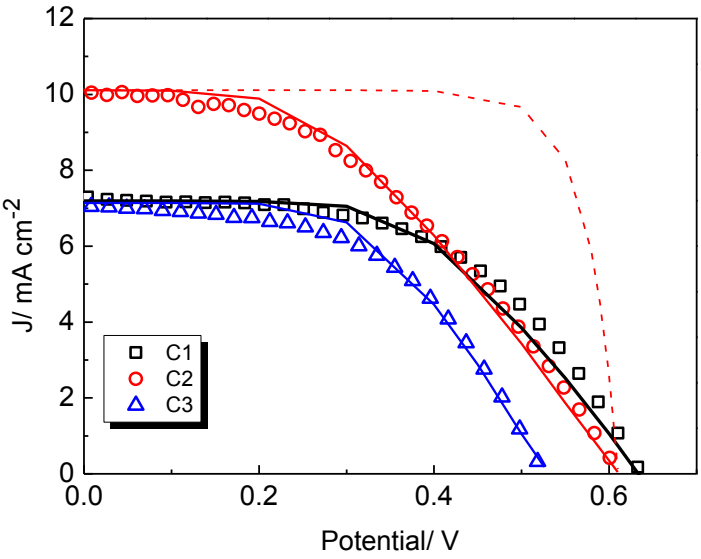

Figure 9.18 Experimental current-voltage curves for solar cells studied in this work (symbols) and simulations (lines). The simulation of C2 without any series resistance is also included (dashed line)

The following common parameters were used to simulate the three configurations: α = 0.12 (estimated from capacitance data, **Table 9.4**), β = 0.7 (estimated from ideality factors, **Table 9.3**), $D^0 = 10^{-7}$ cm^2 s^{-1} (estimated from **Figure 9.13**) and $n_0 = 10^{15}$ cm^{-3}. Results for the simulations are shown in **Figure 9.18**. When solving the equation without any series resistance, the resulting IV curve reproduces a non-ideal diode with a factor *m* approximately equal to *1/β*, as can be seen in **Figure 9.18** (dashed line) for C2. The values obtained for the adjustable parameter k_r^0 are $1.4\cdot10^{-3}$ s^{-1}, $4\cdot10^{-3}$ s^{-1} and $3\cdot10^{-2}$ s^{-1} for configurations C1, C2 and C3, respectively. According to **Equation 2.58** these values lead to a pseudo-first order electron lifetime of $1.7\cdot10^{-3}$ s, $5\cdot10^{-3}$ s and $3.3\cdot10^{-4}$ s at the experimental V_{oc} (1 sun illumination, **Figure 9.1**) for configurations C1, C2 and C3, respectively (**Table 9.8**). By fitting the photocurrent at the maximum power point, the series resistance acting in the cell can be extracted and the full IV curve reproduced. Values of R_sA = 28.5 Ω cm^2 were obtained for C1 and C2, and R_sA = 20.5 Ω cm^2 for C3. A summary of the different fitting parameters with the respective experimental values can be found in **Table 9.8**.

Table 9.8 Kinetic recombination constant $k_r(n)$, lifetimes (τ) and R_s·A obtained from the fitting and from EIS measurements (**Figure 9.9**) at V_{oc} at 1 sun illumination (**Figure 9.1**). The values for C1 correspond to the electron lifetime before the correction of the Fermi level shift.

Cell	k_r^0 (s^{-1})	τ (s) (at V_{oc}) (fitting)	τ (s) (at V_{oc}) (obtained from EIS)	R_sA (Ω cm^2) (fitting)	R_sA (Ω cm^2) (experimental)
C1	$1.4\cdot10^{-3}$	$1.7\cdot10^{-3}$	$2.4\cdot10^{-2}$	28.5	25.1
C2	$4\cdot10^{-3}$	$5.0\cdot10^{-3}$	$1.0\cdot10^{-2}$	28.5	13
C3	$3\cdot10^{-2}$	$3.3\cdot10^{-4}$	$3.2\cdot10^{-3}$	20.5	21.3

The obtained lifetimes are one order of magnitude lower than the experimental ones. In the case of C3, ion transport in the electrolyte is likely to have a significant contribution, which is ignored in this modelling. A more detailed model such as the one reported recently by Barnes et al.[32] is probably required to correctly simulate the IV curve in this case.

The series resistance R_s would correspond to the sum of the TCO resistance, the contribution of the counter-electrode, and the resistance of the electrolyte (**Section 3.6.1**). The fitting values (**Table 9.8**) are very close to those that can be extracted from the impedance spectra in **Figure 9.3**. The result of the modelling indicates that the main

reason for the low fill factor of the cells (**Figure 9.1**) is the series resistance, rather than the non-linearity of recombination. However, additional factors may contribute to a low fill factor such as a poor injection when the voltage approaches the open-circuit value[54].

The Fermi level profiles for configuration C1 that arise from the numerical solution of the continuity equation at open circuit and short circuit are shown in **Figure 9.19**.

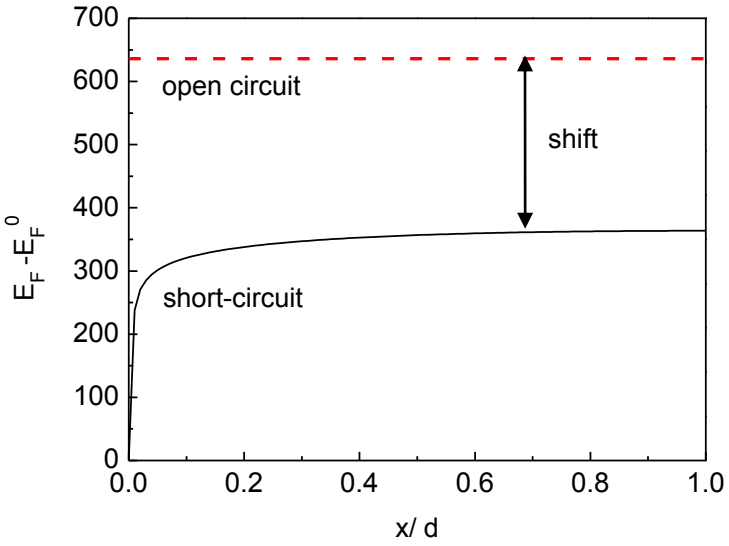

Figure 9.19 Fermi level profiles at short-circuit and open circuit for configuration C2. The approximate Fermi level shift is indicated in the graph.

A Fermi level shift of 0.273 V is predicted between short circuit and open circuit conditions. This value is quite close to the experimentally determined shift of 0.227 V (**Figure 9.10c**).

9.10. Conclusions

In this Chapter ZnO-based dye solar cells with different configurations, involving two dyes and organic as well as ionic-liquid-based electrolytes have been studied. The main aim of this work was to describe the recombination and transport properties of ZnO-based solar cells. In addition, it was studied if the same theories and approximations formulated for TiO_2 can be applied to describe the behaviour of ZnO cells. Finally, it was aimed to indentify the factors, which determine the lower performance of ZnO-based solar cells with respect to TiO_2.

Much higher photocurrents are obtained using the organic dye D149, pointing to the limitation of the ruthenium dye N719 as sensitizer for ZnO. The overall efficiency of the cells is greatly determined by the poor fill factors, especially when high

photocurrents are obtained. Simulation of the IV curves points out that the main reason for the low fill factor of the cells is the series resistance, rather than non-ideality effects. The origin of a high series resistance for the ZnO-based solar cells is not clear at the moment, but might be related with a poor injection in the case of sensitized ZnO. The fact that TiO_2 cells prepared by the same procedure, using the same substrates, sealing process and cell area, yield much higher fill factors for similar photocurrents (**Appendix 11.11**) seems to discard fundamental failures of the preparation procedure as potential origins of the high resistance. In addition, the FTO/ZnO system could be a critical parameter and more work is necessary to optimize the ZnO film properties as well as the FTO/ZnO interface.

Non-ideality effects are observed both in recombination and in transport properties. The light-intensity dependence of the photovoltage for ZnO cells is clearly non-ideal. This non-ideality is usually found for TiO_2 cells as well and may be a result of sub-linear recombination kinetics. In this study, it is found that the ideality factor depends on the dye and the electrolyte employed. Interestingly, V_{oc} profiles turn out to be more ideal for xanthenes dyes (**Chapter 5**) than for the other dyes studied here. If non-ideality is indeed caused by recombination via surface states, then a possible deterioration/damage of the surface by dye adsorption (which is expected to be more critical in the case of ZnO), may strongly influence this effect.

The transfer parameter obtained from the fitting of the charge transfer resistances (as extracted from EIS measurements) is an empirical estimation of the reaction order in sublinear recombination kinetics. This parameter is found to depend also on the composition of the different ZnO cells. It yields values different from the reaction orders obtained from the V_{oc} versus light intensity plots. This could be an indication that sublinear recombination kinetics with a possible involvement of surface states in electron transfer is not the only reason for non-ideality. One possibility is that the assumption of an ideal dependence of free electron concentration with respect to voltage is wrong. In this case additional factors need to be defined and taken into account in order to determine the relation between ideality factor and sublinear reaction order.

The voltage-dependence of the capacitances as measured from EIS is weakly exponential and very similar for all configurations. It must be noted that a movement of the conduction band edge under illumination can lead to a weaker voltage dependence

of the capacitance in comparison to the respective Fermi level dependence. However, according to the measured accumulated charge (**Appendix 11.12**), band shift effects appear to be negligible for this kind of ZnO nanoparticles. The observed behaviour of the capacitance has been attributed to localized band gap states in the ZnO structure. The trap distribution parameter obtained from EIS measurements of the capacitance does not predict the experimental profile of the open circuit voltage decay. This could be a further indication of non-linear recombination kinetics.

An excellent agreement was observed between the electron lifetimes determined independently using three different techniques (IMVS, OCVD and EIS measurements). The slope of a semilogarithmic plot of lifetimes versus voltage points again to non-linear recombination kinetics.

The transport resistance can be estimated by combining EIS and IMPS data. This approach circumvents the problem of transport resistance determination when a clear Warburg feature is not observed in the impedance spectra. Furthermore, it can be very useful to avoid the interferences of the cathode in the fitting of impedance data. Anyhow, similar values of the transport resistance are obtained at low voltages from both methods (EIS and EIS+IMPS). This seems to indicate that an estimation of the charge transport resistance can be obtained from impedance measurements at low voltages even if the Warburg feature is not observed.

A pronounced non-ideality is found for the transport properties in ZnO solar cells for all configurations. Several factors can contribute to this high non-ideality, e.g. strong electron-electron interactions in the conduction band due to the lower dielectric constant of ZnO as compared to TiO_2 and a non-ideal dependence of free electron concentration on voltage.

The electron diffusion lengths for the cells are much longer than the film thickness in all cases, including the ionic liquid configuration. Therefore, 100% collection efficiency is expected. Besides, electron diffusion lengths show an exponential increase with applied voltage that is indicative of non-linear recombination.

Once corrected for band displacements, recombination resistances, lifetimes and electron diffusion lengths indicate that solvent-free ionic-liquid electrolytes lead to

significantly more rapid recombination kinetics than the other configurations. As a consequence, a much lower photovoltage is obtained for this type of cells.

Applying a model based on the total electron concentration, the experimental IV curves have been fitted. The simulation yields a difference in the Fermi level at short circuit and open circuit that supports the viability of short circuit voltage measurements to estimate the position of the Fermi level at short circuit.

In summary, the behaviour of ZnO dye solar cells has been analyzed according to the same theories as used in TiO_2 dye solar cells. Different characteristic parameters, as for example a much smaller distribution parameter, have been obtained for ZnO with respect to TiO_2. In general, it is found that the diffusion model can only describe the behaviour of ZnO cells provided non-ideality of free electrons is empirically accounted for. Assuming the validity of the theoretical descriptions for ZnO, differences of the cell performance with respect to TiO_2 are not due to poor electron collection.

As can be seen in **Appendix 11.8**, the incident photon-to-current efficiencies are ~70% for C2, and only ~30% for C1 and C3 at the maximum of the dye absorption. As was described in **Chapter 2**, the IPCE depends on the efficiency of light absorption by the dye, on injection and on the efficiency of electron collection at the anode. For ZnO cells based on the N719 dye, the main limitation of the IPCE could be a low light harvesting efficiency of the sensitized films, together with a poor injection from the dye to the semiconductor due to the presence of Zn^{2+}/dye aggregates.

On the other hand, optical studies described in **Chapter 8** proved the good light harvesting properties of ZnO sensitized with the organic dye D149. According to absorptance measurements, an IPCE of 90 % is expected assuming 100% collection efficiency and 100% injection efficiency. In addition, dye coverage studies point to monolayer coverage of the ZnO surface by D149 dye molecules. Therefore, if diffusion lengths are several orders of magnitude longer than film thickness, the reason for the low IPCE values observed should be attributed to poor injection efficiency.

In addition to the energy difference between the LUMO level of the dye and the conduction band level in the semiconductor, the injection efficiency is determined by several parameters as, for example, the electronic structures of the dye molecule and the semiconductor, respectively. Although the position of the conduction band of ZnO is

similar to TiO_2, the density of states is one order of magnitude lower for ZnO[28]. Besides, a poor injection efficiency of ZnO can be associated to its lower dielectric constant with respect to TiO_2, which can affect charge separation dynamics. Ultrafast injection kinetics have been reported for ZnO[55,56]. However, recently Cai et. al[54] have demonstrated that the thermodynamic competition between charge transfer from the LUMO level of the dye to the conduction band and backward charge transfer from the conduction band to the LUMO level should be considered in the evaluation of injection efficiency. This back reaction will depend to a great extent on the electronic properties of the semiconductor and its coupling with the dye. Hence, the low dielectric constant of ZnO may enhance the back reaction, leading to lower injection efficiency. Furthermore, this effect will be larger at high voltages (close to open-circuit), so that an additional deterioration of the fill factor could be produced.

9.11. References to Chapter 9

1. Quintana, M., Edvinsson, T., Hagfeldt, A. & Boschloo, G. Comparison of dye-sensitized ZnO and TiO_2 solar cells: studies of charge transport and carrier lifetime. *The Journal of Physical Chemistry C* **111**, 1035-1041 (2007).
2. Oekermann, T., Yoshida, T., Minoura, H., Wijayantha, K.G.U. & Peter, L.M. Electron Transport and Back Reaction in Electrochemically Self-Assembled Nanoporous ZnO/Dye Hybrid Films. *The Journal of Physical Chemistry B* **108**, 8364-8370 (2004).
3. Oekermann, T., Yoshida, T., Boeckler, C., Caro, J. & Minoura, H. Capacitance and Field-Driven Electron Transport in Electrochemically Self-Assembled Nanoporous ZnO/Dye Hybrid Films. *The Journal of Physical Chemistry B* **109**, 12560-12566 (2005).
4. Galoppini, E., Rochford, J., Chen, H., Saraf, H., Lu, Y., Hagfeldt, A., & Boschloo, G. Fast Electron Transport in Metal Organic Vapor Deposition Grown Dye-sensitized ZnO Nanorod Solar Cells. *The Journal of Physical Chemistry B* **110**, 16159-16161 (2006).
5. Horiuchi, T., Miura, H., Sumioka, K. & Uchida, S. High Efficiency of Dye-Sensitized Solar Cells Based on Metal-Free Indoline Dyes. *Journal of the American Chemical Society* **126**, 12218–12219 (2004).
6. Guillén, E., Idígoras, J. & Anta, J.A. Solvent-Free ZnO dye-sensitised solar cells. *ECS Transactions* **25**, 111-122 (2010).
7. Zaban, A., Ferrere, S. & Gregg, B.A. Relative Energetics at the Semiconductor/Sensitizing Dye/Electrolyte Interface. *The Journal of Physical Chemistry B* **102**, 452-460 (1998).
8. Nakade, S., Kanzai, T., Kubo, W., Kitamura, T., Wada, Y. & Yanagida, S. Role of electrolytes on charge recombination in dye-sensitized TiO_2 solar cell (1): The case of solar cells using the I^-/I_3^- redox couple. *Journal of Physical Chemistry B* **109**, 3480–3487 (2005).
9. Saito, M. & Fujihara, S. Large photocurrent generation in dye-sensitized ZnO solar cells. *Energy & Environmental Science* **1**, 280-283 (2008).

10. Bisquert, J. & Mora-Seró, I. Simulation of Steady-State Characteristics of Dye-Sensitized Solar Cells and the Interpretation of the Diffusion Length. *The Journal of Physical Chemistry Letters* **1**, 450–456 (2010).
11. Walker, A.B., Peter, L.M., Lobato, K. & Cameron, P.J. Analysis of Photovoltage Decay Transients in Dye-Sensitized Solar Cells. *The Journal of Physical Chemistry B* **110**, 25504-25507 (2006).
12. Villanueva-Cab, J., Wang, H., Oskam, G. & Peter, L.M. Electron Diffusion and Back Reaction in Dye-Sensitized Solar Cells: The Effect of Nonlinear Recombination Kinetics. *The Journal of Physical Chemistry Letters* **1**, 748-751 (2010).
13. O'Regan, B.C. & Durrant, J.R. Kinetic and Energetic Paradigms for Dye-Sensitized Solar Cells: Moving from the Ideal to the Real. *Accounts of Chemical Research* **42**, 1799-1808 (2009).
14. Peter, L. "Sticky Electrons" Transport and Interfacial Transfer of Electrons in the Dye-Sensitized Solar Cell. *Accounts of Chemical Research* **42**, 1839-1847 (2009).
15. Jennings, J.R. & Wang, Q. Influence of Lithium Ion Concentration on Electron Injection, Transport, and Recombination in Dye-Sensitized Solar Cells. *The Journal of Physical Chemistry C* **114**, 1715–1724 (2010).
16. Cameron, P.J., Peter, L.M. & Hore, S. How Important is the Back Reaction of Electrons via the Substrate in Dye-Sensitized Nanocrystalline Solar Cells? *The Journal of Physical Chemistry B* **109**, 930-936 (2005).
17. Wang, M., Chen, P., Humphry-Baker, R., Zakeeruddin, S.M. & Gratzel, M. The Influence of Charge Transport and Recombination on the Performance of Dye-Sensitized Solar Cells. *ChemPhysChem* **10**, 290–299 (2009).
18. Bisquert, J. Chemical capacitance of nanostructured semiconductors: its origin and significance for nanocomposite solar cells. *Physical Chemistry Chemical Physics* **5**, 5360–5364 (2003).
19. Bisquert, J., Fabregat-Santiago, F., Mora-Sero, I., Garcia-Belmonte, G., Barea, E. M. & Palomares, E. A review of recent results on electrochemical determination of the density of electronic states of nanostructured metal-oxide semiconductors and organic hole conductors. *Inorganica Chimica Acta* **361**, 684–698 (2008).
20. Hagfeldt, A., Boschloo, G., Sun, L., Kloo, L. & Pettersson, H. Dye-sensitized solar cells. *Chemical Reviews* **110**, 6595-6663 (2010).
21. *Dye-Sensitized Solar Cells*. Edited by K. Kalyanasundaram. (EPFL Press: 2010).
22. Watson, D.F. & Meyer, G.J. Cation effects in nanocrystalline solar cells. *Coordination Chemistry Reviews* **248**, 1391–1406 (2004).
23. Fabregat-Santiago, F., Bisquert, J., García-Belmonte, G., Boschloo, G. & Hagfeldt, A. Influence of electrolyte in transport and recombination in dye-sensitized solar cells studied by impedance spectroscopy. *Solar Energy Materials and Solar Cells* **87**, 117-131 (2005).
24. González-Pedro, V., Xu, X., Mora-Seró, I. & Bisquert, J. Modeling High-Efficiency Quantum Dot Sensitized Solar Cells. *ACS Nano* **4**, 5783-5790 (2010).
25. Fabregat-Santiago, F., Bisquert, J., García-Belmonte, G., Boschloo, G. & Hagfeldt, A. Influence of electrolyte in transport and recombination in dye-sensitized solar cells studied by impedance spectroscopy. *Solar Energy Materials and Solar Cells* **87**, 117–131 (2005).
26. Bisquert, J. Theory of the Impedance of Electron Diffusion and Recombination in a Thin Layer. *The Journal of Physical Chemistry B* **106**, 325–333 (2002).
27. Wang, Q., Ito, S., Grätzel, M., Fabregat-Santiago, F., Mora-Seró, I., Bisquert, J., Besssho, T. & Iami, H. Characteristics of high efficiency dye-sensitized solar cells.

Journal of Physical Chemistry B **110**, 25210–25221 (2006).
28. Boschloo, G., Edvinsson, T. & Hagfeldt, A. Dye-sensitized nanostructured ZnO electrodes for solar cell applications. *Nanostructured Materials for Solar Energy Conversion* 227-254 (2006).
29. Wang, H. & Peter, L.M. A Comparison of Different Methods To Determine the Electron Diffusion Length in Dye-Sensitized Solar Cells. *The Journal of Physical Chemistry C* **113**, 18125–18133 (2009).
30. Bisquert, J. & Vikhrenko, V.S. Interpretation of the Time Constants Measured by Kinetic Techniques in Nanostructured Semiconductor Electrodes and Dye-Sensitized Solar Cells. *The Journal of Physical Chemistry B* **108**, 2313-2322 (2004).
31. Jennings, J.R., Liu, Y., Wang, Q., Zakeeruddin, S.M. & Gratzel, M. The influence of dye structure on charge recombination in dye-sensitized solar cells. *Physical Chemistry Chemical Physics.* (2011). DOI: 10.1039/C0CP02605K
32. Barnes, P.R.F., Anderson, A.Y., Durrant, J.R. & O'Regan, B.C. Simulation and measurement of complete dye sensitised solar cells: including the influence of trapping, electrolyte, oxidised dyes and light intensity on steady state and transient device behaviour. *Physical Chemistry Chemical Physics.* **13**, 5798-5816 (2011).
33. Guillén, E., Fernández-Lorenzo, C., Alcántara, R., Martín-Calleja, J. & Anta, J. Solvent-free ZnO dye-sensitised solar cells. *Solar Energy Materials and Solar Cells* **93**, 1846-1852 (2009).
34. Guillén, E., Azaceta, E., Peter, L.M., Arnost, Z., Tena-Zaera, R. & Anta, J.A. ZnO solar cells with an indoline sensitizer: a comparison between nanoparticulate films and electrodeposited nanowire arrays. *Energy Environmental Science.* (2011). DOI:10.1039/C0EE00500B
35. Peter, L.M. Characterization and Modeling of Dye-Sensitized Solar Cells. *The Journal of Physical Chemistry C* **111**, 6601-6612 (2007).
36. Boschloo, G. & Hagfeldt, A. Activation Energy of Electron Transport in Dye-Sensitized TiO_2 Solar Cells. *The Journal of Physical Chemistry B* **109**, 12093-12098 (2005).
37. Cao, F., Oskam, G., Meyer, G.J. & Searson, P.C. Electron Transport in Porous Nanocrystalline TiO_2 Photoelectrochemical Cells. *The Journal of Physical Chemistry* **100**, 17021-17027 (1996).
38. Fisher, A.C., Peter, L.M., Ponomarev, E.A., Walker, A.B. & Wijayantha, K.G.U. Intensity Dependence of the Back Reaction and Transport of Electrons in Dye-Sensitized Nanocrystalline TiO_2 Solar Cells. *The Journal of Physical Chemistry B* **104**, 949-958 (2000).
39. Wang, H., Nicholson, P.G., Peter, L., Zakeeruddin, S.M. & Grätzel, M. Transport and Interfacial Transfer of Electrons in Dye-Sensitized Solar Cells Utilizing a $Co(dbbip)_2$ Redox Shuttle. *The Journal of Physical Chemistry C* **114**, 14300-14306 (2010).
40. Schlichthörl, G., Park, N.G. & Frank, A.J. Evaluation of the Charge-Collection Efficiency of Dye-Sensitized Nanocrystalline TiO_2 Solar Cells. *The Journal of Physical Chemistry B* **103**, 782-791 (1999).
41. Dloczik, L., Ileperuma, O., Lauermann, I., Peter, L.M., Ponomarev, E.A., Redmond, G., Shaw, N.J. & Uhlendorf, I. Dynamic Response of Dye-Sensitized Nanocrystalline Solar Cells: Characterization by Intensity-Modulated Photocurrent Spectroscopy. *The Journal of Physical Chemistry B* **101**, 10281-10289 (1997).
42. Nakade, S., Kanzaki, T., Wada, Y. & Yanagida, S. Stepped Light-Induced Transient Measurements of Photocurrent and Voltage in Dye-Sensitized Solar Cells: Application for Highly Viscous Electrolyte Systems. *Langmuir* **21**, 10803-10807

(2005).
43. Lagemaat, J.V.D. & Frank, A.J. Nonthermalized electron transport in dye-sensitized nanocrystalline TiO_2 films: Transient photocurrent and random-walk modeling studies. *Journal of Physical Chemistry B* **105**, 11194–11205 (2001).
44. Jennings, J.R., Ghicov, A., Peter, L.M., Schmuki, P. & Walker, A.B. Dye-sensitized solar cells based on oriented TiO_2 nanotube arrays: Transport, trapping, and transfer of electrons. *Journal of the American Chemical Society* **130**, 13364–13372 (2008).
45. Barnes, P.R.F., Anderson, A.Y., Koops, S.E., Durrant, J.R. & O'Regan, B.C. Electron Injection Efficiency and Diffusion Length in Dye-Sensitised Solar Cells Derived from Incident Photon Conversion Efficiency Measurements. *The Journal of Physical Chemistry C* **113**, 1126-1136 (2009).
46. Anta, J.A., Mora-Sero, I., Dittrich, T. & Bisquert, J. Interpretation of diffusion coefficients in nanostructured materials from random walk numerical simulation. *Physical Chemistry Chemical Physics*. **10**, 4478-4485 (2008).
47. Ito, S., Zakeeruddin, S. M., Humphry-Baker, R., Liska, P., Charvet, R., Comte, P., Nazeeruddin, M. K., Pechy, P., Takata, M., Miura, H., Uchida, S. & Grätzel, M. High-efficiency organic-dye-sensitized solar cells controlled by nanocrystalline-TiO_2 electrode thickness. *Advanced Materials* **18**, 1202–1205 (2006).
48. Bisquert, J. Interpretation of electron diffusion coefficient in organic and inorganic semiconductors with broad distributions of states. *Physical Chemistry Chemical Physics.* **10**, 3175-3194 (2008).
49. Krüger, J., Plass, R., Grätzel, M., Cameron, P.J. & Peter, L.M. Charge Transport and Back Reaction in Solid-State Dye-Sensitized Solar Cells: A Study Using Intensity-Modulated Photovoltage and Photocurrent Spectroscopy. *The Journal of Physical Chemistry B* **107**, 7536-7539 (2003).
50. Jennings, J.R., Li, F. & Wang, Q. Reliable Determination of Electron Diffusion Length and Charge Separation Efficiency in Dye-Sensitized Solar Cells. *The Journal of Physical Chemistry C* **114**, 14665–14674 (2010).
51. Villanueva, J., Anta, J.A., Guillén, E. & Oskam, G. Numerical Simulation of the Current−Voltage Curve in Dye-Sensitized Solar Cells. *The Journal of Physical Chemistry C* **113**, 19722–19731 (2009).
52. Villanueva-Cab, J., Oskam, G. & Anta, J.A. A simple numerical model for the charge transport and recombination properties of dye-sensitized solar cells: A comparison of transport-limited and transfer-limited recombination. *Solar Energy Materials and Solar Cells* **94**, 45–50 (2010).
53. Anta, J.A., Casanueva, F. & Oskam, G. A numerical model for charge transport and recombination in dye-sensitized solar cells. *Journal of Physical Chemistry B* **110**, 5372–5378 (2006).
54. Cai, J., Satoh, N. & Han, L. Injection Efficiency in Dye-Sensitized Solar Cells within a Two-Band Model. *The Journal of Physical Chemistry C* **115**, 6033-6039 (2011).
55. Furube, A., Katoh, R., Yoshihara, T., Hara, K., Murata, S., Arakawa, H. & Tachiya, M. Ultrafast Direct and Indirect Electron-Injection Processes in a Photoexcited Dye-Sensitized Nanocrystalline Zinc Oxide Film: The Importance of Exciplex Intermediates at the Surface. *The Journal of Physical Chemistry B* **108**, 12583-12592 (2004).
56. Yoshihara, T., Katoh, R., Furube, A., Murai, M., Tamaki, Y., Hara, K., Murata, K., Arakawa, H. & Tahiya, M. Quantitative Estimation of the Efficiency of Electron Injection from Excited Sensitizer Dye into Nanocrystalline ZnO Film. *The Journal of Physical Chemistry B* **108**, 2643-2647 (2004).

Chapter 10

Discussion and Outlook

10. Discussion and outlook

In this thesis the photovoltaic performance of dye-sensitized solar cells based on the semiconductor ZnO in combination with different kinds of dyes and electrolytes has been studied in detail.

One of the main objectives of the thesis has been the search for a suitable dye for ZnO. Several dyes have been explored, including xanthene derivatives, ruthenium-complex dyes and indoline derivatives. It was found that the sensitization process with organic dyes is not as critical as with ruthenium-complex dyes, indicating a higher stability of the ZnO surface in the former case. In general, ruthenium dyes, as the common N719, were found not to be appropriate for ZnO due to the deterioration of the semiconducting film upon sensitization and the consecutive aggregation of Zn^{2+}/dye complexes in the pores. Among all the dyes studied, the best performing ZnO cells have been obtained with the organic dye D149. ZnO dye solar cells sensitized with this indoline derivative dye yield much higher photocurrents than cells with the ruthenium sensitizer N719. The sensitization of ZnO with D149 has been studied in detail. It turns out that in the case of D149 the photocurrent is independent of the sensitization time. Most likely the dye molecules form a monolayer on the surface of ZnO and aggregation seems to be insignificant. Efficient sensitization and very good absorption properties of D149 are the key factors for its higher performance with respect to the other dyes tested, including ruthenium-complexes.

The second aim of this thesis has been to evaluate the suitability of ionic liquid-based electrolytes for the development of ZnO solar cells with high long-term stability. The performance of these devices is found to depend not only on the viscosity of the ionic liquid, but also on the nature of the anions of the ionic liquid and their interaction with the semiconductor, respectively. A clear improvement of the photovoltage has been found with electroactive anions, which interact with the ZnO surface. However, this interaction can also provoke the desorption of dye molecules, especially when the interaction between ZnO and the sensitizer is very weak (as in the case of the D149 dye). In addition, a strong recombination, which causes low photovoltages, has turned out to be the main limitation of the ZnO solvent-free solar cells analyzed in this thesis. Remarkable efficiencies have been obtained, however, for solvent-free ZnO solar cells sensitized with the organic dye D149. Nevertheless, desorption of the dye turned out to

be critical, especially in the presence of electroactive anions, which interact with the ZnO surface. This instability in ionic liquid electrolyte prevented the fabrication of a completely solvent-free and stable ZnO solar cell based on an organic dye. The exploration of alternative ionic-liquid electrolyte compositions or the modification of the ZnO surface is, therefore, required for fabricating stable devices based on ZnO films sensitized with this organic dye. Besides, organic dyes with alternative anchoring groups may overcome the weak dye-oxide interaction observed. In this respect, preliminary tests with alternative dyes have been very promising, showing very good stability in the presence of ionic liquid electrolytes. Strong adsorption has been proved, for example, for an indoline dye coded D358 with two carboxylic groups in its structure (in contrast to only one carboxylic group in D149), and for perylene derivatives with anhydride groups instead of carboxylic groups (**Appendix 11.3.4**).

Taking into account that one of the most interesting properties of ZnO is its flexibility in synthesis and morphology, the influence of the semiconductor morphology on the performance of ZnO based solar cells has been studied. A comparative study of D149-sensitized ZnO electrodes based on nanowire arrays and electrodes based on randomly oriented nanoparticles have been carried out. The main conclusion of this study is that the performance of the one-dimensional nanostructures studied here is not limited by a low light harvesting as could have been expected as a consequence of the relatively low surface area. Nanowire-based solar cell performance seems to be limited by poor injection from the dye to the nanowires and/or strong recombination. Spin-coated nanoparticles deposited on the surface of the nanowires decrease significantly electron recombination and lead to an improvement of the photovoltage and fill factor of the cells and of the overall performance of the devices. This fact strongly suggests that surface modification may significantly improve the performance of the electrodeposited nanowire arrays studied here. Further research to establish whether poor injection is also contributing to the low performance of the nanowire-based solar cells is necessary.

Finally, a comprehensive study of the electronic and recombination properties of ZnO dye-sensitized solar cells was carried out. The behaviour of ZnO dye solar cells has been described using the same theories as used for TiO_2 dye-sensitized solar cells, but with different characteristic parameters: small values of the trap distribution parameter, similar recombination reaction order and stronger non-ideal effects in the transport

properties. The reliability of the transport resistance values obtained from impedance data is questionable because the transmission-line feature attributed to electron transport is not observed in ZnO impedance spectra. A simple analysis based on the combination of two techniques (EIS and IMPS) has turned out to be an appropriate strategy for the estimation of the electron transport in dye-sensitized solar cells. Interestingly, the estimated diffusion lengths for ZnO cells, including cells based on ionic liquid electrolytes, are significantly larger than the film thickness, indicating that collection efficiency approaches 100% in these devices.

After a complete study of the electronic, recombination and optical properties of ZnO solar cells, it is concluded that either light harvesting or poor injection efficiency are the limiting factors rather than electron collection efficiency. In conclusion, good electronic properties of ZnO have been shown in systems involving several combinations of dyes and electrolytes. Dye desorption in the presence of electrolyte, formation of ZnO/dye aggregates and a low injection efficiency constitute problems, which still have to be solved satisfactorily. In this regard, in this thesis some strategies have been suggested, which may help in the future to further optimize the performance and the stability of ZnO based dye-sensitized solar cells.

11. Appendix

11.1. Comparison between equivalent circuits

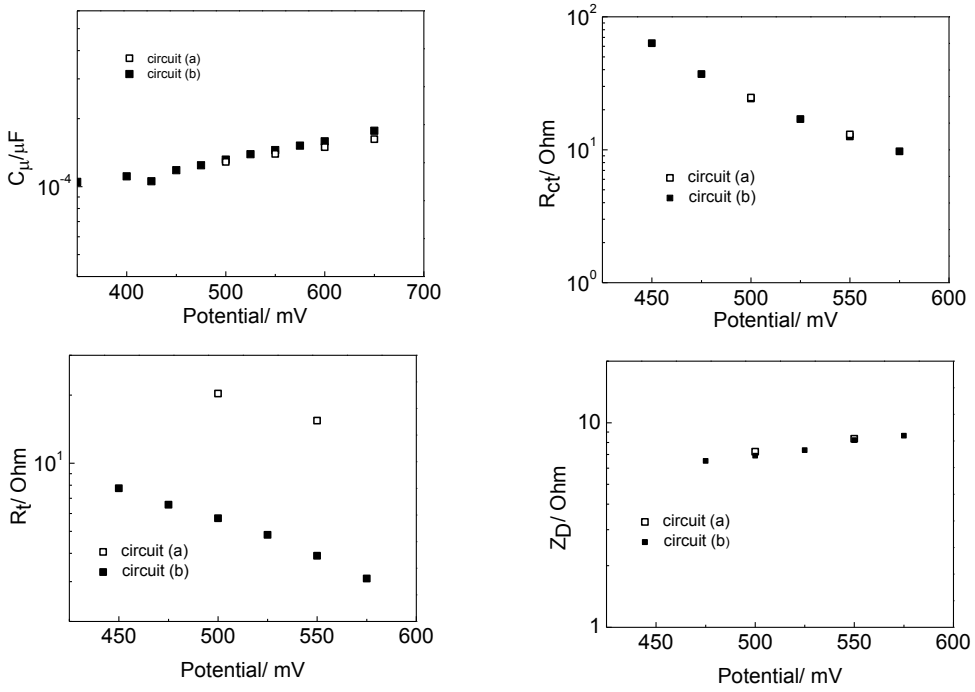

Figure 11.1 Comparison between the two equivalent circuits used in this thesis. Sample: FTO/ZnO nanoparticules/D149/PMII+I_2/ pt-FTO. (a) Charge transfer resistance, (b) capacitance, (c) transport resistance and (d) diffusion impedance in the electrolyte.

11.2. Optical profilometry measurements

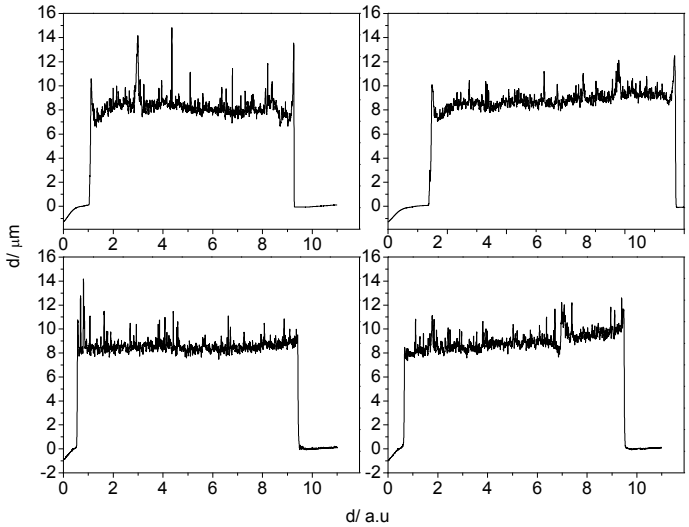

Figure11.2 Optical profilometry measurements for a film deposited by doctor blading from a colloidal suspension of a mixture of Evonik and PIKEM nanopowders. The graphs show four profiles for different scanning lines.

11.3. Sensitizers for ZnO dye-sensitized solar cells

11.3.1. Comparison of different forms of Eosin dye

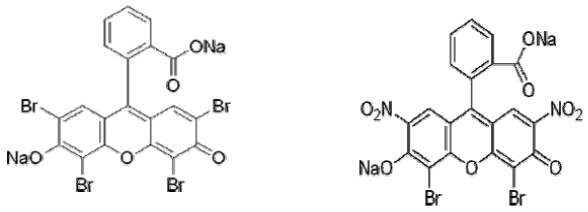

Eosin Y (salt form) Eosin B

Figure 11.3 Dye molecules of Eosins Y (salt form) and B.

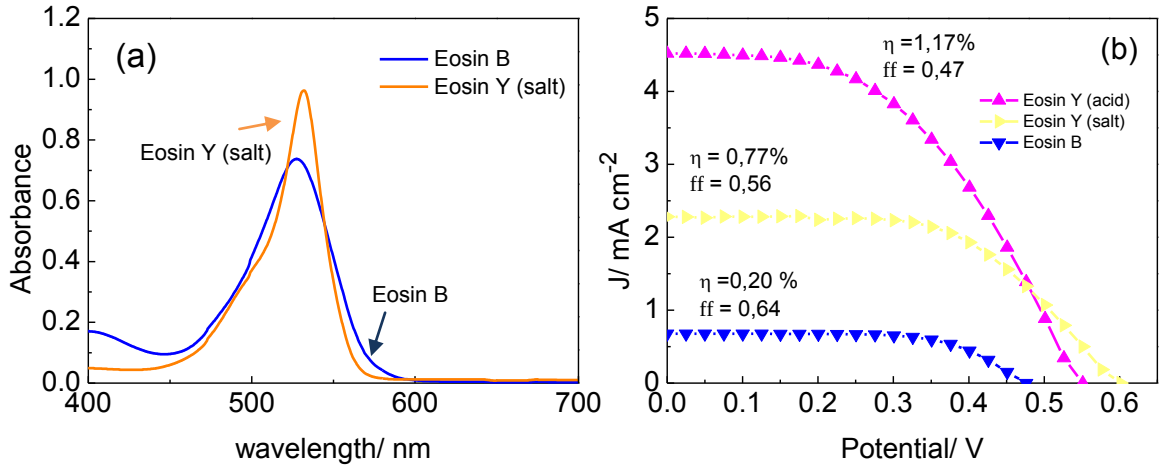

Figure 11.4 (a) Absorbance spectra of Eosin Y (salt) and Eosin B. (b) IV curves for the three types of Eosins.

11.3.2. N-Aryl Stilbazolium dyes

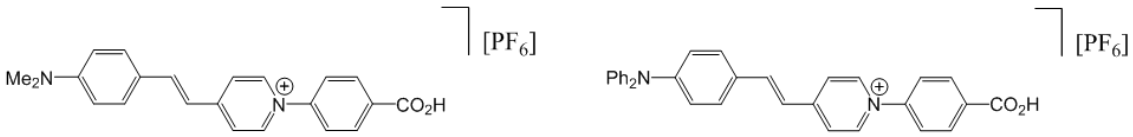

Figure 11.5 Molecular structures of (a) [7]PF6 and (b) [8]PF6 dyes.

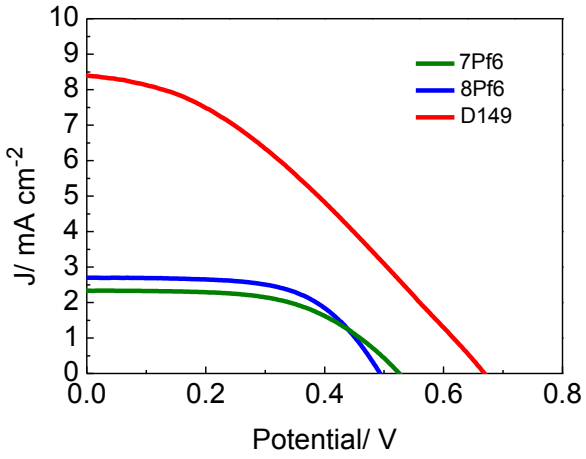

Dye	J_{sc} (mA cm^{-2})	V_{oc} (V)	FF
7Pf6	2.3	0.524	55.9
8Pf6	2.7	0.492	60.4
D149	8.4	0.668	35.1

Figure 11.6 and Table 11.1. IV curves and photovoltaic parameters of D149, [7]PF6 and [8]PF6 dyes. Electrolyte solution: 0.05 M I_2, 0.5 M TBAI in acetonitrile/ethylencarbonate (1:4). Dye solution: 0.5mM dye/ 1mM chenodeoxicholic acid in acetonitrile. Immersion time in dye solution: 30 minutes. Illumination: AM 1.5, 100 mW cm^{-2}.

11.3.3. ZnO sensitized with Ruthenium-based dyes

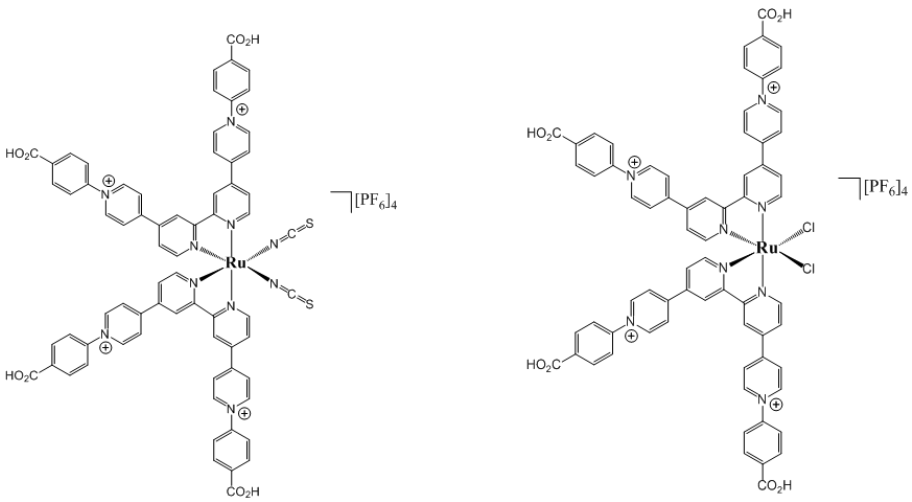

Figure 11.7 Ruthenium-complex sensitizers: YT-NCS (left) and YT-C1 (right).

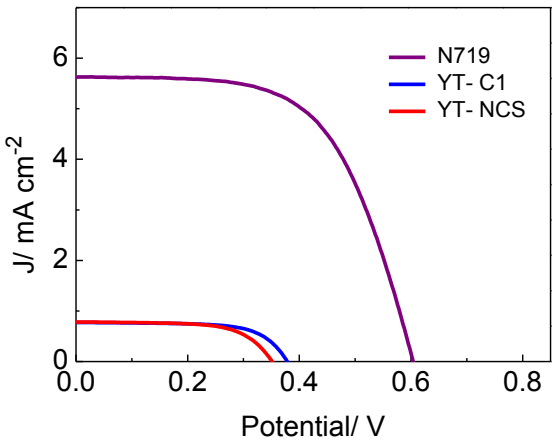

Dye	J_{sc} (mA cm^{-2})	V_{oc} (V)	FF	η%
N719	5.63	0.603	0.60	2.0
Yt-C1	0.77	0.378	0.66	0.2
NCS	0.78	0.351	0.64	0.2

Figure 11.8 and Table 11.2. IV curves and photovoltaic parameters of N719, YT-NCS and YT-C1 dyes. Electrolyte solution: 0.03M I_2, 0.6 M PMIMI, 0.1M GuSCN, 0.5M TBP in acetonitrile. Dye solution for N719: 0.5mM in ethanol. For the other two dyes: 0.5 mM in DMSO. Immersion time in dye solution: 60 minutes. Illumination: AM 1.5, 100 $mWcm^{-2}$.

11.3.4. ZnO sensitized with perylene derivatives

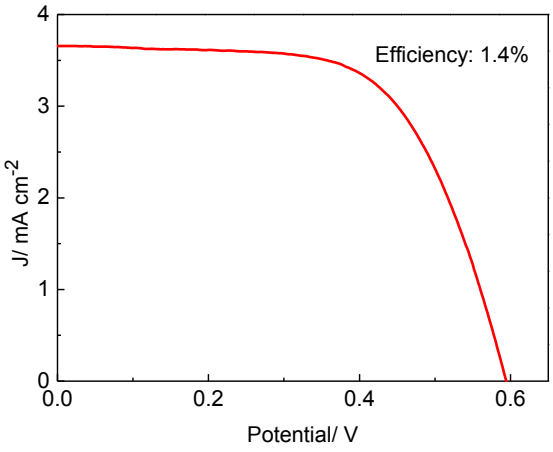

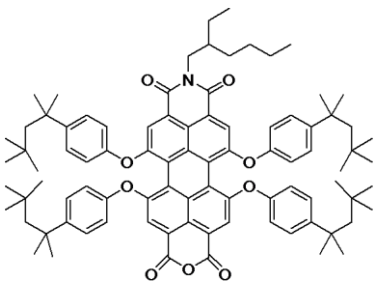

Figure 11.9 Current-voltage curve (left) of a ZnO cell sensitized with the perylene derivative dye shown on the right side. Electrolyte solution: 0.05 M I_2, 0.5 M TBAI in acetonitrile/ethylencarbonate (1:4). Dye solution: 0.05 mM in cyclohexane. Immersion time in dye solution: 60 minutes. Illumination: AM 1.5, 100 $mWcm^{-2}$.

11.4. Triiodide light absorption

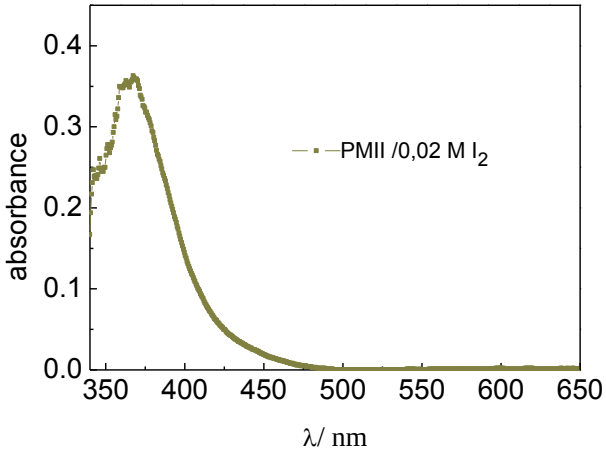

Figure 11.10 Absorption spectrum of PMII + I_2 (0.02M).

11.5. EIS Spectra as a function of the PMII content

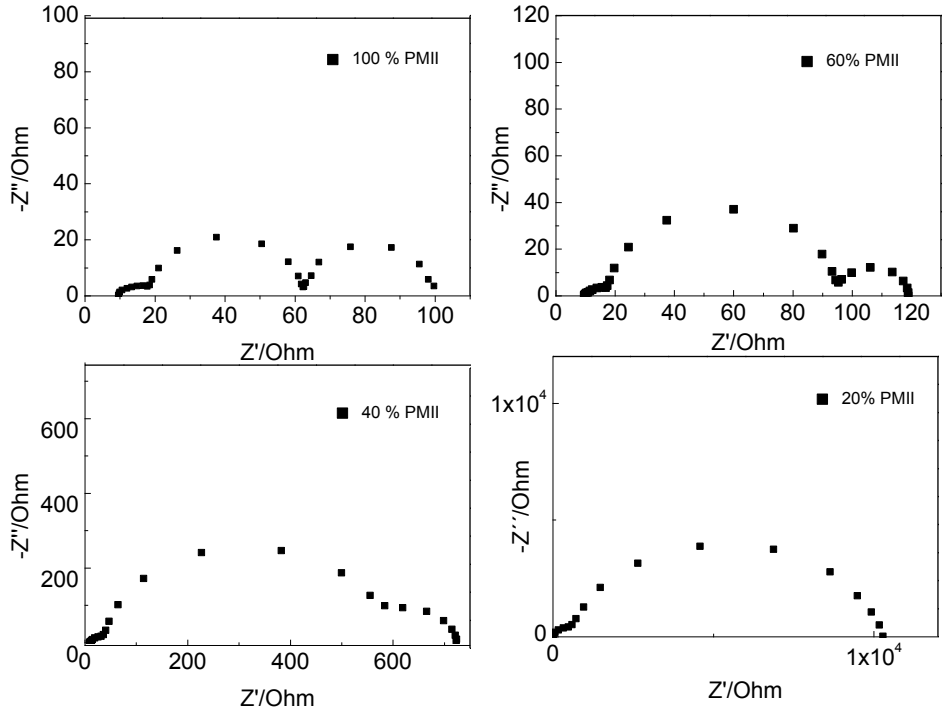

Figure 11.11 Evolution of the EIS spectra as a function of the PMII content. See **Chapter 6** for details.

11.6. The effect of annealing on the properties of NW arrays

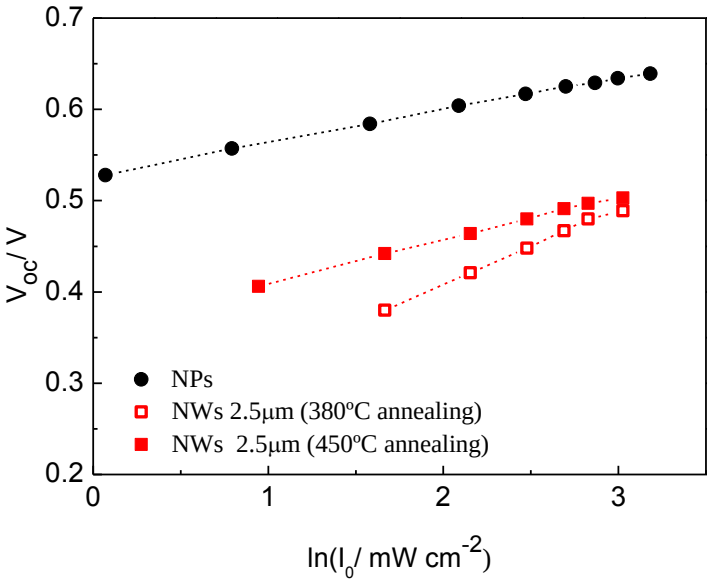

Figure 11.12 Open circuit photovoltage as a function of light intensity for nanoparticle and nanowire samples (2.5 μm) annealed a different temperatures.

11.7. The effect of electrodeposition on blocking layers

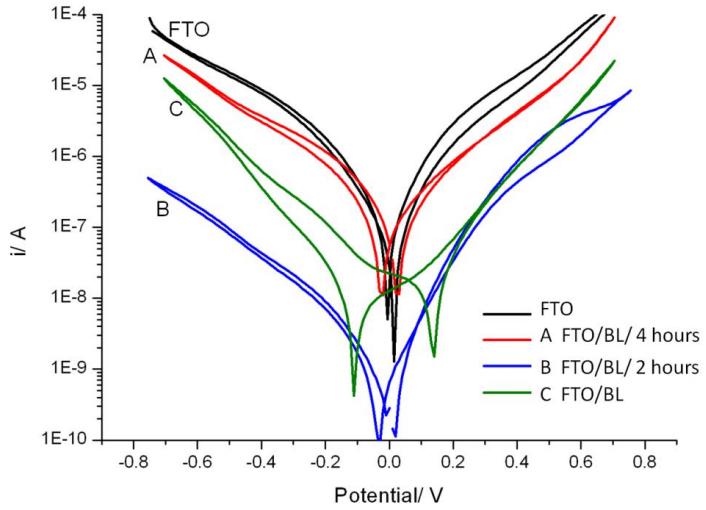

Figure 11.13 Tafel plots of current density versus cell voltage for thin-layer cells constructed with bare FTO, FTO/BL, FTO/BL after 4 hours of electrodeposition and FTO/BL after 2 hours of electrodeposition.

11.8. Incident photon-to-current spectra for ZnO-based solar cells

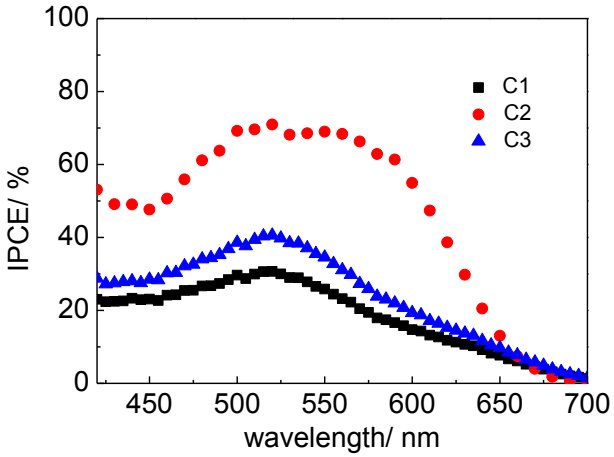

Figure 11.14 IPCE spectra for configurations C1, C2 and C3.

11.9. "Short circuit voltage" measurements for nanowire-based dye-sensitized solar cells

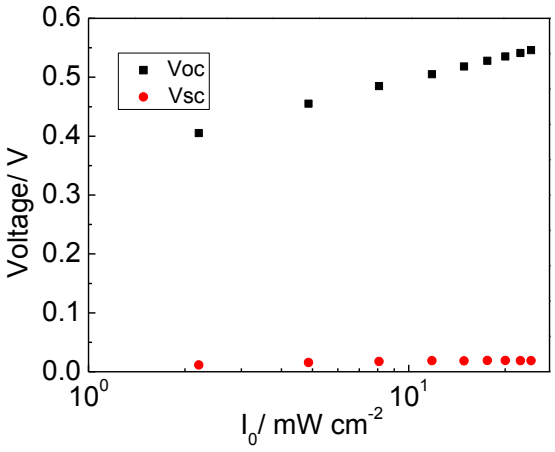

Figure 11.15 Short circuit voltage and open circuit voltage for the nanowires 5 μm length described in **Chapter 8**.

11.10. Numerical factor γ

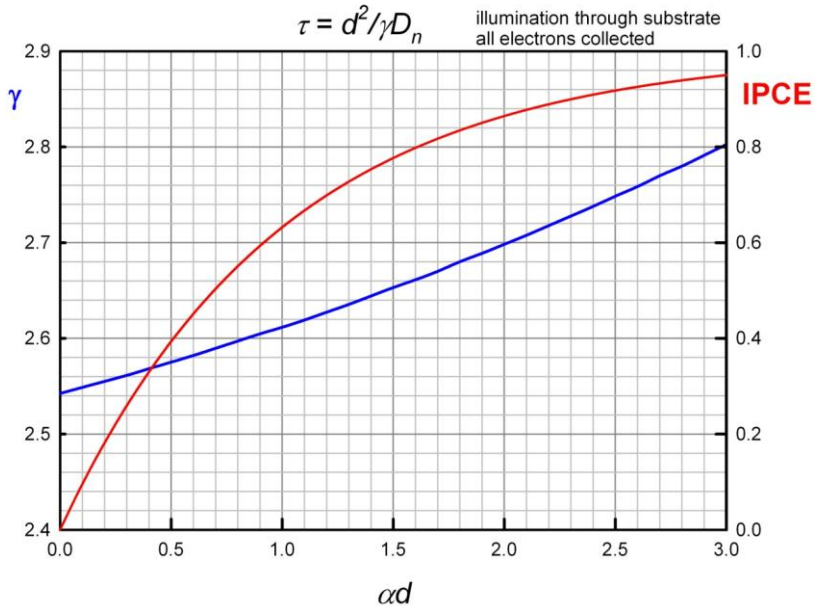

Figure 11.16 Plot of the numerical factor γ as a function of *αd* for substrate side illumination.

11.11. TiO_2-based dye-sensitized solar cell

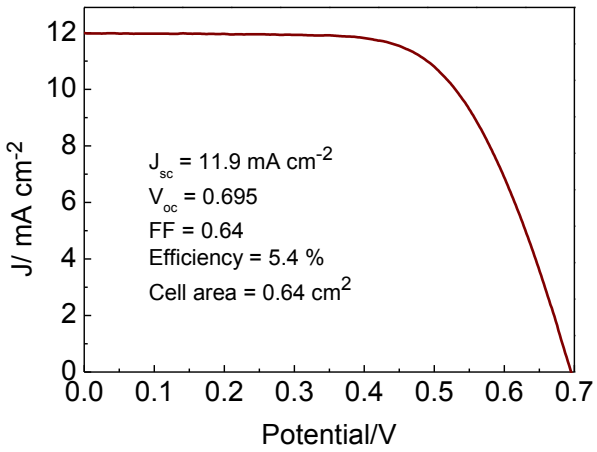

Figure 11.17 IV curve for a TiO_2 cell sensitized with N719. Electrolyte solution: 0.05 M I_2, 0.5 M TBP, 0.5 M LiI in acetonitrile. Dye solution for N719: 0.05 mM in ethanol. Immersion time in dye solution: 12 hours. Illumination: AM 1.5, 100 mW cm^{-2}.

11.12. Accumulated charge

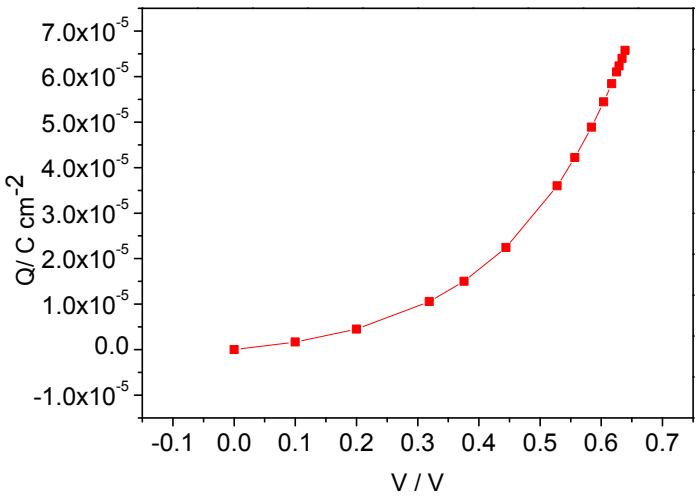

Figure 11.18 Accumulated charge obtained from the integration of the capacitance data from 0 to open circuit photovoltage.

11.13. Numerical solution of the continuity equation

The continuity equation in terms of the total electron density (**Section 3.6**) for configurations 1, 2 and 3 (**Section 10.9**) is solved by means of the Forward Time Centered Space (FTCS) method using the Lax scheme and with the following boundary conditions[1,2]

$$n(x=0,t)=n_v^0; \qquad n(x,t=0)=n_v^0; \qquad \left.\frac{\partial n(x,t)}{\partial x}\right|_{x=d}=0 \qquad (11.1)$$

where $n^0{}_V$ is the density at the TCO contact and d the film thickness. These boundary conditions are a consequence of fast electron transfer at the TCO/mesoporous oxide interface. The electron density at the contact, $n^0{}_V$, is an increasing function of the applied bias V, as shown below:

$$n_v^0 = n_0^0 exp\left(\frac{\alpha q V}{kT}\right) \qquad (11.2)$$

with n_0^0 being the density in the dark and at zero bias at the contact, q is the elementary charge, k the Boltzmann constant, T the absolute temperature and α the characteristic parameter of the trap energy distribution.

The numerical solution of **Equation (2.57)** with boundary conditions (11.1) and (11.2) gives rise to an electron density profile whose gradient at x=0 ($J_{sc}=(\partial n/\partial x)_{x=0}$) originates the photocurrent. The application of an external bias increases the electron density at the contact and reduces the gradient, so that the photocurrent becomes smaller. The numerical solution for increasing bias makes it possible to obtain the full current-voltage curve from the short circuit situation, in which V = 0 up to the open circuit situation, for which the photocurrent computed from the electron density gradient is approximately equal to zero.

The generation term $G(x)$ (electrons m^{-3} s^{-1}) is evaluated form

$$G(x) = \int_{\lambda_{min}}^{\lambda_{max}} \phi_{inj} I_0(\lambda) \alpha_{cell}(\lambda) exp(-\alpha_{cell}(\lambda)x)\ d\lambda \qquad (11.3)$$

where ϕ_{inj} is the electron injection quantum yield and α_{cell} is the absorption coefficient of the cell (m^{-1}) as a function of wavelength (λ). The incident photon flux $I_0(\lambda)$ (photons m^{-3} s^{-1}) is given by

$$I_0 = \frac{2\pi f c}{\lambda^4} \left(exp\left(\frac{hc}{\lambda kT}\right) - 1 \right)^{-1} \qquad (11.4)$$

where f is a parameter that is adjusted to give the required solar irradiance. The absorption coefficient of the cell α_{cell} can be related to the absorption coefficient of the dye in solution α_{sol} by

$$\alpha_{cell}(\lambda) = \alpha_{sol}(\lambda)\ \frac{C_{dye}(cell)}{C_{dye}(solution)} \qquad (11.5)$$

where C stands for the concentration of the dye either in solution or when adsorbed at the mesoporous oxide.

To complete the application of the numerical model, a series resistance, R, can be introduced into the calculation. In this case, the voltage V entering equation (11.2) is

replaced by $V=V+JAR$, where J is the current density and A the geometrical surface area. The continuity equation is solved for this new voltage and the new current obtained is utilized to modify the voltage. The process is repeated until consistency between successive values of J is achieved for a fixed value of R. This consistency was implemented here by assuming convergence of three significant figures in J.

11.14. The effect of blocking layers in nanoparticle-based DSCs

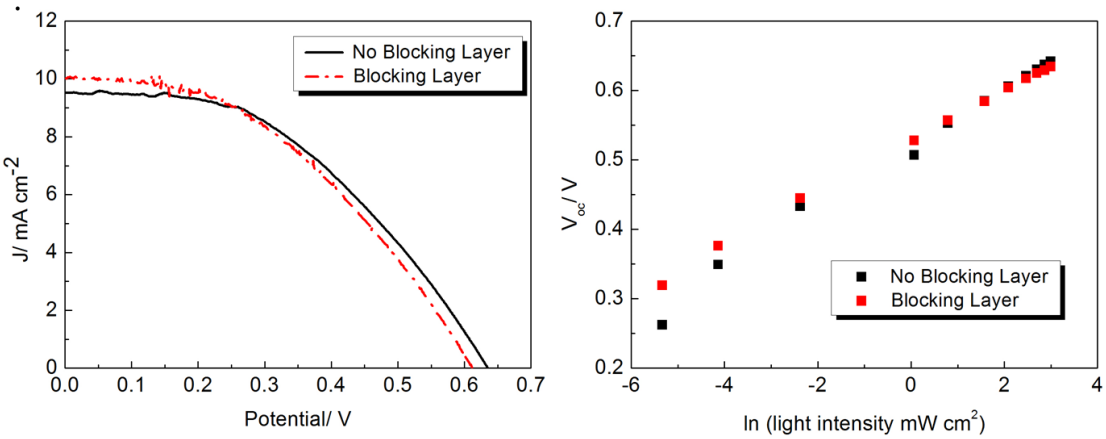

Figur 11.19 IV curves (left) and open circuit voltage versus light intensity (right) for a cell with and without blocking layer.

11.15. References to Appendix

1. Villanueva, J., Anta, J.A., Guillén, E. & Oskam, G. Numerical Simulation of the Current−Voltage Curve in Dye-Sensitized Solar Cells. *The Journal of Physical Chemistry C* **113**, 19722–19731 (2009).
2. Anta, J.A., Casanueva, F. & Oskam, G. A numerical model for charge transport and recombination in dye-sensitized solar cells. *Journal of Physical Chemistry B* **110**, 5372–5378 (2006).